Nageur Marangoni dans des écoulements externes

Camille Perret

Université Claude Bernard Lyon 1

THESE de DOCTORAT DE
L'UNIVERSITE CLAUDE BERNARD LYON 1

Ecole Doctorale N° 52
Physique et Astrophysique de Lyon

Discipline : Physique

Soutenue publiquement le 24/10/2024, par :
Camille PERRET

Marangoni swimmer in external flows

Devant le jury composé de :

Isabelle Cantat	Université de Rennes	Présidente
Emmanuelle Rio	Université Paris Saclay	Rapporteure
Matthieu Roché	CNRS	Rapporteur
Jean-Philippe Matas	Université Lyon 1	Examinateur
Étienne Reyssat	CNRS	Examinateur
Christophe Ybert	CNRS	Directeur de thèse
Cécile Cottin Bizonne	CNRS	Co-directrice de thèse
François Detcheverry	CNRS	Co-directeur de thèse

N° National de Thèse : 2024LYO10201

THÈSE DE DOCTORAT DE L'UNIVERSITÉ DE LYON

opérée au sein de

l'université Claude Bernard Lyon1

École Doctorale 52

Physique et Astrophysique de Lyon

Spécialité du doctorat : **Physique**

Présentée et soutenue publiquement le 24 Octobre 2024

par **Camille PERRET**

Marangoni swimmer in external flows

Directeur de Thèse : M. Christophe Ybert

Devant le jury formé de :

Mme.	Emmanuelle Rio	*Université Paris Saclay*	Rapportrice
M.	Matthieu Roché	*CNRS*	Rapporteur
Mme.	Isabelle Cantat	*Université de Rennes*	Examinatrice
M.	Jean-Philippe Matas	*Université Lyon 1*	Examinateur
M.	Étienne Reyssat	*CNRS*	Examinateur
M.	Christophe Ybert	*CNRS*	Directeur
Mme.	Cécile Cottin Bizonne	*CNRS*	Co-Directrice
M.	François Detcheverry	*CNRS*	Co-Directeur

Institut Lumière Matière
10 rue Ada Byron
69622 Villeurbanne CEDEX, France

École doctorale PHAST ED 52
4 rue Enrico Fermi
69622 Villeurbanne Cedex

Remerciements

En 2021, un peu perdue mais ravie d'avoir passé six mois à faire nager de petits bateaux avec du savon, j'ai décidé de tenter le concours de l'école doctorale. C'est ainsi qu'a débuté une aventure de trois ans sur les nageurs de Marangoni. C'est à l'issue de ma soutenance, que je me retourne sur ces années pour écrire ces mots.

Mes premiers remerciements vont à Christophe, Cécile et François, mes directeurs et directrice de thèse. Merci de m'avoir accompagnée et guidée pendant ces trois années avec une bienveillance incroyable. Sans vous, cette thèse n'aurait pas été la même. Merci de m'avoir offert une précieuse liberté pour explorer des projets parallèles, comme l'enseignement, la médiation scientifique et les activités avec la Teamdoc. Vous m'avez toujours encouragée, même lorsque ces projets empiétaient un peu sur mon temps de recherche. Vous m'avez également donné l'opportunité d'explorer les aspects scientifiques qui me tenaient à cœur et de trouver ma place au sein d'un projet déjà bien avancé. Vous avez été les meilleurs directeurs et directrice de thèse que j'aurais pu imaginer. Et si je n'étais pas totalement sûre de vouloir faire une thèse au départ, je ne regrette aucunement ce choix après la rédaction et la soutenance ! J'ai adoré écrire et présenter mon travail, créer une histoire et découvrir tous les liens et le contexte qui entourent ma recherche. . Dire au revoir aux nageurs a été bien plus difficile que je ne l'aurais imaginé.

Je tiens également à exprimer ma profonde gratitude à l'ensemble des membres de mon jury de thèse : Emmanuelle Rio, Matthieu Roché, Isabelle Cantat, Jean-Philippe Matas et Étienne Reyssat pour le temps consacré à rapporter ce manuscrit, à examiner et à présider ma soutenance.

Un grand merci à Maxime et Marianne pour votre travail lors de vos stages, votre dynamisme et le regard neuf que vous avez apportés. Vous avez été une véritable bouffée d'air frais à la fin de mes deuxième et troisième années. Pour reprendre la belle formulation de Clément, j'espère que "la dynastie des nageurs" continuera à grandir et que des doctorant · e · s et stagiaires liront ces lignes et poursuivront ce travail avec autant d'enthousiasme.

Un immense merci à toutes celles et ceux qui ont fait vivre la Teamdoc et qui ont repris le flambeau avec tant d'énergie, de créativité et de bonnes idées. Un mot particulier pour Chloé : désolée de t'avoir nommée présidente, mais je sais que tu seras absolument géniale dans ce rôle. Bon courage à toutes et à tous pour la suite de cette belle aventure !

De nombreuses personnes m'ont aidée tout au long de cette thèse, et il est difficile de toutes les citer, particulièrement dans une équipe aussi dynamique que “Liquides et Interfaces”. Une pensée toute particulière pour celles et ceux qui ont commencé en même

temps que moi : Julie, Gaëtan, Fred, Guillaume, Manon, Thomasso, Changwoo et Nasser. Merci pour votre bonne humeur, nos pauses café et le soutien indéfectible face aux hauts et aux bas de la thèse. Sur le plan scientifique, un grand merci à Hélène pour ton aide précieuse dans le développement de la méthode d'inversion, ainsi qu'à Gilles et Matthieu pour la fabrication du dispositif expérimental, ainsi que pour toutes les améliorations et réparations qui l'ont perfectionné.

Un immense merci à mes co-bureaux, Guillaume et Fred, qui ont rendu ces trois années passées devant un ordinateur inoubliables. Guillaume, merci pour les découvertes cinématographiques, humoristiques et musicales. J'ai adoré choisir des colormaps avec toi, découvrir de nouvelles fonctionnalités Python et LaTeX, et bénéficier de ton aide précieuse sur mes codes et modèles. Fred, merci pour les références musicales obscures, ta patience face à mes interruptions, et nos discussions animées. Vos blagues resteront probablement les aspects les plus mystérieux et incompréhensibles de cette thèse. Vive la bataille navale, Hearthstone, et les lancers de Maltesers !

Hors du laboratoire, un grand merci à la team médecine : Anne-Lise, Aline, Aude, Suzanne, Juliette et Émilie. Vous m'avez rappelé que la thèse, finalement, c'était un peu les vacances, et d'avoir essayé de comprendre ce que je faisais (non, ce ne sont pas des bulles). Bon courage pour vos fausses thèses à venir ça va être super ! Plein de bisous également à la team Medphy/Pâtisserie : Anh Thu, Meïsanne et Nabila. Nos brunchs ont été de vrais rayons de soleil lors de mes retours à Paris, vivement les prochains !

Enfin, je tiens à remercier ma famille et mes parents pour leur soutien indéfectible, même à distance. Vous avez toujours su trouver les mots pour m'encourager dans les moments difficiles, pour être venus à ma soutenance, et pour votre aide incroyable lors du pot de thèse.

Et pour finir... merci du fond du cœur à Maxime. Merci de m'avoir suivie à Lyon, d'avoir vécu cette thèse à mes côtés, et surtout, de m'avoir soutenue sans relâche pendant la rédaction et la soutenance. Sans toi je me serais nourrie de chips et de houmous pendant 4 mois et je n'aurais pas pu me donner à 1000% sur l'écriture.

Abstract

Interfacial swimmers are objects that self-propel at an interface by generating surface tension gradients, typically through the continuous release of surfactants. If the propulsion mechanism of symmetric swimmer is now well understood, the experimental characterization remains for now limited, as it focuses primarily on the swimming velocity. This global measure, however, conceals several underlying mechanisms that are intricately interconnected. A more detailed experimental characterization is needed which would provide deeper insights into the key physical mechanisms driving the complex problem of Marangoni swimmer. Moreover, the interactions of these interfacial swimmers with external potential remain unexplored. Accordingly, the goals of this thesis are twofold. First, to provide the first comprehensive characterization of a Marangoni swimmer in a stationary state, assessing the forces acting on the swimmer, the flow field, and the surfactant distribution. Second, to study the interaction of Marangoni swimmers with external couplings, such as a flow field or a harmonic potential. We design a novel experimental setup that allows simultaneous measurement of force and flow in a stationary state, offering a fresh perspective by examining a fixed swimmer in a controlled flow. Our approach reveals several key findings. First, the force exerted by the fluid on the swimmer changes sign when the flow velocity increases and cannot be simply reduced to the sum of capillary force and drag experienced by a passive disc. Second, we could measure the stationary interfacial flow fields under different advection conditions. Third, we develop a new approach that combines experimental data with numerical modeling to reconstruct the surface pressure field from the observed surface flow. Using an equation of state, we then derive the surface concentration field of surfactant, overcoming the curse of "hidden variables". Finally, we explore the swimmer behavior under external potentials, examining two scenarios: coupling with a spring and interaction with a water flow. In the spring scenario, the swimmer exhibits an ellipsoidal trajectory with amplitude decreasing with advection, a behavior that was qualitatively reproduced by a simple model, suggesting that the primary factors are the swimmer self-propulsion and the changes in surfactant distribution induced by advection. In the second scenario, we analyze the trajectories of the swimmer in simple shear flow and vortex conditions. Despite the system complexity, a toy model—disregarding the details of surfactant distribution and propulsion mechanisms and focusing only on spontaneous velocity and rotation by the flow—was able to capture the qualitative behavior of the swimmers.

Keywords: interfacial swimmer, Marangoni flows, hydrodynamics, concentration field, force balance.

Résumé

Cette thèse se situe à l'interface entre l'hydrodynamique et la matière active et s'intéresse à la propulsion spontanée de nageurs interfaciaux, aussi appelés nageurs Marangoni. Un gradient de tension superficielle génère des écoulements dans le liquide sous-jacent, un phénomène connu sous le nom d'effet Marangoni. Ce mécanisme est utilisé par certains insectes pour se propulser en relâchant un tensioactif derrière eux, créant ainsi un gradient de tension superficielle qui les propulse vers l'avant. En exploitant un principe similaire, on peut fabriquer des objets artificiels capables de libérer continuellement un tensioactif pour s'autopropulser : les nageurs de Marangoni.

Si les mécanismes de propulsion des nageurs de Marangoni sont bien compris qualitativement, une description quantitative complète reste encore à établir. Bien qu'il existe des modélisations théoriques et numériques des nageurs interfaciaux, il manque cependant des données expérimentales. La majorité des études réalisées s'intéressent principalement à la propulsion et caractérisent la vitesse de nage. Cette dernière est une variable globale qui masque de nombreux mécanismes sous-jacents étroitement interconnectés. Cette absence de données expérimentales rend difficile l'évaluation de la fiabilité des modèles existants et de leurs hypothèses sous-jacentes. De plus, les méthodes numériques actuelles sont limitées dans leur capacité à représenter fidèlement les systèmes expérimentaux, car elles ne peuvent atteindre les mêmes régimes. Par conséquent, ces méthodes n'offrent pas encore une compréhension approfondie ni une vision complète des phénomènes observés en laboratoire. Enfin, bien que les écoulements Marangoni soient impliqués dans des situations variées et aient suscité de nombreux travaux, leur compréhension théorique et leur modélisation continuent de poser des défis importants. Ce travail a donc pour objectif d'éclairer ces deux questions, avec une double implication : pour la matière active, en approfondissant notre compréhension de la dynamique des nageurs individuels et pour l'hydrodynamique, en explorant les écoulements de Marangoni associés au mouvement d'une source mobile. La problématique générale étant posée, nous résumons maintenant nos principaux résultats.

La première réalisation significative de cette thèse est la mesure expérimentale des forces agissant sur le nageur, des écoulements générés et de la distribution du tensioactif. Pour ce faire, nous avons développé un nouveau dispositif expérimental (Fig. 1) permettant de maintenir le nageur fixe dans un écoulement contrôlé de vitesse U. Le dispositif permet une mesure simultanée de la force appliquée par le fluide sur le nageur et des écoulements générés. Contrairement à de nombreuses études, nos résultats ne se limitent pas à la vitesse de nage.

En bref, nous avons observé que la force appliquée par le fluide sur le nageur change de signe, diminuant de 10 µN à $U = 4\,\mathrm{cm\,s^{-1}}$ à −30 µN à $U = 12\,\mathrm{cm\,s^{-1}}$. L'approche numérique montre que la force totale agissant sur le nageur ne peut être simplement décomposée en une force capillaire et la force de traînée subie par un disque passif. Les écoulements de Marangoni influencent significativement la force de traînée, indiquant leur rôle crucial dans la dynamique du nageur..

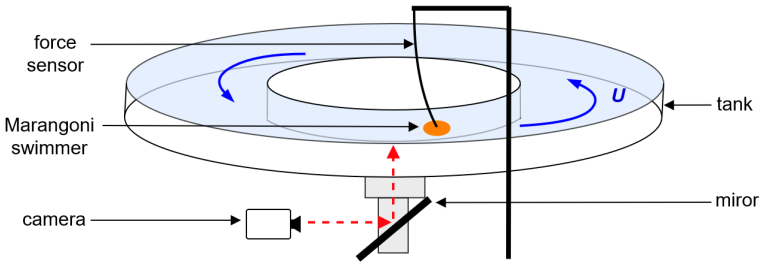

Figure 1: **Dispositif expérimental.** Le dispositif développé dans cette thèse permet de maintenir le nageur fixe tout en contrôlant la vitesse d'advection U du fluide et donne accès simultanément à la force appliqué par le fluide sur le nageur et aux écoulements générés.

Nous avons ensuite obtenu le champ d'écoulement interfacial complet dans un état stationnaire pour différentes vitesses d'advection. L'accès à la distribution des surfactants s'est révélé être l'aspect le plus difficile. Dans la majorité des travaux, la concentration des surfactants reste une « variable cachée » et une seule mesure 1D de la tension superficielle derrière un nageur Marangoni a été réalisée. Pour relever ce défi, nous avons introduit une approche hybride qui combine des données expérimentales avec une modélisation numérique pour reconstruire le champ de pression de surface à partir de la connaissance de l'écoulement de surface. Notre méthode permet de déduire un champ d'écoulement tridimensionnel à partir d'un écoulement bidimensionnel, accédant ainsi aux contraintes de Marangoni à l'interface. En validant cette méthode à la fois numériquement et expérimentalement sur un système bien connu, le bateau de Marangoni, nous avons démontré que notre approche reste fiable en présence de bruit et d'un échantillonnage limité, similaire aux conditions expérimentales.

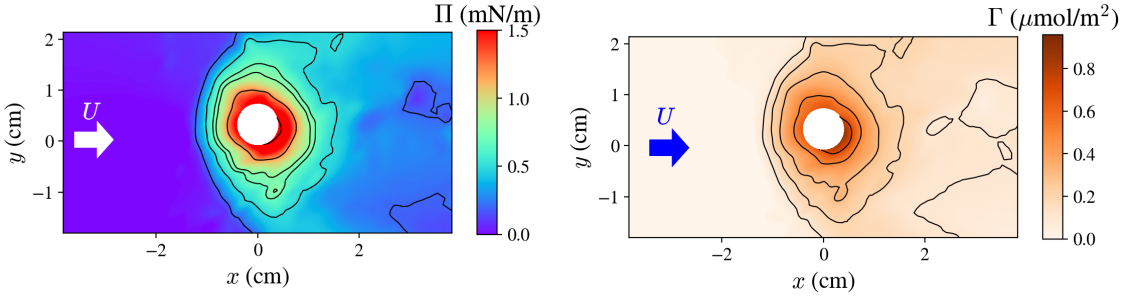

Figure 2: **Champs de pression de surface et de concentration.** Pour une vitesse d'advection U égale à la vitesse de nage, champs de pression de surface (gauche) et champs de concentration interfacial de camphre (droite). Le cercle blanc correspond au nageur.

Enfin, nous avons appliqué la méthode développée au nageur de Marangoni, obtenant

ainsi la première visualisation expérimentale du champ de pression de surface autour d'un nageur (Fig. 2 gauche) et de son sillage chimique (Fig. 2 droite). Cela nous a permis d'évaluer les composantes de la force agissant sur le nageur, telles que les forces de traînée et capillaires, tout en ouvrant de nouvelles questions sur la dynamique de transport des surfactants.

Le deuxième objectif était d'explorer la dynamique des nageurs de Marangoni dans un écoulement imposé. Cette exploration a pris deux formes. La première est un nageur attaché à un ressort dans un écoulement advectif, puis un nageur libre dans un écoulement de cisaillement simple et dans un vortex.

Un nageur attaché à un ressort présente un comportement inattendu, exhibant une trajectoire ellipsoïdale à faible vitesse d'advection, dont l'amplitude diminue quand l'advection augmente. De manière surprenante, le mouvement s'arrête avant que la vitesse d'advection n'égale la vitesse de nage. Bien que les écoulements de Marangoni soient connus pour induire des instabilités, ils ne sont pas le mécanisme principal dans ce cas. Le comportement observé est bien reproduit par un modèle simple qui ne tient pas compte des écoulements de Marangoni, suggérant que les facteurs principaux sont l'auto-propulsion du nageur et les changements dans la distribution des surfactants causés par l'advection.

La seconde situation expérimentale étudiée implique des nageurs Marangoni se déplaçant dans des champs d'écoulement : un écoulement de cisaillement simple et un autre plus complexe, un vortex. Les trajectoires des nageurs ont été significativement affectées par l'advection. Malgré la complexité du système, un modèle très simple qui ignore tous les détails de la distribution des surfactants et du mécanisme de propulsion—ne retenant qu'une vitesse spontanée et une rotation induite par l'écoulement—a réussi à capturer le comportement qualitatif des nageurs.

Contents

Chapter 1

State of the art

Table of Contents

1.1 Surface-driven self-propelled object

Active matter and swimmers. Active matter is a field of study that has developed tremendously over the past 30 years. It is concerned with the collective properties of assemblies of self-propelled particles capable of consuming energy to produce motion. Due to this energy consumption, these systems are intrinsically out of thermal equilibrium, breaking equilibrium properties such as detailed balance or time-reversal symmetry [1]. Active matter encompasses a broad range of objects, from biological molecular motors [2] and bacteria [3], to macroscopic ones like schools of fishes and flocks of birds [4]. One can easily imagine the experimental challenge to study the collective behavior of a hundred birds or fishes in the lab. Moreover, living organisms have complex behaviors due to cognition, making it difficult to isolate effects purely driven by activity. Therefore, much effort has been devoted to developing experimental models for active matter whose properties can be controlled and tailored. One intuitive approach is to mimic the mechanical actions that animals use to induce motion, such as the flagella of bacteria or the wings of birds. However, designing an artificial flagellum is complex; it requires building a nanoscale robot that replicates the structural complexity and mechanical adaptability of natural bacterial flagella [5, 6].

If we consider an object evolving in a fluid, a new possibility for propulsion arises: altering the local environment to induce motion [7]. This mechanism of self-propulsion has been widely explored [8–13] as producing an object without moving part and releasing passively a surface-active product is less difficult than designing nanorobots. In these cases the propulsion occurs either by generating gradients in the surrounding fluid that interact with the particle to create movement (self-phoretic effects) or by modifying interfacial properties to induce a force that propels the particle. Throughout this thesis, we will be interested in self-propelled objects that evolve in liquid environments, and we will use the word swimmer to designate them.

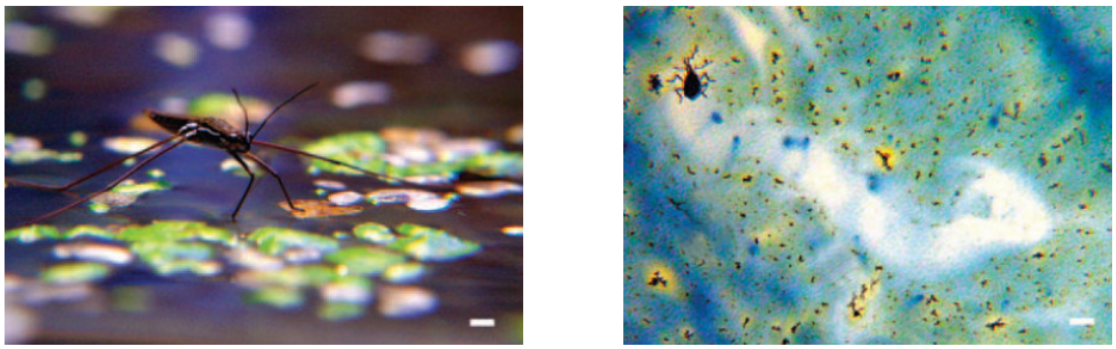

Figure 1.1: **Insect changing locally surface tension for transient self-propulsion.** (Left) *Gerris* using surface tension to maintain its body upon water. (Right) *Microvelia* using surface tension to self-propel. To visualise the motion, a blue dye is placed at the water surface, the surfactant released at the rear of the insect generates flows swiping away the dye present in the liquid, hence the white color behind the insect. Both pictures are taken from [14]. Scale bars correspond to 1 mm.

Propulsion by modifying the surface tension. If the object evolves at a liquid interface one property that can be used is the surface tension, characterizing the property of the interface between two fluids. Reducing surface tension is not a common method for displacement in nature, as it must remain high enough to support the animal weight and avoid sinking (Fig. 1.1 left). Nonetheless, some aquatic insects of a few millimeters, *velia* and *microvelia* [14], emit a chemical behind them which reduces the surface tension (Fig. 1.1 right). As a result, there is a surface tension difference between the front and the rear which propels the insect toward the high surface tension area and makes it move forward. This locomotion method allows *microvelia* to have a short transient motion at a speed of $17\,\mathrm{cm\,s^{-1}}$, which is twice their normal walking speed.

Marangoni propulsion. Similar to the transient propulsion observed in some aquatic insects, artificial objects can be designed for continuous propulsion by steadily releasing a substance into their environment. Creating a gradient of surface tension through the constant release of solute or heat is called Marangoni propulsion, which causes the object to propel from the area of lower surface tension to higher surface tension. A well-known example is the camphor boat, which has attracted interest in active matter studies [15–17] and is also popular with the general public as an easy experiment to make at home or during the "Fête de la science". A typical camphor boat, typically 2 cm in size, can achieve speeds of approximately $5\,\mathrm{cm\,s^{-1}}$.

Marangoni propulsion in the bulk. Aside from the interface, gradients of surface tension can also be harnessed to design objects that propel within the bulk of a fluid, such as Marangoni droplets. Compared to Marangoni swimmers evolving at the interface, Marangoni droplets have only recently appeared in laboratory [18]. Their design can be as simple as pure water droplets slowly dissolving in a surfactant-saturated oil phase, allowing them to swim for hours. Unlike interfacial swimmers, which often have directional propulsion, Marangoni droplets are isotropic by design and must spontaneously break symmetry to propel themselves [19, 20]. This propulsion is achieved through a nonlinear coupling of their physico-chemical dynamics with the resulting internal and external fluid motion [21]. Marangoni droplets are much smaller than most interfacial swimmers, with a typical radius $a \sim 10{-}100\,\mu\mathrm{m}$ and swimming velocity $V \sim 1{-}100\,\mu\mathrm{m\,s^{-1}}$.

Types of interfacial Marangoni swimmers. In this PhD, we focus specifically on swimmers operating at liquid surfaces, excluding the Marangoni droplets presented above. Since almost any chemical compound can alter surface tension to some extent, distinguishing these objects based solely on their chemical composition is not particularly informative. Instead, a more meaningful classification can be based on the shape of the swimmer and the method by which the surfactant is released. Marangoni swimmers can generally be categorized into three types (Fig. 1.2):

- **Dissolving swimmers** are the simplest to construct, as they are made entirely of surfactant. They can take the form of a droplet or solid scrap [22, 23]. However, studying these swimmers can be challenging because their size changes over time as the surfactant dissolves into the liquid.

- **Loaded swimmers** consist of a matrix, typically a gel or metal-organic framework [24–27], that is loaded with surfactant. Unlike dissolving swimmers, loaded swimmers retain their shape throughout the experiment, which simplifies the study of their motion. The soft nature of the matrix also enables the creation of various shapes, offering flexibility in design.
- **Boats** typically consist of a rigid or semi-rigid passive structure paired with an active component where the surfactant is released [28, 29]. Such a design allows for the controlled release of surfactant from specific locations on the swimmer, thereby generating directional propulsion.

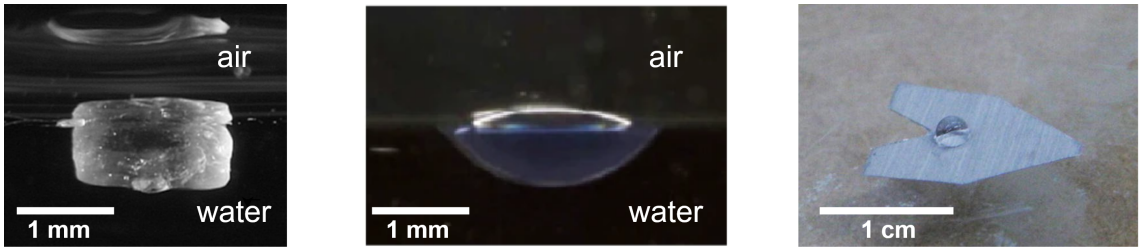

Figure 1.2: **Types of Marangoni swimmers.** Examples of the different types of Marangoni swimmers, from left to right: aspirin [23] (dissolving swimmer), polyethylene glycol in alginate capsule [25] (loaded swimmer), aluminum-ethanol [29](boat).

Application. Propulsion using surface tension has been known for a long time, with the first written observation of capillary propulsion for camphor grains dating back to 1686 [30]. However, after some early studies in the 19th century, interest in this phenomenon faded during the 20th century, and the origin of the propulsion mechanism remained unclear. In the last three decades, interest in Marangoni swimmers has witnessed a revival with the rise of active matter [12]. A detailed history is available in the PhD introduction of Dolachaï Boniface [31]. Marangoni swimmers have attracted significant attention due to their ease of design and ability to sustain motion for extended periods. The primary focus has been on exploring their collective dynamics, including phenomena such as oscillation [32], pattern formation [33], and synchronization [13, 34]. Unlike macroscopic systems like flocks of birds or schools of fish, artificial swimmers offer interesting examples of purely physical interactions, featuring no agent-based decision-making or complex cognitive systems.

Beyond fundamental research, Marangoni swimmers hold promise for various practical applications. They can be designed as biocompatible [35, 36] and offer exciting prospects for biomedical and environmental applications, including targeted drug or cargo delivery, chemical analysis and sensing, and environmental decontamination. Additionally, these systems can be used in energy conversion and power generation for example by using Marangoni boats to rotate microgears and generate electromotive force [37].

Focus on the individual object. Until now, research has mainly focused on the collective behavior of Marangoni swimmers or on optimizing their design to achieve specific objectives such as faster speeds, rotational motion, or extended duration of movement.

However, despite being studied for a long time, it may come as a surprise that our understanding of the behavior of individual Marangoni swimmers remains incomplete. Most characterizations are basic, often limited to determining whether the object swims and at what velocity. This approach overlooks the complexities of the fluid dynamics around the swimmer, including the detailed flow patterns and wake that the swimmer leaves behind. Additionally, the distribution of chemicals, both in the bulk fluid and at the interface, is not well understood, nor is the impact of these swimmers on their surrounding environment. The interaction between the swimmer and its immediate surroundings can significantly influence its motion, making the problem far richer and more complex than simply measuring the swimming velocity.

In the following sections, we will first review the fundamental physical concepts necessary to understand the propulsion mechanisms. Next, we will provide a comprehensive overview of the current understanding in the field, examining the state-of-the-art in Marangoni swimmer research and related systems. Our discussion will include a close look at existing models, particularly those that often overlook the impact of Marangoni flows. We will then delve into the nature of Marangoni flows themselves, exploring how they influence swimmer behavior. Finally, we highlight the aspects that are currently missing in the experimental characterization of Marangoni swimmers.

1.2 Fundamentals of surface tension and capillary forces

The Marangoni propulsion based on the gradient of surface tension is a capillary phenomenon, hence we introduce here the basic physics. Thorough accounts can be found in classical book [38] for instance.

1.2.1 Surface tension

Physical origin. Surface tension, often denoted as γ, arises from the cohesive forces between liquid molecules [39]. At an interface, the liquid molecules have fewer neighbors than those in the bulk, resulting in a decrease in cohesive energy. Therefore, creating a surface costs an amount of work corresponding to the free energy difference between the molecules at the surface and their previous state in the bulk. One consequence of the free energy penalty induced by interfaces is that a system tends to minimize its surface area to reduce energy, which explains the spherical shape of bubbles and droplets when not constrained by other forces such as gravity.

Capillary force. Surface tension can also be seen as a lineic force tangent to the interface. As a simple illustration, consider a liquid film supported by a rectangular frame composed of three fixed sides and a fourth one moving freely along the normal direction x (see Fig. 1.3). Spontaneously, the free side moves toward the inside part of the frame, such that the film surface is reduced. If there is nothing to

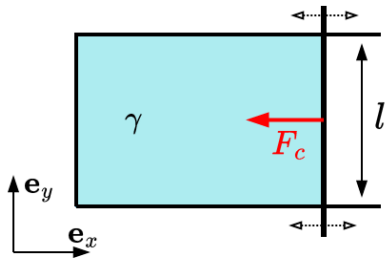

Figure 1.3: **Illustration of the capillary force**. A soap film is bounded by a rectangle frame with a free-moving side of length l, and $\mathbf{F}_c = -2\gamma l \mathbf{e}_x$ here.

stop the free side motion, it moves until the liquid film disappears. On the contrary, if we want to extend the film length we have to apply some force to oppose the capillary force $\mathbf{F}_c$ generated by the surface tension:

$$\mathbf{F}_c = \int_{\partial\Omega} \gamma(l)\mathbf{n}\,\mathrm{d}l\,, \tag{1.1}$$

with $\partial\Omega$ the contact line where the interface is attached to the object, $\mathbf{n}$ the unit vector normal to the contact line contour and pointing outward.

1.2.2 Surfactant

Structure and properties. A surfactant is a chemical species that modifies surface tension. Many surfactants are amphiphilic organic compounds with a hydrophobic "tail" and hydrophilic "head". Their amphiphilic structure drives surfactants to accumulate at interfaces with the tail toward the air and the head toward the water. This arrangement forms an adsorbed monolayer between the polar and apolar surroundings, reducing the interfacial energy and lowering surface tension. The diversity in surfactant molecules, including variations in the hydrophilic head (e.g., anionic, cationic, nonionic, or zwitterionic) and the hydrophobic tail (e.g., chain length and branching), allows for fine-tuning of their surface activity, making them versatile agents in various applications such as detergents [40], vaccine [41] or oil recovery [42].

Surfactants can be further categorized into soluble and insoluble types, depending on their ability to dissolve in the surrounding liquid. Soluble surfactants, which dissolve in the bulk liquid, can reach the interface through diffusion and adsorption, while insoluble surfactants remain confined to the interface, forming a monolayer. The solubility of the surfactant is critical when considering the dynamics of surface tension modification [43].

Modifying surface tension. At thermodynamic equilibrium, the surfactant bulk concentration c, the surface concentration Γ, and surface tension γ are related by a state function. A general relation between surfactant concentration and surface tension can be deduced from the Gibbs equation:

$$\Gamma = -a\mathcal{R}T\left(\frac{\partial\gamma}{\partial a}\right)_{T,\,p}, \tag{1.2}$$

where a represents the activity of the solute, $\mathcal{R}$ the gas constant, T the absolute temperature and p the pressure. For a solute concentration below the saturation, we can assume $a \simeq c$ and that $\Gamma = K_H c$, with K_H, the Henry isotherm coefficient. At low activity:

$$\gamma = \gamma_0 - \kappa\Gamma, \tag{1.3}$$

with γ_0 the surface tension of a bare interface when $\Gamma = 0$, κ a constant coefficient. Equation (1.3) is similar to the perfect gas equation where the "surface pressure" $\gamma - \gamma_0$ and Γ are related linearly.

1.2.3 Marangoni effect

A gradient of surface tension generates flows. A liquid whose local surface tension is higher will pull harder on its surroundings than where the surface tension is lower (Eq. (1.1)). The resulting stress at the interface induces a boundary condition of the form:

$$\overline{\boldsymbol{\sigma}} \cdot \mathbf{n} = \boldsymbol{\nabla}_s \gamma, \tag{1.4}$$

where $\mathbf{n}$ is the unit vector normal to the interface pointing away from the liquid and $\boldsymbol{\nabla}_s$ is the surface gradient operator defined as $\boldsymbol{\nabla}_s f = \boldsymbol{\nabla} f - (\boldsymbol{\nabla} f \cdot \mathbf{n})\mathbf{n}$, γ is the surface tension and $\overline{\boldsymbol{\sigma}}$ represents the stress tensor in the liquid. Note in the above formulation, we have neglected the stress tensor in the gaz phase owing to the viscosity contrast with the liquid. Because a fluid at rest cannot sustain shear stress, it will induce a capillary flow known as Marangoni flow (Fig. 1.4).

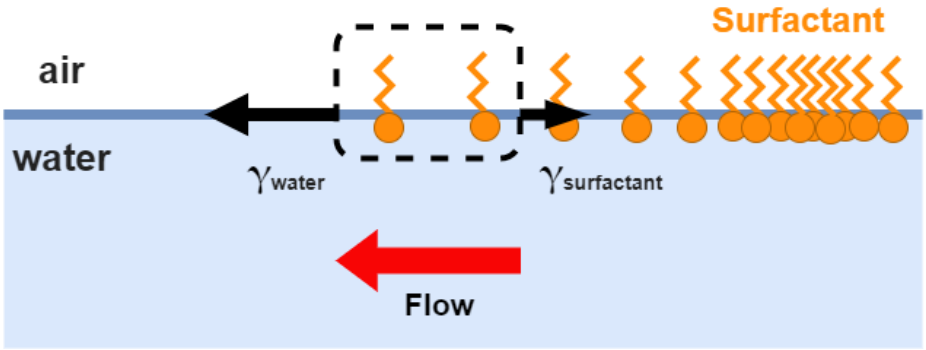

Figure 1.4: **Marangoni effect at the air and water interface.** A gradient of surfactant molecules (represented by the orange molecules) induces a gradient of stress at the air-water interface. Because the surface tension of pure water (γ_{water}) is greater than that of the surfactant-covered regions ($\gamma_{surfactant}$), a flow of liquid is generated, moving from the area of lower surface tension to the area of higher surface tension.

Marangoni flows are ubiquitous. Heterogeneities at the air-water interface, such as variations in temperature, solute concentration, or liquid composition, can modify surface tension. As a result, Marangoni effects are ubiquitous in both natural and industrial contexts [44]. One of the most well-known examples of the Marangoni effect in action is the formation of "tears of wine" (Fig. 1.5 left) [45]. At the meniscus, alcohol evaporates more rapidly than in the bulk liquid, leading to a higher surface tension causing the wine to climb up the glass, forming a liquid rim. The rim is unstable and eventually breaks up due to the Rayleigh-Plateau instability, producing the characteristic falling tears. Marangoni flows also play a critical role in the stabilization of foams and soap films (Fig. 1.5 center) [46]. In these cases, the Marangoni effect slows down the drainage of liquid from the film, helping to maintain its structure and stability over time. Besides, the Marangoni effect is exploited in industrial processes, such as the drying of silicon wafers (Fig. 1.5 right) [47]. During wafer drying, surface tension gradients are manipulated to prevent the formation of water spots and ensure a clean, uniform surface, which is essential for the production of high-quality semiconductor devices.

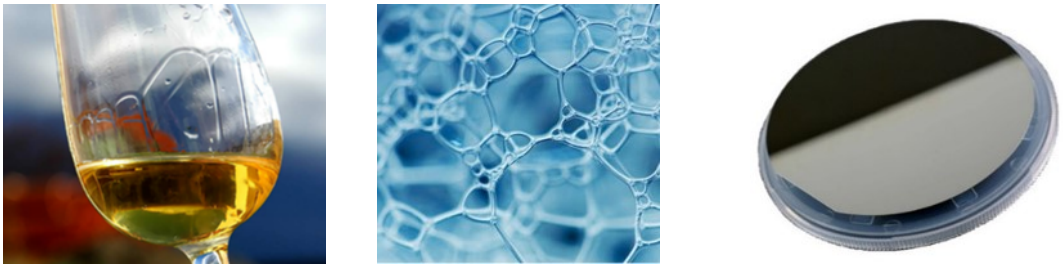

Figure 1.5: **Relevance of Marangoni effect.** (Left) Tears of wine, (center) foam stabilization, and (right) silicon wafer drying.

1.3 Physics of Marangoni swimmers

We saw that propulsion can arise from surface tension gradients and that objects can be designed to release passively a surface-active chemical and self-propel: Marangoni swimmers. Having introduced the fundamental concepts related to propulsion driven by surface tension, we now explore the physics of Marangoni swimmers.

A strongly coupled problem. Before delving into detailed models, let us consider a qualitative, hand-waving description to grasp the complexity of a Marangoni swimmer (Fig. 1.6). The basic mechanism is as follows: the swimmer releases surfactant, creating a gradient in surface tension, which in turn generates a capillary force that propels the swimmer forward. As the swimmer moves, it generates a flow that induces a drag force $\mathbf{F}_\mathrm{d}$ opposing its motion. However, the swimmer displacement and the resulting flow modify the surface tension gradients through advection, thereby altering capillary force propelling the swimmer. Additionally, the surface tension gradient produces Marangoni flows, which further influence the overall flow field and modify the drag force experienced by the swimmer. As a result, the dynamics of the swimmer involve a coupled problem, where both hydrodynamics and transport are interdependent (Fig. 1.6), resulting in a bidirectional coupling. Even though the problem seems clearly defined and its fundamental physical components well understood, their combination leads to real challenges. Due to the complexity, several simplified models have been developed to decouple transport and hydrodynamics, and we review some of these approaches below.

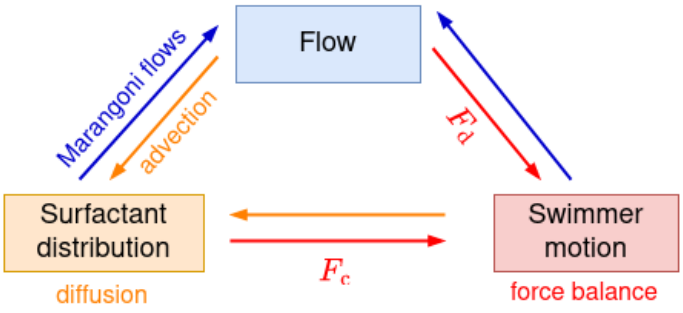

Figure 1.6: **Time-dependent coupling.** Illustration of the coupling between all physical aspect of the Marangoni swimmer problem. The transport problem is in orange, the hydrodynamical problem in blue, and the force balance in red.

1.3.1 Asymmetric swimmer

The simplest type of Marangoni swimmer is similar to the insects that propel themselves on water by releasing surfactant asymmetrically, typically on one side only. The asymmetry in surface tension is directly encoded in the design of the swimmer. Such designs have been widely explored experimentally [15, 17, 48, 49] and are considered in many theoretical descriptions [29, 50–52].

1.3.1.1 Toy model, capillary force *vs.* viscous drag

The first model developed to understand the swimmer motility properties corresponds to the basic picture of a surface tension unbalance imposed between the front and the rear of a floater. Assuming that the surfactant remains confined to only one side of the swimmer, one can compute the spontaneous swimming velocity [29, 53]. In steady state, the swimmer dynamic verifies equilibrium of all the forces. Here only two forces are considered: the capillary force F_c and the drag force F_d.

The gradient of surface tension $\Delta\gamma$ along the swimmer contour l generates a net force $F_c \sim \alpha l \Delta\gamma$ where αl is the characteristic length of the rear contact line. The drag force is assumed to be the same as that experienced by a passive object of the same shape moving with velocity V, $F_d = K l^p V^n$, $n = 1, 3/2$, $p = 1, 3/2$, K a constant depending on the swimmer geometry and the characteristics of the fluid. The exponents n and p depend on the flow regime, $n = 1$ and $p = 1$ for Stokes flow, and $n = 3/2$ and $p = 3/2$ for the viscous drag boundary layer. Balancing the capillary and drag forces provides the spontaneous swimming velocity:

$$V = \left(\frac{\Delta\gamma \ \alpha}{K l^{p-1}} \right)^{-1/n}, \qquad n = 1,\ 3/2 \quad p = 1,\ 3/2. \tag{1.5}$$

The model proposed here is the simplest possible approach and effectively introduces the contributions of motor (capillary force) and drag forces. However, it does not delve into the underlying physics of each element, nor does it explain in detail how these forces are actually generated in a real system. For example, while the gradient of surface tension generates the capillary force, it also induces Marangoni flows, which may alter the drag force compared to that experienced by a passive object moving at the same velocity. Furthermore, the model takes the surface tension gradient as a given starting point without providing a method to compute it based on the specific characteristics of the swimmer and its environment.

1.3.1.2 Diffusion model

Insoluble surfactant. After the simplest model just presented, a step further was taken by Lauga *et al.* [54] by considering a continuous distribution of surface tension and the influence of Marangoni flows on drag. They considered a swimmer disk that releases an insoluble surfactant with a specified concentration along its perimeter. The model, neglects advection, and the flow field has no influence on the surfactant distribution. Under these conditions, the surfactant distribution is governed by a purely diffusive transport equation an it is thus decoupled from the flow problem. The surfactant distribution is then used to calculate the capillary force and set the boundary conditions for the flow

problem. The viscous drag force is determined from the resulting hydrodynamic velocity field.

The steady state velocity is obtained by balancing these two forces:

$$V = \frac{\mathcal{R}Tc_1\pi}{4\mu a^2}, \tag{1.6}$$

where $\mathcal{R}$ is the gas constant, T the absolute temperature, μ the viscosity, a the swimmer radius, c_1, the first term in the cosine series describing the prescribed concentration along the disk contour. When neglecting Marangoni flows, the swimming velocity is overpredicted by 50% [54], indicating that Marangoni flows introduce a resistive effect that slows down the swimmer. The calculation can be further simplified using the Lorenz reciprocal theorem [55] and the approach has been extended to account for swimmers with oblate or prolate shape.

Heat source. A complementary approach considers heat as the driving factor [56] instead of insoluble surfactant, introducing a diffusive transport mechanism in three dimensions. The model considers a punctual source shifted from the swimmer center by a distance b. The resulting velocity of the swimmer is given by:

$$V = \frac{\chi\kappa\mathcal{J}}{32\eta\pi Da}, \tag{1.7}$$

where $\chi = b/a$ is a dimensionless number quantifying the asymmetry, a the swimmer radius, η the fluid viscosity, D the diffusion rate, and $\mathcal{J}$ the heat release rate of the point source. We can point out that the velocity is proportional to the asymmetry.

Conclusion. While the above model provides an initial prediction of the swimming velocity, it is constrained to specific regimes: Stokes flow and diffusion-dominated transport. The latter condition is crucial as it simplifies the complex dynamics of a Marangoni swimmer by decoupling the hydrodynamic problem from the transport equation. Moreover, these models are limited to asymmetric swimmers, as considering an isotropic source with purely diffusive transport would result in no driving force and, consequently, no motion.

1.3.2 Symmetric swimmer

At first glance, the motion of a symmetric object seems counterintuitive, as asymmetry is typically required to generate capillary propulsion. However, numerous experiments with disk-shaped swimmers have shown that the motion of a symmetric interfacial object is not only possible but also relatively easy to achieve [24, 57–59]. What mechanism underlies this spontanenous propulsion?

1.3.2.1 Symmetry breaking

Qualitative description. To understand qualitatively the motion of symmetric interfacial swimmers, consider an initial velocity perturbation from the immobile state. Such a perturbation breaks the initial symmetry, leading to convective transport that polarizes the system along the direction of motion. In other words, once the disk starts moving, the

surfactant distribution becomes asymmetric, resulting in a net capillary force acting on the object. The initial perturbation thus enhances the asymmetry of surfactant around the swimmer, creating positive feedback and potentially increasing the speed. The initial motion arises from an instability driven by convective transport.

Analytical prediction. The spontaneous symmetry-breaking mechanism for isotropic Marangoni swimmer has been firmly established analytically [60, 61]. Studies explore two different systems: droplets in the bulk [60] and interfacial camphor disc [61]. Both studies demonstrate that above a certain threshold, the system transitions from a stable, non-moving state to a spontaneously moving one with broken symmetry. Specifically the transition happened above a critical Marangoni number, which is a dimensionless number representing the ratio of advective to diffusive transport in the system. As the Marangoni number increases, so does advection compared to diffusion, which enhances the nonlinearity in the system. For a critical value, the nonlinearity becomes sufficient to break the symmetry of the solute concentration field around the particle, leading to spontaneous self-propulsion.

Michelin et al. [60] not only predict the symmetry-breaking but also provide detailed predictions of the resulting swimming velocity and its dependence on the Marangoni number, incorporating the full complexity of nonlinear interactions [60]. In contrast, Chen et al. [61] use a simplified model that primarily captures the essential features of surface tension-driven motion in interfacial camphor discs, without delving into the full complexity of the nonlinear interactions. Their study focuses more on the qualitative demonstration of the transition to motion than on the precise characterization of the resulting velocity. In the following, we present other models that have been proposed to better capture the dependencies of the swimming velocity with respect to the swimmer intrinsic properties.

1.3.2.2 Point source model with advection

Presentation of the model: For a symmetric camphor swimmer a point source model can be developped in the advection-dominated regime [24]. Several key assumptions are made:

- **Flat swimmer.** The swimmer is considered to have infinite buoyancy, lying flat on the surface with no immersed volume.
- **Surface-bulk exchange.** The surfactant is modeled either entirely at the interface (insoluble) or in the bulk (soluble), ignoring the additional complexity induced by the absorption/desorption kinetics.
- **Linear dependence between surface tension and concentration.** The surface tension γ is linearly related to the surfactant concentration Γ (Eq. 1.3), assuming Γ is far from saturation.
- **Flat interface.** The interface is assumed flat, simplifying the geometry and neglecting Laplace pressure. This assumption is legitimate as the capillary number, comparing the viscous drag forces to the surface tension forces, is low.

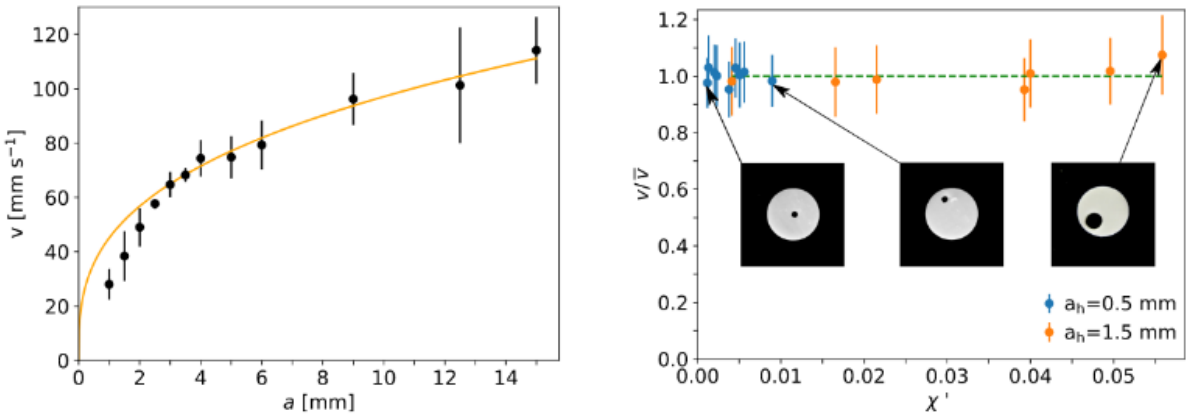

Figure 1.7: **Dependence of the swimming velocity.** Experimental results for a camphor swimmer, an agarose gel disc loaded with camphor. (Left) Size dependence of the swimming velocity. The continuous line is a fit to $v \propto a^{1/3}$. (Right) Impact of the asymmetry quantified by χ'. The velocity is normalized by the average value $\overline{v}$.

The model describes the steady motion of a point source moving at constant velocity v releasing at constant rate solute or heat. The concentration field follows the advection-diffusion equation, with a uniform advecting flow fixed by the swimmer motion. Thus, the model accounts for advection in a simplistic way, neglecting Marangoni flows and flow perturbation associated with the finite size of the swimmer. Moreover, to decouple the transport from the hydrodynamic problem, the drag force is approximated as that of a passive disc not releasing surfactant.

Prediction. The model predicts that propulsion velocity increases sublinearly with the swimmer radius a. Specifically, for large swimmers, the velocity scales as $V \propto a^{1/3}$. In the advection-dominated regime (high Péclet number), the model also predicts that small asymmetries in the swimmer shape have little to no effect on propulsion velocity, suggesting robustness against minor imperfections. Finally, the model indicates that at large Péclet numbers, the velocity scales as the square root of the Marangoni number M, a dimensionless number related to the system intrinsic properties, such as chemical activity and swimmer size. M can be seen as quantifying the strength of the propulsion mechanism.

Comparison with experiments. The prediction of the point source model are compared with experiment made with camphor swimmer: agarose gel disc loaded with camphor [24], corresponding to the loaded swimmer type introduced earlier. The velocity is measured for different swimmer radius (Fig. 1.7 left). Except for the smallest swimmers, the experimental data align reasonably well with the model prediction, following a power law with an exponent of 1/3, confirming the sublinear dependence of velocity on swimmer size (Fig. 1.7 left). However, the model tends to overestimate the actual propulsion velocities by a factor of 10. The impact of asymmetry is studied (Fig. 1.7 right) by making a hole in the swimmer and quantified by the parameter χ' the distance between the hole and the center of the swimmer. Experiments show no significant dependence on swimmer asymmetry, consistent with the model predictions in the advection-dominated

regime (Fig. 1.7 right). Overall, the predictions of the point-source model appear to be semiquantitative, a somewhat unexpected achievement given the simplifications involved.

1.3.2.3 Including Marangoni flows

Numerical approach to the coupled problem. Recent works have gone beyond the simple point-source model to include Marangoni flows by using numerical approach [25, 31]. The first study focuses on camphor swimmers, similar to those in previous studies, and investigates the role of Marangoni flows in the self-propulsion of symmetric swimmers [31]. This study specifically examines how these flows influence swimming velocity and the conditions for spontaneous motion. The main improvements include accounting for finite diffusion and incorporating the drag forces associated with Marangoni flows, which were previously neglected [24]. The second study considers a slightly different object: PEG-Alginate capsules, gel half-spheres loaded with surfactant. This study addresses a more complex system by relaxing more of the earlier assumption: the swimmer is no more flat, and they consider surfactant release over the whole surface. In both studies finite element method allows for the resolution of complex, coupled transport and hydrodynamics that are not easily addressed by simpler models. However, despite these advancements, the models remain limited in their ability to fully replicate experimental conditions as they focus on Stokes flow regimes, whereas typical experiments involve Reynolds number of 10^2.

Importance of the Marangoni flows. The work of Boniface *et al.* [62] finds that Marangoni flows play a critical role in the low-velocity regime near the onset of swimming. They contribute to the symmetry-breaking necessary for spontaneous motion and introduce complex behaviors such as bistability and hysteresis in the swimming velocity. A critical Marangoni number M_c above which spontaneous swimming occurs. The transition is discontinuous, leading to a sudden onset of motion, and exhibits a region of bistability where both motionless and swimming states are possible. In the high-velocity regime, the influence of Marangoni flows becomes less significant. The full numerical models, including Marangoni flows, align well with experimental data, with predictions within $10 - 15\%$ of the experimental values [25] across a wide range of conditions in the low-velocity regime. For higher velocities, the simpler point-source models already capture the main trends [24].

Conclusion. These two works [25, 62] demonstrate that while Marangoni flows are crucial in determining the onset and stability of swimming in the low-velocity regime, their influence diminishes at higher velocities. These studies highlight the importance of Marangoni flows in swimmer dynamics. Consequently, the following section will delve deeper into the characterization of Marangoni flows.

1.4 Marangoni flows

Aside from swimmers, Marangoni flows are also present in a wide variety of situations, and they have an important role in natural or industrial processes. Despite being known since 1865 [63], Marangoni flows are still the focus of recent work as their transient nature

makes them challenging to study experimentally [64–69]. In this section, we review some configurations that involve Marangoni flows and share some similarities with our system and could give some first insight on our more complex system.

1.4.1 Fixed source

Before destabilizing and starting to move, a Marangoni swimmer reduces to a fixed source of surfactant on a liquid subphase. As a starting point to understand Marangoni flows, we begin by considering this simpler configuration. A series of work [70–72] focuses on the thin-film situation where a drop of surfactant solution is deposited onto thin films, typically around 1 µm. However, these configurations differ significantly from the conditions experienced by Marangoni swimmers, where the flows occur in much thicker water layers, ranging from 1 to 10 cm. Therefore, we focus here on studies and models that consider a fixed source of surfactant in finite or deep water configuration, which are more relevant to our system.

1.4.1.1 Spreading on an infinite half-space

Heat source or soluble surfactant. The surface tension gradient generated by a punctual source induces a Marangoni flow which spreads the surfactants. The problem of a solute spreading from a source has been solved analytically for a point heat source of constant power on an infinite half-plane liquid subphase [73]. The flow verifies the Navier-Stokes equation, with heat acting as the surface-active quantity. Although this study focuses on thermal effects, the results apply to perfectly soluble surfactants as the transport is not limited to the interface. Remarkably, the solution is valid at arbitrary Reynolds number. The study explored various heat source strengths, quantified by the parameter A, which is proportional to the power of the source, and obtained the streamlines and isotherms (Fig. 1.8). For a weak heat source, the temperature distribution is dominated by diffusive transport (Fig. 1.8, right bottom). For a stronger source, divergent Marangoni flows appear leading to a rising flow beneath the heat source (Fig. 1.8 right top) compressing the isotherm lines (Fig. 1.8 upper-right).

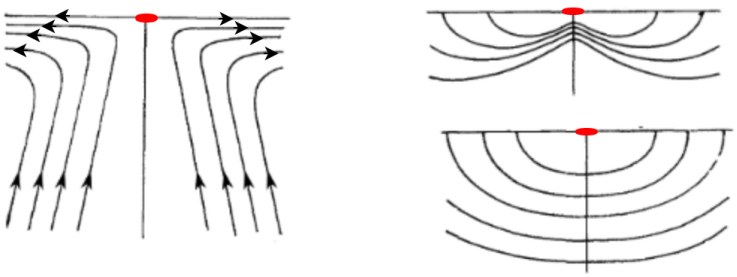

Figure 1.8: **Flow and temperature field around a point source.** The power of the heat source is represented by the parameter A. (Left) Streamlines for $A = 2.24$. (Right) Isotherms for $A = 2.24$ and $A = 0.44$ (top and bottom respectively). The red spot indicates the heat source position. Figures are from [73].

No diffusion limit. Other studies have explored the transient spreading and flow around a fixed source of soluble or insoluble surfactant under the assumptions of infinite Marangoni number, no diffusivity, and Stokes flow [74, 75]. Specifically, the model allows studying the non-linear interplay between Marangoni flows and surfactant advection in the simplest form thus proposing some exact analytical solutions and testbed for future numerical experiments. A significant result from these works is that the interfacial velocity can be expressed as a convolution of the surface concentration. Building on this foundation, recent research has mapped the 1D spreading of insoluble surfactants to a complex Burgers equation [76], and for finite diffusion proposed complete set of exact solutions for viscous Marangoni spreading [77]. The last work highlights the crucial role of the initial surfactant distribution in determining the subsequent evolution [77].

Effective diffusion. From the approach of Thess [74, 75] an effective diffusion coefficient can be defined to account for the advection caused by Marangoni flows [78]. Such an approach was also proposed to describe experimental observation, suggesting that incorporating an effective diffusion into the surfactant transport equation can effectively capture the contribution of Marangoni advection [52, 79]. An estimation has been made for the effective diffusion coefficient D_{eff}, analytically in the limit of high viscosity and/or low diffusivity $D_{\text{eff}} = 10^{-4}\,\text{m}^2\,\text{s}^{-1}$[1] [78] or for weak Marangoni convection $D_{\text{eff}} = 10^{-3}\,\text{m}^2\,\text{s}^{-1}$ [79]. Compared to the natural diffusivity $D = 10^{-10}\,\text{m}^2\,\text{s}^{-1}$, including Marangoni effect leads to a much faster spreading. Both cases consider a fixed camphor particle and the effective diffusion coefficient may differ from a moving one. However, the concept of effective diffusion is not always justified and should be used with caution. In 2D case, there are no scenarios where Marangoni spreading can be mapped to a diffusion process [77]. Even though the idea of effective diffusion is sometimes invoked, it appears difficult, in general, to map a transport process dominated by Marangoni convection onto a simple diffusive process.

1.4.1.2 Surfactant spreading in a pool, quasi steady-state

Punctual source flow features. Several experimental setups have been developed to study Marangoni flows under quasi-steady conditions in axisymmetric [64, 65] or rectilinear configuration [66, 67]. In both configurations, two distinct regions are observed (Fig. 1.9): (*i*) within a critical distance L from the emission point, the flow is fast and divergent; (*ii*) beyond L, the flow destabilizes and vortices appear. The critical distance L and the maximal flow velocity u_{max} mainly depend on the surfactant chemical properties and are correlated to the critical micellar concentration (CMC) [65].

The predicted scaling laws governing the interfacial and bulk flows can be modelled [66] by considering the coupling between flows and surfactant dynamics. First, the Marangoni flow transports the surfactant over a larger distance from the source than simple diffusion would, increasing the surface exchange with the bulk. Secondly, the flow sweeps the subphase, enhancing the vertical concentration gradient and leading to more efficient diffusion. The main approximation is that the vertical length scales are much smaller than the horizontal ones. This argument predicts a critical spreading distance $L \propto \Delta\gamma^{-3/4}$

[1] A simple estimation can be made considering a typical length ξ_0 (for example the swimmer size), then computing a characteristic Marangoni velocity in Stokes regime $\eta U_0/\xi_0 = \Delta\gamma/\xi_0$. Thus, $D_{\text{eff}} \sim U_0\xi_0$

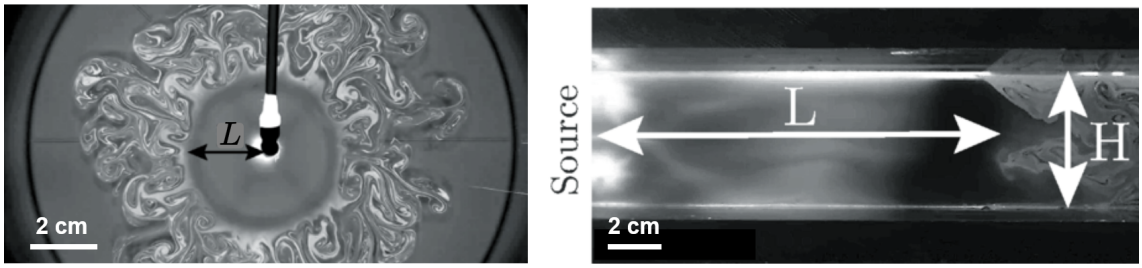

Figure 1.9: **Flow around a fixed source of surfactant.** Oil droplets are mixed with the surfactant solution to visualize the interfacial flow. Marangoni flows extend to a distance L. Top view of the axisymmetric where $L = 2.46\,\text{cm}$ (left) and rectilinear configuration $L = 9.6\,\text{cm}$ (right). Pictures are taken from [65].

and maximum velocity $u_{\max} \propto c^{*1/4}$ with c^* being either the CMC or the limit solubility. These predictions match experimental measurements [65, 66]

Another key feature is the evolution of the interfacial flow velocity $u(r)$ with respect to the distance r from the source (in the radial spreading area $r < L$). Experiments [68] and theoretical prediction [69] show that for an axisymmetric configuration, $u(r) \propto r^{-n}$ where n equal to 3/5 or 1 for adsorbed or solubilized surfactant respectively. These results suggest a significant difference in the behavior of adsorbed versus solubilized surfactants, highlighting the importance of surfactant properties in Marangoni flows. Experiments were also carried out with camphoric acid embedded in an agar gel matrix, which is similar to a fixed and loaded swimmer. The results show that camphoric acid follows the signatures of an adsorbed surfactant. However, the concentration considered is not specified making extrapolation to camphor swimmer difficult.

Finally, a recent work using fluorescent surfactant [64] evidences the influence of container size and water depth on L. Fluorescent surfactant allows observing recirculation flows below the water surface.

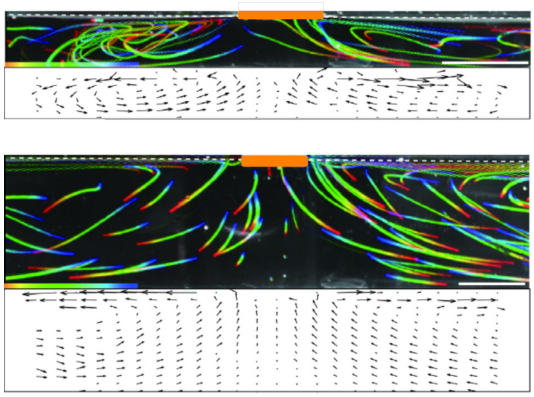

Figure 1.10: **Flow field under a fixed camphor swimmer.** Side view of the typical Marangoni flow profiles for a finite size surfactant source (camphor scrap) for two water depths 5 mm (top) and 20 mm (bottom) [80]. Scale bars correspond to 1 cm.

Non punctual source. One experimental study investigates the flow field that develops beneath a fixed camphor disc, focusing on the effect of water height [80]. At the interface,

the flow diverges from the swimmer and two counter-rotating vortices develop underneath (Fig. 1.10). Decreasing the water height reduces the extent of the vortices (Fig. 1.10 top) and the maximal flow velocity. The induced flows qualitatively look like the prediction of [73], where the flow rises directly beneath the source (Fig. 1.8). These observations provide a starting point to consider the influence of the swimmer spatial extent on the flow.

Conclusion. The case of a fixed source provides a first glimpse of the flow generated around a Marangoni swimmer. It clearly shows the large spatial extent and velocity of Marangoni flows. Both experimental findings and theoretical models converge on the main scaling laws governing the critical spreading distance, maximum flow velocity, and the evolution of flow with respect to the distance from the source. These scaling laws and the interfacial and volume flows have also been observed for fixed camphor swimmers. The surfactant spreading is mainly governed by the surfactant CMC and the surfactant dynamic, either adsorbed or solubilized. Finally, the water height seems to impact the Marangoni flows.

1.4.2 Mobile source

Compared to the fixed source, for a mobile source of surfactant, the literature is rather scarce, and we found only one analytical description [81]. It considers the spreading of a localized monolayer of insoluble surfactant discharged from a point source that moves at a constant speed. All the results are obtained assuming shallow water conditions and Stokes flow and will not typically apply to a Marangoni swimmer, which typically evolves above 1 cm of water at Reynolds 100.

For an asymmetric swimmer, there is little experimental characterization but only in a transient state. The obtained flow field expands to 10 swimmer size, with a radial dilatation of the interface downstream. Finally, the case of a symmetric Marangoni swimmer was studied numerically as presented above [25, 31] but it remains far from the experimental regime and needs several nontrivial assumptions.

1.4.2.1 Flow around an asymmetric swimmer

Motor or resistive contribution? For asymmetric swimmers it is possible to make some predictions about the effect of Marangoni flow on propulsion. However, the outcome is not straightforward as some theoretical studies predict a resistive contribution [54] while other predicts a motor contribution [82]. Both approaches consider Stokes flow and purely diffusive transport. The main difference is that the latter study assumes shallow water, with depth comparable to the swimmer thickness. Going beyond the Stokes regime a numerical and experimental study [83] show that the motor contribution of the Marangoni flows in shallow water leads to "reverse Marangoni surfing": propulsion toward low surface tension area. The swimming direction is set by the balance between the net surface tension force acting along the swimmer edge and the force exerted on the submerged area of the surfer by the flow. Similarly, numerical work has shown that, depending on the imposed swimming velocity, the drag force generated by Marangoni flows can either contribute as a motor or a resistive force [31].

Experimental characterization of the interfacial flow. Only a few works obtained the complete flow field around an asymmetric camphor swimmer [83–85]. Whatever the type of surfactant used, the general features of the flow field remain the same. Looking from the top, the induced flow extends over a distance around ten times the swimmer size and the maximal velocity is about the swimmer speed, with a velocity upstream 10% higher. The flow field is asymmetric and the interface dilates downstream, spreading radially from a source point roughly one diameter from the swimmer edge (Fig. 1.11 left). The source point corresponds to the position of the surface tension minimum. If its presence was expected, the location is surprising as we could expect the minimum of surface tension to be located next to the surfactant release. However, even if the surfactant bulk concentration is maximal close the surfactant release region, a finite adsorption time is needed to reach the interface [43]. During this time the disc has moved away. If this provides a first explanation of the position of the source point it is necessary to look at the bulk flow (Fig. 1.11 right) to get a complete picture.

Flow below the swimmer. The previous studies [83–85] also obtain the flow field under the swimmer (Fig. 1.11). Typically, two counter-rotating vortices are observed: one directly beneath the swimmer and another positioned to the left of the source point. These vortices are essential for mass conservation; as the interface moves to the right, an equal mass of fluid beneath it must move leftward to balance the flow. The formation of these vortices is influenced by the water depth [82]. For a water height close to the swimmer thickness layers, only a single, narrow clockwise-rotating vortex forms on the side opposite the chemical release. The vortex generates a viscous force, which can propel the swimmer toward the region of lower surface tension. As a result, reverse Marangoni surfing occurs, causing the swimmer to move in direction opposite to usual propulsion.

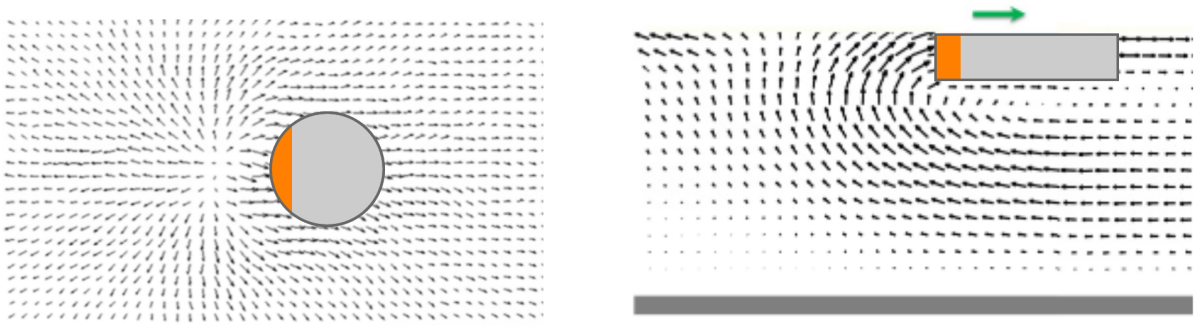

Figure 1.11: **Marangoni flows around an asymmetric swimmer.** Experimental flow field around a Marangoni swimmer top view (left) and side view (right) with respect to a fixed frame of reference. Images are taken from [83]. The part coated with surfactant is indicated in orange and the swimmer is propelling to the right. The swimmer radius is 2.25 mm.

1.4.2.2 Symmetric swimmer

Experimental characterisation. Finally, considering the symmetric Marangoni swimmer, a first experimental characterization of the flow field close to the interface was done during the thesis of Clément Gouiller [86]. The obtained flow field shows features similar

to those of an asymmetric swimmer. There is an upstream-downstream asymmetry with the flow field spreading radially behind the swimmer. Obtaining the field was experimentally challenging as the swimmer never arrived in the same swimming direction and the trajectory was not rigorously straight resulting in a blurring from the averaging. It could lead to inaccuracy in the obtained flow velocity.

Complete flow field in the swimmer frame of reference. From numerical work presented earlier [62] (Subsec. 1.3.2, page 11) the complete flow field around a symmetric camphor swimmer can be extracted. These results are discussed in detail in Boniface's PhD thesis [31]. The model includes the full coupling between the hydrodynamics and the transport of surfactant, with a particular focus on Marangoni flows in a steady-state regime. All results are obtained in the swimmer frame of reference.

The simulations reveal a well-defined hydrodynamic wake characterized by a divergent flow at rear, where the flow velocity exceeds the swimmer velocity by roughly a factor of two(Fig. 1.12 left). A separatrix, which is a line that no particles coming from the front can cross (Fig. 1.12 left, purple dashed line), defines the boundary of this wake. Close to the swimmer, the separatrix expands rapidly, approximately following a square root dependence. Far from the swimmer, the wake width remains almost constant or shows minimal evolution (Fig. 1.12 right). Another significant feature is the stagnation point at the apex of the separatrix (Fig. 1.12 left, pink cross), where the fluid velocity drops to zero. As the Marangoni number M increases, effectively increasing the efficiency of Marangoni propulsion, the distance between the stagnation point and the swimmer center decreases (Fig. 1.12 right). For large M, the stagnation point can move beneath the swimmer surface, maybe only possible because point source release. Interestingly, no vortices form below the swimmer, indicating that despite the strong Marangoni effects, the flow remains laminar and avoids recirculation in that region.

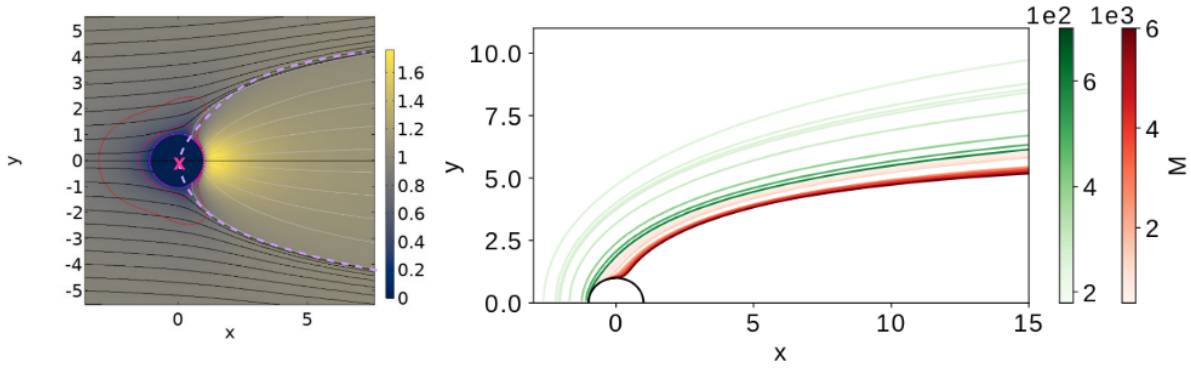

Figure 1.12: **Flow field around a symmetric swimmer.** (Left) Velocity field ($M = 2500$, $\mathrm{Pe} = 35.6$) in Stokes regime. The magnitude of velocity is indicated by the color. The red full lines indicate isovelocity. The pink cross corresponds to the stagnation point where $v = 0$ and the purple dashed line to the separatrix. (Right) Evolution of the separatrix with respect to the Marangoni number M. There are two color bars, the green gradient one goes up to $M = 700$, and the red gradient one goes from 800 to 6000. Figures are from the thesis [31].

1.5 Toward a complete experimental characterization

When designing a new self-propelled object, most studies focus on two primary questions: "Does it swim?" and, if so, "At what velocity?" This approach results in a single observable—swimming velocity—often being the only metric evaluated. In the case of camphor swimmers, even the simplest models, which assume punctual release of surfactant, no diffusion, and no Marangoni flow, successfully capture the essential elements needed to predict swimming velocity based on the swimmer radius or intrinsic asymmetry [24]. Recently, more advanced numerical studies that include Marangoni flows have been conducted [25, 62]. However, the lack of extensive experimental data makes it difficult to thoroughly validate these results. The goal of this PhD work is to address this gap by proposing a comprehensive experimental characterization of Marangoni swimmers, focusing on the following aspects:

- **Force balance.** Understanding the forces at play is crucial for a complete description of swimmer dynamics. In addition to the swimmer velocity, a detailed force balance analysis will reveal the interplay between the various forces and their influence on swimmer behavior.
- **Flow field.** Capturing the complete flow field around the swimmer is essential for understanding how Marangoni flows affect movement and stability. Experimental data on flow patterns will provide insights into the interaction between the swimmer and its surrounding fluid environment.
- **Surfactant distribution.** Mapping the surfactant distribution provides critical information about the local variations in surface tension and their impact on swimmer dynamics.

This detailed study aims to provide a deeper understanding of the factors that influence Marangoni swimmers beyond just their velocity, offering new insights into their complex behavior. This final section reviews the current state-of-the-art in these areas, highlighting the existing studies and limitations and reviewing techniques that could be applied to fill these gaps.

1.5.1 Flow field

Current understanding. In earlier sections, we reviewed the Marangoni flows generated by moving surfactant sources (Subsec. 1.4.2 page 18) and examined the interfacial and bulk flow around asymmetric [83, 84] and symmetric Marangoni swimmers [85, 86]. These studies have begun to outline the flow characteristics but often consider transient states, with limited data and difficulties in averaging results due to variations in swimming direction and spontaneous velocities.

Future directions in measuring Marangoni flow. To measure the flow field, several standard techniques, such as particle image velocimetry (PIV) and optical flow, are available and easily applicable. Significant progress can be made by obtaining stationary flow fields, which are often assumed in theoretical models but challenging to capture experimentally and work should be done to design an appropriate experimental setup.

Additionally, exploring flow velocities beyond those associated with spontaneous swimming will offer a more comprehensive understanding of the dynamics. Such an approach will enhance the accuracy of theoretical models and provide valuable insights into the complex behavior of Marangoni swimmers.

1.5.2 Force balance

Current understanding. Force measurements were made for a camphor boat [52]. The boat is attached to a surface tensiometer, and when propelling forward, it pulls on the tensiometer with a force F_m (Fig. 1.13). The driving force can easily be computed from the measured F_m and the angle of the wire holding the boat with force and torque balance. For a boat spontaneously moving at $V = 6.6\,\mathrm{cm\,s^{-1}}$ Suematsu *et al.* measured $F_w^0 = 23 \pm 2\,\mu\mathrm{N}$. Here as the boat is not moving and remains confined, the surfactant tends to accumulate at the rear and the driving force measured may be larger than for a moving boat. They proposed an analytical estimation of the capillary force propelling a boat using an effective diffusion coefficient for camphor to account for the Marangoni flow, in that case, the force obtained is much lower, and $F_w = 4.2\,\mu\mathrm{N}$.

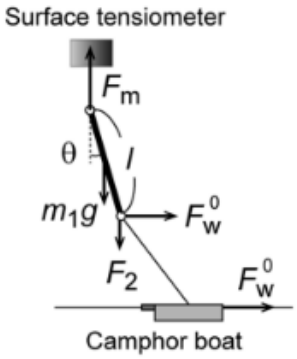

Figure 1.13: **Force measurement.** A camphor boat is attached to a surface tensiometer and the force F_m is measured. It can be related to the driving force F_w^0 through force and torque balance. The figure is from [52].

Future directions. If the study of Suematsu *et al.* [52] proposes a first order of magnitude of the driving force propelling a camphor boat, the measure should be extended to a symmetric camphor swimmer. Moreover, a new setup should be designed to measure the force on a moving boat, or a fixed boat with a water flow to avoid accumulation of surfactant at the rear leading to a larger driving force than when translating. Finally, as for the flow field a study outside the spontaneous swimming velocity would be interesting.

1.5.3 Surfactant distribution and surface tension field.

The distribution of surfactant around a camphor swimmer is essential to understand the generated Marangoni flows and to assess the capillary force propelling the swimmer forward. However, in the vast majority of experiments, the surfactants can not be visualized and they often remain as "hidden variables" [87], a common challenge in the understanding of surfactant systems such as bubbles, drop and foams.

Numerical characterization of the surfactant distribution. The finite element approach in Boniface's thesis [31] provides a characterization of the surfactant distribution around a symmetric camphor swimmer (Fig. 1.14). The computation reveals an asymmetric surfactant distribution with more surfactant at the rear and iso-concentration

curves having an egg-like shape (Fig. 1.14 left). As the release is symmetric, the surfactant field also extends upstream. The width of the chemical wake W is quantified by the standard deviation of the surfactant distribution perpendicular to the direction of motion. The study finds that the wake width maintains a sublinear shape across the entire tested range of Marangoni numbers $M = 256 - 6000$ (Fig. 1.14 right), closely following a power-law $W \sim x^{\alpha}$ relationship with an exponent $\alpha \sim 0.4$. The extension of the wake reaches a plateau for large Marangoni number as the flow field.

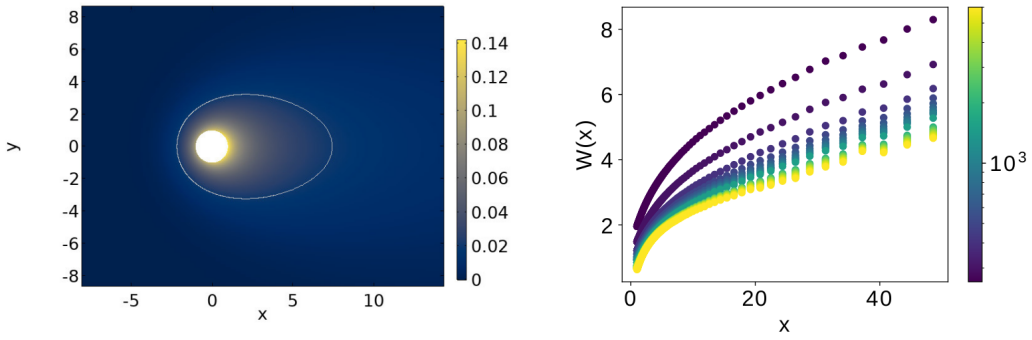

Figure 1.14: **Surfactant distribution around a camphor swimmer.** (Left) Surface concentration c (Pe=1), the white line is the iso-concentration $c = 0.02$. The colorbar indicates the concentration. (Right) Width of the chemical wake, the color bar represents the Marangoni number.

Experimental characterisation. Measuring or visualizing surfactant concentration and distribution is challenging, which is why no experimental comparisons with the above numerical results are available at the moment. If some surfactant may be made fluorescent [64, 88], it is not the case for camphor. One could imagine switching to another surfactant, but we would then face two problems: (*i*) as we are interested in the distribution at the interface, we would observe only a monolayer of fluorescent surfactant and the signal may not be sufficient. (*ii*) One of the main advantages of camphor is its volatility at ambient temperature which prevents saturation of the interface and enables the swimmer to maintain steady motion. Such advantages will not necessarily be present with another surfactant. Therefore to avoid saturation of the interface we would have to significantly reduce the time of experiments over which motion is observed. Given these constraints, we focus on a direct consequence of surfactant distribution: surface tension, which is the primary driver of the swimmer propulsion. This section reviews both traditional and advanced techniques for measuring surface tension, evaluating their applicability to our specific situation.

1.5.3.1 Traditional way to measure surface tension

Droplet shape measurement. These methods analyze the shape of a droplet. The shape depends on the competition between the capillary and gravitational forces and can be described by the classical Laplace equation:

$$\gamma \left(\frac{1}{R_1} + \frac{1}{R_2} \right) = \Delta p = \Delta p_0 + \Delta \rho g z, \tag{1.8}$$

where R_1 and R_2 are the two principal radii of curvature, Δp is the pressure difference across the interface, Δp_0 is the pressure difference at the drop apex, $\Delta\rho$ is the density difference between the liquid and air and g is the gravitational acceleration constant. Surface tension is determined by fitting the shape of the drop to the Young-Laplace equation. The principal assumptions are: (*i*) the drop is symmetric about a central vertical axis, (*ii*) the drop is not in motion, tension, and gravity are the only forces shaping the drop. The main two techniques are the pendant drop (or bubble) and sessile drop (or bubble) [89, 90]. Both techniques are easy to use as they only require a camera and some image analysis software to fit the drop profile [91]. However, these methods are not usable for in situ measurements.

Intrusive method. The second type of technique involves using a probe in contact with the liquid and can provide local surface tension measurements. The probe (plate, ring, or rod) is immersed into the liquid and slowly pulled up bringing a meniscus of liquid with it due to capillary force (Fig. 1.15). The increase of interfacial area induces a force F pulling the probe toward the interface. The value of the force is measured by a microbalance and can be directly related to the surface tension:

$$\gamma = \frac{F}{p\cos\theta}, \tag{1.9}$$

where p is the perimeter of the three-phase contact line and θ is the contact angle measured for the liquid meniscus in contact with the object surface. The two main techniques are the Wilhelmy plate (Fig. 1.15 left) and the De Noüy ring method (Fig. 1.15 right) [92, 93]. Both techniques are commercially available and easy to apply. However, high-accuracy measurements require perfect wettability of the probe surface, if not achieved, it requires correction. Moreover, for the De Noüy ring method, the largest source of error is caused by the deformation of the ring, which is a very delicate probe and subject to accidental deformation during handling and cleaning. If these methods can be used in situ and on several locations to obtain a 2D field of surface tension the direct contact of the probe and the interface may modify the surfactant distribution and generate hydrodynamic perturbations.

1.5.3.2 Advanced non-intrusive optical techniques.

Quasi-elastic light scattering. Quasi-elastic light scattering (QELS), also known as dynamic light scattering (DLS), is a valuable technique for measuring interfacial tension and surface flow speed in liquids. This method involves directing a laser beam at the liquid interface and observing the light scattered by capillary waves, which are induced by thermal fluctuations. The scattered light undergoes a frequency shift, which is detected and analyzed to provide insights into the properties of the interface (Fig. 1.16 left). By examining these frequency shifts, QELS can yield detailed information about the dynamics of the liquid surface, including interfacial tension and the movement of surface waves.

Application to camphor swimmer. QELS was already used to measure the surface tension across a camphor boat [48, 95], between two interacting boats [16] or across an oil droplet [96]. The measure shows a difference of $3 \pm 1\,\mathrm{mN\,m^{-1}}$ between the front and

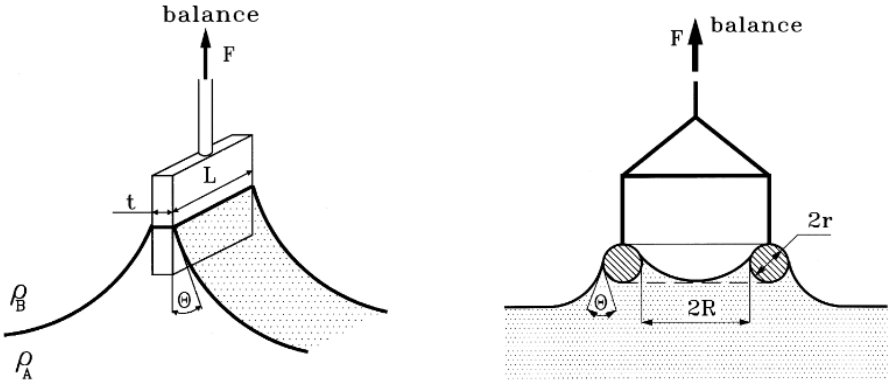

Figure 1.15: **Intrusive methods to measure surface tension.** These methods use a probe to pull up liquid, the induced force is measured by a microbalance and can be related to the surface tension. Depending on the technique, the shape of the probe changes, (left) Wilhelmy plate and (right) De Nouy ring. Illustration taken from [94].

the rear of a camphor boat (Fig. 1.16 right). However, the obtained measurement is 1D, and may not capture the more complex case of a symmetric swimmer as is released all around the swimmer. Moreover, the technique requires precise experimental setups and sophisticated equipment, making it challenging to use without specific experimental tools and expertise. The need for dynamic tracking systems and high-resolution detectors indicates that QELS is not easily implemented with basic laboratory equipment and requires specialized instruments and technical know-how.

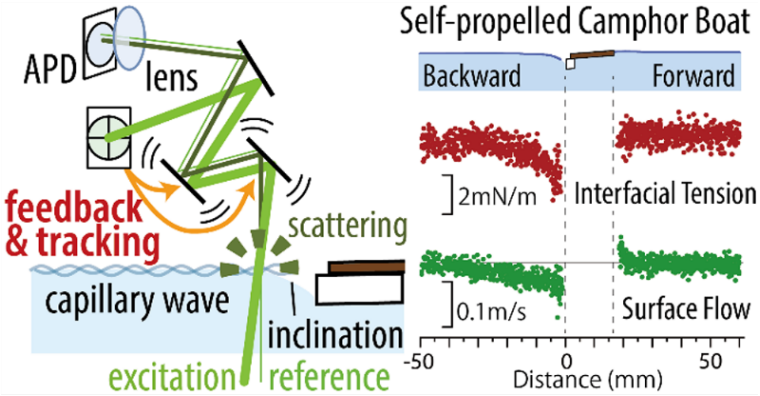

Figure 1.16: **Quasi-elastic light scattering.** Quasi-elastic light scattering (QELS) to measure the surface tension around a camphor boat. (Left) Schematic of the experimental setup of the QELS method with dynamic optical tracking. (Right) From top to bottom: experimental system, surface tension measurement, flow velocity measurement. The figure is taken from [48].

In conclusion, while quasi-elastic light scattering is a highly effective method for measuring interfacial tension and surface flow speed, it requires specific experimental tools and expertise to ensure accurate and reliable results. Moreover, it is a point measurement and determination of the 2D surface field can be prohibitive in terms of acquisition time and system stationarity. For now, no technique seems to be able to measure the 2D surface pressure field around a camphor swimmer.

1.6 Summary and questions

In this state-of-the-art chapter, we presented the propulsion mechanisms driven by surface tension and introduced the classical physical phenomena associated with capillarity. We then focused on the primary subject of this PhD, the camphor swimmer: a centimeter-sized agarose gel disc loaded with camphor. The existing literature mainly focused on the propulsion mechanism, particularly the spontaneous symmetry breaking inducing motion and the resulting swimming speed. Notably, most existing models are strongly simplified and often neglect Marangoni flows due to their complexity, despite the Marangoni effect being the primary driver of motion.

Two recent numerical studies attempted to include Marangoni flows but relied on several drastic assumptions and failed to reach the experimental regime. Despite these limitations, the numerical results still match fairly well the experimental data for swimming velocity which is the only observable available and no real conclusion could be drawn on the impact of the assumption. Indeed, apart from the swimming velocity no observable are available. Although initial characterizations of the flow field and capillary force have been attempted, they are often not accessible for symmetric swimmers, and typically only one value for the swimming speed is reported, which limits the possibility of comparison.

For all those reasons, a more detailed experimental characterization is needed. The goal of this PhD is accordingly to fill this gap and fully characterize a Marangoni swimmer experimentally. This novel approach will provide essential experimental guidance for identifying the underlying mechanisms and their properties in this highly complex problem, where theoretical resolution alone may not suffice. To completely describe the problem, all aspects of the swimmer dynamic should be tackled: (*i*) the force balance, (*ii*) the Marangoni flows generated, (*iii*) the camphor field around the swimmer. The main questions remaining after this state-of-the-art can be summarize as follows:

(i) **What are the various forces at play ?**

Understanding the forces acting on the swimmer is crucial for predicting its motion and stability. Developing methods to isolate and quantify these forces individually, as well as understanding their combined effect, will be key to fully characterizing the swimmer dynamics.

(ii) **What is the complete flow field generated by a symmetric Marangoni swimmer?**

While the flow field has been evaluated for asymmetric swimmers or camphor boats, the flow around a symmetric swimmer remains an open question. We could expect it to be more complex. Since the surfactant is not just released at the rear, Marangoni flows should extend upstream as well. An additional question concerns the contribution of these flows to the swimmer mobility: are they driving the motion or resisting it? Finally, there is a need to develop a setup where the swimmer is observed in steady state, so that high quality data can be accessed and a direct comparison made to the steady swimming considered in models.

(iii) **How is the surfactant (camphor) distributed around the swimmer?**

Both the force balance (through capillary forces) and the Marangoni flows depend on the distribution of surfactant around the swimmer. Moreover, understanding the

interfacial distribution could provide crucial insights into the dynamics of camphor (e.g., dissolution, transport), which are essential for accurate modeling. However, measuring the surfactant field experimentally is very challenging, and traditional experimental techniques to measure surface tension are not suitable for in situ measurement around a camphor swimmer. Proposing a new experimental technique to measure the 2D field of concentration is therefore a major direction to explore for achieving a comprehensive description of Marangoni swimmers systems.

(iv) **How does a Marangoni swimmer interact with a prescribed flow?**

While the previous points focus on the behavior of a single, isolated Marangoni swimmer, it is also crucial to understand how these swimmers interact with their environment, particularly under externally imposed conditions. This PhD research extends beyond the study of isolated swimmers by exploring how Marangoni swimmers behave when subjected to external forces. This exploration not only deepens our understanding of Marangoni swimmers but also has broader implications for understanding the behavior of chemically active objects in dynamic settings.

To answer these questions, this thesis presents a set of experimental and numerical tools to fully characterize a camphor swimmer. Moreover, we developed an experimental setup that allows us to apply controlled external flows to the swimmers. This setup provides a unique opportunity to investigate the dynamics of self-propelled swimmers in scenarios where they are influenced by external factors—an area that has received limited experimental attention so far. By studying the response of a single interfacial swimmer to various external forcing, such as steady flows or a harmonic potential, we aim to uncover new insights into how these swimmers adapt and respond in more complex and realistic environments.

The manuscript is structured as follows. The second chapter introduces the materials and methods used throughout this thesis, including the experimental setup, swimmer fabrication process, and numerical analysis tools. In the third chapter, we characterize the force balance by attaching the swimmer to a spring, exploring instabilities observed at low flow velocities through analytical models and numerical simulations. The fourth chapter focuses on the stationary flow generated by the swimmer, beyond the swimming velocity. In the fifth chapter, we propose a new experimental and numerical approach to obtain the surface tension field from the flow field. In the sixth chapter, we apply this new method to the case of the camphor swimmer and obtain the first experimental characterization of the surface pressure and concentration field. Finally, in the seventh chapter, we move to a slightly different topic and consider the behavior of a Marangoni swimmer in a shear flow and a vortex. The corresponding literature review will be presented at the beginning of this last chapter.

Chapter 2

Methods and tools

Table of Contents

2.1 Introduction

The primary objective of this thesis is to provide a comprehensive characterization of Marangoni swimmers, which are interfacial objects that self-propel using surface tension gradients. Our focus is specifically on symmetric camphor swimmers—centimeter-sized agarose gel discs loaded with camphor. To extend beyond a basic analysis of swimming speed, we have developed a novel experimental setup that enables simultaneous measurement of both forces and flow fields. Our approach involves transitioning to a fixed frame of reference, where the Marangoni swimmer remains stationary in a controlled flow field.

This chapter introduces the experimental and numerical methodologies employed and developed throughout this PhD research. We begin by detailing the fabrication process of the camphor swimmers. Next, we describe the experimental setup and the techniques used for force measurement. Following this, we discuss the numerical tools utilized for tracking the swimmer and reconstructing the flow field. The chapter concludes with an overview of the finite element methods applied in this study.

2.2 Experimental

2.2.1 Swimmer crafting

2.2.1.1 Symmetric swimmers

We mainly used a symmetric camphor swimmers as a chemical source for the experiments. They are disks made of agarose gel loaded with precipitated camphor (Fig. 2.1). Camphor is an interesting surfactant to use to modify surface tension as it is volatile and will evaporate quickly, avoiding saturation and providing a self-cleaning interface which allows a longer and steadier motion of the swimmer. The same swimmers were used in other related work [24, 59, 97].

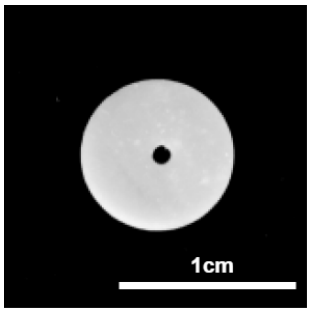

Figure 2.1: **Symmetric swimmer.** Photography of a symmetric camphor swimmer of radius 4 mm and 0.5 mm thickness. The hole at the center allows attaching it to a force sensor

The agarose gel is initially a solution of agarose $\sim 5\%$ in weight and millipore water. We followed the protocol established by previous studies [33]:

- The first step is to obtain a melted agarose[1] gel by using a microwave. Next, we eliminate bubbles formed by maintaining the gel in a liquid state for $20-30$ minutes

[1] ref. 3810, Carl Roth

with a hot ($T > 80$°C) water bath. During this process, the gel is contained in a closed container to avoid water loss by evaporation.

- The second step is to create a sheet of agarose gel. To do so, the melted gel is poured on a plate and quickly spread with a metal bar. The plate and the metal bar are specifically designed to obtain a sheet of agarose gel with the desired thickness. Irregularities, such as bubbles or bumps, and the borders of the sheet are cut out. Before being loaded with camphor, the agarose gel sheet is soaked for at least two hours in methanol[2]. It allows the removal of the unfixed water in the agarose gel and replaces it with methanol, such that water does not interfere during the next step.

- The third step is to load the agarose gel with camphor[3]. The sheet is immersed into a solution of methanol saturated with camphor, around 1.1 g/mL of camphor for methanol at 20°C, for at least 12 hours. The loaded agarose gel sheets can be conserved in this state for several weeks.

- The fourth step is to remove the methanol and precipitate the camphor inside the agarose gel sheet. The sheet is soaked in two baths of millipore water solution saturated with camphor, for 30 seconds each. Whereas it was initially transparent, the sheet turns white during the process because of the camphor precipitation. A camphor-saturated aqueous solution is used instead of millipore water to avoid camphor release into the bath and then prevent any early aging phenomena. The second bath is used to remove the camphor crystals formed over the sheet during the first bath. Then, the loaded agarose gel sheet is conserved during the experiments day in a sealed container filled with camphor-saturated water.

- The fifth and last step is to punch the disks with a circular puncher (Biopsy Punch). The swimmers are ready to use immediately. The final objects are swimmers with a radius of 4 mm and a thickness $e = 0.5$ mm. Before putting them into the water we punch the swimmer center to attach it to the force sensor.

The experimental protocol can be adapted to obtain other shapes such as ellipses, stars, rectangles, etc. In that case, we cut the shape directly in the agarose sheet, before loading it with camphor. Indeed, this step is too long and the cutting board is too dirty to be used directly on loaded sheets. The shape is cut using a cutting plotter[4]. The piece of agarose gel produced can be cleaned without risking early aging or contamination. Afterwards, the fabrication protocol follows the same steps as mentioned above.

2.2.1.2 Asymmetric swimmers: camphor boat

A second type of Marangoni swimmer used is the traditional camphor boat. It consists of a piece of plastic where a camphor pellet is glued on one side.

[2]ref. 322415, Sigma Aldrich
[3]ref. A10936, Alfa Aesar
[4]Graphtec CE5000.

Boat shape. A plastic sheet of 0.1 mm thickness is cut with a cutting plotter to obtain a boat of dimension detailed in Fig. 2.2, similar to the one described in [48]. To maintain the boat at a fixed position and attach it to the force sensor, a hole of 1 mm of diameter is made using a *Biopsy Punch* 2 mm from the apex of the boat. A second hole is made 10 mm away to add a second capillary and ensure no motion during the whole experiment. All plastic boats are cleaned with soap, thoroughly rinsed with clean and ultrapure water, and stored in a hermetically sealed container.

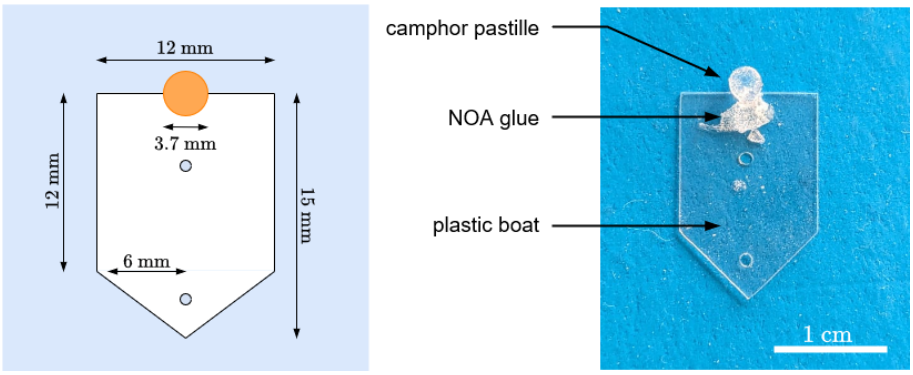

Figure 2.2: **Camphor Boat.** (Left) Illustration of the shape of dimension, (right) photo of the fabricated boat used in the experiments.

Pure camphor pellet. The source of surfactant propelling the boat is a pellet made of pure camphor, with a diameter of 3.7 mm and a thickness of 1 mm. Since camphor initially comes in powder form, we use a laboratory pellet press to compress the powder under 100 bar. To ensure consistent pellet size, the amount of powder is weighed beforehand. The prepared pellets are stored in a sealed container for a few days before being used in experiments. The pellet is then glued to the rear of the boat using *Norland Optical Adhesive 87*[5]. The high viscosity of the glue prevents it from spreading near the edges of the boat, avoiding potential pollution and additional Marangoni effect not related to camphor. To center the pellet, we use a template drawn on a transparent sheet. The glue is then reticulated using a UV pen[6] for typically 30 s. Once assembled, the boat is stored in a clean container for less than one day before use.

2.2.2 Setup

We developed a new experimental system that enables simultaneous force and flow measurements in a stationary state. The swimmer is placed in a circular rotating pool generating a stationary flow field and attached to a force sensor. To our knowledge, this is the first time such a setup has been used in the literature. The primary advantage of this experimental setup is the fixed position of the swimmer, which allows for consistent measurements and reproducibility of experimental conditions which contrasts with traditional experiments where the swimmer move freely [83, 84]. The setup also provides precise control over the flow speed, enabling exploration beyond the swimmer spontaneous swimming

[5]ref.8701B NOA 87 Norland Products
[6]ref. E-UVPEN Polydispensing system

velocity. Furthermore, the flow prevents the accumulation of camphor at the rear of the swimmer, addressing a limitation seen in previous force measurements where the swimmer was fixed without underlying flow [52]. Finally, the design is straightforward and easy to construct, eliminating the need for complex pumping systems to circulate water, as required in straight channel setups.

However, it is important to mention the potential drawbacks. The curvature of the channel may induce geometrical distortion, which must be accounted for in the analysis. Additionally, the gradient in flow velocity across the channel can create a different flow field compared to a straight channel configuration, making comparisons to theoretical predictions less relevant. The closed system can also lead to the saturation of camphor or other surfactants over time. To mitigate saturation effects, despite the relatively large water volume (1 L), we limit the experimental time to under 5 minutes and clean the interface between each experiment.

Rotating pool. We use a transparent cylindrical tank with a circular channel of inner radius 10 cm and outer radius 20 cm (Fig 2.3). A motor makes the tank rotate creating a stationary solid-body rotation flow within the channel. Unless mentioned otherwise, the pool is always filled with $h = 1$ cm of ultrapure water. The central part of the tank can be removed, if needed, giving a cylindrical pool with a radius of 20 cm. The swimmer is maintained at a fixed position using a force sensor. We used a *Baumer HXC40* camera equipped with a *Nikon 24–85 mm f/2.8-4D IF AF NIKKOR* objective placed below the swimming pool with a mirror at 45° to record the position of the swimmer and the water flow.

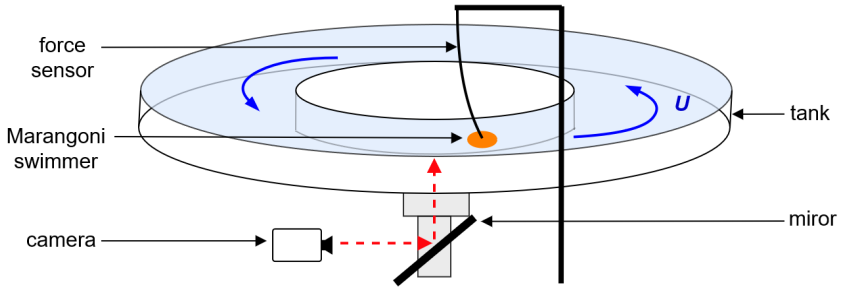

Figure 2.3: **Experimental set-up.** The circular tank is rotating generating a controlled stationary flow, the swimmer is maintained at a fixed position allowing simultaneous force and flow measurements.

Generated flow field. As the tank rotates, it generates a solid-body rotational flow, where the flow velocity $\mathbf{u}_{\text{solid}}$ at a distance $\mathbf{r}$ from the center of the tank is proportional to the angular speed ω, specifically $\mathbf{u}_{\text{solid}} = \boldsymbol{\omega} \times \mathbf{r}$ (Fig. 2.4). In the following, the global flow field will be denoted as $u(r)$, while the velocity at the center of the channel—experienced by the swimmer— will be denoted as $u(r = 15\,\text{cm}) = U$. The flow field can be visualized by adding tracers; we use hollow glass spheres[7] that remain at the air-water interface. By utilizing numerical analysis tools such as Particle Image Velocimetry or Optical Flow, the flow field can be accurately reconstructed (Fig. 2.4). These algorithms are presented in

[7] ref. Easy composite Glass Bubbles (Microspheres) FP-GB-01

more detail later on (Sec. 2.3, page 36). Given that the flow field generated in this setup is stationary, it is possible to consider the time-averaged field instead of relying solely on instantaneous measurements, thereby increasing the reliability of the measurements—a key advantage of this setup. Measurement of the time-average interfacial velocity shows a linear dependency with the radius of the tank (Fig. 2.4) confirming the solid rotation profile. The uncertainty on the velocity is at most $2\,\mathrm{mm\,s^{-1}}$.

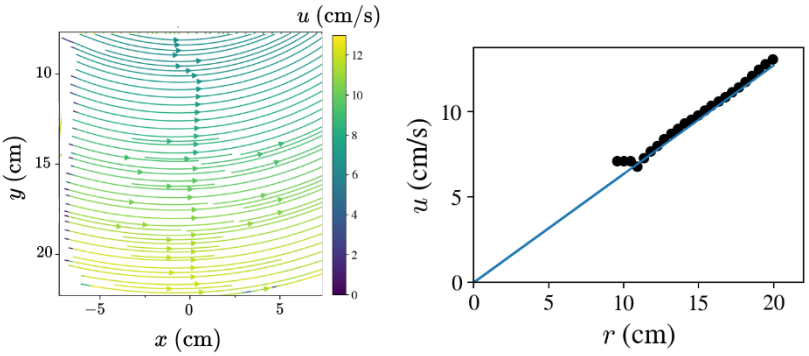

Figure 2.4: **Flow field.** Water flow generated by the solid rotation of the tank. (Left) Average streamlines, the color indicates the flow velocity. (Right) Norm of the velocity with respect to the distance to the tank center. The blue line corresponds to the expected velocity for $\omega = 0.64$.

Cleaning protocol. The velocity of the swimmer can be sensitive to surface contamination from dust, oils from skin contact or residual chemicals from previous experiment, making it essential to maintain a clean environment for accurate experimentation. Therefore, it is necessary to protect the setup and to follow a strict cleaning protocol. Given that the tank contains 1 L of ultrapure water, completely renewing the water between each experiment is impractical. To keep the surface clean, we periodically removed any contaminants by using a pump to suck the water surface. Additionally, all equipment that comes into contact with the water is thoroughly cleaned using ethanol and water. The tracers used to visualize the flow field are first washed in two successive baths of ethanol and water to remove any impurities, then heated at 200 °C for 40 minutes to ensure complete drying. The process is repeated twice to maximize cleanliness and ensure that the flow measurements remain uncontaminated.

2.2.3 Force measurement

To measure the resulting force applied on the swimmer for different advection speed, it is attached to a force sensor acting as a spring. The force measured corresponds to the restoring force of the spring on the swimmer $\mathbf{F}_\mathrm{s}$ which balance, the drag $\mathbf{F}_\mathrm{d}$ applied by the flow underneath the swimmer and the capillary force $\mathbf{F}_\mathrm{c}$ from the gradient of surface tension around it. For an immobile swimmer all the forces equilibrate and $-\mathbf{F}_\mathrm{s} = \mathbf{F}_\mathrm{c} + \mathbf{F}_\mathrm{d}$.

Fabrication of a force sensor. The force sensor was fabricated by heating a Pasteur pipette and manually pulling on both ends while the glass was still soft. Since the process

is not perfectly reproducible, each capillary was individually calibrated to correlate the measured bending to the applied force. Additionally, some capillaries exhibited significant deviations or irregularities at the tip and were therefore eliminated to avoid potential inaccuracies. To calibrate the sensor, small pieces of parafilm with known masses were attached to the tip, and the resulting bending was measured (Fig. 2.5 left). The deflection of the capillary was found to be linear with the applied force, reproducible, and independent of the orientation (Fig. 2.5 right). By modeling the capillary as a spring, a stiffness k can be defined which allows calculating F_s from the measurement of the displacement dx of the tip $F_\mathrm{s} = dx \times k$ (Fig. 2.5).

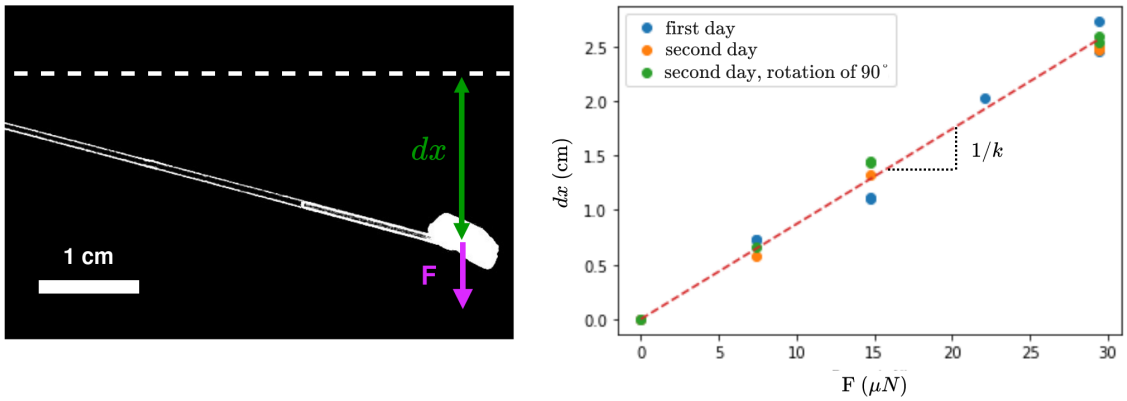

Figure 2.5: **Calibration of a glass capillary.** (Left) Side picture of a force sensor tip during calibration with a piece of parafilm. The dashed white line indicates the horizontal from the other end. (Right) Calibration curve for the same capillary on two different days and with a rotation of 90 degrees of the capillary.

Drag force on an interfacial object. Before measuring the force applied by the water flow on an active camphor swimmer, we want to validate our experimental technique. To achieve this, we used inert disks with known drag characteristics from the literature [98] and which can be used as test bed. The disks, made of plastic with a thickness of 100 µm, had radii ranging from 3 mm to 8 mm and floated at the water surface. The relationship between the force exerted by the fluid F_drag on the disc and velocity U depends on the Reynolds number Re a dimensionless quantity corresponding to the ratio of the inertial forces to the viscous forces. It can be defined as $\mathrm{Re} \equiv \rho U a/\eta$ where ρ is the density of the fluid, a the radius of the disk and η the dynamic viscosity. In our experiment, the typical Reynolds number is $\mathrm{Re} = 300$, thus we are far from the Stokes regime and we expect to observe the formation of a boundary layer under the disc. In this regime, the friction experienced by centimeter-sized bodies sliding on water can be computed using the Blasius condition [98]:

$$F_\mathrm{d} = -\alpha\rho\sqrt{\nu}(aU)^{\frac{3}{2}} \tag{2.1}$$

where $\alpha = 1.64$ and ν is the kinematic viscosity of the fluid.

Experimental results for a passive disc. For a disc with a radius of 4 mm, Eq. (3.1) describes well our experimental data with the theoretical value of $\alpha = 1.64$ (Fig. 2.6 left).

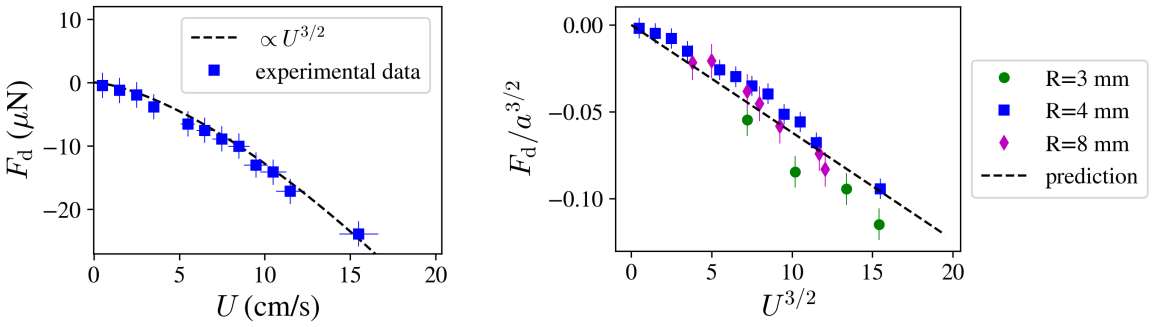

Figure 2.6: **Drag force on an interfacial passive plastic disc.** (Left) Evolution of the drag force F_d on a passive disc of 4 mm with respect to the advection velocity U. Squared symbols indicate experimental measurements, and the dashed line is the theoretical prediction of Eq. (1) with $\alpha = 1.64$ (Right) Measurement of the normalized drag force applied on passive discs of radius 3, 4 and 8 mm. The points are the experimental measurement and the dashed line is the analytical prediction.

To check if Eq. (3.1) still holds for other radii, we can rewrite it as:

$$\frac{F_{\text{drag}}}{a^{3/2}} = -\alpha\rho\sqrt{\nu}U^{3/2} \tag{2.2}$$

and we obtain a linear relationship between $F_{\text{drag}}/a^{3/2}$ and $U^{3/2}$. We use this relation to plot all the data obtained for discs of different radii on the same graph (Fig. 2.6 right) and we observed that all points collapse on a single linear curve which corresponds to the theoretical prediction (Eq. (2.2)).

Conclusion. We found that for a passive disc $F_{\text{drag}} = -\alpha\rho\sqrt{\nu}(aU)^{\frac{3}{2}}$. Our results, are consistent with prediction from the literature, validate our new setup to measure the force applied by a water flow on an object of radius between 3 and 8 mm at the air-water interface.

2.3 Images analysis

Having introduced and validated the physical setup for measuring the restoring force F_s corresponding to the balance between the drag force F_d and the capillary force F_c for an immobile swimmer, the next step is to analyze and interpret the data generated during the experiments. In this section, we discuss the various numerical methods employed, including swimmer tracking, Particle Image Velocimetry (PIV), and optical flow techniques. These tools are essential for extracting precise information about the swimmer dynamics and the flow characteristics that influence its behavior.

2.3.1 Tracking algorithm

To analyze the swimmer motion accurately, we extract position data from video recordings, identifying the swimmer location in each frame and reconstructing the trajectory based on these positions.

Circular swimmer. For circular swimmers, the Hough Circle Transform [99] is employed to determine the swimmer position. By detecting the coordinates of the circle center (Fig. 2.7), we obtain precise location. Given the uniform background and clear image contrast, applying the transform directly is feasible without additional preprocessing. The Python library OpenCV[8] facilitates this process with its efficient implementation of the Hough Circle Transform.

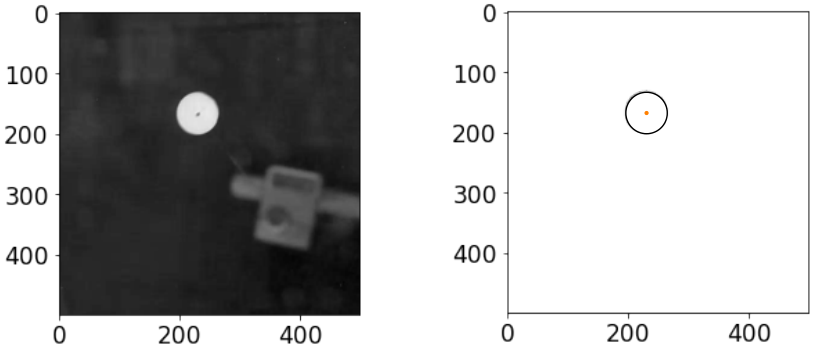

Figure 2.7: **Tracking.** (Left) Example of an experimental image, the swimmer is the white circle, in the background the laboratory stand holding the force sensor is visible. (Right) Results of the image processing, the orange point indicates the center of the circle found by the Hough transform, it coincides with the swimmer center. The swimmer is 4 mm radius, the units are in pixels.

Camphor boat. Tracking the camphor boat is more complex due to its irregular shape. Standard algorithms are not available, so manual tracking is necessary. Using *ImageJ*, we manually extract the positions of each corner of the boat. For the camphor pellet, the Hough Circle Transform is again used to determine its position accurately.

2.3.2 Particle image velocimetry

To reconstruct the flow around an interfacial object, Particle Image Velocimetry (PIV) is used [100]. PIV is an optical method of flow visualization used to obtain instantaneous velocity measurements by recording the transportation of seeding or tracer particles carried by the moving fluid. In our experiment, the fluid is seeded with glass bubbles, also called micro-sphere or micro-balloons, hollow glass spheres that stay at the air-water interface[9]. A key feature of PIV is that it is a quantitative method of flow field mapping where we can obtain, simultaneously, velocity vectors everywhere within the measurement region. PIV is also a non-intrusive method to the extent that tracers are well-chosen and do not modify the flow. In contrast, point measurement techniques would necessitate

[8] Documentation on the Hough tranform from OpenCV is available here https://docs.opencv.org/3.4/d4/d70/tutorial_hough_circle.html

[9] Glass bubbles stay at the interface as long as they are intact and clean. An additional benefit of the cleaning protocol is that it helps remove broken glass bubbles, which sink during the cleaning process (in the ethanol or water bath) and are not collected for subsequent steps.

physically moving a probe across the measurement region, a time-consuming process that can disturb the flow [100].

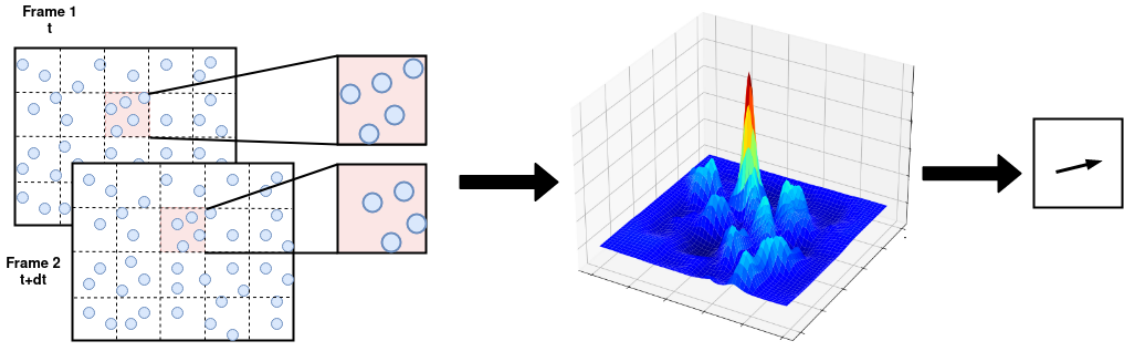

Figure 2.8: **Principle of the PIV method.** (Left) Images are divided into small interrogation areas (IA), and each IA of consecutive images are cross-correlated. (Center) Result of the cross-correlation between two consecutive images. The peak represents the more probable displacement in pixels in the (x, y) plane, between the two images. (Right) Displacement vector obtained for a pair of IA.

Methodology overview. The flow is illuminated so that the tracers become visible, since the tracers are only present at the interface, white light is sufficient and no laser sheet is necessary. The motion of the seeding particles is used to calculate the velocity field. For this purpose, a sequence of image frames is recorded. Then two consecutive images are divided into small subsections called interrogation areas (IA) (Fig. 2.8 left). The local displacement Δx, for each IA is given by the signal peak, of a cross-correlation function [101] (Fig. 2.8 center). Knowing the time interval Δt between two consecutive frames, the velocity v associated with the center of the IA can be computed as follows:

$$v_x = \frac{\Delta x}{\Delta t}. \tag{2.3}$$

A velocity vector map over the whole target area is obtained by repeating the cross-correlation for each interrogation area over the two image frames captured by the camera.

PIV in practice. It is essential to meet certain conditions to obtain a reliable measurement and reduce uncertainties [102, 103]: (*i*) the density of particles should be high (> 1 particle in each interrogation area). (*ii*) The displacement between two consecutive images should be smaller than half of the IA. (*iii*) Particles should not influence fluid flow, be easily visible, and follow faithfully the liquid velocity. To meet these criteria, the size of a tracer and the response time of the tracers should be smaller than the characteristic length and time scales of the speed variation. We will verify these two properties in the next paragraph. (*iv*) The tracers should not modify the surface tension. For that, we wash the tracers carefully and store them in a hermetic container (Subsec. 2.2.2). In the following section, the choice of glass bubbles as tracers for studying the flow at high Reynolds numbers around an interfacial object is discussed.

Glass bubbles are reliable tracers. For an object to be a reliable tracer, it must accurately follow the flow without altering it. Two key conditions must be met: the tracer size should be smaller than the typical length scale of flow variation and its response time should be shorter than the characteristic timescale of the flow. We estimate the length scale of speed variation by considering the thickness of the boundary layer beneath the disc or swimmer, $\delta = R/\sqrt{\mathrm{Re}} \approx 400\,\mu\mathrm{m}$. Our glass bubbles have a size $r_{\mathrm{tracer}} = 50\,\mu\mathrm{m}$, which is smaller than the boundary layer thickness. Hence, the glass bubbles are suitable for PIV as their size does not significantly affect the liquid flow.

Additionally, the tracers must faithfully follow the liquid velocity. To ensure this, the characteristic timescale of flow speed variation is approximated by $t_{\mathrm{flow}} = U/R \approx 1\,\mathrm{s}$, should be larger than the response time of the tracers t_{tracer}. For a spherical particle in Stokes flow, the response time can be estimated using Newton second law:

$$m\frac{dv}{dt} = -6\pi\eta r_{\mathrm{tracer}} U, \tag{2.4}$$

with $m = \rho \times \frac{4}{3}\pi r_{\mathrm{tracer}}^3$, which gives,

$$t_{\mathrm{tracer}} \approx \frac{\rho r_{\mathrm{tracer}}^2}{\eta} \approx 25 \times 10^{-2}\,\mathrm{s}. \tag{2.5}$$

Since $t_{\mathrm{tracer}} < t_{\mathrm{flow}}$ the glass bubbles will faithfully follow the liquid flow, making them a suitable choice for PIV tracers.

PIV algorithm parameters: For PIV analysis, we utilized the open-source module *OpenPIV*[10] in Python to perform cross-correlation between image pairs. The algorithm offers a large range of parameters that can be adjusted to process the data, including options for replacing or filtering detected vectors. To ensure that our analysis closely reflects the experimental conditions and given the good quality of our data and simplicity of the flow field, we chose to disable all replacement and smoothing options. We retained only the initial filtering step to maintain data integrity while minimizing modifications. A detailed list of the parameters used in our analysis is provided in Appendix. 2.5. While PIV provides valuable velocity data, there are scenarios where tracer density may not meet requirements, especially near the swimmer or within its wake. In such cases, we complement our analysis with another optical technique called Optical Flow.

2.3.3 Optical flow

A technique complementary to PIV. Reliable measurements using PIV require a sufficient density of tracers within each interrogation window. However, this condition may not always be met, particularly in regions close to the swimmer or within its wake. To address this limitation, we complement PIV with Optical Flow, another optical technique that tracks tracer movement. Optical Flow is a computer vision method that analyzes how pixel patterns change across consecutive images, revealing the apparent motion of objects or features. The main principle is based on assuming the local constancy of brightness, meaning pixels maintain their intensity over time. The primary goal is to estimate the velocity of these pixels, providing information on the global motion within the image.

[10] All documentation is available here: http://www.openpiv.net/index.html

Lucas-Kanade Method For our optical flow analysis, we use the Lucas-Kanade method [104], which technique involves several key steps:

- Assuming the constancy of pixel brightness over time.
- Computing spatial gradients in horizontal and vertical directions for each pixel to determine the rate of intensity change.
- Defining a local spatial window around each pixel where motion is assumed to be constant.
- Linearizing the motion equation within the local window, resulting in a set of linear equations for estimating optical flow parameters.
- Utilizing the least squares approach to solve the system of linear equations for each pixel, yielding the local optical flow vector.
- Iteratively applying this process across the entire image or selected regions, refining optical flow estimates.

The Lucas-Kanade method is particularly effective for analyzing relatively small motions and regions where the motion can be approximated as uniform over a local neighborhood. However, its performance may be limited in cases involving large displacements or complex motion patterns. In such scenarios, advanced techniques or supplementary algorithms may be required.

Pyramidal approach. To enhance the adaptability of the Lucas-Kanade method across varying scales of motion, we employ a pyramidal approach [105]. This technique involves creating an image pyramid by progressively downscaling the input image into multiple levels, each representing a different resolution. The Lucas-Kanade method is then applied iteratively at each level, beginning with the coarsest resolution and moving to the finest. Optical flow estimates obtained at each level serve as initial values for the subsequent, finer level. This approach ensures robustness and accuracy in capturing both large and small-scale motion variations within the visual data. For our implementation, we utilize the Python plugin for optical flow provided by *OpenCV*[11], and we use the function *goodFeaturesToTrack*[12] to identify key features in the images [106]. The method aims to identify corners or textured regions in an image, which are stable and distinguishable enough to be reliably tracked. The idea is that these features should be robust against changes in viewpoint, lighting, and other variations that might occur between frames of a given video.

2.4 Finite elements methods

During this thesis, our experimental results will be compared to previous numerical work [31] made with finite element methods (FEM), and some computations will also be made

[11]Documentation for the optical flow function of *OpenCV* is available here: https://docs.opencv.org/3.4/d4/dee/tutorial_optical_flow.html

[12]Documentation for the function *goodFeaturesToTrack* is available here: https://docs.opencv.org/4.x/d4/d8c/tutorial_py_shi_tomasi.html

using FEM. Therefore, we introduce here the general principle. The FEM is a numerical method used to solve partial differential equations (PDEs) and ordinary differential equations (ODEs) by approximating their solutions. It was initially developed for structural analysis [107] but has since expanded to a wide range of applications due to its versatility and robustness [108–110]. The core idea behind FEM is the discretization of a complex system into smaller and simpler parts, known as finite elements. The discretization allows approximating PDEs, which can then be solved using numerical techniques. Unlike some other methods, FEM does not require uniform discretization; instead, it can adapt to local features, such as regions with large gradients or intricate geometries, by using a finer mesh in those areas. The flexibility of FEM makes it particularly powerful in handling complex geometries and multicomponent systems [111].

One of the key strengths of FEM is its applicability to a vast array of physical problems, including structural analysis, heat transfer [112], fluid flow [113], and electromagnetic potential [114]. In this thesis, we exploit FEM ability to address coupled problems, particularly mass transport and fluid flow. We will be using Comsol for our FEM calculations, a commercial software using finite elements method specialized for multiphysics applications. While FEM is a powerful tool, it does have limitations, such as high computational costs for large-scale problems and potential difficulties in handling complex boundary conditions.

Conclusion

We have developed a new experimental setup to measure simultaneously the force and the flow around an interfacial object. The force measurements were validated for a passive disc. For the flow field, we confirmed that the flow generated is indeed solid body rotation. We also presented numerical tools for image analysis, such as PIV and optical flow, which will be applied in the following chapters to reconstruct the flow field. Additionally, the finite element method will be used to compare with previous results and assess the usual hypotheses for modeling Marangoni swimmers. While each of these techniques is traditional and well-established, their combination in this context may offer a novel approach.

2.5 Appendix: PIV parameters

Detail of the parameters used to run the OpenPIV algorithm on our data.

```
'Region of interest'
#Allow to select ROI: (xmin,xmax,ymin,ymax) or 'full' for full image
settings.roi = 'full'

'Image preprocessing'
# 'None' for no masking, 'edges' for edges masking, 'intensity' for
    intensity masking
settings.dynamic_masking_method = 'None'

'Processing Parameters'
settings.correlation_method='circular' # 'circular' or 'linear'
```

```
11 settings.normalized_correlation=False
12 settings.num_iterations = 3 # select the number of PIV passes
13 settings.windowsizes = (256,128, 64,32)
14 settings.overlap = (128,64, 32,16) # This is 50% overlap
15 settings.subpixel_method = 'gaussian' # methode used for subpixel
       interpolation: 'gaussian','centroid','parabolic'
16 settings.interpolation_order = 3 # order of the image interpolation for the
       window deformation
17
18 'Scaling'
19 settings.scaling_factor = 1 #the length will be in pixel
20 settings.dt = 1 #the time will be in fame
21
22 'vector validation options'
23 # choose if you want to do validation of the first pass: True or False
24 settings.validation_first_pass = True
25 'Validation Parameters'
26 # The validation is done at each iteration based on three filters.
27 # The first filter is based on the min/max ranges. Observe that these
       values are defined in terms of minimum and maximum displacement in pixel
       /frames.
28 settings.minmax_u_disp = (-15, 15)
29 settings.minmax_v_disp = (-30,10)
30 # The second filter is based on the global STD threshold
31 #settings.std_threshold = 5 # threshold of the std validation
32 # The third filter is the median test (not normalized at the moment)
33 #settings.median_threshold = 1 # threshold of the median validation
34
35 'Outlier replacement or Smoothing options'
36 # Replacement options for vectors that are masked as invalid by the
       validation
37 settings.replace_vectors = False # Enable the replacement.
38 settings.smoothn=False #Enables smoothing of the displacement field
39
40 'Output options'
41 # Select if you want to save the plotted vectorfield
42 settings.save_plot = True
43 # Choose whether you want to see the vector field or not
44 settings.show_plot = False
45 settings.scale_plot = 500 # select a value to scale the quiver plot
```

Chapter 3

Spring-attached swimmer in imposed flow

Table of Contents

Introduction

The first new experimental observable that is easily accessible with our setup is the force $\mathbf{F}$ exerted by the fluid on the swimmer which corresponds to the sum of the capillary force $\mathbf{F}_c$ from the gradient of surface tension and the drag force $\mathbf{F}_d$ from the flow : $\mathbf{F} = \mathbf{F}_c + \mathbf{F}_d$. In an earlier work [52], first experimental measurements were made for a camphor boat of 2 cm. Suematsu and coworkers measured a force exerted by the fluid of $F = 23 \pm 2\,\mu N$. In their experiment, since there was no flow, the measured force could be directly attributed to the propulsion force $F = F_c$, neglecting potential drag induced by Marangoni flows. However, the boat was maintained at a fixed position allowing camphor to accumulate at the rear, leading to a larger force than when the boat is moving. Their experimental measurement gives an order of magnitude for the capillary force.

In the experimental setup we designed (Fig. 2.3, page 33), the swimmer is placed in a flow of imposed velocity. More precisely, the swimmer is attached to a glass capillary acting as a spring and the circular tank rotates generating a flow u_{solid}. In the following the flow velocity will be indicated by the ratio $\chi = U/V$ between the velocity at the center of the channel U and the swimming velocity V. The glass capillary is calibrated such that we can compute the restoring force of the spring $\mathbf{F}_s$ from the displacement d from the original without a swimmer attached. And for an immobile swimmer, $\mathbf{F}_s$ balances the force exerted by the fluid: $-\mathbf{F}_s = \mathbf{F} = \mathbf{F}_c + \mathbf{F}_d$. In the following discussion, the measured force will be denoted by F, and if not specified the "force" will always refer to the force exerted by the fluid on the swimmer.

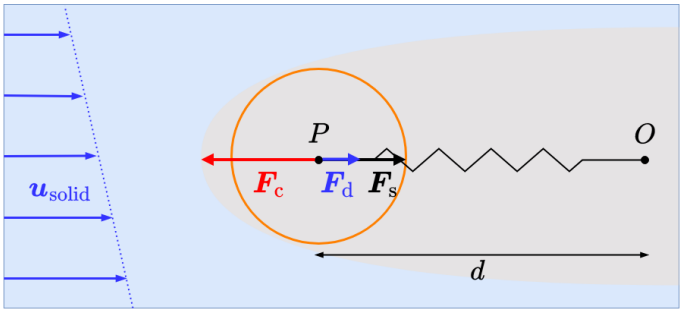

Figure 3.1: **Marangoni swimmer in a flow of imposed velocity.** Schematic top view of the experimental situation. The swimmer (orange circle) is attached at its center P to a glass capillary acting as a spring. The equilibrium position of the spring without flow or swimmer attached is O. We measure the restoring force of the spring $\mathbf{F}_s$ resulting from the balance between the capillary force $\mathbf{F}_c$ and the drag force $\mathbf{F}_d$.

As a reminder, a simple illustration of the force balance, we first considered the case of a passive disc (Subsec. 2.2.3, page 34) not releasing surfactant. In that simple case, the force exerted by the fluid is equal to the drag force. For a passive disc, we expect the drag force to be:

$$F_d = -\alpha\rho\sqrt{\nu}(aU)^{3/2}, \tag{3.1}$$

where ρ is the fluid density, ν its kinematic viscosity, a the radius of the interfacial object, U the fluid velocity and $\alpha = 1.6$ a constant [98]. Our experimental measurements of F match the analytical prediction and are consistent with previous experimental measurements [98], validating our setup to measure the force on an interfacial object.

In this chapter, we study the trajectories and force balance of a symmetric camphor swimmer attached to a spring (Fig. 3.1). We first measure the force applied by the fluid on the swimmer for different flow velocity. We observe two regimes, first at low flow velocity the force is positive, showing the capillary force is larger than the drag and the swimmer moves against the flow. When the flow velocity is equal to the swimming velocity, the force exerted by the flow vanishes, which indicates a swimming point. Finally, for larger flow velocity the force becomes negative, and the swimmer is dragged by the flow. Previous results from finite element methods also exhibit similar behavior [62] and show that the force applied by the fluid cannot be reduced to the capillary force generated by the gradient of surfactant and the drag force on a passive disc. The Marangoni flows generate an additional force.

At low flow velocity the swimmer does not have a fixed equilibrium position but exhibits a circular trajectory. Increasing the flow decreases the amplitude until the swimmer stops moving. We study this behavior in the second part of this chapter. We first characterize the instabilities experimentally and then develop a toy model for a punctual source attached to a spring without diffusion. We move to the finite diffusion case with finite difference simulation. Both approaches qualitatively reproduce the experimental observation with and without flow, suggesting the instabilities are not due to the generated Marangoni flows but are rather generic of self-propelled objects in a harmonic confining potential.

3.1 Force balance

3.1.1 Experimental characterization

Protocol. In this chapter, the swimmer is an agarose gel disc loaded with camphor (Subsec. 2.2.1, page 30). It has a radius of 4 mm and propels at an average speed $V = 7 \pm 1$ cm/s in quiescent water. Previous studies [24] have shown although camphor swimmer can swim for several hours, its swimming velocity is time-dependent. It decreases significantly during the first 500 s and approaches a smaller rate of change in the velocity. Therefore, as the quantities we are interested in (forces, flow field, surfactant distribution) may depend on the swimming velocity and/or may also be time-dependent, we decided to follow the same protocol and realize our measurement after $700 - 900$ s of swimming as it enables us to repeat the experiment easily. In practice, we let the swimmer move in a first tank filled with 1 cm of ultrapure water. After 9 min we remove the swimmer and attach it to the force sensor in the main circular tank. This process takes approximately 2 min. Then we record a set of images of the swimmer and the water flow for less than one minute. The swimmer is then removed from the main tank and the surface is cleaned by sucking the surface using a pump to avoid contamination by any external agent such as dust. If necessary, the water height is refilled to maintain $h = 1$ cm. Afterward, a new swimmer is put in the pre-swimming tank and the process is repeated with another swimmer or a different flow velocity.

What do we expect? Water flow advects the camphor, thus breaking the radial symmetry that would apply for an immobile swimmer and increasing the camphor concentration dowstream (Fig. 3.1). As a result, Marangoni swimmers tend to swim against

the water flow. Depending on the imposed flow velocity we expect to observe different regimes:

- $\chi < 1$. The advection speed is lower than the spontaneous swimming velocity (Fig. 3.2 left). Thus, the capillary force $\mathbf{F}_c$ is larger than the drag force exerted by the fluid $\mathbf{F}_d$ and the swimmer would like to swim against the flow but the capillary is holding it back. So we expect to measure a positive deviation of the capillary and therefore, a positive force.
- $\chi > 1$. The advection speed is now larger than the swimming speed (Fig. 3.2 right). Thus, $\mathbf{F}_c < \mathbf{F}_d$ and the swimmer is dragged away by the flow and the spring prevents it from drifting away. Therefore, we expect $\mathbf{F}_s < 0$.
- $\chi = 1$. In between these two regimes, we expect to find a stable position: the swimming point where total force vanishes and no deviation of the force sensor is observed. It means that the drag force cancels the capillary force which should happen when $U = V$.

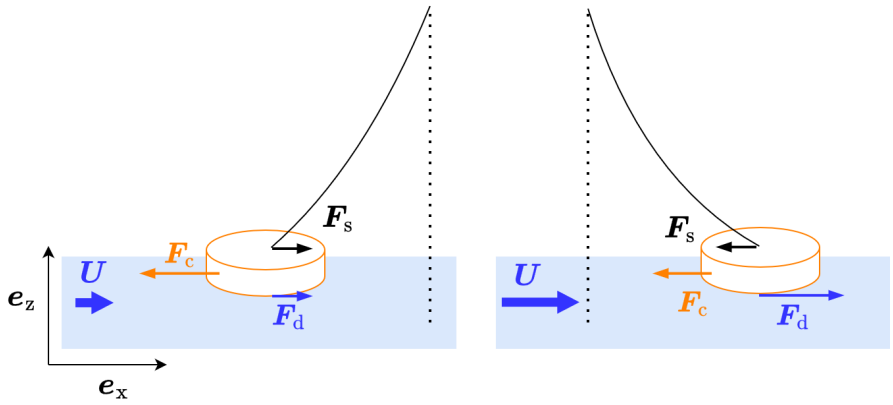

Figure 3.2: **Force balance.** Side view of the expected behavior of a Marangoni swimmer (orange disc) at low flow velocity $\chi < 1$ (left) and large flow velocity $\chi > 1$ (right).

The force changes sign. For a camphor swimmer the measured force is completely different from that observed for the passive disc (Fig. 3.3) and the relation $F \propto U^{3/2}$ does not apply. The behaviors depend on the flow velocity with a change of sign at $\chi = 1$. In more details:

- For $\chi < 1$, *ie* flow velocity lower than the swimming velocity, the force exerted is positive and the swimmer moves against the water flow.
- For $\chi > 1$, the force is negative, so the swimmer is swept by the current. In addition, the force seems to decrease linearly with χ. And for very large values of the flow velocity, the force seems to approach that of a passive disc
- For $\chi \simeq 1$ there is a stable position in which the force exerted on the swimmer vanishes, it corresponds to a swimming point. In this study, the swimming point was observed at $U = V = 6.8\,\mathrm{cm\,s^{-1}}$ which aligns well with the swimming velocity of $V = 7 \pm 1\,\mathrm{cm\,s^{-1}}$ reported in previous work [24], with a difference of only 3%.

It is important to note that a different camphor swimmer was used for each advection speed, and several capillaries with stiffness values k ranging from 5×10^{-2} to $2\times10^{-1}\,\mathrm{N\,m^{-1}}$ were employed. The standard deviation between measurements for the same flow velocity across different swimmers and capillaries resulted in an error bar of ($\pm2\,\mu$N).

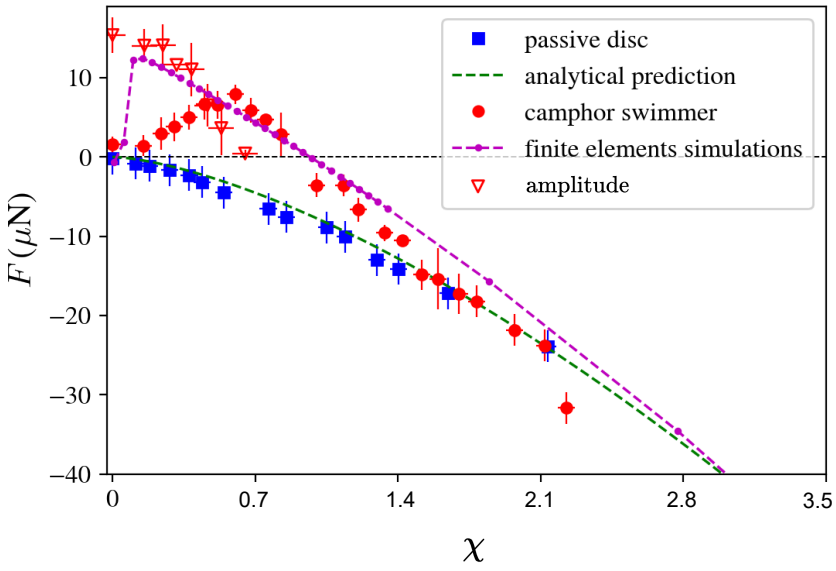

Figure 3.3: **Force on an active camphor swimmer.** Experimental measure of the force on an interfacial object: passive plastic disc (blue squares) and camphor swimmer (red dots). The dashed green curve is the theoretical prediction from Eq. (3.1) for a passive disc. Empty triangles correspond to the average radius of the ellipsoidal trajectory of the swimmer when unstable. Error bars are evaluated from the standard deviation between experimental measurement for different swimmer and spring stiffness at the same flow velocity. Finite element method results for $M = 15000$, $\mathrm{Sc} = 10$ (purple doted curve), the data are rescaled to correspond to experimental units, see Subsec. 3.1.2.

Instabilities. In addition to the expected change of sign at $\chi = 1$, at low flow velocity $\chi < 0.6$ the swimmer exhibits an ellipsoidal trajectory. In that case, the average position was used to compute an average force exerted by the spring. The average amplitude of the trajectory is reported with red empty triangles (Fig. 3.3). As the flow velocity increases, the amplitude of the instabilities decreases until the swimmer reaches a fixed position. The instabilities seem to stop around $\chi = 0.6$ when the force reaches its maximum value. The origin of these ellipsoidal trajectories will be explored in detail in Sec. 3.2 page 49. Before doing so, we compare the experimental force measurement with numerical computations.

3.1.2 Comparison with finite element methods

We want to adapt the numerical computation made by Boniface *et al.* [62] to obtain the capillary and drag force outside the spontaneous swimming velocity.

Numerical system. The main assumptions are the usual ones: (*i*) flat swimmer and flat interface, (*ii*) surfactant far from saturation and linear relationship between the concentration and the surface tension, (*iii*) imposed flux and punctual surfactant release, (*iv*) steady state. As compared to [62], the geometry of the system is slightly modified to better fit our experimental setup, we consider a circular channel of 20 cm outer radius and 10 cm width.

Dimensionless numbers. To make the governing equations dimensionless, we consider four dimensionless numbers: Reynolds Re, Péclet Pe, Marangoni M, and Schmidt Sc numbers. As usual, the Reynolds number indicates the relative magnitude of inertial and viscous effects in the Navier-Stokes equation. The Péclet number compares the surfactant transport by advection to diffusion. The Schmidt number is the ratio of momentum and mass diffusivity in the liquid. The Marangoni number M corresponds to a Péclet number based on the Marangoni velocity and compares advective transport by such flows with diffusion. We considered $M = 15000$ and $\mathrm{Sc} = 10$. Under these conditions, the swimming velocity corresponds to a Péclet number $\mathrm{Pe}_{\mathrm{swim}}$ is 100 and the Reynolds number is 10. These values suggest that a boundary layer forms around the swimmer, resulting in a nonlinear drag force. Although this regime differs from the experimental conditions where $M \sim 10^{10}$ and $Sc \sim 10^3$, the model should still capture the qualitative impact of drag due to its relevance in the same flow regime. Achieving the experimental conditions numerically is not feasible because the transport and hydrodynamic boundary layers become very thin, requiring an extremely fine mesh over a large area, which leads to convergence issues.

Results and comparison with experiments. To adimensionalize the experimental values, several parameters are required (such as the flux of camphor, diffusion coefficient, etc.), which are not known *a priori* and would require several assumptions. Therefore, we chose to adapt the finite element results for qualitative comparison with the experiments. The dimensionless swimming Péclet number, $\mathrm{Pe}_{\mathrm{swim}}$, corresponds to $\chi = 1$, and the force scale is adjusted such that, for large advection, we recover the behavior observed in the passive disc case.

The qualitative behavior observed in the numerical simulations is consistent with the experimental results, showing a positive force for $\chi < 1$ and a negative force for $\chi > 1$ (Fig. 3.3, purple dashed line with circles). The force reaches its maximum around $\chi \simeq 0.1$. The slight discrepancy in the position of this maximum force between the experiment and simulation is likely due to instabilities observed in the experiment; for $\chi < 0.4$, we report the average position of the swimmer, whereas, in the numerical computation, the swimmer is fixed making comparison not straightforward. After reaching its maximum, the force decreases linearly, consistent with experimental observations. For $\chi > 3$, we observe a force proportional to the flow velocity raised to the power of 3/2. The prefactor obtained using Eq. (3.1) is $\alpha = 1.96$, whereas a value of 1.64 is expected for a passive disc [98]. The regime $F \propto U^{3/2}$ was not clearly observed in the experiment, potentially because the advection velocity was too low, only reaching up to $\chi = 2$ in the experimental setup.

Neglecting Marangoni flows. The finite element method enables a detailed analysis of all components of the force exerted by the fluid on the swimmer, beyond the resultant

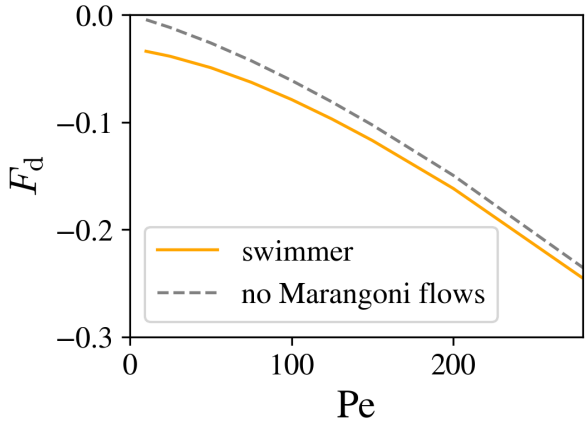

Figure 3.4: **Drag force.** Finite element computation to obtain the drag force on a camphor swimmer for $M = 15000$ and $\mathrm{Sc} = 10$ (orange line), and turning off the Marangoni term generating the Marangoni flows (gray line). The results are dimensionless.

force. For a self-propelled object, a straightforward approach would be to consider the total force as the sum of the capillary force and the drag force that a passive disc would experience. In other words, assuming that Marangoni flows do not contribute to the drag. To test this assumption, we deactivated the Marangoni term, which is responsible for generating flows due to the surfactant gradient in the simulation. The observed drag force changed upon deactivation of the Marangoni term (Fig. 3.4), highlighting that the drag force due to Marangoni flows is significant and cannot be neglected. Consequently, a thorough understanding of the forces acting on a camphor swimmer necessitates accounting for the entire water flow, including the effects of Marangoni flows.

Conclusion. The force dynamics acting on an interfacial Marangoni swimmer differs significantly from those on a passive disc. A positive force is observed at low flow velocities, which increases to a maximum before decreasing linearly with flow speed, leading to a characteristic swimming point when $U = V$. Notably, in the low-velocity regime, the swimmer is not fixed and exhibits ellipsoidal trajectories. These instabilities will be explored in greater detail in the next section. The numerical computation displays similar behavior with the force changing sign when advection matches swimming velocity. For large flow velocity, up to three times the swimming speed, the force will be proportional to $U^{3/2}$ as for the case of the passive disc. However, this regime is only partially observed experimentally due to limitations in the achievable flow velocities. Moreover, the simulations reveal that the force acting on a camphor swimmer cannot be simply decomposed into the sum of drag on a passive disc and propulsion from capillary forces. The presence of Marangoni flows introduces a significant drag component, indicating that the entire water flow field must be considered for an accurate force balance.

3.2 Instabilities at low flow velocities

Because this section is somewhat lengthy, we give first an overview of its content. Our goal is to understand the origin of the elliptical trajectory observed at low flow velocities.

To do so, we develop an analytical approach based on the toy model developed in [24]. The model decouples the advection-diffusion and hydrodynamic problems, allowing for an understanding of the spontaneous symmetry-breaking mechanism, and the prediction of swimming velocity, even for high Péclet numbers. However, this analytical development is only possible without diffusion and at small advection velocities. In this regime, where the diffusion coefficient is neglected, the surfactant forms a line behind the swimmer, hence the name "string model" used in the following for brevity. For more general situations involving finite diffusion, we rely on numerical simulations. In both approaches, we entirely neglect the Marangoni flows induced by the surfactant gradient.

We first consider the simple situation without advection. Despite crude assumptions, these two approaches reproduce the circular trajectory observed experimentally, indicating that these instabilities are not driven by Marangoni flows. The string model underpredicts the radius of the trajectory. One possible explanation is the accumulation of surfactant over time, which may generate an additional radial force. To test this hypothesis, we introduced a ring-like source of surfactant in the model and observed that it increased the trajectory radius. However, quantitatively combining the effects of the string model and ring source to match the simulation results is not straightforward.

When adding a small advection, the behavior of the swimmer varies depending on the spring stiffness and the Marangoni number, resulting in a shift of the trajectory either upstream or laterally. As the flow velocity further increases, the trajectories are no longer circular and become almost one-dimensional, with their amplitude gradually decreasing before the swimming point. Experimentally, while the change in trajectory shape with flow velocity is challenging to observe due to noisier data, we do notice a decrease in amplitude, which also stops before the swimming point. In conclusion, the string model provides a qualitative understanding of the swimmer oscillations and the observed decrease in amplitude. Marangoni flows do not appear to play a major role in the observed behavior.

3.2.1 Experimental characterization

Description. We first characterize extensively the instabilities in the swimmer position observed when it is attached to a spring for low advection ($\chi < 0.6$). Without advection, the swimmer motion is circular (Fig. 3.5 left). As the flow velocity increases, the motion becomes more complex and noisy. The amplitudes of the perpendicular component $F_\perp$ (Fig. 3.5 top right) and parallel component $F_\parallel$ (Fig. 3.5 bottom right) to the water flow decrease and eventually vanishes. Notably, the amplitude reaches zero for an advection lower than the swimming velocity in both directions around $\chi = 0.6$.

Origin of the oscillation: fluid vorticity? One hypothesis for the origin of these elliptical movements is that the velocity gradient within the channel induces a torque on the swimmer, causing it to rotate. If this were the case, we would expect the trajectory to consistently rotate in the same direction. However, counting the number of clockwise versus counterclockwise rotations N, we obtain $N = 41/40 = 1.025$, indicating no significant preference for a particular rotation direction. The elliptical motion is not solely driven by the unidirectional torque induced by the velocity gradient.

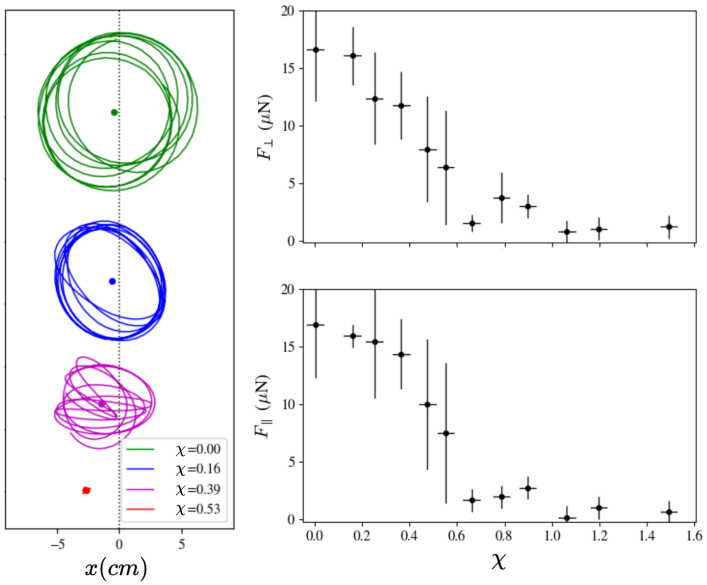

Figure 3.5: **Trajectories at low advection.** (Left) Experimental trajectories for different flow velocities. The trajectories are shifted vertically for better visualization. The point corresponds to the average position used to compute the average value of the force. (Left) Average force amplitude during the motion at low flow velocity, in the direction perpendicular to the flow (top) or parallel to it (bottom).

Orientation of the swimmer. The observed ellipsoidal trajectories may arise from a preferred swimming direction if the swimmer is not perfectly isotropic. To investigate this, we compare the swimmer orientation with its swimming direction. We track the swimmer orientation by placing a small black marker on top of the swimmer and measuring the angle between the marker and the vector $\mathbf{e}_x$ (Fig.3.6 left, orange angle). The swimming direction is defined by the angle between the displacement of the swimmer between two consecutive positions and the vector $\mathbf{e}_x$ (Fig.3.6 left, blue angle). The periods of rotation differ, with respectively 5.5 s and 2 s for the swimmer orientation and the trajectory (Fig. 3.6 right). For reference, the period of rotation of the tank was 34 s. These differences suggest that there is no significant preferred swimming direction for the swimmer.

Conclusion. For a camphor swimmer attached to a spring in a solid rotation flow, instabilities arise at low advection. We observe that the swimmer follows an ellipsoidal trajectory, with amplitude decreasing as advection increases. Our observation indicates that there is no preferred rotation or swimming direction, suggesting that these movements are not due to a gradient in flow velocity or asymmetry in the swimmer. In the following, we will explore these trajectories in more detail using an analytical toy model and numerical simulations.

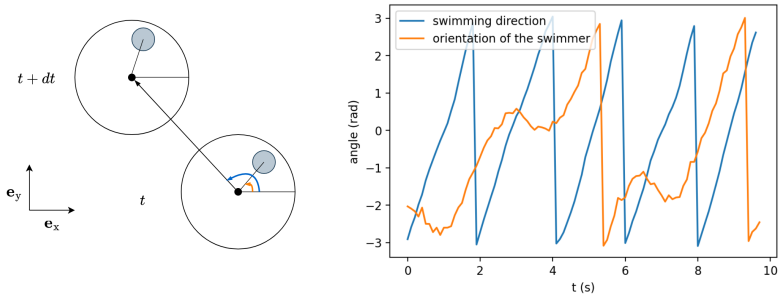

Figure 3.6: **Orientation of the swimmer.** (Left) Representation of the swimmer at two different times, the gray circle is the marker placed on top of the swimmer. The swimming direction corresponds to the blue angle and the swimmer orientation to the orange one. (Right) Evolution of the swimming direction and the orientation of the swimmer with respect to time.

3.2.2 Modelling

3.2.2.1 Physical situation and parameters

Model and hypothesis. We consider a point source at the air and water interface attached to a spring with stiffness k, moving at constant velocity $\|\mathbf{V}\|$ and releasing surfactant from its center at constant rate J (Fig. 3.7). The surfactant concentration is denoted as $\phi(r,t)$. The position of the source point is defined in polar coordinates by a distance $\rho(t)$ and an angle $\theta(t)$. The underlying fluid is moving from left to right at a velocity $\mathbf{U} = U\mathbf{e}_x$. We consider that the surface tension γ decreases linearly with the concentration of surfactant Γ as $\gamma = \gamma_0 - \kappa\Gamma$, with κ a constant parameter and γ_0 the surface tension of a bare interface. The validity condition of the linear assumption are discussed in Subsec. 1.2.2 (page 7). The non-uniform distribution of surfactant along the swimmer edge generates a capillary force $\mathbf{F}_c$. The main approximation of the toy model is to decouple the concentration and hydrodynamics problems by assuming that the drag force $\mathbf{F}_d$ is the one experienced by the swimmer in the absence of chemical release. The drag force is given by the Stokes drag on an interfacial disc $\mathbf{F}_d = -C\eta a\mathbf{V}$, where C is a numerical prefactor dependent on the swimmer shape, and η is the fluid viscosity. Here we consider a disc floating at the air and water interface so $C = 16/3$ [115]. Additionally, the spring induces a restoring force $\mathbf{F}_s = -kR\,\mathbf{e}_r$. As inertia is not included in the model, the swimmer velocity is determined by the balance between the capillary force, the drag force, and the restoring force of the spring.

Boundary conditions. We will always consider the same boundary conditions for the surfactant distribution, the Neumann boundary condition[1] at the flow exit edge and the Dirichlet boundary condition at all other edges (lateral and entry) where we fixed $\phi = 0$. The only exception will be in the absence of water flow, where edges adopt the Neumann boundary condition to allow surfactant spreading in all directions.

[1]The Neumann boundary condition specifies the derivative of the function at the boundary, typically written as $\frac{\partial\phi}{\partial n} = 0$, indicating no flux across the boundary.

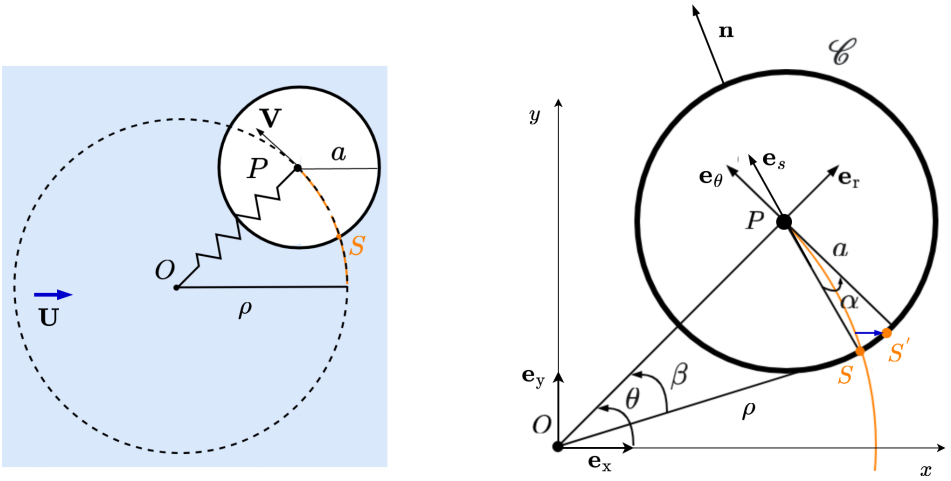

Figure 3.7: Illustration of the situation. (Left) The swimmer is attached to a spring and moves with velocity $\mathbf{V}$ along a circular trajectory. (Right) Zoom on the swimmer and notations. The orange line represents the surfactant not spreading behind the swimmer as $D = 0$.

Dimensionless forces expressions. We can now write a set of dimensionless equations based on three dimensionless numbers:

$$\mathrm{Pe} \equiv \frac{aV}{D}, \quad M \equiv \frac{a\kappa J}{\eta D^2}, \quad K \equiv \frac{ka}{\eta D}, \quad \chi \equiv \frac{U}{V}, \tag{3.2}$$

where D is the diffusion coefficient of camphor. The Péclet number Pe compares the contribution of advection to that of diffusion in the transport process. In this framework, the Péclet number corresponds to the swimming velocity. The Marangoni number M compares the transport induced by Marangoni stress to the diffusion transport. K quantifies the relative strength of the spring force compared to the viscous drag force exerted by the fluid. While M characterizes the intrinsic properties of the system, Pe is the observable of interest. Finally, χ compares the fluid velocity to the spontaneous swimming velocity V when the swimmer is not attached to a spring. In this paragraph, we introduce a notation to distinguish dimensional quantities by using a tilde $\tilde{(\,)}$, while dimensionless quantities are represented without it. To make the problem dimensionless, we use the particle radius $\tilde{a}$, the characteristic diffusion time over the swimmer size, and a typical concentration Γ^*:

$$\tilde{r} = \tilde{a}r, \quad \tilde{t} = \frac{\tilde{a}^2}{\tilde{D}}t, \quad \tilde{\Gamma} = \Gamma^*\Gamma, \quad \tilde{F} = \tilde{\eta}\tilde{D}F. \tag{3.3}$$

To obtain the typical concentration we consider that the source emits surfactant at a constant rate $\tilde{J}$ so over a time interval $\Delta\tilde{t}$ it releases a quantity $\tilde{J}\Delta\tilde{t}$ of surfactant over an area $\tilde{D}\Delta\tilde{t}$ [2]. Therefore, the typical concentration is given by $\Gamma^* = \tilde{J}/\tilde{D}$. Next, we express

[2] In the absence of advection, diffusion induces a spreading over a distance $\sqrt{D\Delta t}$.

the three forces acting on the interfacial swimmer in their dimensionless forms:

$$\tilde{\mathbf{F}}_{\mathrm{v}} = -C\tilde{\eta}\tilde{a}\tilde{\mathbf{V}}, \qquad \mathbf{F}_{\mathrm{v}} = -C\mathrm{Pe}\ \mathbf{e}_\theta, \tag{3.4a}$$

$$\tilde{\mathbf{F}}_{\mathrm{s}} = -\tilde{k}\tilde{R}\ \mathbf{e}_{\mathrm{r}}, \qquad \mathbf{F}_{\mathrm{s}} = -KR\ \mathbf{e}_{\mathrm{r}}, \tag{3.4b}$$

$$\tilde{\mathbf{F}}_{\mathrm{c}} = \int_{\mathscr{C}} \tilde{\gamma}(\tilde{l})\mathbf{n}\, dl \qquad \mathbf{F}_{\mathrm{c}} = M\int_{\mathscr{C}} \gamma(l)\mathbf{n}\, dl \tag{3.4c}$$

with $\mathscr{C}$ the swimmer contour, $\gamma(l)$ the surfactant concentration along the swimmer edge with curvilinear coordinate l, and $\mathbf{n}$ the unit vector normal to the swimmer contour and pointing outside (Fig. 3.7).

3.2.2.2 Analytical approach for low diffusion

Assumption on the surfactant diffusion. In order to solve the problem analytically, we consider the toy model under the assumption that the diffusion coefficient D vanishes and the surfactant is insoluble, meaning it will remain at the interface and almost not spread. We will call this limit the string model in the following. In this case, the surfactant forms a line behind the swimmer[3], which traces reflect the trajectory of its center P (Fig. 3.7). We assume that any residual surfactant from previous rotations does not significantly impact the current motion. There are two possible origins for this assumption: the surfactant may have disappeared due to evaporation or spread over an area larger than the swimmer radius, making the gradient negligible. As our model does not account for evaporation, the assumption will be valid for long rotation periods, corresponding to large radii or small swimmer velocity.

Capillary force. Under the previous assumption, the distribution of surfactant along the swimmer edge is non-zero only at a single point, denoted as S (Fig. 3.7 left). Consequently, the capillary force aligns with the unit vector $\overrightarrow{SP}$, denoted as $\mathbf{e}_{\mathrm{S}}$ in the following. The direction of the capillary force vector can be expressed as $\mathbf{e}_{\mathrm{S}} = \sin\alpha\ \mathbf{e}_{\mathrm{r}} + \cos\alpha\ \mathbf{e}_\theta$ where α is the angle between the capillary force and the swimming velocity. Therefore, the capillary force can be written as $\mathbf{F}_{\mathrm{c}} = M/\mathrm{Pe}\ \mathbf{e}_{\mathrm{S}}$.

3.2.2.3 Numerical approach for finite diffusion

When the diffusion coefficient is finite, the surfactant spreads on the interface, making it challenging to solve the problem analytically. In such cases, numerical methods are used to compute the surfactant concentration field. We use two approaches to solve the problem numerically: (*i*) following the same method as in [24] we consider that the surfactant spreading is controlled by a Green function and we integrate it over time or (*ii*) we simulate the diffusion of surfactant on a lattice using finite difference methods.

Green function. With the first method, the surfactant spreading is controlled by a linear equation with a Green function $G(\mathbf{r}, t)$. The field ϕ at a given time t and position

[3]The surfactant distribution can be a narrow Gaussian distribution. The string model remains accurate as long surfactant does not spread wider than the swimmer size.

$\mathbf{r}$, can be expressed as:

$$\phi(\mathbf{r}, t) = J \int_{-\infty}^{t} G(\mathbf{r} - \boldsymbol{\rho}(t'), -t')dt', \tag{3.5}$$

where $\rho(t)$ is the swimmer position (Fig. 3.7 left). Integrating the Green function over time provides the surfactant concentration field around the swimmer. The surfactant spreading is governed by pure diffusion so its Green function is the Gaussian:

$$G(\mathbf{r}, t) = \frac{e^{-\frac{\mathbf{r}^2}{4t}}}{4\pi t}, \tag{3.6}$$

While this method provides precise calculations of the surfactant concentration over the swimmer edge, it can become computationally expensive, as it requires re-evaluating the Green function at each new position over all the previous times.

Finite difference. Alternatively, we use the finite difference method to solve numerically partial differential equation by approximating derivatives with finite differences. For that, both the spatial domain and the time interval need to be discretized and the value of the solution at these discrete points is approximated by solving algebraic equations containing finite differences and values from nearby points. In our case the spreading of the surfactant follows a dimensionless diffusion equation:

$$\frac{\partial \phi}{\partial t} = \frac{\partial^2 \phi}{\partial x^2} + \frac{\partial^2 \phi}{\partial y^2}. \tag{3.7}$$

If we discretize time with index k and space with indices i and j, the finite-difference formulation is given by:

$$\frac{\phi_{i,j}^{k+1} - \phi_{i,j}^{k}}{\Delta t} = \left(\frac{\phi_{i+1,j}^{k} + \phi_{i-1,j}^{k} - 2\phi_{i,j}^{k}}{\Delta x^2} + \frac{\phi_{i,j+1}^{k} + \phi_{i,j-1}^{k} - 2\phi_{i,j}^{k}}{\Delta y^2} \right). \tag{3.8}$$

The quantity $\phi_{i,j}^{k}$ denotes the surfactant concentration at time step k and position i, j. For convergence, the maximum time step must be smaller than $\Delta t_{\max} = \delta x^2 \times \delta y^2 / (2 \times (\delta x^2 + \delta y^2))$ [116] with δx and δy the resolution in the x and y direction respectively. In our simulation, we will consider a time step $\Delta t = \Delta t_{\max}/2$ and a typical grid spacing $\delta x = \delta y = 1/7$, meaning we will have 7 grid points in one swimmer radius and a box size of 20×20 swimmer radius. Although this method requires interpolation of the grid over the disc edges, it is relatively easy to implement and does not require extensive computational time.

3.2.3 Motion without flow

We first consider the simplest case without advection. Experiments show that the swimmer motion is circular (Fig. 3.5 left, page 51). We compare the prediction of the string model without diffusion and numerical simulation for finite diffusion.

3.2.3.1 Analytical prediction - string model

Force Balance. Assuming circular trajectory and balancing the forces results in a set of coupled equations involving the rotation radius R and the Péclet number wich is equivalent to the swimming velocity:

$$R^2 = \frac{M}{2K\mathrm{Pe}}\,, \qquad \mathrm{Pe}^2 = \frac{M}{C}\sqrt{1-\frac{1}{4R^2}}. \tag{3.9}$$

These equations yield:

$$\frac{16K^4}{C^2M^2}R^8 - \frac{4K^4}{M^2C^2}R^6 = 1, \qquad \frac{C^2}{M^2}\mathrm{Pe}^4 + \frac{K\mathrm{Pe}}{2M} = 1. \tag{3.10}$$

Although explicit solutions to the fourth and eighth-order equations can be derived, they are rather cumbersome for analysis and approximation can be made introducing $\xi \equiv K/\sqrt{CM}$ and assuming $\xi \ll 1$ (Eq. (3.17), page 66). Such assumption is valid when the spring is flexible enough compared to the Marangoni number or, in another way, the radius is large enough. The result and comparison between the approximation (Eq. (3.17), page 66) are presented in Appendix 3.4.1 page 66. The approximate solution performs better for larger values of M (Fig. 3.14).

Conclusion. In the zero diffusion coefficient limit, we derived an analytical expression of the swimming velocity and the radius with respect to the Marangoni number and the spring stiffness and show that an approximate expression describes well the trend for a large Marangoni number. Our findings reveal that the radius increases with the Marangoni number while both the radius and Péclet number decrease with increasing spring stiffness. We now aim to compare these analytical results with numerical simulations for a finite diffusion coefficient.

3.2.3.2 Comparing with numerical simulation

Convergence of the trajectories. In the absence of water flow, the swimmer trajectory is circular with a given radius R centered around the origin (Fig. 3.8 left). Increasing the stiffness of the spring decreases the radius. In 2D, the concentration field of a steady source never reaches a steady state and as the swimmer trajectory is confined by the spring the surfactant accumulates along the swimmer path (Fig. 3.8 center & right). However, we are not interested in the surfactant concentration average value along the contour (whose contribution to Eq. (3.4c) vanishes) but in the gradient of surfactant along the swimmer edge, a quantity that converges over time (Fig. 3.8 right). As a result, the forces acting on the swimmer, and consequently its trajectory, also converge over time.

Differences. When comparing theoretical predictions to numerical simulations, it is important to consider the differences in assumptions and parameters. The string model assumes a diffusion coefficient close to zero and that previous surfactants disappeared after one rotation. On the other hand, the numerical simulation uses a finite diffusion coefficient and allows the surfactant to accumulate along the swimmer path (Fig. 3.8 center & left). However, the surfactant has spread extensively[4] after a complete rotation of the

[4]After one rotation, the surfactant has spread over more than four swimmer diameters and the concentration of surfactant in front of the swimmer is less than 10% of the amount released (Fig. 3.8 center).

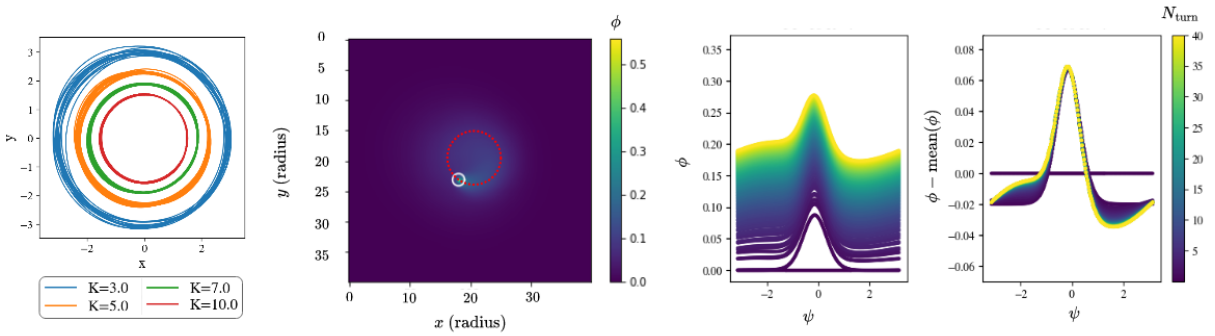

Figure 3.8: **Numerical simulation, swimmer attached to a spring without advection** (Left) The trajectories were obtained with numerical simulation for $M = 100$ and different spring stiffness K. (Center) Field of surfactant ϕ over the whole simulation box, the swimmer is the white circle and its trajectory is indicated by the dashed red line. The colormap indicates the amount of surfactant. (Right) The concentration of surfactant along the swimmer edge and the difference with the average quantity along the swimmer contour ψ. In both graphs, the colormap indicates the number of turns N_{turns} made by the swimmer.

swimmer, so we can expect that it should have a minor impact on the swimming velocity. Therefore, reasonable comparisons can still be made between the theoretical predictions and the simulation results.

Radius. The string model captures the main ingredients of the relation between R, K, and M (Fig. 3.9 top). For Marangoni numbers larger than 50 the model underpredicts the radius compared to what we observed in the simulation (Fig. 3.9 top left). The discrepancy may be due to surfactant accumulating at the center of the trajectory, creating a larger radial force (Fig. 3.8 left). When plotting the simulation radius against the exact solution (Fig. 3.9 top right) most of the data points collapse on a single line with a slope[5] of 1.46. The consistent deviation from a slope of 1 suggests that while the string model qualitatively captures the correct scaling behavior, it quantitatively underestimates the radius by a constant factor.

Critical Marangoni Number. Depending on the spring stiffness, there is a critical Marangoni number, M_c, below which no motion occurs, and the swimmer remains at a stable equilibrium position at $R = 0$ (Fig. 3.9 top left). Our simulations show critical Marangoni numbers of $M_c = 10, 25, 50$ for spring stiffness values $K = 1, 3, 10$, respectively. The critical Marangoni number can be estimated considering that motion is possible when the capillary force exceeds the restoring force[6] leading to $M_c \sim K$. However, the actual M_c observed is higher than predicted. The discrepancy may result from the time required for surfactant to accumulate and form a sufficient gradient and from the drag force, not taken into account here that can further resist motion. No critical Marangoni number is

[5]Data point below $R = 1$ are not taken into account for the fit has the string model is only valid for sufficiently large R.

[6]The capillary force $F_c \propto Ma$ and the drag force for a displacement around the swimmer size $F_s \propto Ka$. Motion is possible if $F_c > F_s$ meaning that $M > K$.

observed for the string model, indeed this model is mainly valid for large R. For small R neglecting surfactant from previous rotations is not a valid assumption. As a result, the model fails to capture the behavior at low M or large K.

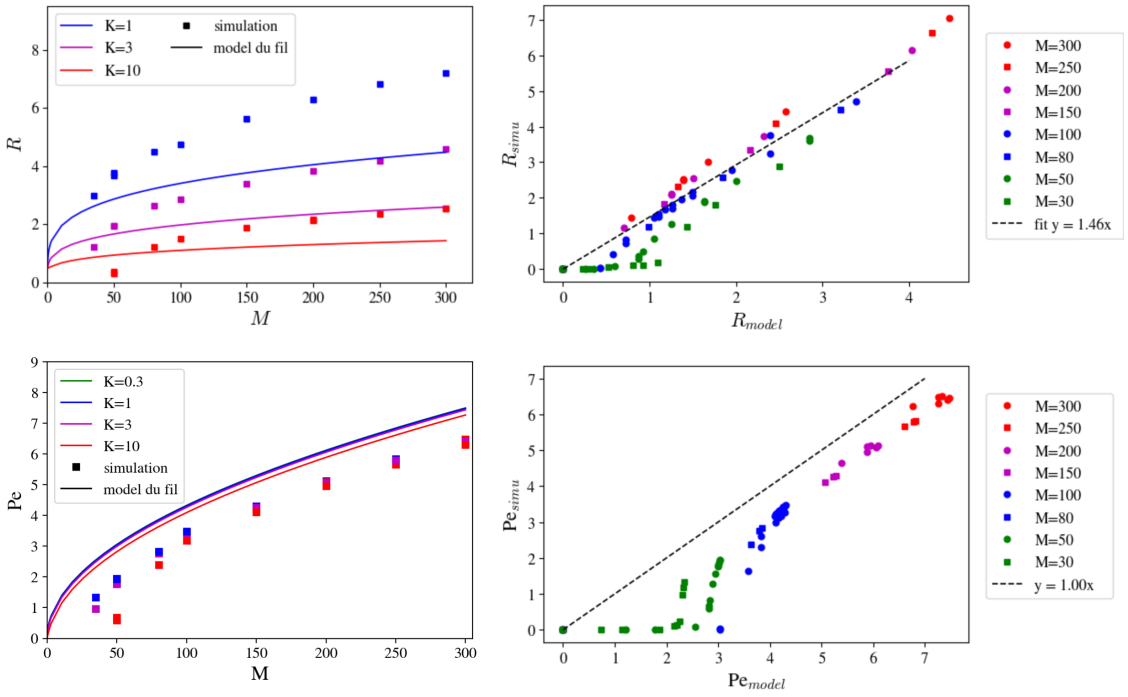

Figure 3.9: **Radius and Péclet number.** Comparison between the string model prediction and the simulation results for the average radius R of the trajectory (top) and Péclet number Pe (bottom). (Left) Evolution with respect to the Marangoni number for the simulation (square points) and string model (continuous line). (Rigth) Radius (or Péclet) obtained with simulation with respect to the exact solution of the string model. The dashed line corresponds to a linear fit with a slope of 1.46 (or 1).

Swimming velocity. The string model slightly overestimates the Péclet number, 10% for $M = 300$ (Fig. 3.9 bottom left). The fact that the data collapse on a line with a slope of 1 (Fig. 3.9 bottom right) indicates that, despite the differences in absolute values, the trend predicted by the string model and observed in the simulations are consistent. Both capture the same qualitative relationship between the Péclet number and the system parameters. The non-zero intercept is due to the critical Marangoni number for motion not captured by the string model.

Conclusion. Compared to the simulation, the string model manages to capture the main features of dependency of the radius in M and K, but it tends to under-predict the radius and over-predict the velocity. However, we observe a critical Marangoni number under which there is no motion for small Marangoni numbers or large spring stiffness. This is not captured at all by the string model. The underestimation of the radius could be due to the accumulation of surfactant at the trajectory center, which increases the capillary force radial component.

3.2.4 Radial force due to the surfactant accumulation

Motivation. The previous string model focuses on the immediate effect of the surfactant release but does not account for the long-time effect of the surfactant distribution and accumulation. We want to study the evolution of the surfactant distribution and whether it can generate an additional radial force. However, the concentration field is time-dependent as it depends on the swimmer position, and its evaluation is not simple. Intuitively, we expect that at long time, the surfactant concentration fields of a circling swimmer and an emitting ring should resemble each other. Therefore, we consider a ring of radius ρ which releases surfactant at the same rate J as the punctual source (Fig. 3.10 top). The calculations are detailed in the Appendix. 3.4.2.

Combining the string model and ring-like source. To combine the string model and the ring of surfactant, we consider that the ring of surfactant is in $\rho = R$ to match the swimmer trajectory. With the new force from the ring of surfactant, the force balance (Eq. 3.9) becomes:

$$\frac{M}{2\mathrm{Pe}R} = KR - \frac{M}{4R}, \qquad \mathrm{Pe}^2 = \frac{M}{C}\sqrt{1 - \frac{1}{4R^2}}. \tag{3.11}$$

These two equations can be solved analytically and we can write an approximation for small spring stiffness as in (Eq. (3.17)). It is not reported here because it is not particularly concise. Compared with the result of the string model the velocity is almost unchanged, less than 10%, for all values of the Marangoni number considered. In contrast, the radius doubles, and it now overestimates the simulation results (Fig. 3.10 bottom). This shows that the surfactant distribution can generate an additional radial force increasing the radius. Moreover, combining the two models quantitatively to match the simulation is not trivial. Indeed, when we take an average between the two models we overestimate the quantity of surfactant as in the simulation the surfactant distribution came from a point source traveling along the ring and not a continuous from the ring itself. Maybe we should consider a different ratio when adding the two models, for example, it seems that taking half of the additional force from the ring gives a better result.

Conclusion. Without advection both the string model and the numerical simulation qualitatively reproduce the circular trajectories observed experimentally, suggesting these instabilities are induced by the self-propulsion without the need to account for Marangoni flows. The motion of a swimmer without external flow is a complex interplay of surfactant effects, spring stiffness, and Marangoni forces. The string model provides a valuable starting point for understanding these dynamics, but further refinements are needed. We introduced a ring source model to account for the accumulation of surfactant at the center of the swimmer trajectory observed in the simulation. This model revealed that surfactant distribution can generate an additional radial force that significantly increases the radius. However, combining the ring source and the string model to recover the result of the simulation is not trivial.

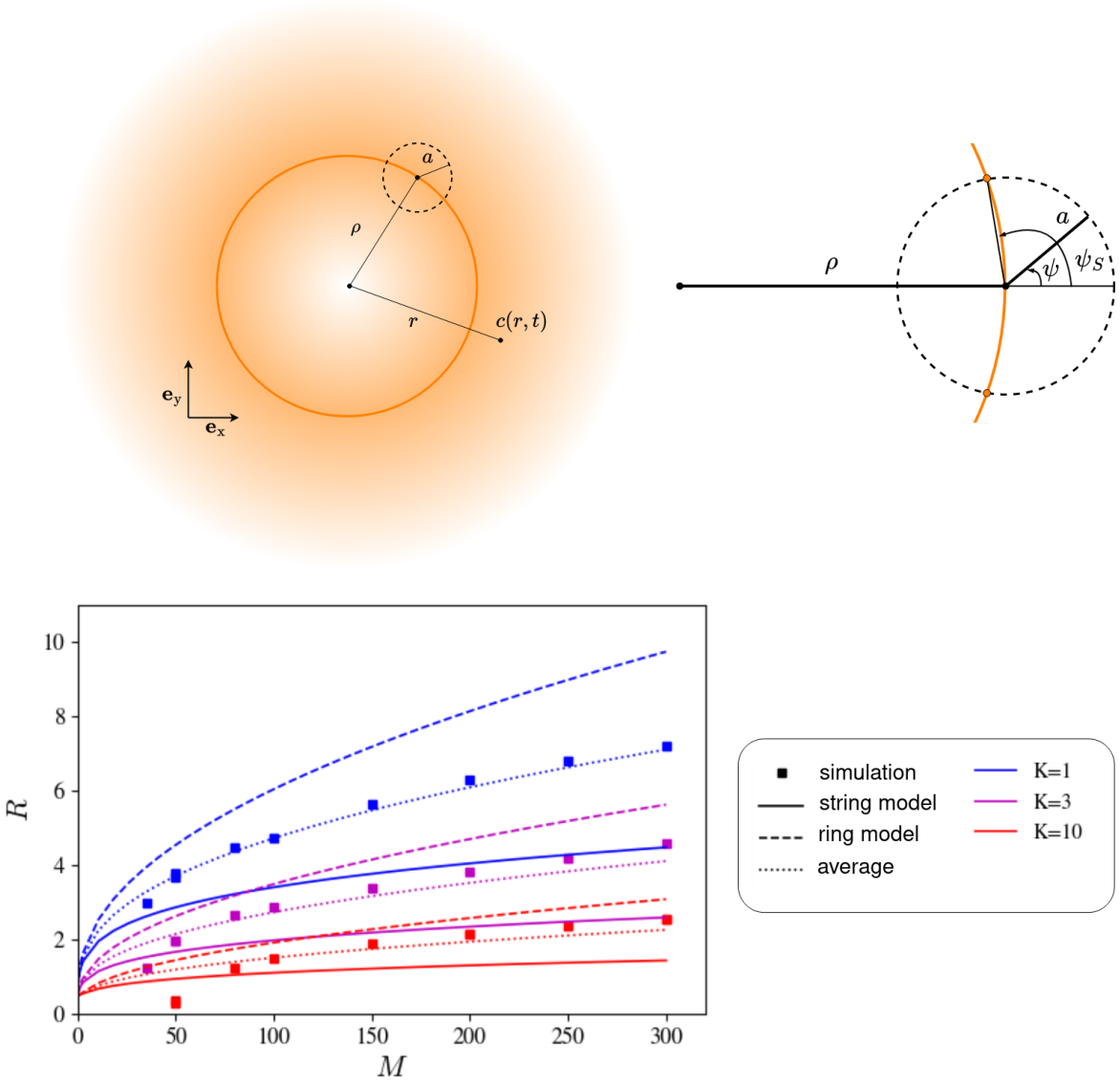

Figure 3.10: **Diffusion of surfactant from a ring-like source.** (Top) Schematics and notations. (Left) The orange gradient indicates the concentration of surfactant and the full orange line is the ring source of surfactant. The dashed circle is the swimmer contour. (Right) Zoom on the swimmer. ψ defines the angle along the swimmer contour and ψ_S the angle of the point of surfactant. (Bottom) Comparison between the numerical simulations (square points) and the analytical model with the ring of surfactant (dashed line) and without (full line). The dotted line corresponds to the average between the two analytical models.

3.2.5 Motion with fluid flow

Motivation. We now want to get closer to the experimental situation and consider the string model and the simulation when there is an imposed fluid flow. The goal is to study the impact of advection on the shape of the trajectories and see if we also observe a shift of the average position against the flow and a decrease in the parallel and perpendicular amplitude.

3.2.5.1 Pertubative approach in the low-advection limit

Perturbation. Coming back to the string model (no diffusion), the advection modifies the line formed by the surfactant behind the swimmer. Therefore, surfactant will be advected and the point S will be shifted to the left to a new point $S^{'}$ (Fig. 3.7). As a result, the direction and norm of the capillary force will be modified. For tractability, we assume that the flow velocity is significantly smaller than the swimmer velocity ($U \ll V$). Thus, in these condition the former circular trajectory and swimmer angular velocity ω will be slightly perturbed by fluid flow. This perturbation can be quantified by a small parameter $\epsilon = U/V$. We seek a time-dependent radius $\rho(t)$ and rotation speed $\dot{\theta}(t)$:

$$\rho(t) = R\,(1 + \epsilon\rho_1(t))\,, \qquad \dot{\theta}(t) = \omega\,(1 + \epsilon\Omega_1(t))\,, \tag{3.12}$$

with $\rho_1(t)$ and $\Omega_1(t)$ two unknown functions that describe the perturbation to the circular trajectory and to the rotation speed.

Modification of the forces. The forces acting on the swimmer will be modified by the fluid flow. As before the spring force is $\mathbf{F}_\mathrm{s} = -K\rho_1(r)\ \mathbf{e}_\mathrm{r}$. In polar coordinates, the swimmer velocity is given by $\mathbf{V} = R\epsilon\dot{\rho}_1\ \mathbf{e}_\mathrm{r} + \mathrm{Pe}\Big(1 + \epsilon\,(\rho_1 + \Omega_1)\Big)\ \mathbf{e}_\theta$, thus the drag force is now:

$$\mathbf{F}_\mathrm{v} = -C\mathrm{Pe}\frac{\mathbf{V}}{\|\mathbf{V}\|} = -C\,(\epsilon R\dot{\rho}_1\ \mathbf{e}_\mathrm{r} + \mathrm{Pe}\ \mathbf{e}_\theta)\,, \tag{3.13}$$

and is unchanged along $\mathbf{e}_\theta$.

The capillary force is $\mathbf{F}_\mathrm{c} = F_\mathrm{c}\ \mathbf{e}_{\mathrm{S}'}$ and its norm depends on the swimmer velocity so it will be modified as $F_\mathrm{c} = M\Big(1 - \epsilon(\rho_1 + \Omega_1)\Big)/\mathrm{Pe}$. The vector $\mathbf{e}_{\mathrm{S}'} = \mathbf{e}_\mathrm{S} - \overrightarrow{\mathrm{S}\,\mathrm{S}'}$ gives the direction of the capillary force. Therefore, we need the new position of point S to define a new angle α. As the intersection of two circles, the coordinates of point S [7] allows us to determine $\cos\alpha$ and $\sin\alpha$:

$$\cos\alpha = \sqrt{1 - \frac{1}{4\rho^2}}, \quad \sin\alpha = \frac{1}{2\rho(t)}. \tag{3.14}$$

Now we evaluate the shift of S due to advection. For a flow velocity U the surfactant point S will move along $\mathbf{e}_x$ of a distance $U \times T_\mathrm{transit}$ during the time T_transit the swimmer took to travel from S to P. This distance can be approximated by an arc of length $g(R) = 2R\arcsin\Big(1/(2R)\Big)$. Here we make two approximations: (i) advecting the surfactant point S will give a new point S' which is still on the swimmer edge. Looking at Fig. 3.7, you can see that the point S' is not obtained by advecting S but by advecting a point slightly above. (ii) The distance traveled by the swimmer from S to P is an arc. Here the trajectory is no more circular, however, as we assumed a small perturbation from the circular trajectory, and if the swimmer is smaller than the radius of the trajectory these approximations are reasonable as they should be of second order in ϵ. Thus, the direction of the capillary force is given by:

$$\mathbf{e}_{\mathrm{S}'} = -\epsilon g(R)\Big(\cos\theta(t)\ \mathbf{e}_\mathrm{r} - \sin\theta(t)\ \mathbf{e}_\theta\Big) + \mathbf{e}_\mathrm{S}. \tag{3.15}$$

[7] $x_S = \rho(t)\left(1 - 1/\left(2\rho(t)^2\right)\right)$ and $y_S = -\sqrt{1 - 1/\left(4\rho(t)^2\right)}$

Solution. By balancing the forces and considering a large radius expansion, we can analyze the perturbation of the circular trajectory. At order zero in ϵ, we recover the previous result without flow as we should. At first order in ϵ, we obtain an expression for the perturbation of the circular trajectory $\rho_1(t)$ as follows:

$$\rho_1(t) = \frac{-2K}{2K^3M + \sqrt{C^7M}}\Big(C_{\cos}\cos\theta(t) + C_{\sin}\sin\theta(t)\Big), \qquad \Omega_1(t) = -\rho_1(t), \tag{3.16}$$

with $C_{\cos} = \sqrt{2}K^{3/2}\,(CM^5)^{1/4}$ and $C_{\sin} = C^2M$.

With the ring of surfactant. What happens if we add the ring-like source of surfactant in the presence of weak advection? The force generated by the ring of surfactant with the perturbed expression of ρ (Eq. (3.12)) is: $\mathbf{F}_{\text{ring}} = M/(\pi R)(1-\epsilon\rho_1(t)+\epsilon^2\dots)\,\mathbf{e}_{\text{r}}$. However, to obtain the expression of ρ_1 and Ω_1 (Eq. (3.16)) we consider a large radius limit ($R \to \infty$). In that case, the force due to the ring will vanish and the perturbation will not be modified. Therefore, the additional force from the ring will only impact the initial radius.

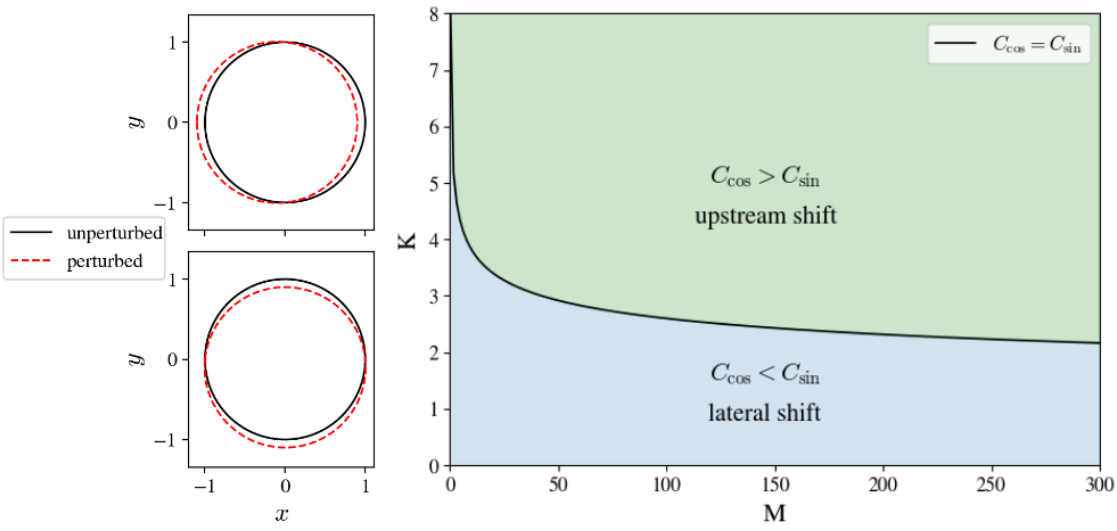

Figure 3.11: **Shift of the trajectories for small advection.** (Left) Evolution of the trajectories in presence of weak advection for high spring stiffness (top) or low spring stifness (bottom). The trajectories without advection are represented by the solid black line, and the perturbed trajectories by the dashed red line. (Right) Evolution of the prefactors $C_{\sin}$ and $C_{\cos}$ in the (M, K) plane. The black line corresponds to $C_{\sin} = C_{\cos}$.

Perturbed trajectories. We now discuss the impact of the perturbation on the shape of the trajectory (Eq. (3.16)). For a small perturbation $\epsilon = 0.1$ and $C_{\cos} = C_{\sin} = 1$ (Fig. 3.11 left), the trajectory closely resembles a circle. Each term of $\rho_1(t)$ induces a different modification: the term $\cos\theta(t)$ moves the trajectory against the flow (Fig. 3.11 left top), while the term $\sin\theta(t)$ causes lateral shifting (Fig. 3.11 left bottom). The direction of the lateral shift, up or down, depends on the rotation direction. Therefore, depending on the magnitude of the prefactors $C_{\cos}$ and $C_{\sin}$ the shape of the trajectory

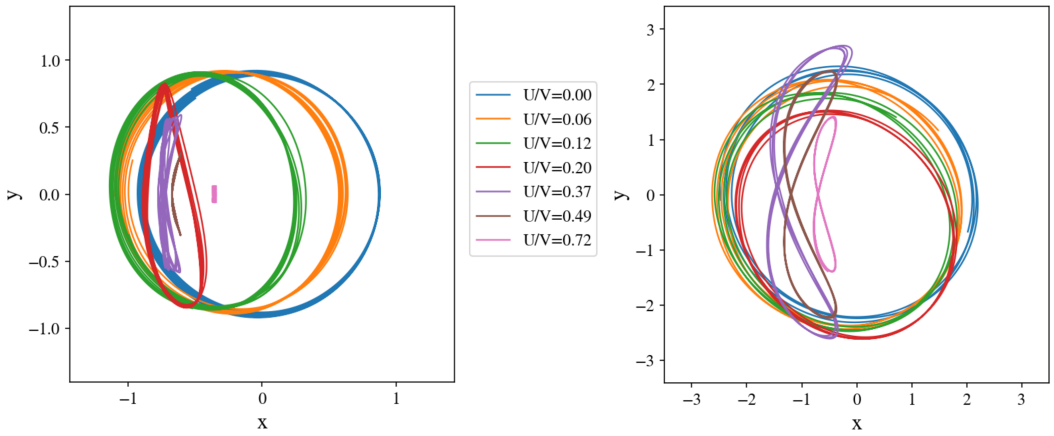

Figure 3.12: **Simulated trajectories for high advection.** Complete trajectories for different flow velocities for $M = 100$, rigid spring $K = 20$ (left) and soft spring $K = 5$ (right).

will be different. In our simulations, we considered a Marangoni number ranging from 30 to 300 and a spring stiffness from 1 to 50. By plotting the values of the prefactors $C_{\cos}$ and $C_{\sin}$ within this parameter range (Fig. 3.11 right) we observe the following trends: for $K < 2$, $C_{\sin}$ is larger, indicating that the perturbed trajectory is expected to shift laterally and will not shift upstream. On the other hand, for $K > 5$, $C_{\cos}$ is always larger, suggesting that the trajectory will primarily shift upstream. We could expect that for very large M the swimmer will always shift upstream.

3.2.5.2 Simulation of the trajectories for strong advection

Shape of the trajectory. Increasing the flow speed modifies the trajectory shape (Fig. 3.12), we observe successively: (*i*) a perfectly circular trajectory (*ii*) an ellipsoidal trajectory shifting either upstream (Fig. 3.12 top left) or laterally (Fig. 3.12 right) depending on the spring stiffness (*iii*) an almost transversal trajectory (*iv*) a fixed swimmer. The lateral shift can occur on either side and is determined by the rotation direction of the swimmer, which is fixed by the initial conditions. The initial condition has no other impact on the trajectories. The trajectory becomes completely transversal around $\chi = 0.34$ for all values of spring stiffness. This transition seems abrupt for soft springs, while it is more gradual for rigid springs.

Surfactant distribution. To explore the origin of the change in trajectory shape from ellipsoidal to almost fully transversal, we consider the surfactant field behavior (Fig. 3.13 top). In the absence of water flow, the surfactant accumulates at the center of the trajectory (Fig. 3.8 center, page 57). For low flow velocities, the surfactant is gradually carried away, creating an asymmetry with more surfactant present downstream. There is still an excess of surfactant at the center of the trajectory. As the flow velocity increases, the surfactant concentration upstream decreases significantly and the accumulation zone shifts from the center of the trajectory toward the rear, eventually disappearing.

1D profile. The modification of the surfactant distribution is clearly visible when examining a cut along the flow direction passing through point O (Fig. 3.13 bottom left). Without advection, the surfactant distribution is symmetric. As advection increases the distribution becomes asymmetric: the upstream extension of the surfactant field decreases, and it accumulates downstream. Further increases in flow speed reduce the amount of surfactant downstream until the accumulation zone vanishes, leaving a constant surfactant concentration downstream for $\chi \simeq 0.34$. Interestingly the accumulation of surfactant disappears for $\chi \simeq 0.34$ as for the change of trajectory shape. Therefore, the change in the shape of the trajectory is directly linked to the modification of the surfactant distribution.

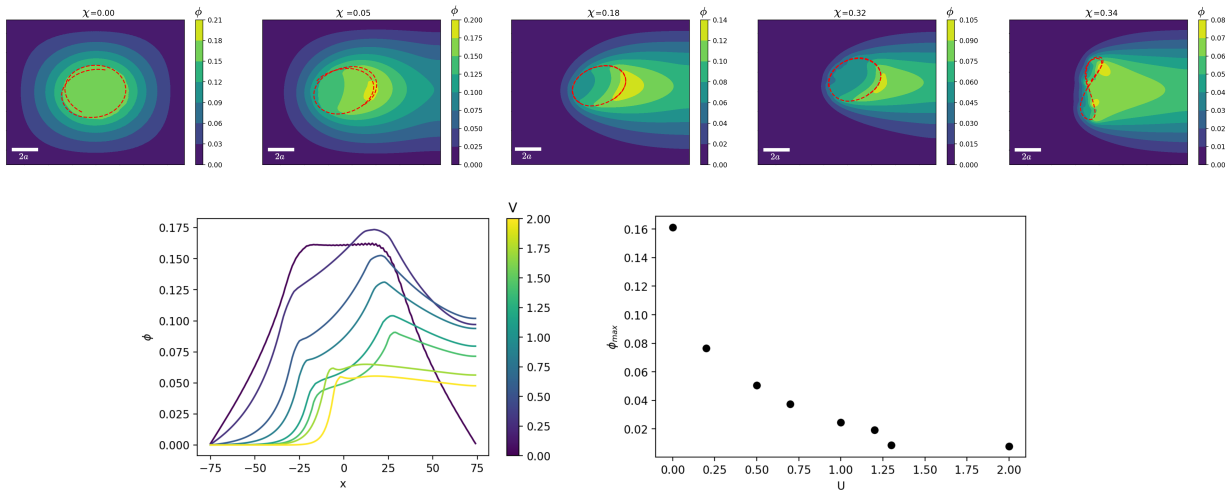

Figure 3.13: **Distribution of the surfactant with respect to the flow velocity**. For $M = 100$ and $K = 10$. The red dashed line corresponds to the swimmer trajectory and the color map corresponds to the contour of the concentration of surfactant. (Bottom left) Average concentration of surfactant along a line at $y = 0$. The color map indicates the flow velocity, $x = -75$ corresponds to the entry edge and $x = 75$ to the exit edge. (Bottom right) Difference between the maximum of the concentration and the value at the exit edge.

3.2.5.3 Comparison with experiments

Comparison with experiments is not direct. Comparing the prediction of the string model or the simulations with the experimental results is not straightforward as the Marangoni number used has completely different orders of magnitude $M \simeq 100$ in the simulation, $M \simeq 10^{10}$ in the experiments. Moreover, if we want to adimensionalize the experimental results, we need the diffusion coefficient of camphor, which is around $10^{-9}\,\mathrm{m}^2/\mathrm{s}$. However, a mathematical model for camphor swimmer motion [117] that describes the effect of Marangoni flows with an effective diffusion coefficient D_{eff} suggests $D_{\mathrm{eff}} = 10^{-3}\,\mathrm{m}^2/\mathrm{s}$, a value six order of magnitude larger. The large value of D_{eff} suggests that the Marangoni flows play a significant role and increase the diffusion coefficient [79]. Therefore, choosing a value of the diffusion coefficient to adimensionalize the results is not trivial. In our experiment the spring stiffness ranges from $k = 2 \times 10^{-4}\,\mathrm{N\,m^{-1}}$ to $k = 5 \times 10^{-3}\,\mathrm{N\,m^{-1}}$, we obtain $0.8 < K_{\mathrm{eff}} < 20$ with bare diffusion and $8 \times 10^5 < K < 2 \times 10^7$

with effective diffusion. We saw in the simulation that depending on the value M and K the trajectory should shift either laterally or against the flow (Fig. 3.11 right, page 62). However, for large Marangoni numbers, the string model predicts that the trajectory should mainly shift upstream for all values of K (Fig. 3.11 right) which is what we observe in the experiments.

Shape of the trajectories. Without water flow, the experimental trajectories are circular, consistent with predictions from the string model and simulations. As the flow increases, the experimental trajectories (Fig. 3.5, page 51) become noisier, and the behavior is less clear than in the simulation (Fig. 3.12, page 63). Overall we observe that the trajectories shift upstream and slightly laterally with a decrease in the radius when the flow velocity increases which matches the prediction of the string model for large Marangoni numbers. However, we do not observe the change in trajectory shape seen in the simulations. Beyond the differences already pointed out, these differences could have several origins : (*i*) In the experiment, flow velocity precision is limited, and the range of flow velocity where trajectories change shape might be narrow, potentially causing us to miss this behavior. (*ii*) In the experiment, we have a shear flow and the vorticity may favor circular trajectories.

3.3 Conclusion

The experimental set-up we developed allows us to measure the resulting force applied by the fluid on an interfacial object submitted to a fluid flow of imposed velocity. The force dynamics acting on an interfacial Marangoni swimmer differ significantly from those on a passive disc, with the force changing sign when the advection matches the spontaneous swimming velocity. Finite elements methods based on previous work [62] display similar behavior and allow to access the detailed force balance showing force acting on a camphor swimmer cannot be simply decomposed into the sum of drag on a passive disc and propulsion from capillary forces. The presence of Marangoni flows introduces a significant drag component, indicating that the entire water flow field must be considered for an accurate force balance and cannot be neglected as in most models.

Notably, at low advection speed, we observed instabilities and the swimmer has an ellipsoidal trajectory. To understand the instabilities observed at low advection, we developed a simplified toy model that decouples the hydrodynamics and surfactant transport problem. This model considers a point source releasing surfactant at a constant rate. The analytical solution is possible without advection for low diffusion cases, while numerical methods are used for more general conditions. The model qualitatively reproduces the experimental behavior, indicating that the instabilities are not primarily due to Marangoni flow but rather result from changes in the surfactant distribution.

3.4 Appendices: string model without advection

3.4.1 Large radius approximation

Although explicit solutions to the fourth and eighth-order equations (Eq. (3.10)) can be derived, they are rather cumbersome for analysis. Hence, we introduce an approximation by defining $\xi \equiv K/\sqrt{CM}$ and assuming $\xi \ll 1$. This approximation is true if we consider that the spring is flexible enough compared to the Marangoni number or, in another way, that the radius is large enough. In this case, we obtain simplified expressions for Pe and R:

$$\mathrm{Pe} \simeq \sqrt{\frac{M}{C}}\left(1 - \frac{\xi}{8} - \frac{\xi^2}{128} + \dots\right), \qquad R \simeq \frac{1}{\sqrt{2\xi}}\left(1 + \frac{\xi}{16} + \frac{5\xi^2}{512} + \dots\right). \tag{3.17}$$

To assess the reliability of the small ξ approximation, we compare it to the exact solu-

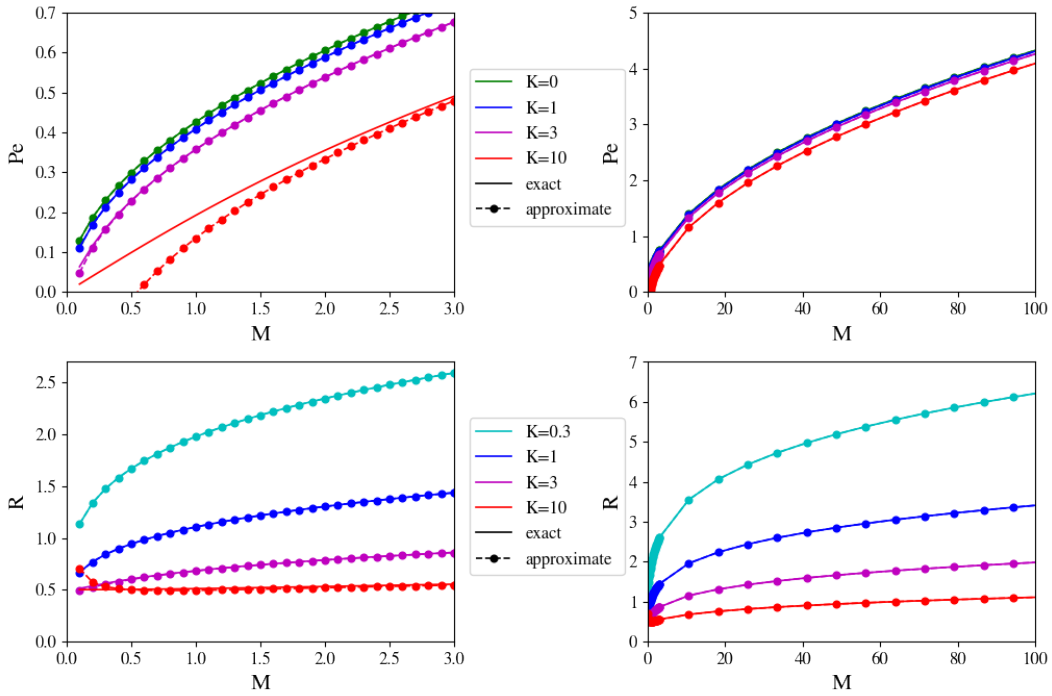

Figure 3.14: **Comparison between the exact and the approximate solution.** Evolution of the Péclet number and the radius with respect to the Marangoni number. Péclet number (top) and radius (bottom) for different spring stiffness, for small (left) and large values of M (right).

tions. Figure 3.14 illustrates the comparison for the Péclet number (top) and the radius (bottom). As expected, the results indicate that the approximate solution performs better for larger values of M. Specifically, when $M = 1$, the approximation yields results within 5% difference for K values smaller than one. On the other hand, for $M = 100$, the approximation remains accurate up to $K = 10$.

Impact of the Marangoni and Péclet numbers. We now discuss the impact of the Marangoni number and the spring stiffness on the radius and the Péclet number.

The radius increases with the Marangoni number and decreases with the spring stiffness (Fig. 3.14), which was expected as M can be seen as quantifying the "motor strength". Regarding the Péclet number, it follows the same trend as the non-attached motion and is just slightly reduced when the spring stiffness increases. The decrease in the Péclet number with increasing spring stiffness can be explained by the increased angle α (Fig. 3.7 right). As the radius decreases, the capillary force becomes less aligned with the swimmer trajectory, resulting in a reduced component along the direction $\mathbf{e}_\theta$. Consequently, when the forces are balanced, the contribution of the capillary force to the swimming velocity is diminished, leading to a smaller Péclet number. These results highlight a complex interplay between the Marangoni number, spring stiffness, radius, and Péclet number. Note that, in the limit of very large R, we recover previous results obtained for a swimmer in translation [24].

3.4.2 Ring model

Model. The aim of the ring source approach is to account for the long time which is not included in the string model as surfactant is assumed to disappear after one rotation. Intuitively, we expect that at long time, the surfactant concentration fields of a circling swimmer and an emitting ring should resemble each other. Therefore, we consider a ring of radius ρ which releases surfactant at the same rate J as the punctual source. In that case, the diffusion equation for the surfactant concentration c is:

$$\partial_t c(r,t) = D\Delta_r c(r,t) + J\frac{\delta(r-\rho)}{2\pi\rho}, \tag{3.18}$$

with r the distance to the center of the ring, Δ_r the radial part of the Laplacian and δ the Dirac delta function. For the boundary condition, namely $r = 0$ and $r \to \infty$ the former is given by symmetry, the latter is chosen to match the simulation. With these boundary conditions, the derivative of the concentration $\partial_\mathrm{r} c(r,t)$ is $\partial_\mathrm{r} c(r=0,t) = \partial_\mathrm{r} c(r\to\infty,t) = 0$.

Concentration distribution in the long time limit. We consider the Laplace transform with respect to the time of Eq. (3.18) with variable s which can be solved analytically. There is a discontinuity in the gradient of concentration in $r = \rho$ so we consider the inner and the outer part of the ring of surfactant respectively $\partial_\mathrm{r} c_\mathrm{in}$ and $\partial_\mathrm{r} c_\mathrm{out}$ and we obtain:

$$\partial_\mathrm{r} c_\mathrm{in}(r,s) = \frac{J\Big(-1+I_0(A)\Big)K_0(A)}{2D\pi s}, \quad \partial_\mathrm{r} c_\mathrm{out}(r,s) = J\frac{I_0(A)K_0(A)-K_0(A)}{2D\pi s}, \tag{3.19}$$

with I_k and K_k the modified Bessel function respectively of the first kind and the second kind of order k and the argument of all Bessel functions is $A = \sqrt{\frac{s}{D}}\rho$. To obtain the concentration field we integrate over r from the origin where the concentration is $c(r = 0, s)$. We consider the long time limit obtained for $s \to 0$. In that case, the inner term is constant with respect to r and the outer concentration c_out is:

$$c_\mathrm{in}(r, t\to\infty) = c(0, t\to\infty), \qquad c_\mathrm{out}(r, t\to\infty) = c(0, t\to\infty) + \frac{J}{2D\pi\rho}. \tag{3.20}$$

Force on the swimmer. To obtain the force on the swimmer F_{ring} we integrate the distribution of surfactant (Eq. (3.20)) over the swimmer contour outside the ring for $-\psi_m < \psi < +\psi_m$. The concentration $c(0,t)$ diverges with time, but it is irrelevant to compute the force on the swimmer. The force can be computed analytically, but the expression is lengthy. Therefore, we consider the limit $\rho \gg 1$ and we obtain an approximate but concise expression:

$$F_{\text{ring}} \simeq \frac{\kappa J}{4D\rho}\left(1 + \frac{2}{3\pi\rho} + \dots\right), \tag{3.21}$$

and we keep only the leading term. Comparing the approximation with the exact expression shows that with two terms there is less than 10% difference for $\rho > 1$ and for one term less than 15% for $\rho > 2$. For simplicity, we consider only the first term in the expansion of the ring force (Eq. 3.21). Therefore, the dimensionless expression of the force is $F_{\text{ring}} = M/(4\rho)$.

Chapter 4

Surface flows around a Marangoni swimmer

Table of Contents

4.1 Introduction

In the previous chapter, we observed that the forces acting on a Marangoni swimmer cannot be simply decomposed into a propulsion force and a drag force akin to that of a passive object. The Marangoni flows generated by the swimmer induce an additional force, making it necessary to characterize the complete flow field to fully understand the swimmer dynamics. If Marangoni flows are a fundamental aspect of the interfacial swimmer problem, their complexity is often neglected in swimming models [24, 117–121].

From an analytical perspective to the best of our knowledge, only one study has provided a full analytical description of the wake for an insoluble surfactant released from a constantly moving point source on a thin liquid film coating a planar substrate [81]. Although their approach offers a comprehensive description of the wake, it relies on assumptions of a thin film and Stokes flow, which do not hold in our experimental system. For Marangoni swimmers, the impact of the Marangoni flows is not obvious as some studies predict a resistive contribution [54], while others suggest a motor-like contribution [82] under shallow water conditions. Both predictions are based on Stokes flow and pure diffusion transport.

Experimentally, only a few studies have captured the complete flow field around asymmetric Marangoni swimmers [83–85]. Although the surfactant used is not always camphor, the general features of the flow remain consistent. Looking from the top, the induced flow extends over a distance around ten times the swimmer size and the maximal velocity is about the swimmer speed. The flow field is asymmetric, with the interface dilating downstream and spreading radially from a stagnation point located roughly one diameter from the swimmer edge. Underneath the swimmer, two counter-rotating vortices form to ensure mass conservation. For symmetric swimmers, initial experimental characterization was presented in a thesis [86] showing similar flow features to those observed in asymmetric swimmers.

However, the methods used so far have significant limitations. Experiments always capture transient flows that differ from steady-state models, making comparisons challenging. Additionally, it is difficult to obtain consistent statistics under the same conditions, as the swimmer, being free to move, never reaches the measurement position with the same angle, trajectory, or previous position. To address these challenges, we introduce a new approach by switching the frame of reference: we consider a fixed swimmer in a controlled underlying flow field. The setup allows us to observe the swimmer under constant conditions and generate a stationary flow field, facilitating direct comparisons with models and numerical predictions.

In this study, we focus solely on interfacial flows because the capillary force driving the swimmer forward is directly related to the interfacial distribution of surfactants. Additionally, obtaining 3D flow measurements is significantly more challenging. Techniques like Particle Image Velocimetry (PIV) are typically 2D, and extending them to three dimensions (as in Tomographic PIV or Stereo PIV) requires multiple cameras, complex calibration, and advanced algorithms to accurately reconstruct the 3D flow field [122]. In the first part, we present the experimental approach used to obtain the complete flow field. Following that, we characterize the stationary flows generated for different advection and compare them with previous numerical simulations [62] and experimental results.

4.2 Experimental protocol to obtain the flow field

In the case of a camphor swimmer, there is a large tracers-free area which appears black around the swimmer (Fig. 4.1 right). The depleted area, which is present on all images and remains consistent over time, has also been observed in a related experiment where a collection of swimmers confined in a circular pool of 18 cm constantly crossing each other trajectories [59]. As the wake behind the swimmer is completely different from the one behind a passive disk (Fig. 4.1 left), we can link the existence of the depleted area to the activity of the swimmer and thus to the chemical camphor cloud. Because of the camphor released, the surrounding of the swimmer has a lower surface tension than the rest of the fluid. It induces Marangoni flows from the swimmer toward the sides of the channels which push back all tracers, leaving the area black. While the physical effect is expected, it poses an experimental challenge to obtain the flow field in the swimmer wake. Indeed, the lack of tracers in this area implies that no information is available on the flow dynamics. In the following, we present an improved experimental protocol developed to study the interfacial flow field everywhere around a Marangoni swimmer.

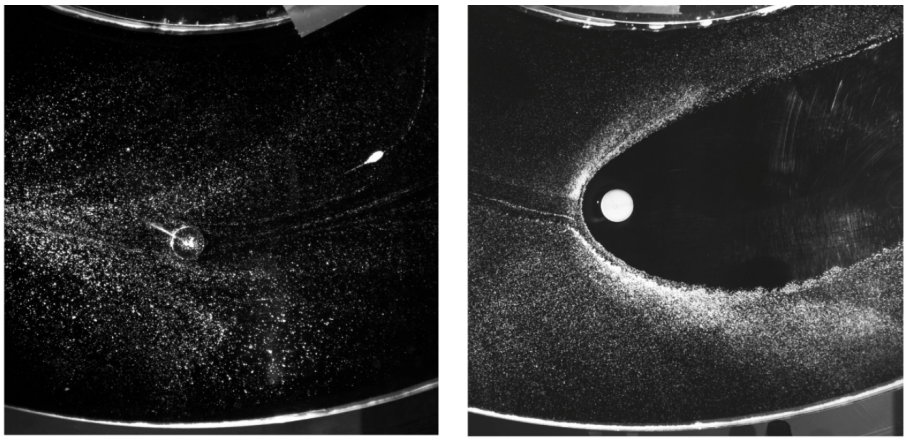

Figure 4.1: **Typical experimental images used to reconstruct the flow field.** The water is seeded with tracers that stay at the air-water interface (small white dot) showing the water flow around a plastic disc (left) or a camphor swimmer (right).

4.2.1 Combination of two techniques

Adding tracers in the wake. To fill the tracer-free area, glass bubbles are sprinkled above the swimmer, and a few of them naturally fall into the wake. However, the density of tracers will be much lower than outside of the wake. Therefore, two complementary optical techniques are used to reconstruct the flow: (*i*) a particle or feature-based approach here **Optical Flow** (OF, Subsec. 2.3.3, page 39) to obtain the flow inside the wake as it follows specific features and can work at low density. (*ii*) **Particle image velocimetry** (PIV, Subsec. 2.3.2, page 37) for the rest of the channel as it works well at high density and is less sensitive to intensity changes.

Combination of techniques to image the whole flow field. In practice, multiple image sequences are captured for each interfacial object studied with different combina-

tions of light and numerical tools:

- White light and PIV: this combination enables observing the region outside the swimmer wake (Fig. 4.2 left). Tracers are not added in the wake area here. With white light, if glass bubbles are sprinkled in the air, they can be observed before they reach the water surface leading to inaccuracies in the flow field.
- Laser sheet with tracer sprinkling and OF: this configuration avoids shining the tracers before they reach the water surface, it allows us to study the flow field in the wake (Fig. 4.2 right). However, the lens used to generate the laser sheet limits the field of view to a 7 cm width, preventing observation of the entire channel compared to the previous combination. Moreover, as the laser sheet shines from the side, some parts remain in the swimmer shadow.

Therefore, at least two acquisitions using different lighting techniques are necessary for each swimmer to obtain a complete understanding of the flow dynamics. In the following, we detail the protocol to obtain the flow field in each region first the external flow (outside the wake), then the internal flow (inside the wake), and finally, how to combine them.

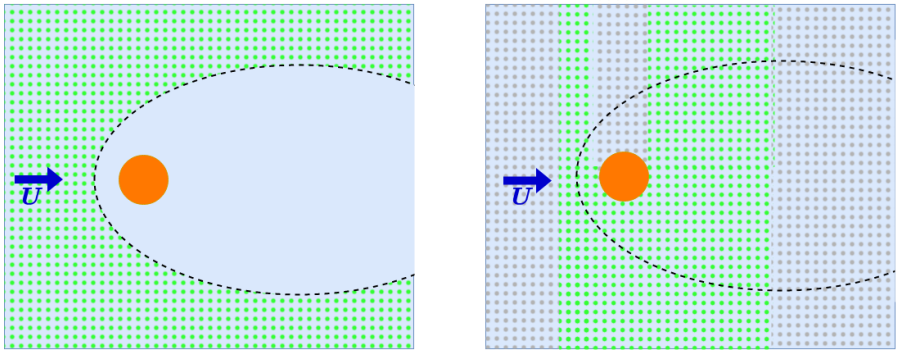

Figure 4.2: **Lighting of the tracers.** The orange circle represents the swimmer, the dashed line is its wake, and the gray dots indicate the presence of glass bubbles. If the dots are green they are illuminated and trackable, if they are gray they are invisible. (Left) White light without adding tracers in the wake, (right) laser sheet, and adding tracers in the wake.

4.2.2 External flow

We observe some tracers in the bulk. We first focus on the external flow. To do so, the water surface is seeded with tracers and illuminated with white light and no tracers should be observed in the swimmer wake. However, during our experiments, some glass bubbles do not stay at the interface and sink in the bulk (Fig. 4.3 left). This is problematic as these suspended tracers will be recorded and analyzed even if they are not relevant to the study of the interfacial flow. Their number seems to be low as only one track was observed in a typical experimental time of 50 s. Therefore, even if suspended glass bubbles may also be present in the external flow, their presence will be completely masked by the large amount of floating tracers and only the inside flow should be handled carefully.

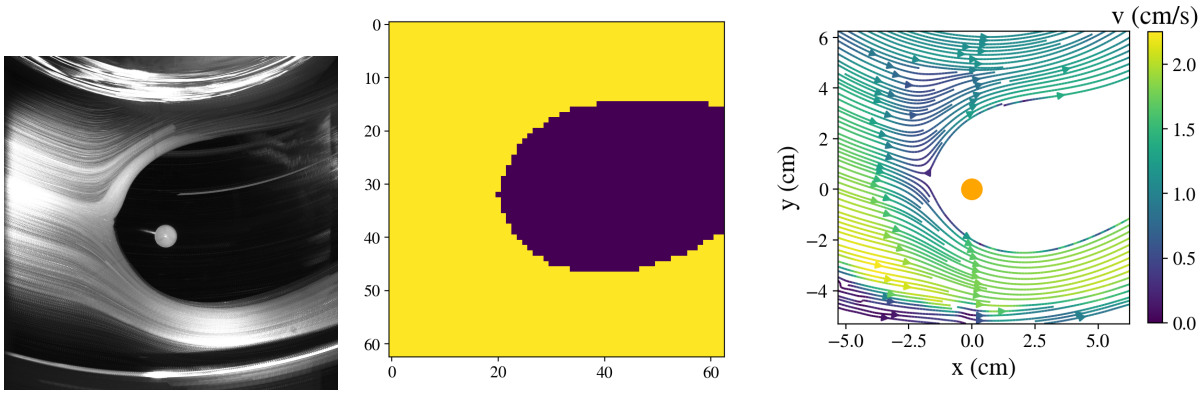

Figure 4.3: **External flow.** Water flow outside of the swimmer wake for $\chi = 0.3$ obtained with PIV. (Left) Max intensity of the image, each white line shows the track of a tracer, (middle) mask, (right) time-averaged flow field obtained with PIV.

Applying a mask on the wake. To address this issue, a mask is applied to all the images to avoid considering the particles in the wake. Initially, a maximum-intensity image is constructed, capturing the highest intensity value for each pixel across the image sequence (Fig. 4.3 left). As a result, the wake contour becomes more visible, making it easier to pinpoint. Next, a threshold is manually determined and used to create a mask of the image (Fig. 4.3 center). The resulting mask isolates the wake for all flow velocities considered. It also eliminates other low tracer density regions that may change between experiments due to factors such as lighting conditions or heterogeneous seeding. Finally, PIV can be performed on the masked image, and temporally averaging all the vector fields provide the stationary flow field outside of the wake (Fig. 4.3 right). It is important to note that this masking approach assumes the consistency of the wake shape throughout the experiments and the steadiness of the flow.

4.2.3 Internal flow

Now that we have obtained the external flow we focus on the internal one. To do so glass bubbles are sprinkled above the water surface and a few of them will fall in the wake allowing access to the flow field close to the swimmer. To avoid imaging tracers before they reach the water surface, the interface is shined using a laser sheet. In the following we detail the experimental setup used to create the laser sheet then we review some issues of the approach such as the swimmer shadow masking a part of the channel and propose some solutions.

Laser sheet to image only the interface. To create the laser sheet, we use an Argon Ion Laser[1]. First, a periscope elevates the beam at the tank level (around 30 cm height) then it passes through a 30° Powell lens[2]. The Powell lens creates a straight, uniform laser line approximately 1 mm thick. Unlike cylindrical lenses which generate Gaussian beam profiles, Powell lenses provide an even distribution of energy along the length of the

[1] Lasos 60-Series LGK 7872 ML Argon Ion laser, 40 mW TEM00, polarized @ 454.5 - 514.5 nm Multi-line, beam diameter 0.66 mm

[2] 30° Full Fan Angle Laser Line Generator Lens from Edmund Optics

entire line. An angle of 30° for the Powell lens is a good compromise between power and the size of the laser sheet. To further reduce the thickness of the laser sheet to 0.5 mm, a convergent lens with a diameter of 15 cm and a focal length of 20 cm is used. Lastly, a parallel-faced glass plate is used to adjust the height of the sheet and accommodate small modifications in the water level.

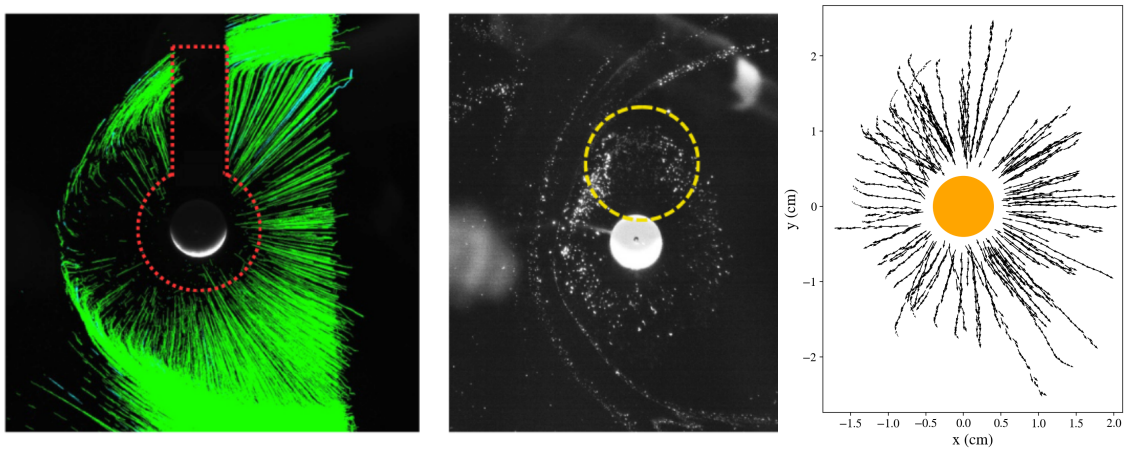

Figure 4.4: **Manual tracking in the swimmer shadow.** Trajectories of the tracers obtained with Optical flow (left); the red area indicates parts where the algorithm cannot follow the particles (swimmer shadows and close surroundings). If we modify the brightness and contrast (center), tracers appear in the shadows (yellow circle). The trajectories were obtained by manually tracking particles in the shadow and close to the swimmer (right).

Manual tracking in the shadow of the swimmer. As the laser sheet comes from the side, a part of the channel is in the swimmer shadow, making it challenging for the optical flow algorithm to track tracers effectively in this region (Fig. 4.4 left). Although increasing the image brightness and contrast improves tracer visibility (Fig. 4.4 center), it also reveals tracers before they reach the water surface and the brush used for sprinkling. Moreover, despite tracers being visible on the images, the area 5 mm away from the swimmer edge doesn't contain any optical flow tracks (Fig. 4.4 left). Therefore, we opt for manual particle tracking as the area is small. We utilize the software *ImageJ* with the *Manual Tracking*[3] plugin to address this limitation. Figure 4.4 right shows that the manually obtained vector field is defined all around the swimmer up to 1 mm from the edge and effectively completes the vector field obtained with OF.

4.2.4 Complete flow field: summing PIV and OF

Each combination of light and algorithm provides us with information on different parts of the channel, and some of them overlap. We have to combine all the data to reconstruct a unique and complete flow field. To do so, we first interpolate the OF data and the manual tracking data on the PIV grid. Then, we create a mask representing the position

[3]Plugin made by Fabrice Cordelière, 2005, https://imagej.net/ij/plugins/track/track.html

of the OF information and extend the mask by two grid sizes. The extension accounts for the fact that data at the edge of the laser sheet may be less reliable. Finally, we obtain the complete field as the weighted average:

$$u_{\text{tot}} = \frac{u_{\text{PIV}} \times \text{mask}_{\text{PIV}} + u_{\text{OF}} \times \text{mask}_{\text{OF}}}{\text{mask}_{\text{PIV}} + \text{mask}_{\text{OF}}}. \tag{4.1}$$

This process allows to obtain the complete flow field around the swimmer up to 1 mm from the swimmer edges, with a sampling interval of 2 mm for different water flow velocities (Fig. 4.5 left). Removing the solid rotation $\mathbf{u}_{\text{solid}} = \mathbf{r} \times \mathbf{\Omega}$, the resulting flow $\mathbf{u}_{\text{dif}} = \mathbf{u} - \mathbf{u}_{\text{solid}}$ field corresponds to a swimmer travelling at $\mathbf{V} = -\mathbf{U}$ (Fig. 4.5 right).

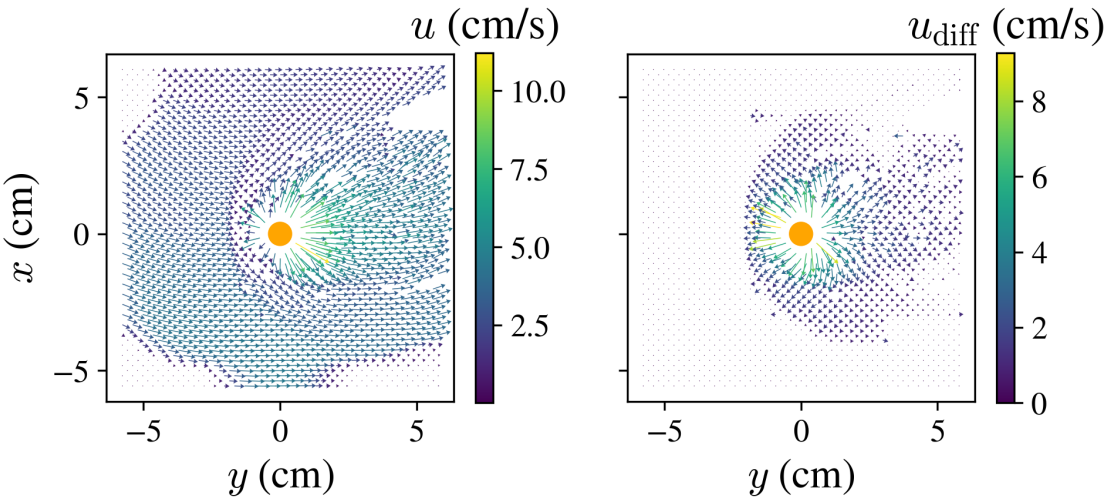

Figure 4.5: **Complete flow field around a camphor swimmer.** For $\chi = 0.3$, (left) flow field obtained by combining PIV and OF analyses and (right) difference with the solid rotation $\mathbf{u}_{\text{dif}} = \mathbf{u} - \mathbf{u}_{\text{solid}}$.

Conclusion

Obtaining the flow field around a source of surfactant is significantly more complex than for a passive disc. The presence of a large wake necessitates combining multiple lighting and numerical techniques to capture the complete flow dynamics. Additionally, the manual tracking of tracers in the swimmer shadow adds a time-consuming task, albeit necessary for capturing flow details in regions where automated algorithms may fail. This study presents the first stationary measurement of the flow field around a symmetric Marangoni swimmer. In the following section, we study the different features of the flow field focusing first on the shape of the wake and then on the flow field around the swimmer.

4.3 Flow field around a Marangoni swimmer

4.3.1 Wake shape

4.3.1.1 Experimental characterization

The wake defines a separatrix. The first noticeable feature of the flow field around a Marangoni swimmer is the wake shape. The Marangoni flows generated push all the tracers away, leaving a depleted area around the swimmer (Fig. 4.1 left). The contour of this area defines a line that no tracers can cross: a separatrix. In the following, we study the shape of this separatrix for different flow velocities.

Geometric transformation to a straight channel. Here, curvature is a complicating byproduct of the experimental setup modifying the shape of the separatrix and complicating analysis. To facilitate comparison with predictions from existing models, it is desirable to return to a simpler scenario where the swimmer experiences a uniform, straight velocity. The simplest assumption is that both problems are identical through a simple geometrical transform. Thus, we transform the image from a circular to a rectilinear channel by going from polar (r, θ) to Cartesian coordinates $(x_{\text{new}}, y_{\text{new}})$:

$$x_{\text{new}} = \theta_{\text{s}} \times r_{\text{s}}, \qquad y_{\text{new}} = r, \tag{4.2}$$

where r_s is the distance between the center of the tank and the swimmer and θ_{s} is the relative angle between the point of interest and the swimmer center.

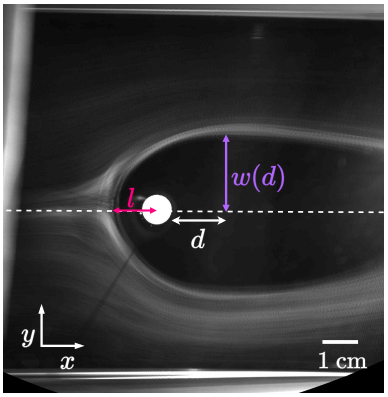

Figure 4.6: **Modified image.** Experimental image transformed to go from a circular to a straight channel. The swimmer is represented by the white circle, with the channel edges visible along the sides (top and bottom) of the image, appearing parallel. We consider the width $w(d)$ of the separatrix at a distance d behind the swimmer, and l the distance to the stagnation point

To apply this method, we first identify the center of the tank using the Hough transform, which detects two circles corresponding to the inner and outer edges of the channel. Averaging the positions of the two detected centers provides a good estimation of the actual center of the tank. Once the center is determined, the transformation adjusts the coordinates to account for the curvature of the channel and the velocity gradient. The resulting image shows parallel channel edges and a more symmetric wake (Fig. 4.6). It should be noted that this is an ad hoc procedure.

Shape of the wake. The separatrix is extracted using the function *contour finding* from *skimage* on the mask defined by thresholding the max intensity image (Fig. 4.6). The function provides a constant valued contour which is easy to define as the only border in the mask corresponding to the separatrix. For all flow velocities, the separatrix has a complex shape that does not close behind the swimmer (Fig. 4.7). To describe quantitatively the shape, we focus on two parameters: w the separatrix width, and l the distance to the stagnation point upstream. The width w is defined as the distance between the center of the channel and the separatrix. The stagnation point corresponds to the zero velocity area upstream at the apex of the wake (Fig. 4.3 right), and l is the distance between this point and the swimmer edge. When the velocity increases, the wake becomes narrower and the distance between the stagnation point and the swimmer center l decreases from 1 cm upstream until it reaches the edges of the swimmer (Fig. 4.7). Even at very large velocities the wake never closes behind the swimmer and reaches a constant width of 2 cm downstream.

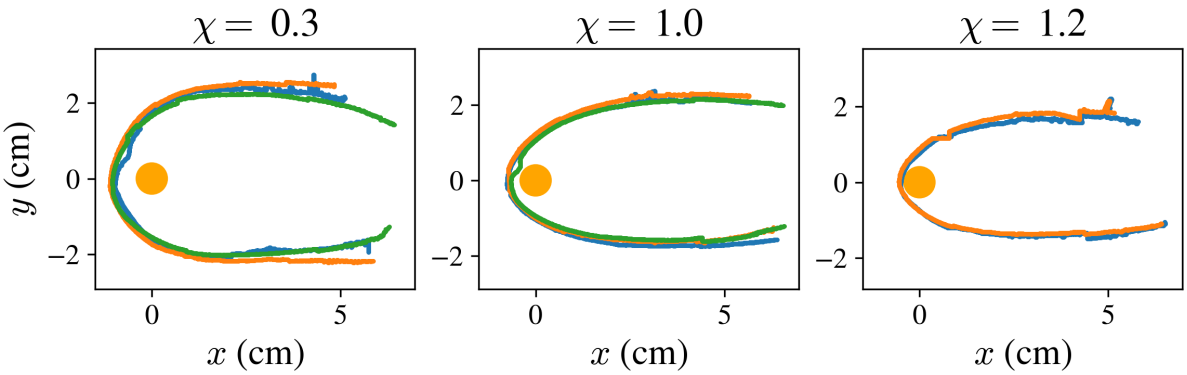

Figure 4.7: **Separatrices reproducibility.** Separatrix for three different swimmers at a given advection speed, from left to right $\chi = 0.3$, 1 and 1.2.

Reproducibility for different swimmers. As the swimming velocity decreases over time, other elements, such as the shape of the separatrix, may also vary. To minimize these effects, the acquisition time was kept below 2 min, allowing the exploration of only one advection speed per swimmer. The short experimental duration ensures that the flow speed can be assumed to be stationary. Consequently, each separatrix was obtained at different advection speeds and with different swimmers. To confirm that the observed effects are primarily due to changes in advection speed rather than intrinsic variations between swimmers, we characterized the variability between them. For a given advection speed, three different swimmers exhibited consistent wake shapes (Fig. 4.7), with a variation of only 0.5 mm between them, confirming the reliability of the results and the effect of advection.

4.3.1.2 Discussion: comparison with earlier works

Camphor disk with punctual release. Using FEM, previous work has obtained the flow field around a moving point source of surfactant in a half-plane with 1 cm of water depth and extracted the separatrix [31]. Although the range of dimensionless numbers

is quite far (Table. 4.1), it allows a first comparison as it fully accounts for Marangoni flows. The numerical wakes are also parabolic-like and do not close behind the swimmer (Fig. 4.8 left). However, as it is a surfactant point-source, the shape of the wake in front of the swimmer is completely different compared to the experiments. There is almost no extension upstream and the stagnation point is located below the swimmer (Fig. 4.8 left).

dimensionless numbers	experiments	FEM
Péclet	4×10^5	1×10^3
Marangoni	6×10^{10}	1×10^6
Reynolds	3×10^2	0
Schmidt	1×10^3	1×10^2

Table 4.1: **Values of the dimensionless numbers.** For the experiments and finite element methods.

Width of the separatrix. Quantitatively comparing the width of the separatrix for $d = a$ and $5a$ from the swimmer with respect to the flow velocity shows that the numerical computation captures the general trends (Fig. 4.8 right). With FEM, the width is reduced by 0.5 cm, which could be due to the point source release of surfactant. At very low flow velocity, FEM predicts a larger separatrix. The discrepancy at low flow velocities could be due to the lateral confinement in the experiments, preventing the wake from extending too much.

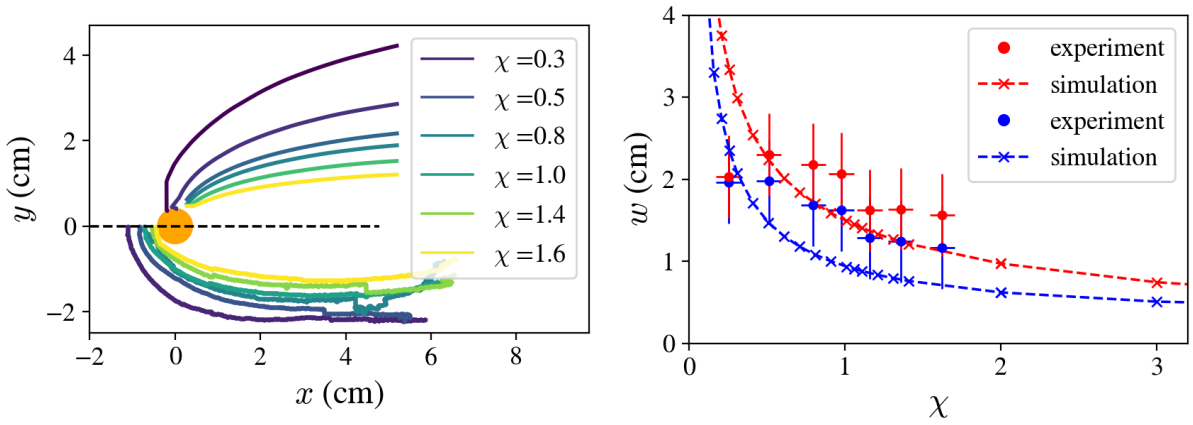

Figure 4.8: **Evolution of the separatrices.** Impact of the advection velocity $\chi = U/V$ on the shape of the separatrix. (Left) The shape of the separatrices obtained with FEM (top) or experimentally (bottom). The color corresponds to the advection speed, and the swimmer is the orange circle with radius $a = 0.4$ mm. (Left) Width of the separatrix at a distance $d = a$ (blue) or $d = 5a$ (red) behind the swimmer for the experiments (points) and FEM (dashed curve).

Achieving the same range of Marangoni and Péclet numbers in FEM is not feasible as it would increase computational time drastically. As a result, FEM shows more surfactant diffusion, leading to lower concentration behind the swimmer, smaller gradients, and

thus weaker Marangoni flows. These factors could also explain the smaller width of the separatrix observed compared to experiments. Due to these differences, the comparison between experiments and FEM remains qualitative.

4.3.2 Complete flow field and hydrodynamic wake

Description of the complete vector field. Understanding the complete flow field of a Marangoni swimmer is crucial for understanding its dynamics. Although transient flow fields have been previously obtained [83, 84, 86], to the best of our knowledge, this is the first stationary characterization outside the swimming velocity. To consider the contribution of the Marangoni flows, we remove the solid rotation and consider $\mathbf{u}_{\text{diff}} = \mathbf{u} - \mathbf{u}_{\text{solid}}$ (Fig. 4.9 right). For all advection speeds, the average flow field obtained shows dilatation of the interface with a radial flow from the swimmer. There is a line behind the swimmer where the velocity is purely parallel and the perpendicular component is zero. Notably, the flow field extends well beyond the separatrix, clearly indicating that the separatrix does not define the limit of the hydrodynamic wake.

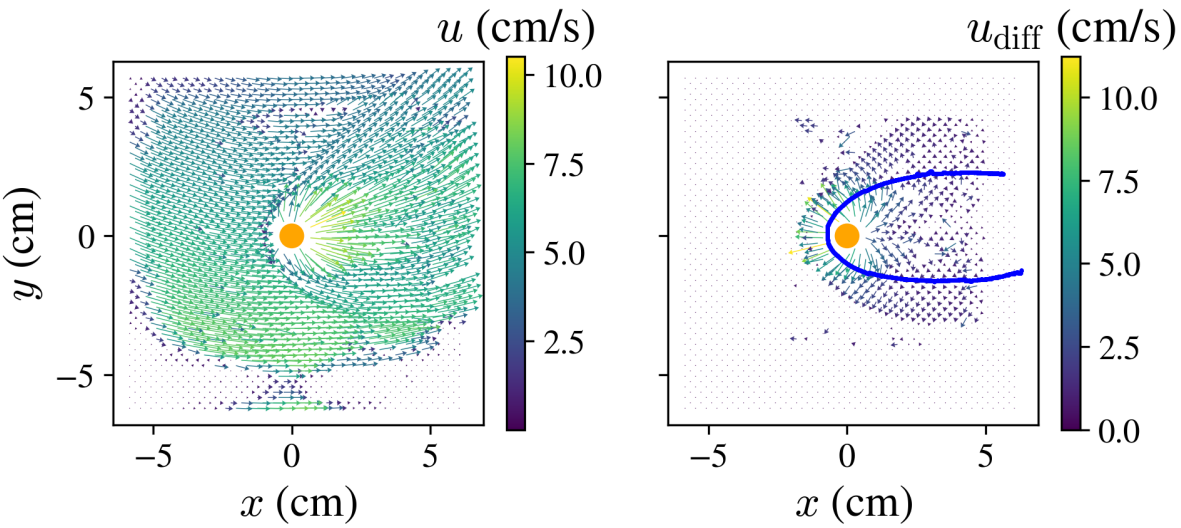

Figure 4.9: **Complete flow field.** For $\chi = 1$, the colors correspond to the velocity norm (left) time-averaged flow field obtained with PIV, (right) difference with respect to solid flow $\mathbf{u}_{\text{diff}} = \mathbf{u} - \mathbf{u}_{\text{solid}}$. The separatrix is plotted in blue.

Reproducibility of the flow field. We measured the flow field around different Marangoni swimmers at the same advection speed and evaluated the standard deviation for the perpendicular $\text{std}_\perp$ (Fig. 4.10 left) and parallel $\text{std}_\parallel$ (Fig. 4.10 right) component of $\mathbf{u} = u_\parallel \mathbf{e}_x + u_\perp \mathbf{e}_y$. The standard deviation of the flow decreases when going away from the swimmer, indicating that measurements are less reliable near the swimmer. Large standard deviation at the bottom of $\text{std}_\perp$ corresponds to the edge of the channel, where tracking becomes less reliable due to discontinuities. On average, the standard deviation is around $1.2\,\text{cm}\,\text{s}^{-1}$ close to the swimmer, decreasing to approximately $0.5\,\text{cm}\,\text{s}^{-1}$ further away. Despite slight differences in the flow field due to individual swimmer variations, the overall pattern and magnitude of flow variability remain consistent.

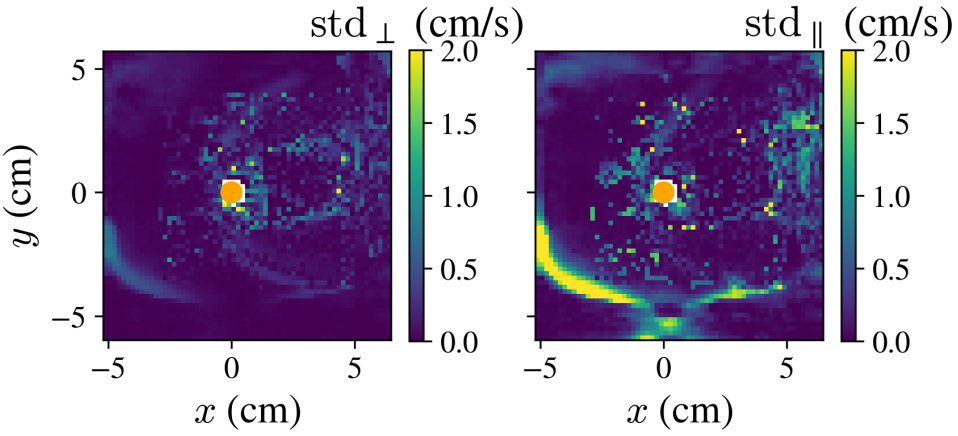

Figure 4.10: **Reproducibility of the complete flow field.** Standard deviation of the velocity component perpendicular $\mathrm{std}_\perp$ (left) and parallel $\mathrm{std}_\parallel$ (right) of the measured flow field $\mathbf{u}$ of three different swimmers for $\chi = 1$.

Slight difference with a swimmer in translation. Assuming the flow measured corresponds to a superposition of a solid rotation and the flow generated by the swimmer removing the solid rotation should correspond to the flows around a swimmer moving at $\mathbf{V} = -\mathbf{U}$. Such an assumption implies that the presence of the swimmer does not significantly alter the characteristics of the solid body rotation and that the gradient velocity does not modify the generation of Marangoni flows. However, the velocity gradient across the channel can modify the Marangoni flows generated. Specifically, the velocity gradient induces inhomogeneous advection of the surfactant, which may lead to a non-symmetric gradient of surface tension and thus non-symmetric Marangoni flows. Therefore, the difference flow field obtained may not be completely equivalent to a swimmer in translation at $\mathbf{V} = -\mathbf{U}$ (Fig. 4.9 right).

Extent of the induced flow. To quantify the extent of the hydrodynamical wake, $\mathbf{u}_{\mathrm{diff}}$, we consider a cut passing by the swimmer. Since the solid rotation has been removed, the flow near the swimmer is expected to resemble that in a straight channel. Therefore, a linear cut along x at $y = 0$ passing through the swimmer was considered (Fig. 4.11 left, dashed black line). The induced flow u_{diff} extends approximately 1 cm upstream and 5 cm downstream at $\chi = 1$ (Fig.4.11 center). To assess the lateral extent of the flow, perpendicular cuts at fixed x positions were examined (Fig. 4.11 left, colorful solid lines). As the distance from the swimmer increases, the amplitude of the perpendicular flow component $u_{\mathrm{diff}\perp}$ decreases (Fig. 4.11 right), with the maximum velocity reducing from 5 cm/s at 0.4 cm from the swimmer edge to 1 cm/s at 5 cm away. Moreover, right behind the swimmer at $y = 0$, $u_{\mathrm{diff}\perp}$ changes sign.

Impact of advection We now examine how advection influences the extent of the hydrodynamical wake and focus on $u_{\mathrm{diff}\perp}$, the perpendicular component of the generated flow. The maximum perpendicular velocity increases with advection speed and decreases as the distance from the swimmer increases (Fig. 4.12 left). The extent of the hydrodynamical wake in the direction of the flow can be characterized by the point where

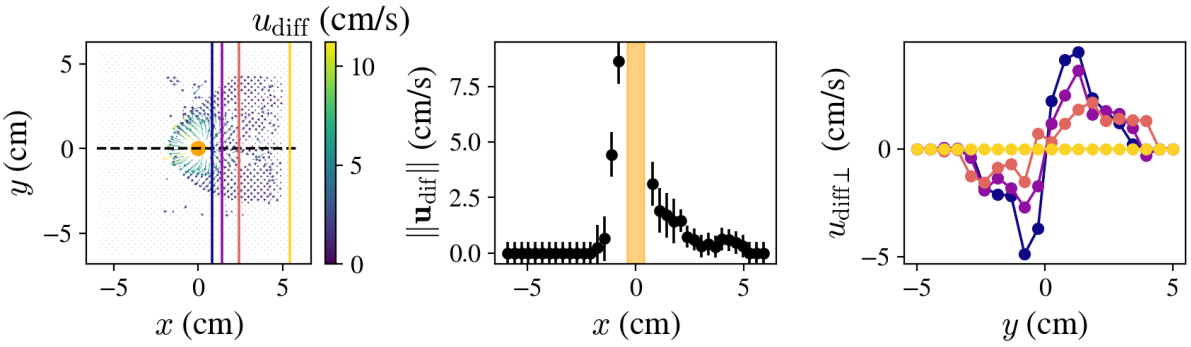

Figure 4.11: **1D profil.** For $\chi = 1$, (left) Differential velocity field $\mathbf{u}_{\text{diff}}$. The dashed black line indicates a horizontal cut along $x = 0$ passing through the swimmer, while the solid colored lines represent vertical cuts at different x positions. (Center) Magnitude of the difference velocity $\|\mathbf{u}_{\text{diff}}\|$ along the horizontal cut. The orange area indicates the swimmer extent. (Right) Perpendicular velocity component $u_{\text{diff}\perp}$ across the vertical cuts, with colors corresponding to those in the left panel.

$\max(u_{\text{diff}\perp(x)}) = 0$, which occurs around 5 cm and appears to increase slightly with higher advection speed.

The width of the hydrodynamical wake, w_{hydro}, is defined as the standard deviation of $u_{\text{diff}\perp}$ along the y-axis at a fixed x:

$$w_{\text{hydro}}(x) = \sqrt{\frac{\int_{-\infty}^{+\infty} y^2 \, |u_{\text{diff}\perp}(x,y)| \, dy}{\int_{-\infty}^{+\infty} |u_{\text{diff}\perp}(x,y)| \, dy}}. \tag{4.3}$$

As advection increases the wake gets narrower (Fig. 4.12 right).

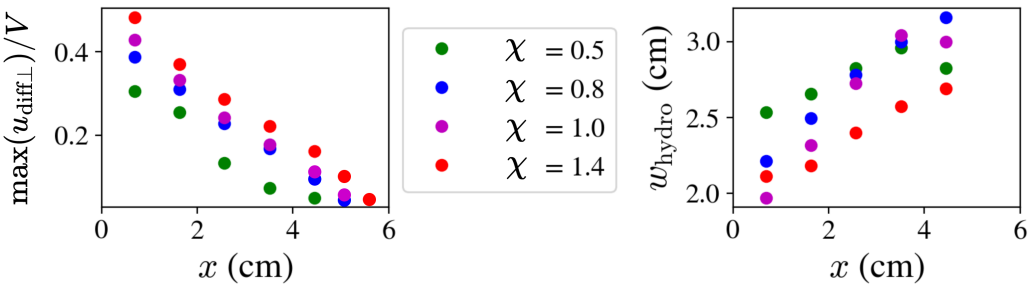

Figure 4.12: **Evolution of the hydrodynamical wake.** (Left) Maximum value of the perpendicular component $u_{\text{diff}\perp(x)}$. (Right) Width of the hydrodynamical wake computed using Eq. (4.3). Both plots show data for different advection speeds $\chi = 0.5, 0.8, 1.0, 1.4$, represented by green, blue, purple, and red points, respectively.

4.4 Conclusion

This chapter presented the first stationary flow field around a Marangoni swimmer outside its swimming velocity. The setup allowed for precise control over the experimental conditions, facilitating the systematic exploration of various flow regimes. The stationary nature of the flow field provided a clear and consistent snapshot of the dynamics, making it particularly useful for comparisons with theoretical models and simulations. However, several limitations must be acknowledged. The stationary flow field generated under controlled advection conditions may differ from the spontaneous swimming behavior of the swimmer. Indeed, compared to previous experimental characterization no source point is observed in the wake [83, 84]. Additionally, the curvature of the tank may introduce distortions in the flow field, necessitating careful analysis. The presence of channel edges is also a concern, as the hydrodynamical wake extends over 6 cm at the lowest velocity, leaving only 2 cm between the wake and the edges, which could influence the flow dynamics.

Despite these limitations, comparison with available models [81] and numerical works [62] shows qualitative agreement. However, these models still fall short of capturing the complete dynamics observed in our experiments.

The interfacial velocity field we obtained opens up opportunities to study the dispersion of surfactants emitted by the swimmer, which could be compared with other studies that have measured the surface tension field or made predictions to estimate an effective diffusion coefficient [52, 78, 79]. Additionally, fully characterizing the swimmer dynamic requires assessing the 3D flow field, which remains to be accomplished. Finally, the results lay the groundwork for future studies on more complex scenarios, including the interactions between multiple swimmers or between swimmers and boundaries, providing valuable insights into collective behaviors and interaction dynamics.

While this chapter and the previous one have focused on characterizing the forces and flow fields around the swimmer at different advection speeds, a complete picture requires exploring the distribution of surfactants. The next chapter presents a novel approach to obtaining the surface tension field directly from the interfacial flow measurement, advancing our understanding of the underlying mechanisms driving Marangoni swimmers.

Chapter 5

Inferring surface tension from the interface velocity field

Table of Contents

5.1 Introduction

The mechanics of interfacial swimmers relies on the force balance which can be deduced from the fluid flow and surface tension field at the object perimeter. Yet, to compute the capillary force if the distribution at the perimeter is essential, the distribution beyond also impacts the flow field properties. Therefore, a full understanding involves characterizing hydrodynamics, the surfactant distribution, and the state equation linking concentration and surface tension. In the second chapter, we first measured the total force applied to a Marangoni swimmer. Yet, isolating the contribution of the capillary force from the surfactant distribution, and the drag force from the flow remains an open challenge. It requires measuring the 3D flow, surface tension, and/or surfactant fields. If experimental studies [83] and numerical investigations [25, 31] have started to obtain a picture of the flow field around a Marangoni swimmer, the distribution of surfactant remains for now inaccessible.

In the vast majority of experiments, surfactants can not be visualized and their presence and spatial distribution are typically inferred from the capillary force, or Marangoni flows generated. Thus, surfactants remain as "hidden variables" in experiments [87] that cannot be measured but can have a deep influence on hydrodynamic phenomena. If the case of a fixed source of surfactant has been studied extensively [65, 66, 68, 69, 123], we are aware of only one analytical study of the surfactant field around a moving source [81] and two recent numerical works for Marangoni swimmer that included Marangoni flows [25, 62]. Therefore, on the experimental side, the surfactant distribution around a mobile source remains a completely open question.

One way to study the distribution of surfactant is to access it indirectly through surface tension measurement. However, obtaining a whole 2D surface tension field, for instance around a source of surfactant, is a challenge. Indeed, traditional methods such as the Wilhelmy plate, Du Noüy Ring, pendant drop, or oscillating jet provide only a global measurement of the surface tension [124]. To measure the local field of surface tension, the Wilhelmy plate method can be used in several different positions [125]. But, this requires having a probe in contact with the interface which could modify the flow field or the surfactant distribution. Therefore, usual techniques are not suitable for in-situ measurements around a Marangoni swimmer. A second type of approach would be to visualize directly the distribution for example by using fluorescent surfactant. For example, self-propelled droplets using fluorescent surfactant have been designed recently [88, 126], it allows following the spreading of surfactant in the bulk and visualizing the trails behind the droplets. This technique has mainly been used to understand repulsive interaction between two droplets and was not used to estimate the quantity of surfactant present or the surface tension. Moreover, to the best of our knowledge, no camphor molecule is fluorescent. One could imagine switching to another surfactant, but we would then face two problems: (*i*) as we are interested in the distribution at the interface, we would observe only a monolayer of fluorescent surfactant and the signal may not be sufficient. (*ii*) One of the main advantages of camphor is its volatility at ambient temperature which prevents saturation of the interface and enables the swimmer to maintain steady motion. Such advantages will not necessarily be present with another surfactant. Therefore, to avoid saturation of the interface we would have to significantly reduce the time of experiments over which motion is observed.

Finally, the last development used quasielastic laser scattering (QELS) to measure light scattering from capillary waves generated by thermal fluctuations of the interface. Such a non-intrusive technique allows simultaneous measurements of surface tension and surface flows and was used in several systems, including self-propelled objects such as camphor boats [48, 95], droplets [96, 127] or amoeba-like oil droplets [128] and provided the 1D surface tension profile. Although it is conceivable to sample multiple positions sequentially to obtain a 2D field, this process is time-consuming and experimentally delicate. Moreover, quasielastic light scattering requires dynamically adjusting and tracking the reference light beams for accurate measurements which is difficult to implement with basic laboratory equipment. Consequently, QELS is not easily transposable to other experimental systems. Overall, it has been hardly possible so far to measure the whole surfactant concentration field, limiting the understanding of interfacial swimmers.

In response to these challenges, this chapter introduces a new method to obtain the 2D surfactant concentration fields around interfacial swimmers. We first present the general principle of the approach. Second, we validate it on data generated numerically. Finally, we consider the experimental system previously caracterized by Nomoto *et al.* [48, 95] and validate our new approach experimentally.

5.2 General presentation of the approach

Marangoni stress and flow. For convenience, we remind the reader that a gradient of surfactant induces stress at the interface, which is defined by the Marangoni boundary condition at the interface:

$$\boldsymbol{\nabla}_{\mathrm{s}}\gamma = \overline{\boldsymbol{\sigma}}_{\mathrm{s}} \cdot \mathbf{n}_{\mathrm{s}}, \tag{5.1}$$

where $\mathbf{n}_{\mathrm{s}}$ is the normal at the interface pointing upward and $\boldsymbol{\nabla}_{\mathrm{s}}$ is the surface gradient operator defined as $\boldsymbol{\nabla}_{\mathrm{s}} f = \boldsymbol{\nabla} f - (\boldsymbol{\nabla} f \cdot \mathbf{n})\mathbf{n}$, γ is the surface tension and $\overline{\boldsymbol{\sigma}}_{\mathrm{s}}$ denotes the stress tensor along the interface. Because a fluid at rest cannot sustain a shear stress, it will be set into motion, a phenomenon known as Marangoni flows.

Surfactant concentration and Marangoni flows: inverting the perspective. As explained before, measuring experimentally the 2D concentration field around a surfactant source is challenging. In comparison, measuring a flow field is less difficult, and several standard methods are available such as particle image velocimetry or optical flow [102, 104, 129]. Therefore, the main idea is to use a measured flow field to infer the surfactant distribution (Eq. (5.1)). The process actually takes three steps. **Step 1**, we measure experimentally the surface velocity field around a Marangoni swimmer. **Step 2**, knowing the surface velocity, it is possible, using finite element methods, to reconstruct the 3D water flow. This provides us the stress at the interface. **Step 3**, by using Eq. (5.1), we deduce from the interfacial stress the local surface tension. The result is a 2D map of the local surface tension, which, provided an equation of state is available, also gives the local surfactant concentration. In the following, we detail each step of this reversed approach and discuss its practical implementation.

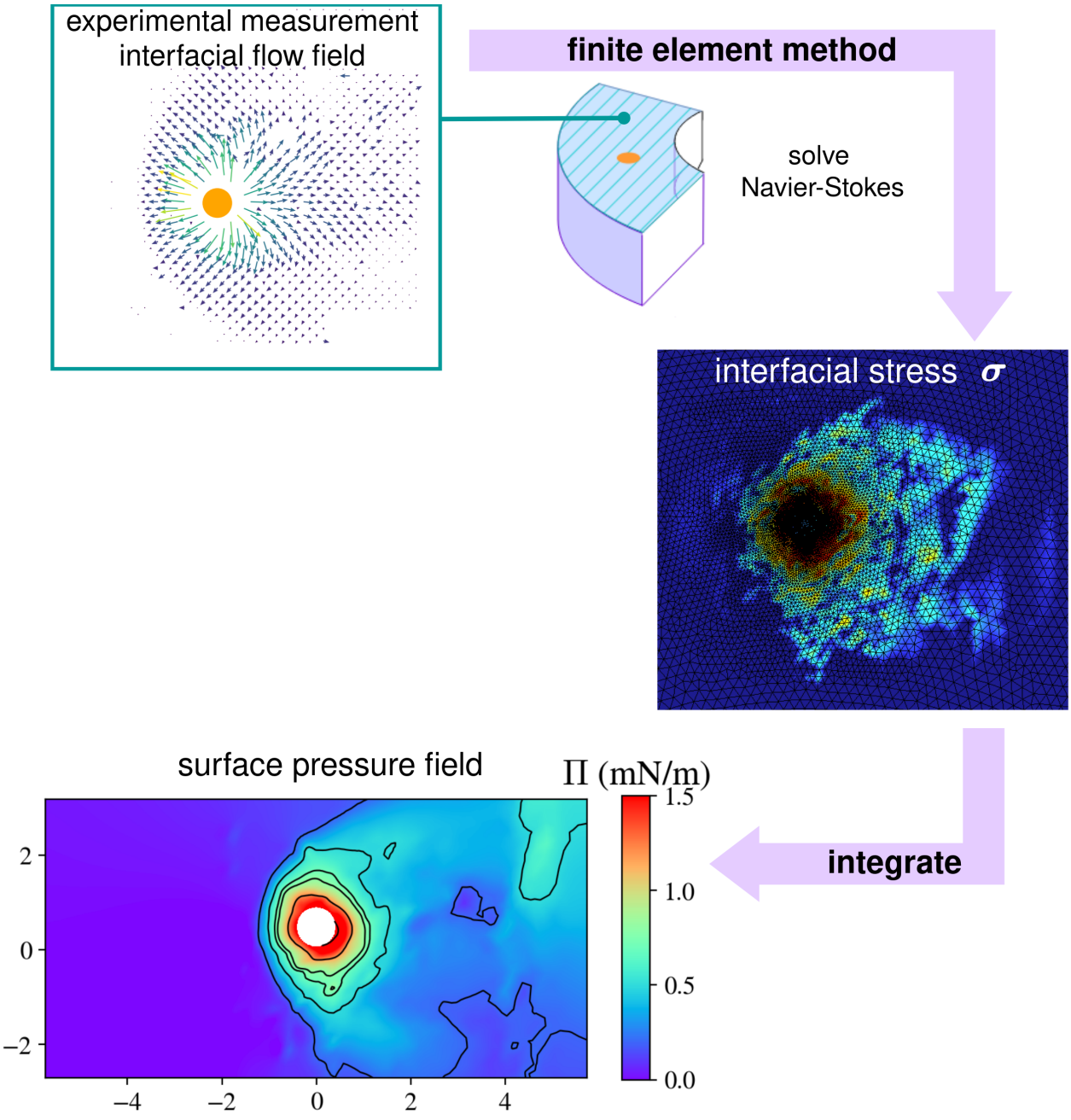

Figure 5.1: **Surface pressure from the interfacial flow.** General presentation of the work flow.

Step 1: 2D flow field around an interfacial object.

The proposed strategy requires to measure the fluid flow at the free surface. Using experimental techniques such as particle image velocimetry and optical flow, one can reconstruct the complete interfacial flow field. To do so, the water is seeded with glass bubbles, hollow glass spheres of 50 µm radius that stay at the air and water interface. Their size makes them reliable tracers and following their displacement gives information on the local flow velocity.

Step 2: Stress field from the 3D flow.

Obtaining the stress distribution at the interface requires knowledge of the 3D flow field, which presents significant experimental challenges. Previous studies have managed to do this partially for simpler axisymmetric problems [68]. However, it requires a stationary flow, and it may not capture the flow gradients developing in the 100 µm[1] boundary layer beneath the water surface. These gradients are crucial for accurately determining interfacial stress but require spatial resolutions beyond those typically achieved in past studies [25, 62]. To overcome these limitations, we adopt a hybrid approach that combines experimental and numerical methods using finite element methods. Specifically, we use the experimentally measured 2D flow field at the interface as the top surface boundary condition. In combination with known conditions on other boundaries, this is sufficient to determine the complete 3D flow within the whole volume, assuming it obeys the Navier-Stokes equation. This step combining experimental and numerical techniques allows us to accurately model the flow field and derive the stress at the interface.

Step 3: Surface tension.

Finally, to obtain the surface tension, it remains to solve Eq. (5.1), namely $\overline{\boldsymbol{\sigma}} \cdot \mathbf{n} = \boldsymbol{\nabla}_s \gamma$. The problem of integrating gradient data is commonly found in optical metrology such as wavefront measurement techniques which reconstruct the wavefront from the slopes measured [130–132]. Likewise, 3D shape measurement for reflective surfaces integrates gradient data to get the surface shape [133]. These techniques only measure the derivatives of the wanted quantity and a 2D integration procedure is necessary to reconstruct the shape from the measured derivatives [134]. A similar approach can be used to obtain the surfactant concentration. Here, the measured derivative is the stress field derived from finite element methods. Equation (5.1) can be discretized on each element of the mesh, resulting in an overdetermined set of equations that can be solved by the least mean square method. We now review the detailed process.

The stress field is defined on the vertex of a 2D triangular mesh. Therefore, it is necessary to define the value of the gradient inside each triangle. For that we consider the **per-cell linear estimation** [135] and extrapolate linearly the values of a function f

[1] According to the Blasius solution conditions the thickness of a hydrodynamic boundary layer δ_h for a laminar flow depend on the Reynolds number Re and the characteristic length a can be estimated as $\delta_h \approx a/\sqrt{\mathrm{Re}}$. Therefore, for a swimmer of 4 mm and Re $\approx$ 500, the thickness of the boundary layer is $\delta_h \approx 100\,\mu\mathrm{m}$

on each vertex ν_i at a generic point p inside a triangle t such that:

$$f(p) = \sum_{\nu_i \in t} \lambda_i f_i, \tag{5.2}$$

where λ_i are the barycentric coordinates of p with respect to the vertices ν_i. Considering a finite difference approach, we can differentiate $f(p)$ with respect to the coordinates of p. The gradient defined that way is constant inside a given mesh element. Since we're dealing with a triangular mesh here, it is more convenient to express the gradient in terms of the vertices of the triangle. Therefore, for a triangle t with vertices ν_i, ν_j and ν_k the gradient of f is:

$$\boldsymbol{\nabla} f_t = (f_j - f_i)\frac{(\boldsymbol{\nu}_i - \boldsymbol{\nu}_k)^\perp}{2A_t} + (f_k - f_i)\frac{(\boldsymbol{\nu}_j - \boldsymbol{\nu}_i)^\perp}{2A_t}, \tag{5.3}$$

where $e^\perp$ denotes edge e rotated by 90°, A_t the area of the considered triangle t, and f_i the value of the function f at the vertex i. We associate the gradient of the function f_t to the center of each triangle.

Then using Eq. (5.3), one can discretize Eq. (5.1) for each triangle of the mesh and express it with matrices as:

$$MX = S. \tag{5.4}$$

In this equation, M is the mesh gradient matrix obtained with Eq. (5.3) with dimension $(2T \times P)$ where T is the number of triangles and P the number of vertices. S is the stress matrix containing the x and y components stacked vertically for each triangle, which thus has dimension $(2T \times 1)$. And X is the surface tension matrix with dimension $(P \times 1)$. As in a triangular mesh each point is shared by 6 triangles and each triangle contains 3 points, there are around twice as many triangles as points. Therefore, we have an overdetermined problem with $2T \simeq 4P$ equations and P unknowns.

Since there is no exact solution that satisfies all equations, we use the **least squares method**. It provides a solution that minimizes the error across all equations. This method gives a relative value of the surface tension. To obtain an absolute value, appropriate boundary conditions have to be applied depending on the geometry of the problem studied. In our situation, if the system is large enough we expect to measure the surface tension of water γ_w far from the surfactant source. However, it would be more convenient if the results did not depend on the value of water surface tension. Therefore, we will consider the surface pressure Π:

$$\Pi = \gamma_w - \gamma, \quad \text{such that} \quad \nabla\Pi = -\nabla\gamma. \tag{5.5}$$

The values of Π are needed on one mesh point to obtain an absolute value of the surface pressure. In practice, for the systems we consider in the following, at least one domain edge is free of surfactant and will be set to $\Pi = 0$.

To conclude this section, this new experimental and numerical approach allows obtaining the 2D surface pressure field around a source of surfactant from a measure of the interfacial flow field. It relies on well-known and easily accessible tools such as finite element methods or particle image velocimetry, making it easy to implement in various systems. In the following sections, we validate this approach on numerical data. In a subsequent chapter (Chap. 5), we will use it for the interfacial swimmer.

5.3 Numerical validation on artificial data.

5.3.1 Presentation of the approach.

While the full process presented earlier is formally exact, the key to validating the method is to assess whether it can withstand a finite noise level as found in experimental data. Moreover, it allows estimating the reliability of the reconstructed surface pressure field as a function of the initial surface flow quality. To do so, instead of measuring the interfacial velocity field experimentally, we generate it numerically from a chosen surfactant distribution. We consider two different systems, (*i*) the simple case of a fixed circular source of surfactant, (*ii*) the more complex situation of a moving source in a canal. Our approach is structured as follows: first, we chose an appropriate surface pressure distribution, which can be challenging due to the absence of standard reference cases (Fig. 5.2). We then derive the interfacial flow field from the imposed surface pressure. Following this, we solve the Navier-Stokes equation with the interfacial flow field as the boundary condition for the top free surface and obtain the 3D flow field. At this step, we can consider either the exact flow field derived to assess the purely numerical error, or we can introduce noise and resolution limitations as in true experimental data to evaluate the sensitivity of the inversion. Finally, the stress field is inverted, and we compare the obtained surface pressure field with the imposed one. The approach followed is summarized by the workflow below (Fig. 5.2).

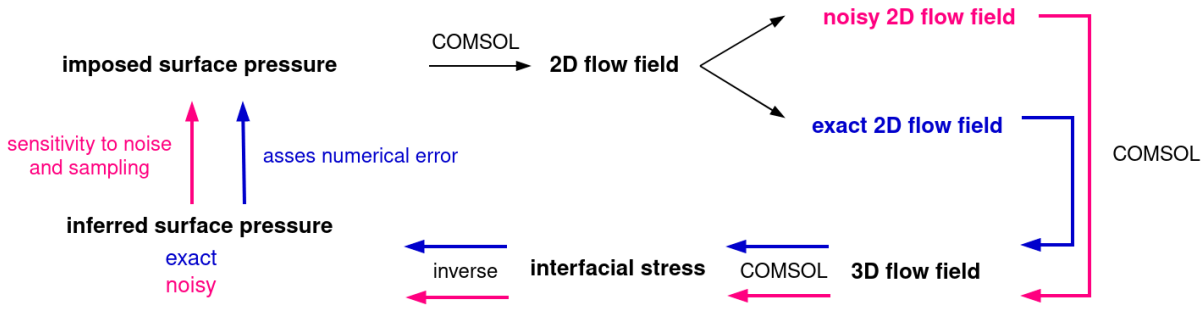

Figure 5.2: **Numerical validation of the method.** Workflow to evaluate the sensitivity to noise and sampling of the input interfacial flow when reconstructing the surface pressure.

5.3.2 Fixed source of surfactant.

Choice of surfactant distribution. To assess the impact of the noise on the interfacial velocity field, we first study the simple case of an axisymmetric fixed source of surfactant. As mentioned earlier there is no reference study of a finite-size solid fixed source. The system most closely related is a punctual source of surfactant, which has been extensively studied, both experimentally and numerically [65, 66, 68, 69, 123]. Despite potential destabilization into complex multi-vortex structures at long distances beyond a critical radius, it typically generates a smooth, axisymmetric, steady flow centered on the surfactant source. In the limit of insoluble or fast equilibrating surfactants, calculations established a power law scaling for the surfactant flow and surface tension [68, 69, 136].

These power-laws reflect the dominance of Marangoni stresses that drive the spreading. Here for simplicity and to maintain consistency with the subsequent section on a mobile source, we chose as a test case a radial, exponentially decreasing surface pressure field:

$$\Pi_{\text{ref}}(r) = \Pi_s \exp(-Ar), \tag{5.6}$$

with $\Pi_s = 2\,\text{mN m}^{-1}$ the surface pressure of the surfactant and $A = 8\,\text{mm}$ (Fig. 5.3 left).

Geometry and mesh. The numerical system is a quarter of a circular tank with 10 cm radius and the surfactant source is placed at the center and has a radius of 4 mm. The tank is 8 cm in height and filled with water (Fig. 5.3 left). In finite elements methods, the mesh must adapt to local gradients with finer mesh elements where spatial variations are more significant. In our case, at the interface, the source contour defines a sharp border between the no-slip and Marangoni stress boundary conditions (Fig. 5.3 right). In the bulk, we have to consider the boundary layer forming under the source. Except for these critical areas, the remaining space does not need a particularly fine mesh, and a coarser mesh can be used without compromising numerical accuracy. The mesh is composed of tetrahedrons, whose size can be adjusted (Fig. 5.3 right). Inside the source and just under the water surface the size of the tetrahedron is constrained between $1.6 \times 10^{-6}\,\text{m}$ to $5.3 \times 10^{-4}\,\text{m}$ with a growth rate[2] of 1.05 Outside these areas, the tetrahedron size is $3.2 \times 10^{-5}\,\text{m}$ to $2.2 \times 10^{-3}\,\text{m}$ with a growth rate of 1.1 Lastly, all boundary conditions have to be defined. We consider a no-slip boundary condition on the source and tank bottom surface. For the tank outside edge, constant pressure is set imposing that all flows go outside the domain, and preventing any backflow. The interfacial flow can be computed from the imposed surface pressure and is used as a boundary condition for the top surface.

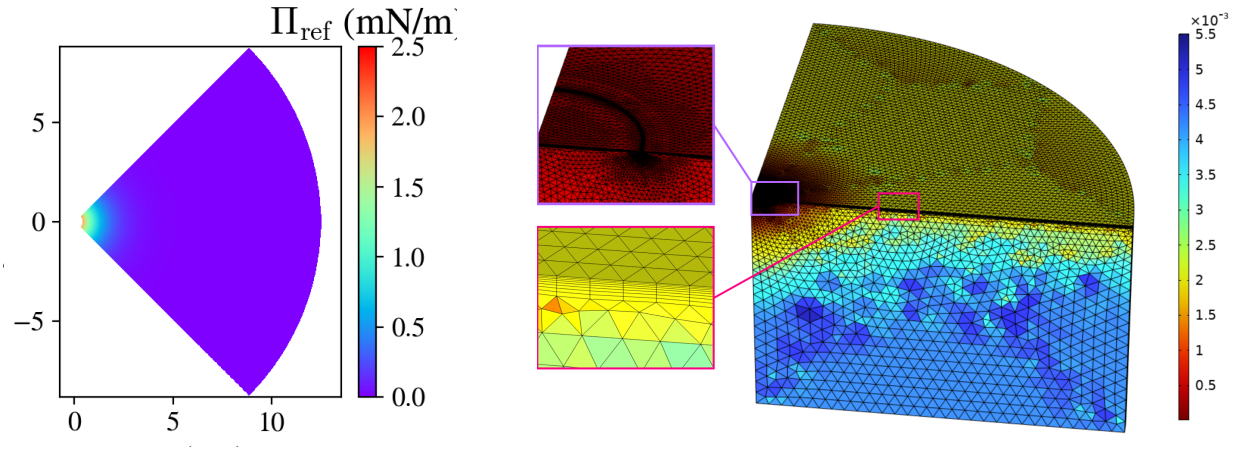

Figure 5.3: **Numerical study of a fixed source of surfactant.** Chosen distribution of surface pressure Π_{ref}, top view (left). Geometry of the system for finite element methods with mesh (right). The color indicates the size of the elements. Zoom on the boundary layers around the swimmer (purple) and under the interface (pink).

[2]The growth rate determines the maximum rate at which the element size can grow from a region with small elements to a region with larger elements. For example, with a growth rate of 1.5, the element size can grow by at most 50% from one element to another.

Finite sampling and noise. The pressure field derived from the intact surface velocity field perfectly matches the imposed field. The good agreement between the two fields shows that the purely numerical error is very low and demonstrates the accuracy of our numerical setup under ideal conditions. To understand how real experimental limitations affect the accuracy of our measurements, we generate velocity fields that are subject to coarse sampling and noise. Specifically, the velocity vectors are sampled every 0.1, 1, 2, or 4 mm, and this distance will be referred as d_s. The noisy vector $\mathbf{u}_{noisy}$ is obtained by adding a noise with amplitude ϵ and angle θ randomly picked from a Gaussian distribution with variance of 10^{-4}, 0.1, 0.5, or 1 cm s^{-1}:

$$\mathbf{u}_{noisy} = \mathbf{u} + \epsilon \begin{pmatrix} \cos\theta \\ \sin\theta \end{pmatrix}. \tag{5.7}$$

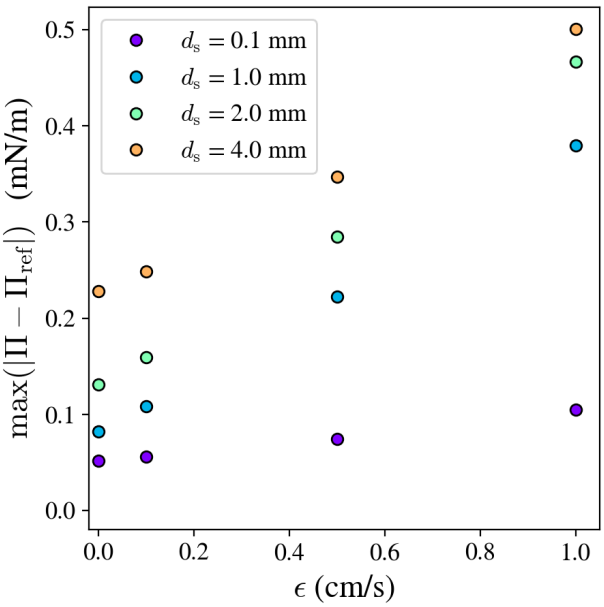

Figure 5.4: **Surface pressure around a fixed source of surfactant.** Maximal error obtained by comparing the imposed surface pressure field Π_{ref} with the computed one Π with respect to the noise level ϵ. The point color indicates the sampling interval d_s. The maximal value of the surface pressure at the source edge is $\Pi = 2.5$ mN m^{-1}.

Sensitivity to velocity discretization and errors. A systematic study of the impact of the noise and sampling on the surface pressure field is presented in Appendix. 5.1. The obtained fields remain radial with iso-concentration lines being close to circular up to $d_s = 4$ mm and $\epsilon = 0.5$ cm s^{-1}. In all cases, the maximum surface pressure value, close to the source edge, is 2 mN m^{-1} which is consistent with the imposed field.

The error between the computed and imposed surface pressure field provides quantitative information on the impact of the sampling interval and noise. The maximal error occurs near the swimmer edge where there is a sharp discontinuity in the stress field. For sampling interval and noise of respectively 2 mm and 1 cm s^{-1} the maximal error is below

$0.5\,\mathrm{m\,N\,m^{-1}}$, 25% of the maximal surface pressure value. The error drops significantly when moving away from the source edge. For $d_s = 4\,\mathrm{mm}$, the first velocity vector is farther from the source edge resulting in an error twice bigger than the error obtained with $d_s = 2\,\mathrm{mm}$ (Fig. 5.3). The large deterioration of the surface pressure field already shows the importance of having vectors as close to the source as possible. For $d_s = 0.1\,\mathrm{mm}$ adding noise has almost no effect, as the error on the reconstructed field increased by only 30% for $\epsilon = 1\,\mathrm{cm\,s^{-1}}$. Whereas for all the other samplings studied, adding noise increases the error by a factor 3 or 4.

Partial conclusion for the fixed source. In conclusion, our first test case successfully demonstrates the feasibility of reconstructing the surface tension field around a fixed source of surfactant using numerical flow field data. The obtained surface tension is consistent with the imposed field, with a maximal error in the vicinity of the source around $0.5\,\mathrm{mN\,m^{-1}}$ observed under the most challenging conditions of high noise level $\epsilon = 1\,\mathrm{cm/s}$ and large sampling interval $d = 4\,\mathrm{mm}$. For less challenging conditions the maximal error is below $0.3\,\mathrm{mN\,m^{-1}}$, which corresponds to 15% of the expected value. The error drops to less than $0.1\,\mathrm{mN\,m^{-1}}$ a few millimeters away from the source and is mainly due to the distance between the first velocity vector and the edge of the source. To conclude, this first test case with a fixed source confirms on a simple situation the validity of the method and leads us to consider a more complex system: a Marangoni swimmer in a channel.

5.3.3 Mobile source of surfactant

No reference surface pressure field for a Marangoni swimmer. We have shown previously that our approach successfully reconstructs the surface pressure field around a fixed solid source of surfactant with and without noise on the input interfacial flow field. However, the case of a Marangoni swimmer (a mobile source of surfactant) is more complex as there is no symmetry nor reference description of the surface pressure field. Therefore we pursue the validation of the numerical steps of our approach to this problem. A few analytical studies account for the finite size of the swimmer in Stokes flow [54, 81, 137]. For finite Reynolds number, numerical methods are needed and two recent works provided insights into the surfactant profile with an asymmetric distribution around the swimmer with higher concentrations at the rear, resembling an egg-like shape [25, 62].

Choice of surface pressure. Given the absence of a reference case for the pressure field around a mobile source of surfactant, we must make an informed assumption about the distribution. We consider an exponentially decaying surface pressure field shifted toward the rear of the swimmer to mimic the effect of advection. In cylindrical coordinates (r, θ), the chosen surface pressure field $\Pi_{\mathrm{ref}}(r, \theta)$ is given by:

$$\Pi_{\mathrm{ref}}(r, \theta) = \Pi_s(1 + \alpha + \cos\theta)\exp\left(-\frac{r - a}{2a}\right), \tag{5.8}$$

where $\Pi_s = 2\,\mathrm{mN\,m^{-1}}$ is the surface pressure of the surfactant released by the source and α is a positive constant that defines the extension of the field in front of the source. Here $\alpha = 0.4$. The obtained field qualitatively resembles previous numerical simulation on

close systems [25, 62] (Fig. 5.5 top). Here we choose to decouple the hydrodynamic and transport problem and the surface pressure distribution will be the same for all advections. This crude assumption allows us to solve only a hydrodynamic problem with the correct range of Reynolds and Peclet numbers. Indeed solving the transport and hydrodynamic problem is significantly more complex as it requires a mesh small enough to capture what is happening in each boundary layer over a large area. In this problem, the transport boundary layer is a hundred times smaller than the hydrodynamic one (1 µm compared to 100 µm[3]) leading to prohibitive computational times when solving both problems. In comparison considering only the hydrodynamical problem allows us to consider a much larger mesh, reducing drastically the computational time.

The surface velocity field displays features similar to those observed in experiments, with an extension upstream in front of the swimmer and a dilatation of the interface downstream [84, 86]. While this approach may not capture all nuances, it is adequate to study the sensitivity of the inversion to noise and sampling and should give insight into the ability of the inversion method to perform on real experimental data.

Geometry and mesh. For finite elements methods, the system is composed of a cylindrical source of surfactant of diameter $a = 4\,\mathrm{mm}$ placed in a rectangular channel that is 10 cm wide filled with 1 cm of water. Due to symmetry, only half of the channel has to be considered (Fig. 5.5 bottom). For convenience, we switch the framework, and the source is placed at a fixed position $(0, 0, 0)$ and the water flow goes from left to right with a velocity $\mathbf{U}$ of 5, 9.4 or $12\,\mathrm{cm\,s^{-1}}$. As before the mesh is composed of tetrahedrons with finer mesh size with a max size of $2 \times 10^{-5}\,\mathrm{m}$ and a growth rate of 1.05 in a circle of equal to 1.25 swimmer radius and just below the water surface to capture significant spatial variations (Fig. 5.5 bottom). Outside these critical areas, a coarser mesh is used with tetrahedrons between $5.6 \times 10^{-4}\,\mathrm{m}$ to $3 \times 10^{-3}\,\mathrm{m}$ and a growth rate of 1.13 A no-slip boundary condition is imposed on both the swimmer and the channel surfaces. For the outside edge, constant pressure is set imposing that all flows go outside the domain and preventing any backflow. For the top surface, the interfacial flow $\mathbf{u}$ can be computed from the imposed surface pressure field and is used as a boundary condition.

5.3.3.1 Reference without noise

A large error. First, we consider the complete vector field derived from the surface pressure distribution without any noise or sampling for three advection speeds. This defines a lower bound on the error. The surface pressure field is independent of the advection speed, so when inverting the stress, we expect to obtain the same surface pressure field for all advection. However, this is not what we observe (see Appendix 5.2). As the flow velocity increases, the reconstructed surface pressure appears to shift towards the rear of the source, with a rise in the maximal value just behind the source. Moreover, the maximal error is $0.25\,\mathrm{mN\,m^{-1}}$ which is comparable to the error obtained on the reconstructed field for the fixed source with noise and sampling interval. In the following, we explore the origin of this large error even without noise or finite sampling interval in the velocity field.

[3]The thickness of the transport and hydrodynamic boundary layers are inversely proportional to the square roots of respectively the Reynolds and the Peclet number.

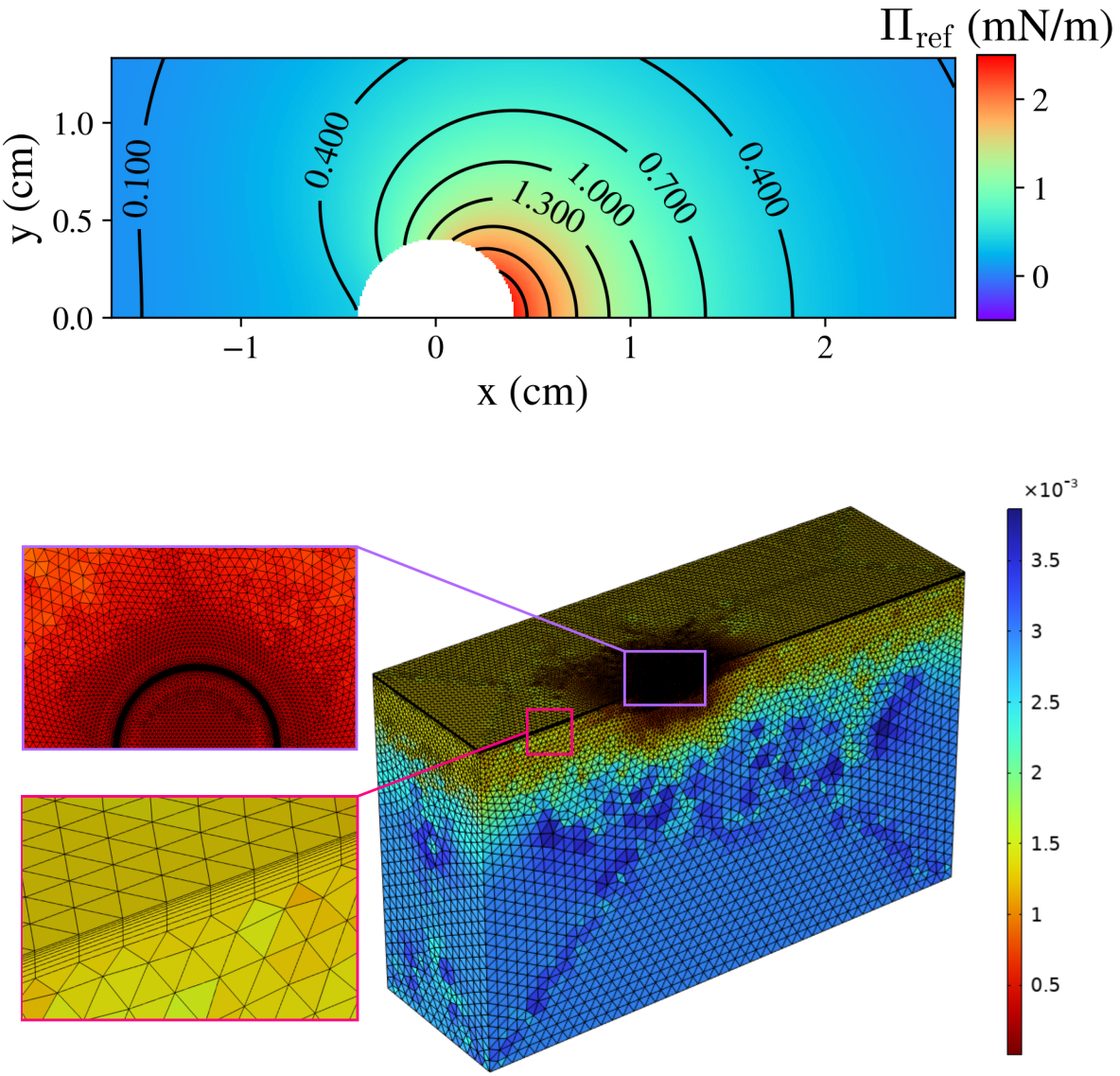

Figure 5.5: **Finite element methods of a mobile source of surfactant in a channel.** (Top) Top view of the chosen surface pressure field Π_{ref}. Black lines indicate isobars. The maximal surface pressure value $\Pi_{\text{ref}} = 2.5\,\text{mN}\,\text{m}^{-1}$ is located downstream just behind the source. (Bottom) Geometry of the channel used and mesh. The colorbar indicates the size of the elements. Zoom on the two boundary layers, around the source (purple) and below the water surface (pink).

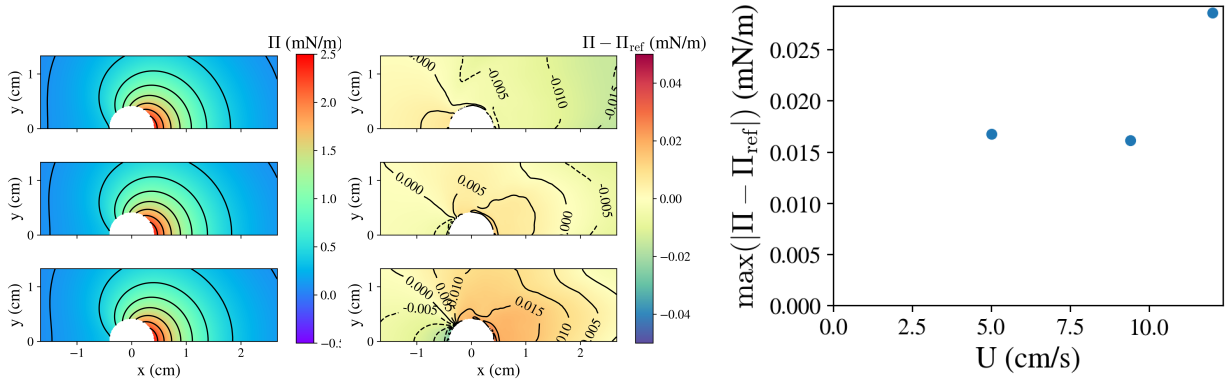

Figure 5.6: **Reconstruction of the surface pressure field around a mobile source from a numerical velocity field without noise.** The inversion is made on the mesh elements at a distance larger than 5% of the source radius from the source edge. From top to bottom the advection velocity increases 5, 9.4 and 12 $\mathrm{cm\,s^{-1}}$. (Left) Computed surface pressure field around the source, the black lines indicate isobars. Difference between the computed surface pressure field Π and the imposed one Π_{ref} (center). Maximal error measured (left).

The error is due to the stress field discontinuity. At the source edge, there is a sharp change in boundary condition from non-slip on the swimmer to an imposed stress at the water surface creating a discontinuity. This makes the reconstruction of the surface pressure field challenging. When advection is added the stress becomes even larger at the interface, increasing the discontinuity and leading to larger error behind the swimmer. This issue is also observed for a passive source that is not releasing surfactant (Appendix. 5.3). In this case, the stress should be non-zero only below the disk, but we observe that it spreads at the surface at a distance d of the source edge, corresponding to 5% of the source radius (Appendix. 5.3). The spreading of the stress at the interface shows that this issue is purely induced by the numerical method. To avoid this numerical artifact, which has no link with the physics of the system, we consider the mesh elements at a distance larger than d from the source edge for inverting the stress field. With this cropped stress field, the surface pressure fields reconstructed are much more consistent for all advection velocities (Fig. 5.6 left) with a maximal value close to $\Pi = 2.5\,\mathrm{mN\,m^{-1}}$ similar to the imposed field. The error maps confirmed a significant decrease of the error all around the source (Fig. 5.6 center) with a maximal error going from $0.3\,\mathrm{mN\,m^{-1}}$ when considering the whole field for inversion to $0.03\,\mathrm{mN\,m^{-1}}$ when considering only the element located at a distance $d = 0.05 \times a$ of the source edge. This demonstrates that the discontinuity of the stress field at the source edge contributes significantly to errors during surface pressure reconstruction, emphasizing the need to handle the area close to the source edge carefully.

Obtaining the capillary force without values at the swimmer edge. While removing mesh rows closest to the swimmer edge improves the quality of the reconstructed field, it also prevents the computation of the capillary force F_c. To circumvent this limitation, we tried to compute the capillary force by extrapolating a series of values computed at radii larger than the swimmer. The expected value, from the imposed surface pressure,

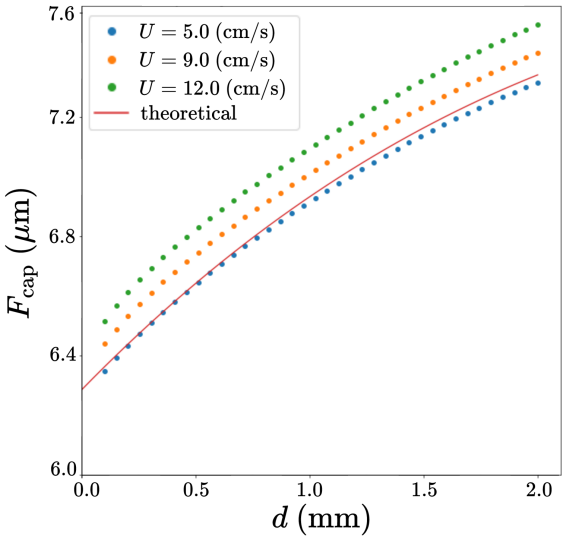

Figure 5.7: **Capillary force for decreasing circle radius.** The capillary force is computed on circles larger than the sources for advection velocity of 5, 9.4 and 12 cm s^{-1} respectively in blue, orange, and green. The continuous red line is the reference value of the capillary force obtained from the imposed surface pressure field.

is $F_c = 6.3\,\mu$N. For low advection velocities ($\mathbf{U} = 5\,\mathrm{cm\,s^{-1}}$), the extrapolated capillary force is $F_c = 6.25\,\mu$N matching the expected value. When the flow velocity increases, the extrapolated capillary force also increases by respectively 1.5% and 3% for 9.4 and 12 cm s^{-1} (Fig. 5.7). To conclude, this configuration without noise and sampling allows us to assess the lower bound of the numerical error of 0.03 mN m^{-1}. This shows that for a situation mimicking a Marangoni swimmer, our inversion method allows us to faithfully reconstruct the surface pressure field and force applied to the swimmer.

5.3.3.2 With noise.

Now that we have evaluated the lower bound of the error 0.03 mN m^{-1} for the reference solution, we evaluate the capability of the inversion method to reconstruct the surface pressure field from a velocity field closer to experimental conditions. To do so, reference surface flow is deteriorated through finite sampling and noise. Velocity vectors are sampled at intervals d_s of 0.1, 1, 2, or 4 mm, and a Gaussian noise ϵ of 10^{-4}, 0.1, 0.5, 1, or 2 cm s^{-1} is added. To account for the discontinuity of the stress field near the swimmer edge, we consider only the stress data after a distance $d = 0.05 \times a$ from the swimmer.

The case of a mobile source shows increased sensitivity to data degradation compared to the fixed source scenario. In the most deteriorated cases, errors reach 0.4 mN m^{-1} which represents 30% of the maximal surface pressure value. Nevertheless, the topology and magnitude of the surface pressure field remain robust across all tested conditions. The maximal surface pressure value behind the swimmer is at most 2.4 mN m^{-1} and the isoconcentration lines remain close to circular (Appendix. 5.4). The error is maximal close to the swimmer edge (Appendix. 5.5) and its value remains below 0.3 mN m^{-1} (Fig. 5.8 left), which is about 15% of the expected surface pressure value, for an intermediate

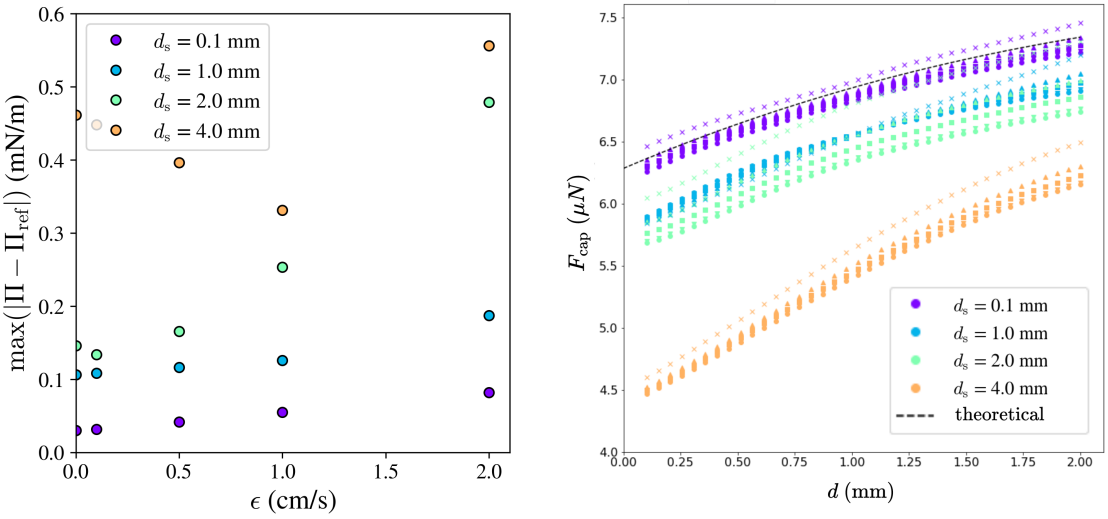

Figure 5.8: **Effect of sampling size and noise on the surface pressure field around a mobile source.** For a flow velocity of $5\,\mathrm{cm\,s^{-1}}$, colors of the marker indicate the sampling size. Maximal error on the reconstructed surface pressure field compared to the imposed one (Left). Capillary force is computed on circles larger than the source (Right). The black dashed line corresponds to the theoretical force value. The noise level is indicated by the symbol shape, with cross, up triangle, square down triangle, and circle for respectively 10^{-4}, 0.1, 0.5, 1, or $2\,\mathrm{cm\,s^{-1}}$

deterioration ($d_s = 2\,\mathrm{mm}$ and $\epsilon = 1\,\mathrm{cm\,s^{-1}}$). Farther from the source edges, the error is always below $0.2\,\mathrm{mN\,m^{-1}}$.

Capillary force on the source. As we remove the initial mesh rows around the source, we have to extrapolate the capillary force F_{cap} using circles of decreasing radius. From the reference surface pressure field, the expected value is $F_{cap} = 6.4\,\mu\mathrm{N}$. For $d_s = 0.1\,\mathrm{mm}$, we obtain the expected capillary force for all noise levels. However, for larger sampling interval of 0.5 mm and 1 mm, deviations from the expected value occur, with $F_{cap} = 5.7 \pm 0.2\,\mu\mathrm{N}$. For the largest sampling distance, the deviation becomes significant, resulting in $F_{cap} = 4.5 \pm 0.3\,\mu\mathrm{N}$. The noise level does not significantly impact the capillary force value compared to the sampling distance, emphasizing the importance of closely spaced data points near the source edge.

Conclusion

In this section, we conducted a detailed numerical validation of our method using artificial surface pressure and velocity fields. Our objectives were twofold. First, we wish to validate the numerical procedures for deriving the stress field from the 3D flow and for inverting this data to obtain the surface pressure field. Second, we wanted to assess the method robustness against variations in sampling and noise levels in the surface flow field input. We considered two scenarios: a fixed circular source of surfactant and a mobile source in a channel. For both, the reconstructed surface pressure field remained accurate up to a sampling interval of 2 mm and a noise level of $1\,\mathrm{cm\,s^{-1}}$.

In the case of the mobile source, the stress field is highly discontinuous at the source edges. This induces that part of the stress that should be located below the swimmer spreads at the interface over the first mesh rows. This artifact is purely numerical, so we remove the closest mesh elements before inverting the stress field. With this approach, we achieved reliable surface pressure fields with the largest error remaining below $0.3\,\mathrm{mN\,m^{-1}}$, or 15% of the expected surface pressure value. However, by doing so we lost information on the surface pressure field close to the swimmer, so we proposed an extrapolation procedure to compute the capillary force that works in up to a sampling distance of 2 mm and a noise level of $1\,\mathrm{cm\,s^{-1}}$.

This validation confirms the reliability of our method in accurately reconstructing surface pressure fields and estimating capillary forces from the interfacial flow, paving the way for experimental validation. We now have a clearer understanding of the maximal level of noise and sampling distance on the measured flow field and can design relevant experimental protocols. In the following, we describe our approach to experimentally measure the flow field around an interfacial object. Our goal is to maintain the noise and sampling distance below $1\,\mathrm{cm\,s^{-1}}$ and 2 mm, respectively.

5.4 Experimental validation: study of a camphor boat

Having validated our method on synthetic data, we now move toward a real system to further assess the feasibility and accuracy of our approach in experimental settings. Our hybrid method, designed to access hidden variables in Marangoni problems and recover the surface pressure field from hydrodynamic-only information, has demonstrated its robustness under controlled numerical conditions. We have seen that even with varying levels of sampling and noise, the method reliably computes the surface tension around both fixed and mobile surfactant sources.

Before exploring the complex situation of a Marangoni swimmer in a water flow, it is crucial to perform a full-scale test on an actual experimental system. Although our specific experimental conditions lack a direct reference in the literature, several studies provide a preliminary benchmark. For instance, Bandi *et al.* [68] managed to capture the complete flow field and surface tension distribution around an axisymmetric fixed source of surfactant. However, there is an uncertainty about the surfactant concentration, and comparing quantitatively the surface tension value is impossible. Additionally, Nomoto *et al.* obtained the 1D surface tension profile across a camphor boat using **quasielastic light scattering** offering valuable comparative data for our analysis [48].

In this section we consider a similar experimental situation to the one explored by Nomoto *et al.* We first measure experimentally the flow field around the boat, then compute the 2D field of surface pressure. Finally, we consider a cut passing by the boat to compare our results with the ones from Nomoto *et al.* and obtain similar results for the flow velocity profile and surface pressure, which end up validating our approach.

5.4.1 Experimental vector field

Experimental setup and protocol. To reconstruct the surface pressure field around a camphor boat (Sec. 2.2.1), we first need to measure experimentally the interfacial flow field. We exploit the rotating tank set-up already used for the camphor swimmer (Fig. 2.3

page 33). In practice, the boat is placed in a circular channel of 10 cm width with an outer radius of 20 cm. The swimmer is attached to two rigid glass capillaries separated by 5 mm to avoid any left-right displacement of the rear. The tank rotates at an angular velocity of $0.4\,\mathrm{s}^{-1}$ which generates a flow of $6\,\mathrm{cm\,s}^{-1}$ at the center of the channel which corresponds to the typical swimming velocity. To capture the flow dynamics around the camphor boat, we follow the same experimental protocol as presented in the previous chapter (Sec. 4.2 page 71) and two successive sets of images are recorded: (*i*) 30 s with white light at 50 fps to obtain the flow around the wake and (*ii*) 60 s with the laser sheet at 50 fps while sprinkling glass bubbles in the wake.

Difference with the experimental system of Nomoto *et al.* The experimental conditions differ slightly from the work of Nomoto *et al.*, where the camphor boat was able to move freely within a smaller circular container. In our system, the flow velocity is always $6\,\mathrm{cm\,s}^{-1}$ corresponding to the average swimming velocity observed across multiple boats. Moreover, we place the boat at the center of the channel whereas in the work of Nomoto *et al.* it was moving along the edge. The central position allows us to measure the full flow field around the boat and avoid any possible interactions with the edge. Despite these differences, preliminary observations indicate that the swimming velocities in both setups are comparable, so we expect that these variations will not significantly impact the surface tension measurements.

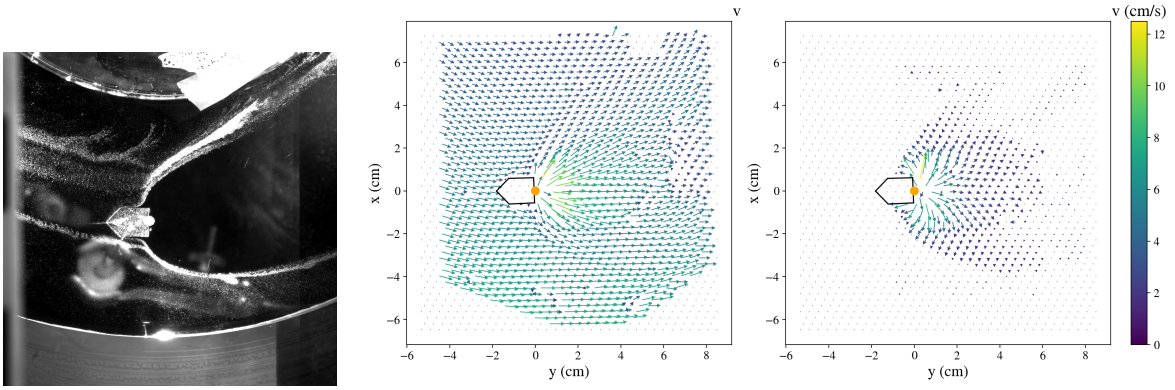

Figure 5.9: **Complete flow field around a camphor boat.** The fluid flow is going from left to right and the velocity at the center of the channel is $U = 6\,\mathrm{cm\,s}^{-1}$. (Left) Typical experimental image used to reconstruct the flow field. The boat is at the center of the channel and the small white dots are the glass bubbles used as tracers. (Center) Time-averaged flow field obtained by combining PIV, Optical Flow, and manual tracking of the tracers. The colormap indicates the norm of the flow velocity. (Right) Difference between the measured flow field and the imposed solid rotation. It is similar to the flow field around a boat in a quiescent fluid moving at $\mathbf{V} = -\mathbf{U}$.

Accumulation of tracers on the boat edge. In contrast to what happens with the swimmer (Fig. 4.1, page 71), the wake does not extend in front of the boat, causing tracers to directly touch the boat edge. The resulting accumulation of tracers complicates the analysis of their motion. The tracers no longer reflect the fluid dynamics but instead, form a pile moving with the flow. To avoid error in the reconstructed flow field, we remove

the area of accumulation upstream corresponding to 1 mm along the boat edge before performing PIV and Optical Flow.

Obtaining the flow field around the boat. In practice, obtaining the complete flow field around the boat is simpler than around a swimmer (Sec. 4.2 page 71). Indeed, as camphor is only released from the rear of the boat, the glass bubbles reach the front of the boat and the wake only forms at the rear (Fig. 5.9 left). Compared to the swimmer, these differences in surface flow significantly reduce the area where tracer sprinkling and manual tracking are necessary. Additionally, as the boat is transparent there is no issue with tracers disappearing in its shadow. Using a combination of Optical Flow, PIV, and manual tracking, we reconstruct the complete flow field around a camphor boat (Fig. 5.9 center). Removing the imposed solid rotation provides a flow field similar to a boat moving at $\mathbf{V} = -\mathbf{U}$ in a quiescent fluid. The boat does not significantly modify the upstream water flow (Fig. 5.9 right). This observation is similar to the plastic disc case. At the rear, the camphor pellet induces a radial dilatation of the interface from a point adjacent to the camphor pellet which was already observed at lower Reynolds number ($\mathrm{Re} = 25$) with asymmetric circular Marangoni swimmers [83].

Noise level. The numerical validation shows that noise in the velocity field significantly impacts the quality of the reconstructed surface pressure. To evaluate the noise on the experimental velocity field, we consider each technique used. First, for the PIV data, we compute the standard deviation between vector fields of each image pair, keeping only one pair every ten images to ensure data independence. This method allows to map the noise levels outside the wake, with maximal values typically around 0.5 cm/s, except near the boat where it reaches 1 cm/s. Regarding the optical flow data, after interpolating them onto the PIV grid, we compute residuals between the original velocity data and their interpolated counterparts at corresponding positions. The noise level is similar to PIV, typically around 0.5 cm/s far from the boat and 1 cm/s below 5 mm from the camphor pellet. These noise levels correspond to the range where we have evaluated our approach to perform well, so we expect to reliably reconstruct the surface pressure field.

5.4.2 Surface pressure Field

We have measured the flow field around a camphor boat with a noise level below $1\,\mathrm{cm\,s^{-1}}$ and a sampling resolution of 2 mm. Our numerical validation indicated that these conditions are sufficient to obtain a reliable surface pressure field with a maximal error of $0.5\,\mathrm{mN\,m^{-1}}$. We then proceed to the following steps of the approach: obtaining the 3D flow field and interfacial stress using finite elements methods and then discretizing the Marangoni stress boundary condition (Eq. (5.1)) to obtain the surface pressure field.

Reconstructing the stress field from the surface flow. The reconstruction step relies on finite elements methods, carried out with Comsol, and requires to replicate the experimental situation. The numerical domain is a part of the circular channel of 10 cm width and an angular sector of $\pi/3$ with a depth of 1 cm. As the boat position may slightly move between experiments (typically less than 1 mm), it is defined by pointing manually each vertex of the boat. The origin is fixed at the center of the pellets at point S ensuring

a consistent frame of reference, and facilitating inter-experimental comparisons (Fig. 5.10 left). The channel edges rotate at angular velocity $\omega = 0.4\,\mathrm{s}^{-1}$, with no-slip boundary conditions applied on all channel and boat surfaces. The remaining boundaries consist of the top surface, where the flow field is prescribed based on experimental measurements, and the exit edge where we chose the less restrictive condition and imposed a constant pressure, lower than inside the channel, ensuring all the flow is exiting (Fig. 5.10 left). As for the case of a fixed and mobile source, a finer mesh is defined at the edge and inside the boat, and a boundary layer is defined below the surface (Fig. 5.10 right). Solving the Navier-Stokes equation provides the 3D flow fields around the boat and the stress at the interface. To invert the stress field and obtain an absolute value of the surface pressure field we impose that $\Pi = 0$ at the entry edge as we expect that the water upstream should be almost free of surfactant[4].

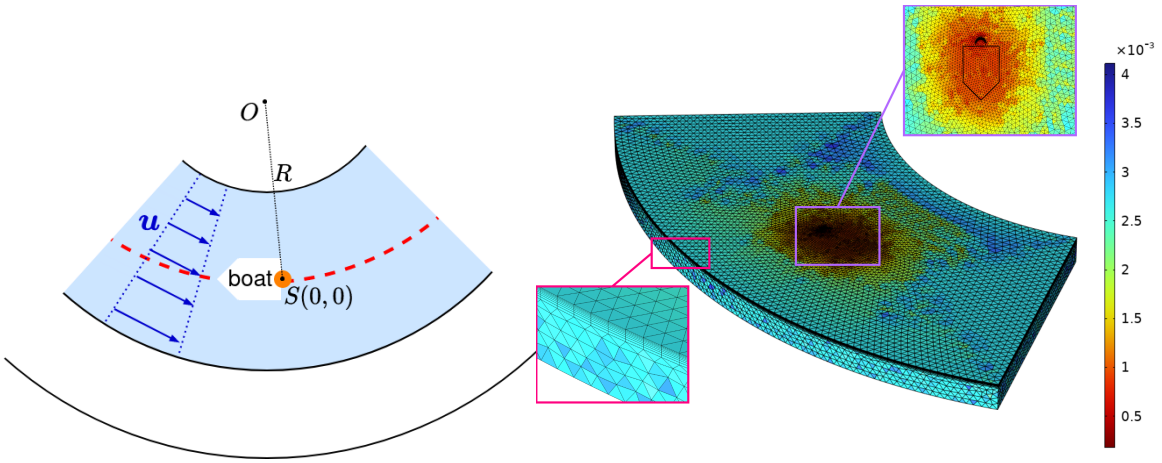

Figure 5.10: **Finite element methods for camphor boat.** (Left) Top view of the geometry used to compute the 3D flow field from the 2D experimental flow around a camphor boat. The origin is placed at the center of the pellet at point S. 1D profiles are plotted according to the red dashed line, for $R = 15.0 \pm 0.1\,\mathrm{cm}$. (Right) Mesh used for finite element method. The color indicates the size of the element. Zoom on the two boundary layers, around the boat and below the water surface.

Surface pressure across the boat. From the surface stress, we obtain the 2D surface pressure field around the boat (Fig. 5.11 left). To the best of our knowledge, this is the first experimental characterization of the 2D surface pressure field around a mobile source of surfactant. We observe concentric circular isobars with a larger surface pressure close to the camphor pellet. To determine precisely the difference of surface pressure $\Delta\Pi$ between the front and the rear of the boat, we consider a circular cut passing by the boat at $R = 15.0 \pm 0.1\,\mathrm{cm}$ (Fig. 5.10 left, dashed red line). An average on four different camphor boats gives $\Delta\Pi = 2.7 \pm 0.3\,\mathrm{mN\,m^{-1}}$ (Fig. 5.11 right). These results are consistent with those reported by Nomoto *et al.* where for a boat moving at $6\,\mathrm{cm\,s^{-1}}$, $\Delta\Pi = 2.5 \pm 0.5\,\mathrm{mN\,m^{-1}}$[48], confirming the reliability of our measurements.

[4]As camphor is volatile at room temperature, we expect that after a full tank rotation, the concentration of camphor at the interface is almost negligible. This hypothesis is confirmed as the wake shape and force balance do not change across several tank rotations.

1D profile. For a more detailed comparison, we consider the 1D velocity and surface pressure profile along the $R = 15.0 \pm 0.1\,\mathrm{cm}$. The position along the line is defined by the curvilinear coordinate s. The gradient of surface pressure generates Marangoni flows whose velocity decays from $u = \pm 6 \pm 1\,\mathrm{cm\,s^{-1}}$ right behind the boat to zero 5 cm away (Fig. 5.12 left). The error bar corresponds to the noise estimate in the previous subsection on the velocity field, $1\,\mathrm{cm\,s^{-1}}$ close to the boat and $0.5\,\mathrm{cm\,s^{-1}}$ farther away. The surface pressure profile is also qualitatively and quantitatively similar with a maximal value of $2.7 \pm 0.3\,\mathrm{mN\,m^{-1}}$ in our experiments decaying over 2.5 cm behind the boat slightly faster than in the work of Nomoto *et. al* where it decays over $3 \pm 1\,\mathrm{cm}$ (Fig. 5.12 right). The error bars are estimated from the numerical validation where for a sampling interval of 2 mm and a noise level of $1\,\mathrm{cm\,s^{-1}}$ the difference from the imposed pressure field was below $0.4\,\mathrm{mN\,m^{-1}}$. Farther from the camphor pellet the noise level drops to $0.5\,\mathrm{cm\,s^{-1}}$ leading to an error below $0.2\,\mathrm{mN\,m^{-1}}$. This experimental validation confirms the efficacy of our method, as it demonstrates similar differences in surface pressure across a camphor boat and observes a comparable behavior of the surface pressure profile behind the boat. Furthermore, our approach provides an error and noise level significantly lower than previous experimental measurements of surface pressure and flow field with quasi-elastic light scattering.

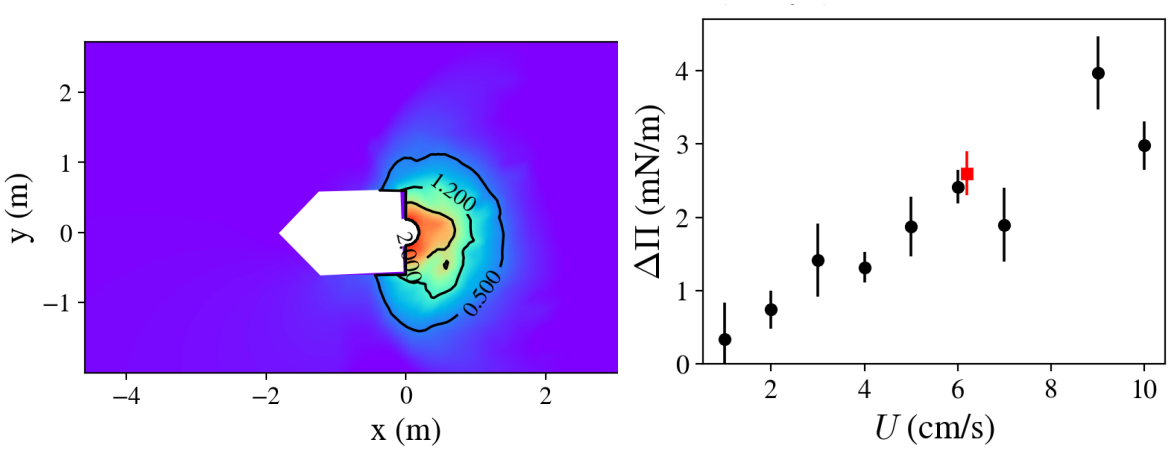

Figure 5.11: **Surface pressure around a Marangoni boat.** Characterization of the surface pressure field around a Marangoni boat, kept fixed with a water flow with velocity of $6\,\mathrm{cm\,s^{-1}}$. (Left) 2D surface pressure field reconstructed from the interfacial flow field measured experimentally. The colormap indicates the value of the surface pressure and the black lines the isobars. The flow is going from left to right. (Right) Surface pressure difference across a Marangoni boat measured by Nomoto *et al.* [48] (black circles) and by us (red square).

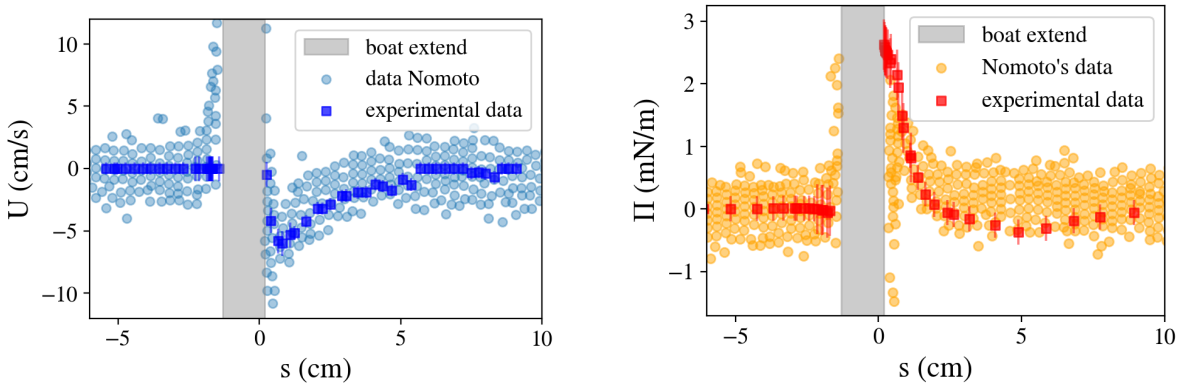

Figure 5.12: **1D velocity and surface tension profile across a Marangoni boat.** Comparison of our experimental data with that of Nomoto along a 1D circular cut at the center of the channel *et al.* [48]. The angular rotation speed of the tank is $0.4\,\mathrm{s}^{-1}$, generating a flow with a velocity of $U = 6\,\mathrm{cm\,s}^{-1}$ at the center of the channel. The grey area indicates the extent of the boat, with positive abscissa corresponding to positions downstream relative to the boat. (Left) Norm of the velocity in the flow frame of reference, i.e., swimmer moving at $\mathbf{V} = -\mathbf{U}$. Our experimental measurements are shown with solid black squares, while data from Nomoto *et al.* are represented by light blue circles. (Right) Surface pressure values, with our data shown as black squares and Nomoto as light orange circles.

5.5 Conclusion

A full description of a Marangoni swimmer propelling at the air-water interface involves characterizing the hydrodynamics and the surfactant distribution. Since surfactants are difficult to visualize, their presence and spatial distribution are typically inferred from indirect measurement. Thus surfactants remain as "hidden variables" in almost all experiments [87]. One way to study the distribution of surfactant is to access it indirectly through surface tension measurement, which is difficult in the case of a Marangoni swimmer. In this chapter, we presented a new method that provides the 2D surface tension distribution from the velocity field. This method involves experimental measurement of the interfacial flow field using PIV and Optical Flow techniques, followed by finite element methods to solve the Navier-Stokes equations and compute the interfacial stress. Finally, integrating the Marangoni boundary condition (Eq. (5.1)) yields the 2D surface tension field.

We first validated the approach numerically, with an arbitrary distribution of surface tension and the generated flow field. This provides a lower bound for the numerical error of $0.03\,\mathrm{mN\,m}^{-1}$. This step highlighted the method sensitivity to discontinuities in the stress field (in our case between the source edge and the surface) leading to larger error at the source edge. This could be avoided by removing the first meshes before inverting the field. Subsequent tests with finite sampling and noise in the flow field demonstrated that our method performs well up to a noise level of $1\,\mathrm{cm\,s}^{-1}$ and a resolution of 2 mm with a maximal error below 15% on the imposed surface pressure. Even under less ideal conditions, the surface pressure field remained qualitatively acceptable, with errors not exceeding 25%. Given the absence of reference measurement for the surface tension around

a Marangoni swimmer, we considered the related case of a Marangoni boat for which the 1D surface tension profile across the boat was obtained by Nomoto *et. al* [48]. We obtained the 2D surface tension field around a camphor boat and measured profiles that are comparable qualitatively and to some extent quantitatively. Taken together, the results obtained in this chapter provide strong evidence that our method allows to infer a whole field of local surface pressure.

Compared to previous attempts [48, 68], our approach presented is based on easily accessible experimental and numerical tools. The main limitation of this technique is the need for a high-quality experimental velocity field, particularly with data points close to the source edge. It may require manually tracking some particles in areas where automatic treatment may fail and increase the time for data treatment. Overall our approach is versatile and can be applied to various experimental problems such as the surfactant spreading from a fixed source, analyzing the stability of thin films and foams, and evaluating the interactions between Marangoni swimmers by assessing the surfactant field.

5.6 Appendices

Fixed source surface pressure field

To assess the impact of the noise on the interfacial velocity field, we first study the simple case of an axisymmetric fixed source of surfactant. The imposed surface pressure distribution is given by equation (5.6). Specifically, the velocity vectors are sampled every 0.1, 1, 2, or 4 mm, and this distance will be referred as d_s. The noisy vector $\mathbf{u}_{\text{noisy}}$ is obtained by adding a noise with amplitude ϵ of 10^{-4}, 0.1, 0.5, or 1 cm s^{-1}. Applying our method to these noisy vector fields provides surface pressure fields with similar features as the imposed one (Fig. 5.3). The isobars are concentric circles with a maximal value around 2.5 mN m^{-1} at the edge of the source (Appendix. 5.1). The reconstruction is faithful up to a noise level of 1 cm s^{-1} and a sampling distance of 0.2 mm.

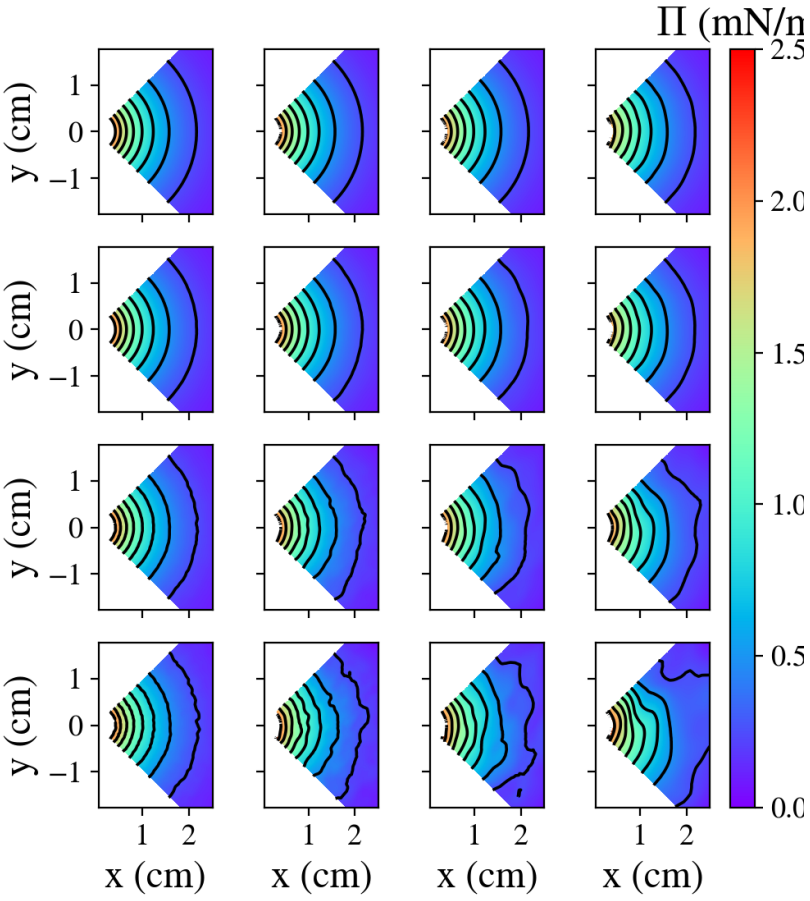

Appendix 5.1: **Reconstruction of the surface tension around a fixed source of surfactant from a numerical interfacial flow field** Field of surface tension obtained by integrating the stress around a source releasing surfactant with $\gamma_s = 2$ mN m^{-1}. The columns correspond to sampling distance of 0.1, 1, 2, or 4 mm. The lines to a noise level of 10^{-4}, 0.1, 0.5, or 1 cm s^{-1}. The colormap indicates the value of the surface pressure and the black lines evidence isobars.

Mobile source surface pressure field without noise

We consider a mobile source of surfactant with a given surface pressure distribution which remains the same for all advection speeds. Therefore, the inferred surface pressure field should be the same for all advection. However, we observe differences (Fig. 5.2 left). The isobars seem to drift toward the rear of the swimmer and the maximal value downstream increases. Computing the error map with respect to the imposed surface pressure shows an increase in the difference with the advection speed (Fig. 5.2 center). The maximal value of the error is located downstream at the edge of the source and goes from $0.04\,\mathrm{mN\,m^{-1}}$ for $U = 5\,\mathrm{cm\,s^{-1}}$ to $0.125\,\mathrm{mN\,m^{-1}}$, 10% of the expected value, for $U = 12\,\mathrm{cm\,s^{-1}}$. The error obtained is way too high for a reference case, where no degradation was done on the interfacial velocity field.

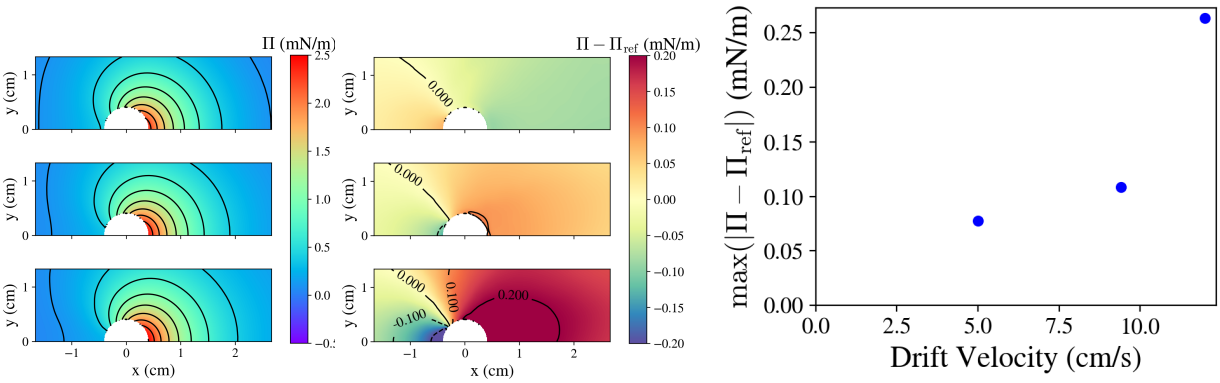

Appendix 5.2: **Reconstruction of the surface pressure field around a mobile source from a numerical velocity field without noise.** Inverting the complete stress field leads to a large error in the inferred surface pressure. From top to bottom the advection velocity increase 5, 9.4 and $12\,\mathrm{cm\,s^{-1}}$. (Left) Surface pressure field around the source, the black lines indicate isobars. (Center) Difference between the computed surface pressure field Π and the imposed one Π_{ref} . (Left) Maximal error measured.

Passive disc

Using finite element simulation we can also consider a passive disc of 4 mm not releasing any surfactants. In this case, the stress should be non-zero only below the disk in the boundary layer [98]. However, we observe that the stress spreads at the surface at a distance d of the source edge, corresponding to 1% of the disc radius (Appendix. 5.3). The spreading of the stress at the interface is a purely numerical artifact due to the strong discontinuity between the disc edge and the water surface. Inverting the stress field will give a non-zero surface pressure value around the disc even if no surfactants are released. To avoid this issue, we will consider the stress field at a distance d of the swimmer edge for integration.

Mobile source surface pressure field with noise

Now that we have evaluated the lower bound of the error $0.03\,\mathrm{mN\,m^{-1}}$ for the reference solution, we evaluate the capability of the inversion method to reconstruct the surface

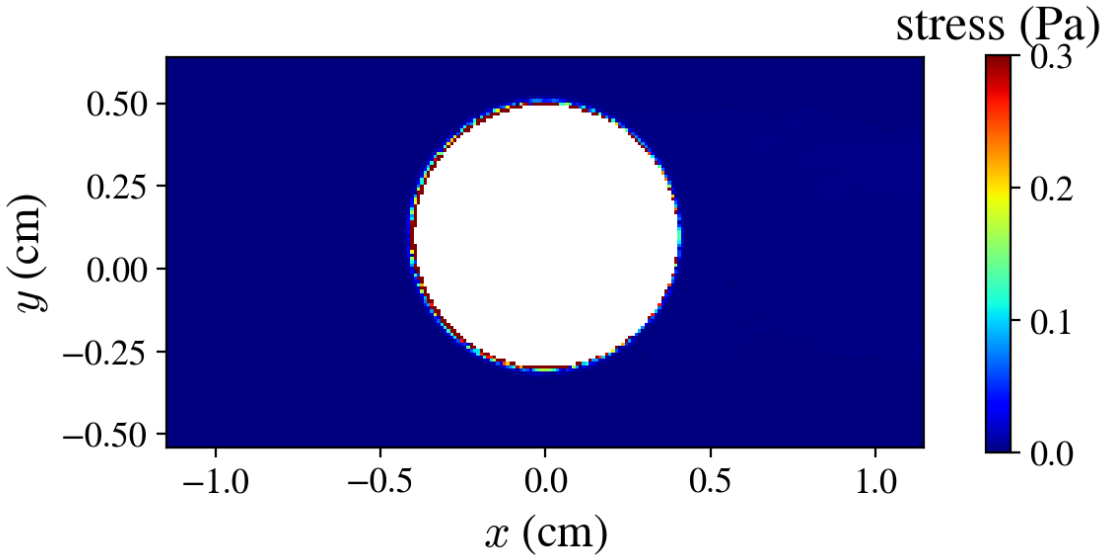

Appendix 5.3: **Stress field around a passive disc.** Stress field obtained with finite element method around a passive disc of 4 mmnot releasing surfactants.

pressure field from a velocity field closer to experimental conditions. To do so, reference surface flow is deteriorated through finite sampling and noise. Velocity vectors are sampled at intervals d_s of 0.1, 1, 2, or 4 mm, and a Gaussian noise ϵ of 10^{-4}, 0.1, 0.5, 1, or 2 $\mathrm{cm\,s^{-1}}$ is added. To account for the discontinuity of the stress field near the swimmer edge, we consider only the stress data after a distance $d = 0.05 \times a$ from the swimmer.

The obtained surface pressure fields qualitatively match the imposed one with the maximal values around 2.5 $\mathrm{mN\,m^{-1}}$ and the isobars remaining close to circular up to a noise level of 1 cm/s and a sampling interval of 0.2 mm (Appendix. 5.4). The map difference between the inferred surface pressure field and the imposed one shows that the maximal error is located downstream at the edge of the swimmer. Even in the most deteriorated situation, the error remains below 0.4 $\mathrm{mN\,m^{-1}}$ which corresponds to 15% of the maximal value. These explorations on artificial data state an optimal ground for the noise and sampling distance allowed on the experimental surface flow to infer faithfully the surface pressure field.

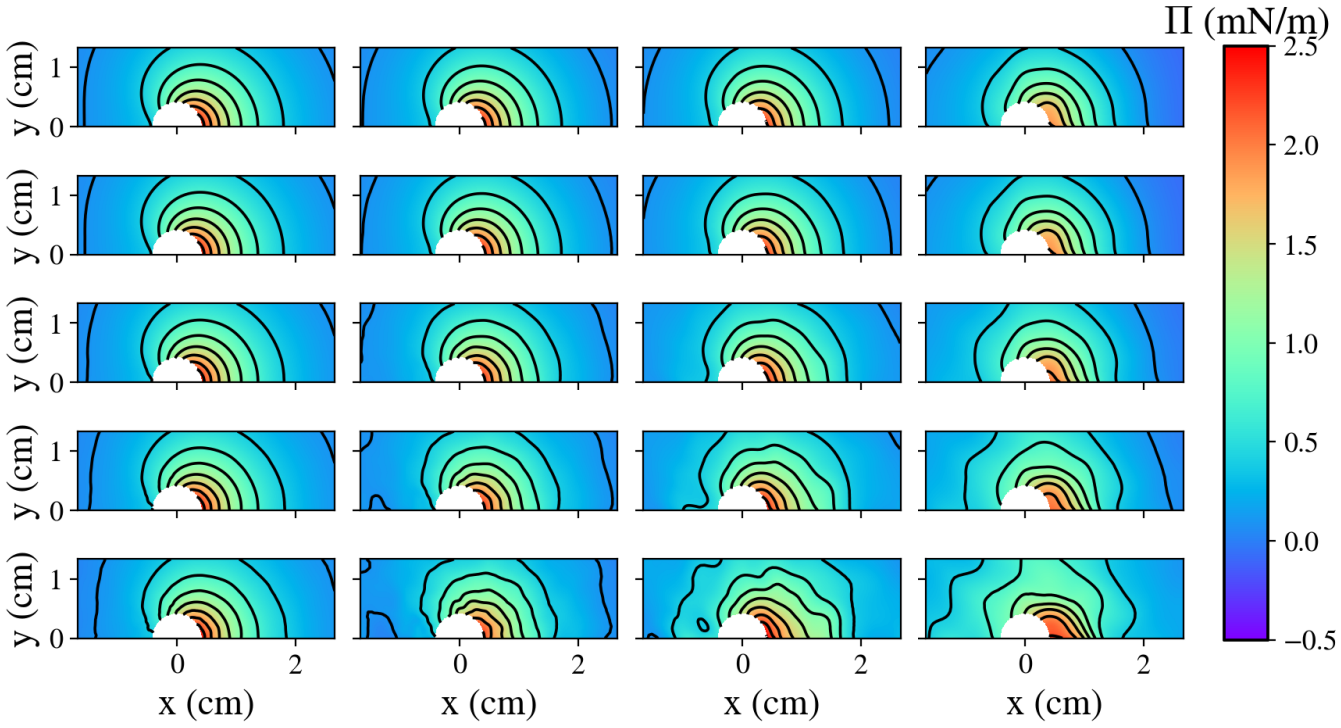

Appendix 5.4: **Reconstruction of the surface pressure around a mobile source of surfactant from a numerical interfacial flow field.** Field of surface tension obtained by integrating the stress around a source releasing surfactant with $\gamma_s = 2\,\mathrm{mN\,m^{-1}}$ for an advection $U = 5\,\mathrm{cm\,s^{-1}}$. The columns correspond to sampling of the surface velocity field 0.1, 1, 2, or 4 mm. The lines to an increasing noise of 10^{-4}, 0.1, 0.5, 1 or $2\,\mathrm{cm\,s^{-1}}$. The colormap indicates the value of the surface pressure and the black lines evidence isobars.

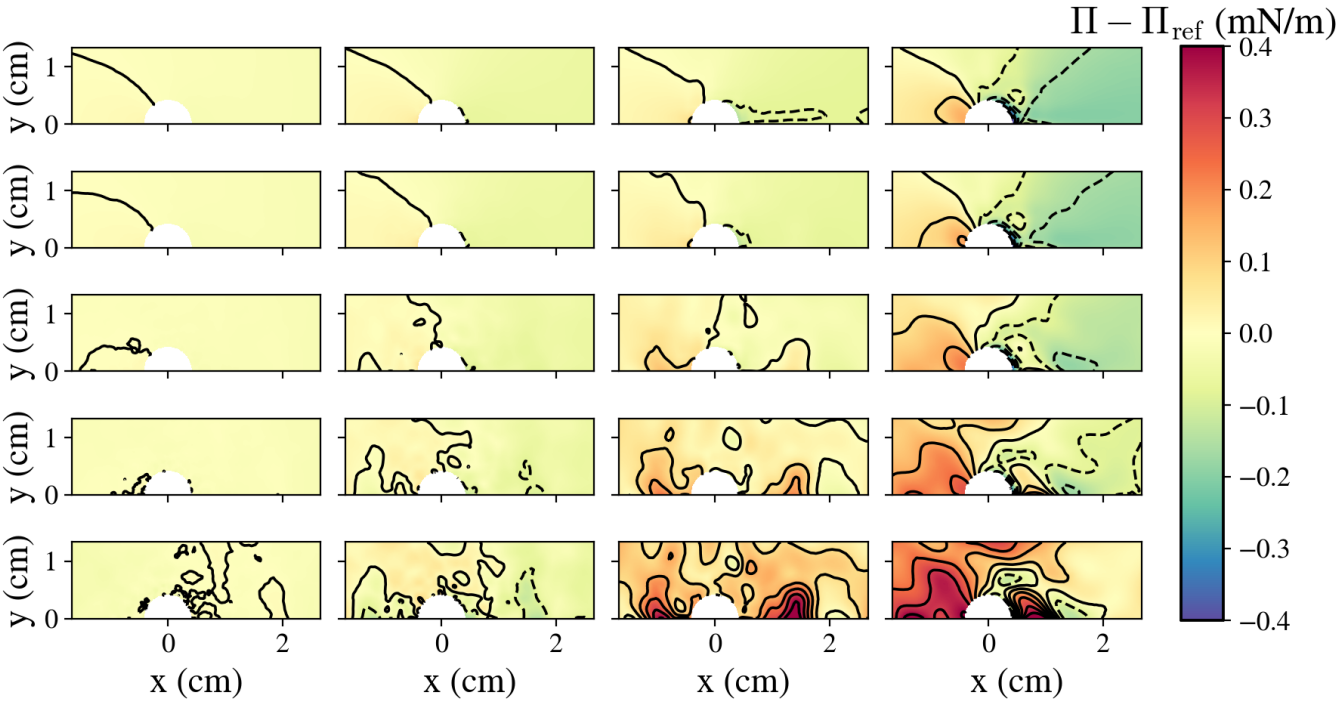

Appendix 5.5: **Error between the reconstructed pressure field and the imposed one for a mobile source of surfacant** Field of surface tension obtained by integrating the stress around a source releasing surfactant with $\gamma_s = 2\,\mathrm{mN\,m^{-1}}$ for an advection $U = 5\,\mathrm{cm\,s^{-1}}$. The columns correspond to sampling of the surface velocity field 0.1, 1, 2, or 4 mm. The lines to an increasing noise of 10^{-4}, 0.1, 0.5, 1 or $2\,\mathrm{cm\,s^{-1}}$. The colormap indicates the difference between the imposed surface pressure field and the black lines evidence isobars.

Chapter 6

Surface tension around a camphor swimmer

Table of Contents

6.1 Introduction

In the previous chapters, we embarked on a detailed experimental study of Marangoni swimmers. In contrast to earlier work, where only a few quantitative observables such as swimming speed [24] or the flow field at the swimming velocities could be measured [83, 84, 86], we have considered the force balance and the flow field around a Marangoni swimmer at various advection speeds, not just the swimming velocity. To fully describe a Marangoni swimmer, the remaining unknown is the surface tension field around the swimmer which is crucial for understanding the generated flow field and propulsion force.

In this chapter, we use the method presented in Chap. 5 to reconstructs the surface tension field from the interfacial flow around a Marangoni swimmer. To briefly recall the different steps involved, the process requires: (*i*) obtaining the interfacial flow field using standard optical techniques such as PIV and optical flow [102, 104, 138], (*ii*) using finite elements to solve the Navier-Stokes with appropriate boundary conditions to obtain the 3D flow and interfacial stress field; (*iii*) integrating the Marangoni stress boundary condition to infer the surface tension field. The approach was validated on numerical and experimental data [48], demonstrating that the reconstruction of the surface tension field is reliable up to a noise level of $1\,\mathrm{cm\,s^{-1}}$ and a sampling distance of 2 mm for the interfacial flow.

In the following, we apply the developed approach to obtain the surface tension field around a symmetric interfacial Marangoni swimmer, the system considered throughout this PhD. We remind the reader that we will consider the surface pressure field, Π, defined as $\Pi(x, y) = \gamma_w - \gamma(x, y)$, where γ_w represents the surface tension of water. From this surface pressure field, and using an equation of state, one can deduce the concentration of camphor. Unlike previous studies on the camphor boat, we explore flow velocity distinct from the swimmer spontaneous velocity and examine the influence on the surface pressure field and surfactant distribution. To the best of our knowledge, this is the first experimental characterization of the 2D surface pressure field around a symmetric source of surfactant. Finally, we integrate the surface pressure along the swimmer contour to estimate the resulting capillary force.

6.2 Surface pressure and concentration fields

The methodology for measuring the interfacial flow field (Chap. 4, page 69) and reconstructing the surface pressure field (Chap. 5, page 83) has been introduced in previous chapters. Before discussing the results obtained for symmetric swimmers at varying advection, we first provide additional specific details regarding the experimental procedure used in this study.

6.2.1 From the flow field to the surface pressure

Experimental protocol. The experimental protocol is the same as the one used to determine the flow field around a swimmer (Chap. 4). The swimmer swims for 9 min in a first tank to reach a swimming velocity of $7 \pm 1\,\mathrm{cm\,s^{-1}}$. It is then attached to a rigid capillary to maintain its position and the tank rotates at angular velocity ω generating a flow field $\mathbf{u}_{\text{solid}} = \boldsymbol{\omega} \times \mathbf{r}$. In the following, the advection speed is defined by the

ratio $\chi = U/V$ where U is the flow velocity at the center of the channel and V is the spontaneous swimming velocity in a quiescent liquid. Once the swimmer is attached, several acquisitions are taken with different lighting to image the whole flow field. We consider only one advection speed for each swimmer, to maintain the experimental time short, typically below 2 min, so that the swimming velocity remains constant. Therefore, each surface pressure field presented in the following was obtained for a different swimmer or advection speed. The water surface is sucked between each swimmer for cleaning and the water level is refilled if needed.

Flow field and noise level. We have previously presented how to obtain the flow field around a Marangoni swimmer combining particle image velocimetry (PIV) and optical flow (OF) (Chap. 4 page 69). The numerical validation of the inversion method shows that noise in the velocity field significantly impacts the quality of the reconstructed surface pressure. The reconstructed surface pressure field was reliable up to a noise level of $1\,\mathrm{cm\,s^{-1}}$ and a sampling interval of 2 mm (Subsec. 5.3.3 page 92). To evaluate the noise on the experimental velocity field, we consider each technique used. First, for the PIV data, we compute the standard deviation between vector fields of each image pair, keeping only one pair every ten images to ensure data independence. This method allows to map the noise levels outside the wake, with maximal values typically around 0.5 cm/s. Regarding the optical flow data, after interpolating them onto the PIV grid, we compute residuals between the original velocity data and their interpolated counterparts at corresponding positions. The noise level is similar to PIV, typically around 0.5 cm/s far from the swimmer and 1 cm/s below 5 mm from the swimmer edge. These noise levels correspond to the range where we have evaluated our approach to perform well, so we expect to reliably reconstruct the surface pressure field.

Finite element methods in practice. The numerical step to obtain the interfacial stress relies on finite elements methods, carried out with Comsol. The numerical domain replicates the experimental situation: a circular channel with inner and outer radii of 10 cm and 20 cm respectively filled with 1 cm of water. We do not model the full tank and consider only an angular sector of $\pi/3$ which appears sufficient to capture the flow around the swimmer and allows reducing computation time. The origin is fixed at the swimmer center, ensuring a consistent frame of reference and facilitating inter-experimental comparisons (Fig. 6.1). As always, the swimmer is flat with zero thickness. The channel edges rotate at a given angular velocity, with no-slip boundary conditions applied on all channel and swimmer surfaces. The remaining boundaries consist of the top surface, where the flow field is prescribed based on experimental measurements, and the exit edge where we chose the less restrictive condition and imposed a constant pressure, lower than inside the channel, ensuring all the flow is exiting. A finer mesh is defined near the edge and inside the disc, and a boundary layer is defined below the surface (Fig. 6.1). Solving the Navier-Stokes equation provides the 3D flow fields, as well as the stress at the interface.

Surface pressure from the stress field. Using finite element methods, we obtain the 3D flow and interfacial stress fields around the swimmer. To invert the stress field and obtain an absolute value of the surface pressure field, we impose that $\Pi = 0$ at the entry edge, as we expect the water upstream to be almost free of surfactant. Such an

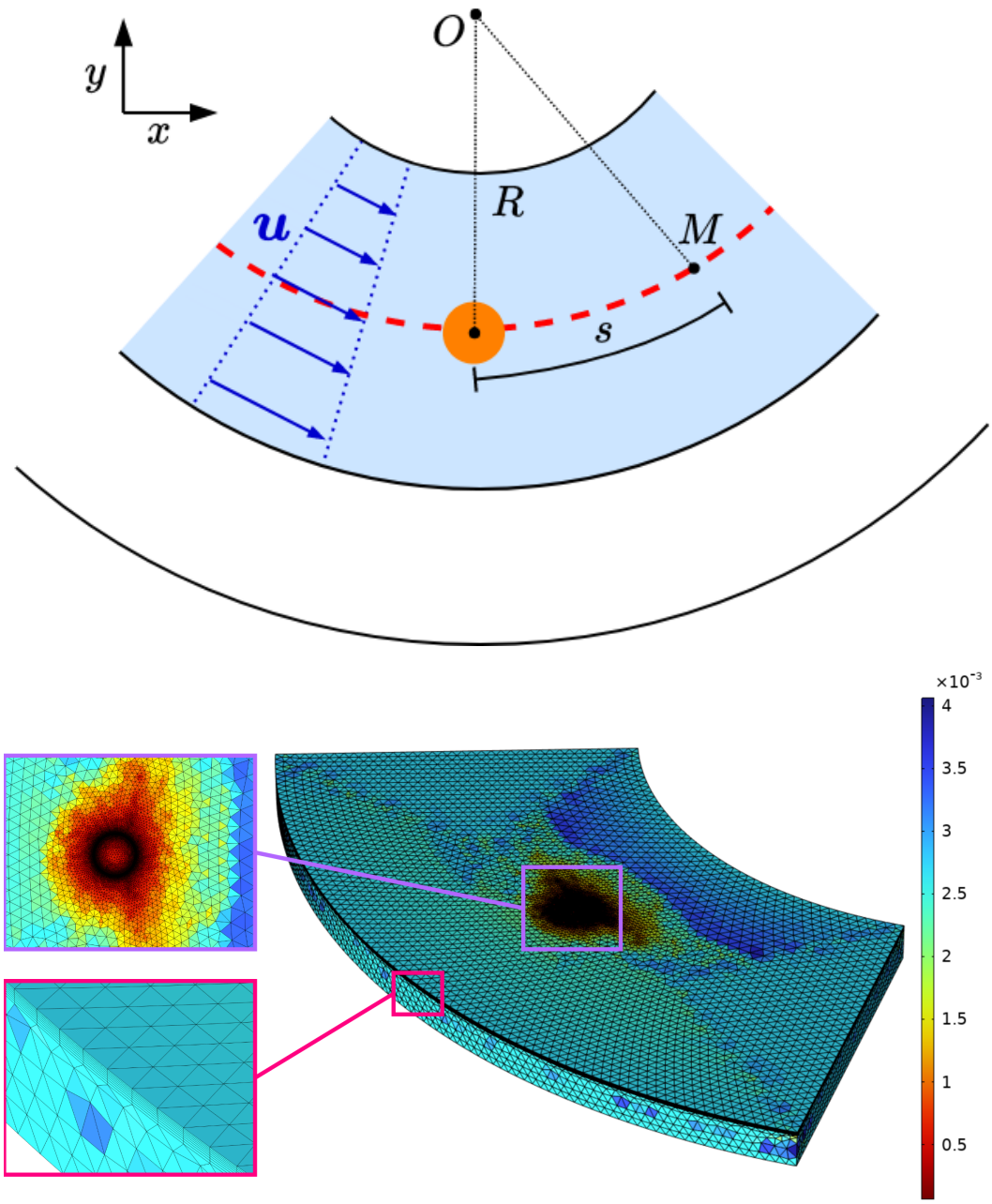

Figure 6.1: **Geometry and mesh used in finite element calculation.** Geometry of the system for finite element methods. (Top) Top view, the swimmer is placed at the center of a 10 cm wide channel at $r = R = 15$ cm from the tank center. The red dashed line defines an arc with $r = R$. (Bottom) Mesh used for finite element computation. The color indicates the size of the elements. Zoom on the boundary layers around the swimmer (purple) and under the interface (pink).

assumption is supported by the fact that the separatrix, flow field, and force measured remain constant throughout several tank rotations.

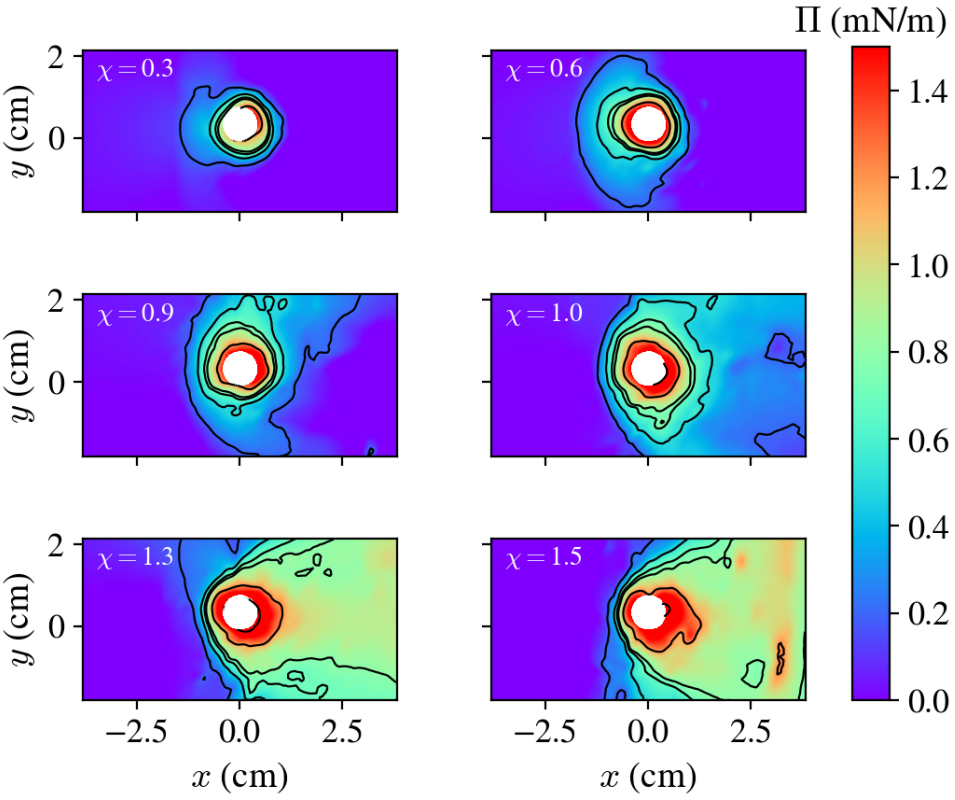

Figure 6.2: **Surface pressure field around a Marangoni swimmer.** Reconstruction of the surface pressure field around six different swimmers (white circle) from the interfacial flow field measured experimentally. The flow goes from left to right and the advection speed is indicated in the top left corner. The color bar indicates the surface pressure value and the black line evidence isobars of 0.2, 0.5, 0.7, 0.8, 1.2, and 2 mN m^{-1}.

Surface pressure field. We now move to the core results of this study: the first experimental characterization of the surface pressure field around a Marangoni swimmer for different advection speed. To the best of our knowledge, until now only theoretical and numerical studies proposed a distribution of the surface pressure around a moving source of surfactant and considered Stokes flow [25, 31] or shallow water condition [139]. In the following, we discuss the evolution of the surface pressure distribution with respect to advection. For low advection speeds ($\chi < 0.7$), the surface pressure increases almost symmetrically around the swimmer, with a large extension in front and isobars around the swimmer appearing as concentric circles (Fig. 6.2 top). As advection becomes stronger, the surface pressure shifts downstream, and the extension upstream decreases (Fig. 6.2 middle). Finally, for large advection speed ($\chi > 1$) the isobars are no longer circular and extend into the wake with a parabolic shape. The extension upstream continues to decrease, and the isobars get closer to each other showing a large gradient upstream.

Reproducibility. Each surface pressure field was obtained for a different swimmer (Fig. 6.2). As the spontaneous swimming velocity of each swimmer can vary, so does the generated flow field and the reconstructed surface pressure field. The reproducibility of the flow field have been discussed earlier (Fig. 4.10, page 80). For each advection speed,

three different swimmers were studied leading to three surface pressure fields. To evaluate the reproducibility of the surface pressure field we compute the standard deviation between the surface pressure field (Fig. 6.3). The maximal value of the standard deviation is 0.35 mN m^{-1} and the average value is bellow 0.1 mN m^{-1} for all advection. Both values are consistent with the error due to the sampling distance and noise on the velocity field, 0.3 mN m^{-1} close to the swimmer and 0.1 mN m^{-1} elsewhere. These results confirm the reliability of our experimental approach in capturing the surface pressure field dynamics.

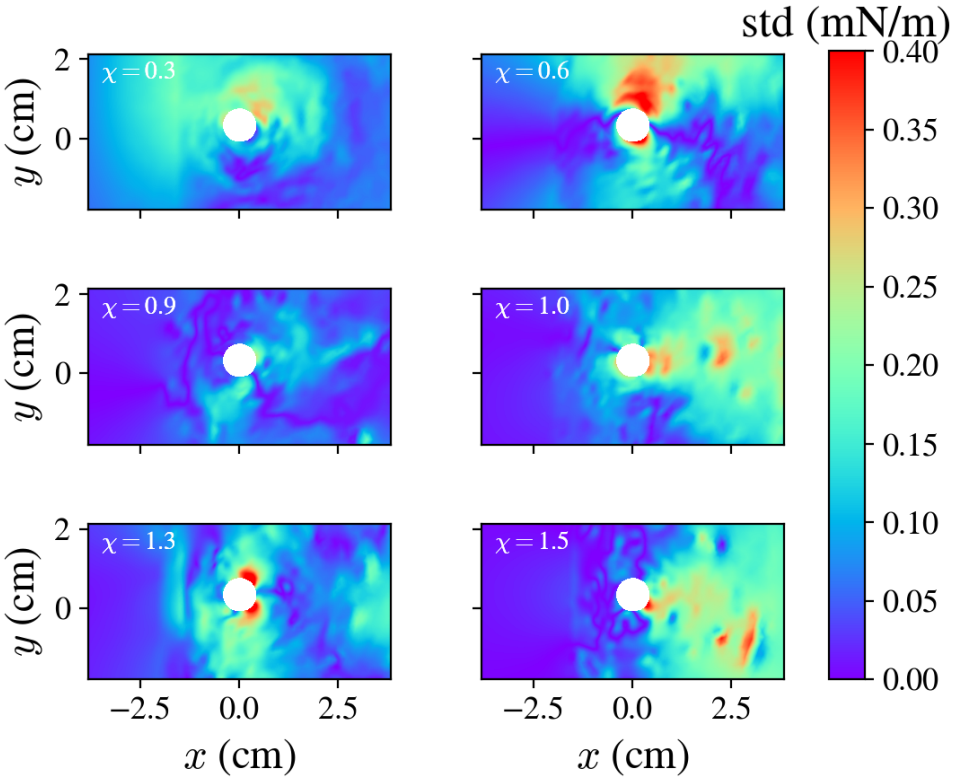

Figure 6.3: **Reproducibility of the surface pressure field.** Standard deviation from the mean surface pressure field between three different swimmers at the same advection speed. The swimmer is the white circle and the color map corresponds to the standard deviation.

1D surface pressure profile. To better evaluate the extension of the surface pressure field we consider the 1D surface pressure profile around the swimmer. To do so, we define a circle cut with radius $r = R = 15$ cm (Fig. 6.1 top, red dashed line). The position of a point M on this line is defined by the curvilinear coordinate s, with s<0 corresponding to an upstream position and $s > 0$ to downstream. As visible in Fig. 6.4 left, when the flow velocity increases the upstream extension of the surface pressure field decreases from 5 cm away from the swimmer edge to less than 1 cm. Conversely, the downstream value increases with the flow velocity from 0 to 1 mN m^{-1}, 2.5 cm away from the swimmer edge. For $s > 3$, the surface pressure values remain constant. The shape of the separatrix similarly remains constant for $s > 3$ (Fig. 4.8 page 78). The observed behavior can

be attributed the chemical wake starting to feel the channel edges, preventing it from expanding laterally any further.

Maximal value at the swimmer edge. Plotting the maximal value of the surface pressure at the swimmer edge upstream and downstream confirms that the maximal value is always downstream leading to upstream swimming (Fig. 6.4 right). The error bars are estimated from the numerical exploration which shows that the error is $0.3\,\mathrm{mN\,m^{-1}}$ close to the source and $0.1\,\mathrm{mN\,m^{-1}}$ away for a sampling of 2 mm and a noise respectively of $1\,\mathrm{cm\,s^{-1}}$ and $0.5\,\mathrm{cm\,s^{-1}}$ (Sec. 5.3). When the flow velocity increases the gap between upstream and downstream increases and is maximal around $\chi \sim 0.9$. Then the gap and the maximal value decrease.

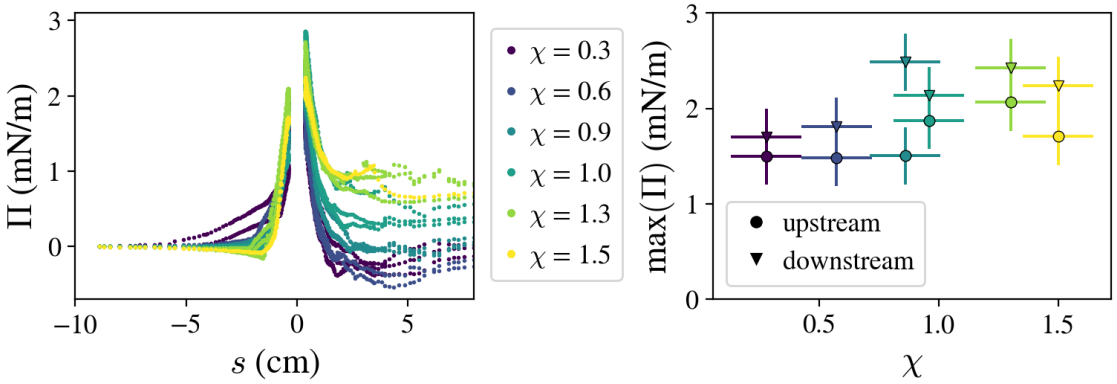

Figure 6.4: **1D surface pressure profile.** Longitudinal profile of surface pressure along the radius $r = R = 15\,\mathrm{cm}$. The color indicates the advection speed. (Left) 1D surface pressure profile. Each curve corresponds to a different swimmer. (Right) Maximal value of the surface pressure at the swimmer edge, upstream (circle) and downstream (triangle). Each pair of points corresponds to a different swimmer.

6.2.2 Concentration of surfactant

Up to this point, we have demonstrated that the mechanics of the system allow us to reconstruct the surface pressure from the surface flow, and we have presented the corresponding results for different advection. However, in many cases, it is desirable to go one step further and determine the surface concentration of the surfactant. Achieving this requires additional information, specifically in the form of a surfactant equation of state, which relates the surface pressure to the surfactant concentration. For a soluble surfactant, this relationship becomes crucial in accurately determining the concentration field at the interface.

Concentration from the surface pressure field. From the surface pressure we can compute the surfactant concentration Γ at the interface. For a soluble surfactant, the surface pressure relates to the bulk concentration c, and a general formula can be deduced from the Gibbs equation:

$$\Gamma = \frac{a}{\mathcal{R}T}\left(\frac{\partial \Pi}{\partial a}\right)_{T,p}, \tag{6.1}$$

where a is the activity of the solute, $\mathcal{R}$ is the gas constant ($8.31\,\mathrm{J\,mol^{-1}\,K^{-1}}$), T is the absolute temperature ($297 \pm 2\,\mathrm{K}$ in our experiments) and p is the pressure. Here, as the surface pressure is small, we are far from the saturated concentration and $a \sim c$ [52]. Assuming $\Gamma = K_H c$ with K_H the Henry isotherm coefficient, in that case, the surface pressure increases linearly with the surface concentration:

$$\Pi = \mathcal{R}T\Gamma. \tag{6.2}$$

Equation (6.2) can be seen as analogous to the two-dimensional form of the perfect gas law, where the surface pressure plays a role similar to that of pressure in the three-dimensional case.

Concentration field. Building on the derived surface concentration, we now analyze how the concentration field evolves under varying levels of advection (Fig. 6.5). At low advection ($\chi < 0.6$), the concentration field is close to circular with a slightly larger extension upstream (Fig. 6.5 top). Increasing advection breaks the symmetry and the value and the extent of the concentration field become much larger downstream going from $\Gamma = 0$ for $\chi = 0.3$ to $0.5\,\mathrm{\mu mol\,m^{-2}}$ for $\chi = 1.5$, $2.5\,\mathrm{cm}$ away from the swimmer (Fig. 6.5 middle and bottom). A surprising observation is the increase in surfactant quantity in the wake of the swimmer. There are two possible explanations for this:(i) the camphor release rate is not constant, and increases with the flow velocity, (ii) increasing advection decreases the diffusion in the bulk. In the following paragraph, we discuss these hypotheses.

Relevance of the constant flux hypothesis. One of the main assumptions used in models for camphor swimmers is the constant release rate of camphor [24, 52, 62, 82]. However, this assumption is not straightforward. For instance, in the case of a heat source with constant temperature in a flow, large advection leads to a higher temperature gradient between the fluid and the source, resulting in increased heat transfer and flux. Similarly, one could imagine that camphor dissolves more easily in water free of any surfactant; therefore, increasing advection leads to a fast flow of clean water, resulting in a larger amount of camphor being released. Such an effect would be obvious in the case of a solid camphor disc directly in contact with water. However, in our case, camphor is embedded in a solid matrix gel. The constant flux assumption implies that the diffusion rate from camphor to the gel and from the gel to the water are equal. Our measurements may suggest that the actual boundary conditions governing camphor release might be more intricate than the simple model of constant flux.

Advection-diffusion of camphor. When advection increases camphor has less time to diffuse in the bulk leading to a larger amount of camphor at the interface. The characteristic distance ϵ a molecule diffuses in time t is given by $\epsilon = \sqrt{2Dt}$, where D is the diffusion coefficient. Here, the time t is also the time it takes for a camphor molecule emitted at the swimmer edge to reach a distance d behind the swimmer $t = d/U$. At $5\,\mathrm{cm}$ from the swimmer edge, for the smallest advection $U \sim 1\,\mathrm{cm\,s^{-1}}$, $\epsilon \sim \sqrt{10D}$. In contrast, for a higher advection speed $U \sim 1\,\mathrm{cm\,s^{-1}}$, $\epsilon \sim \sqrt{1D}$, so the diffusion of camphor in the bulk for the largest advection is about three times lower. A simple order of magnitude

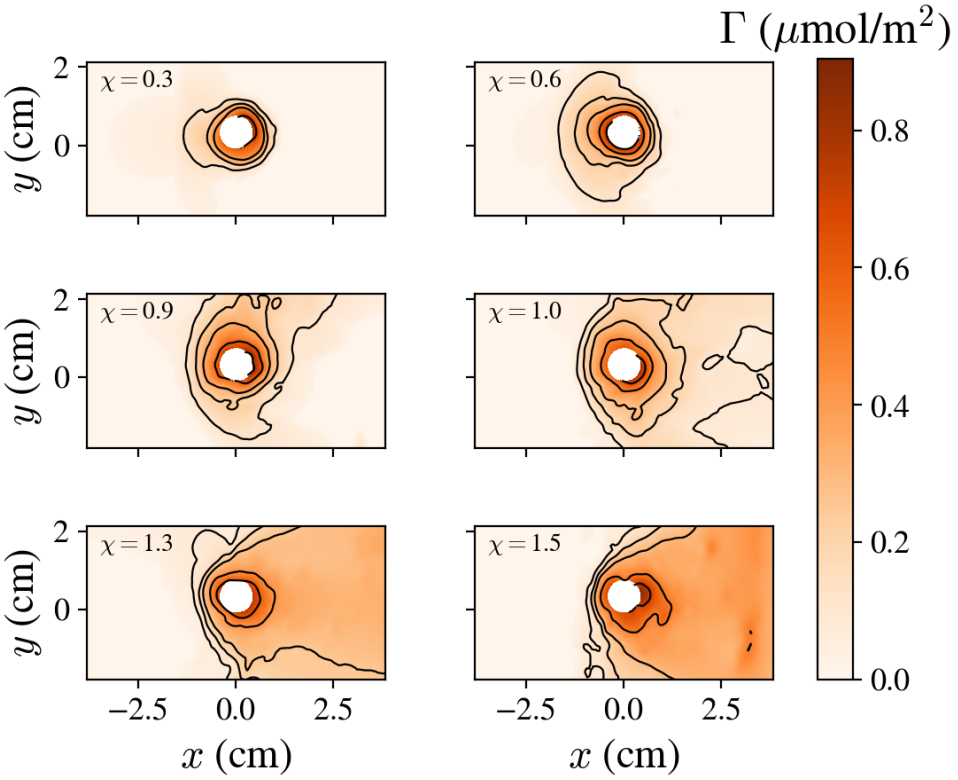

Figure 6.5: **Surface concentration around a Marangoni swimmer.** Concentration of camphor around 6 different Marangoni swimmers (white circle). The concentration is derived from the surface pressure field (Fig. 6.2) using Eq. (6.2). The color bar indicates the concentration value and the black line evidence iso-concentration of 0.1, 0.2, 0.3, 0.5, and 0.7 µmol m^{-2}.

estimate confirms our assumption: increased advection limits the diffusion of camphor into the bulk, causing it to accumulate more at the interface.

Conclusion. In this section, we presented the first experimental characterization of the surface pressure and concentration field around a Marangoni swimmer. The obtained fields challenge some classical hypotheses used to model camphor swimmers. Our results suggest that detailed knowledge of the surfactant properties is essential for comprehensive modeling. It includes the equations of state, as well as the kinetics of exchange, dissolution, and absorption at the interface – parameters that are not always well understood. Notably, previous studies by Bandi and Mandre [68, 69] on a fixed source of camphoric acid found that the generated velocity fields were consistent with predictions for an insoluble surfactant. In comparison with the fixed source, the complexity of the surfactant dynamics appears to increase when dealing with a mobile source, as in the case of the Marangoni swimmer. Therefore, it is all the more valuable to develop a reverse experimental approach to provide a more accurate and detailed understanding of the system. Additionally, further exploration of the 3D flow dynamics could be done to compare our results with other experimental works and validate our observations [83–86]. Finally, our results should be compared with the chemical wake obtained numerically during the Phd

of Dolachaï Boniface[31] where he found that the width w follows a power law $w \sim x^{\alpha}$ where $\alpha = 0.4$.

6.3 Force balance

In the previous sections, we obtained the full 2D pressure field around the swimmers and discussed how it offers new insights and perspectives on the description of surfactant transport. However, when it comes to understanding the dynamics of the swimmer, the mechanical information derived from the surface flow alone provides sufficient elements to address the forces at play.

We now evaluate each force acting on the swimmer: first the drag force F_{d} due to the advection velocity then the capillary force F_{c} generated by the non-uniform distribution of surface pressure along the swimmer edge. In the following the component of a force $\mathbf{F}$ in the flow direction will be denoted $F_{\parallel}$ and the component perpendicular to the flow direction $F_{\perp}$ such that $\mathbf{F} = F_{\parallel}\mathbf{e}_{\mathrm{x}} + F_{\perp}\mathbf{e}_{\mathrm{y}}$.

6.3.1 Drag force

Computing the drag force. The easiest element of the force balance to access is the drag force. It can be computed by integrating the stress field over the surface of the swimmer:

$$\mathbf{F}_{\mathrm{d}} = \int_{\delta S} \boldsymbol{\sigma} \cdot \mathbf{n} \, \mathrm{d}A, \tag{6.3}$$

where $\boldsymbol{\sigma}$ is the stress tensor, $\mathbf{n}$ is the outward-pointing normal vector to the surface, and δS represents the surface area of the swimmer over which the stress is integrated, here the bottom surface of the swimmer. The integral accounts for the stress distribution over the swimmer surface, providing the total drag force applied by the water flow. In practice, it can be computed directly in Comsol.

Drag force on a passive disc. We first verify that the mesh is fine enough to correctly evaluate the drag force on an interfacial object. To do so we consider the same geometry for a disc not releasing surfactant and solve the complete problem without imposing the surface flow field and considering a stress-free condition at a pristine air-water interface. The obtained drag force quantitatively matches the theoretical prediction obtained with the Blasius equation and earlier experimental measurement see details in Appendix. 6.1. The agreement suggests that the mesh used allows to evaluate correctly the force on an interfacial disc.

Drag force on a Marangoni swimmer. Evaluating the drag force on a Marangoni swimmer from the derived stress field provides results different from the passive disc. The parallel drag force is lower, showing that the Marangoni flows generated may decrease the drag force. Moreover, the perpendicular force is directed toward the inside edge showing that the flow velocity gradient impacts the drag force. It is important to recognize that evaluating these forces is possibly the most challenging and demanding aspect of our method, and caution should be exercised to avoid over-interpreting the above observations.

However, it is worth noting the possibility of surfactants imposing driving forces not only through edge capillary action but also by altering viscous drag as discussed in other models [62]. The idea aligns with the understanding that flow structure can significantly impact the overall force balance, as already observed with reverse Marangoni propulsion where the boat moves against capillary asymmetry [55, 82].

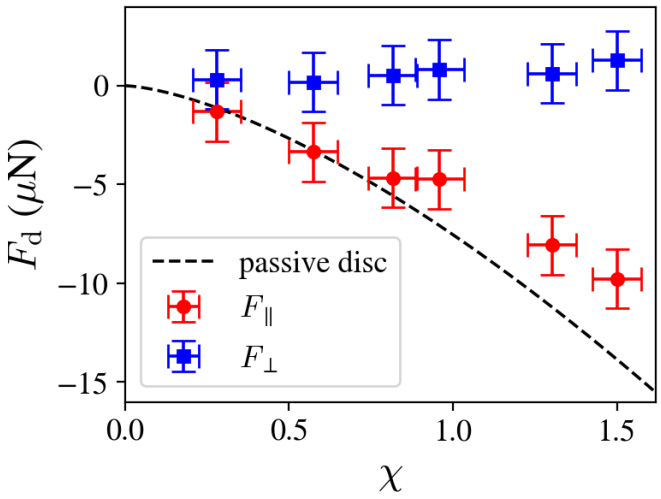

Figure 6.6: **Drag force on a Marangoni swimmer.** Drag force computed from the stress field reconstructed with finite element methods from the interfacial flow field. The points indicate the parallel (red) and perpendicular components of the force with respect to the flow direction. The dashed line corresponds to the case of a passive disc. The errorbars are given by the standard deviation of the drag force for three different swimmers and the error on χ due to variation in the spontaneous swimming velocity $V = 7 \pm 1\,\mathrm{cm\,s^{-1}}$.

6.3.2 Capillary force

Computing the capillary force. From the surface pressure field obtained, we can compute the capillary force by integrating along the swimmer contour:

$$\mathbf{F}_c = \int_0^{2\pi} a\Pi(a,\theta)\mathbf{n}\,\mathrm{d}\theta, \tag{6.4}$$

where $\mathbf{n}$ is the normal unit vector pointing outward the swimmer. As the experimental vector field starts 1 mm away from the swimmer, the reconstructed surface pressure values at the swimmer edge may not be trustworthy. Therefore, in the following, we discuss different approaches to evaluate the capillary force either directly or by extrapolation.

Different way to evaluate the capillary force. We can evaluate the capillary force in three different ways: (*i*) using directly the surface pressure value at the swimmer edge, (*ii*) extrapolating the surface pressure at the swimmer edge from the reliable flow field part (1 mm away from the edge), (*iii*) considering circles of decreasing radius to compute the force. We present the extrapolation for $\chi = 0.9$. First, we consider the surface pressure value with respect to the distance r_s to the swimmer center at given angle θ_s

(Fig. 6.7 left). We fit linearly the values between $0.5\,\mathrm{cm} < r_s < 0.8\,\mathrm{cm}$, as we know the experimental vector field is more reliable in that area (Fig. 6.7 center). For all advection speeds, this process tends to slightly increase the surface pressure values downstream and decrease the values upstream. The second approach considers increasing the circle with excess radius δa (Fig. 6.7 left) to evaluate the capillary force. Increasing the radius of 0.5 mm significantly increases the capillary force from 2.5 to 10 µN. For a larger circle, the force decreases and reaches a plateau. For all advection the maximum value of the force is observed for $\delta a \sim 0.5\,\mathrm{mm}$. We will consider this value for an upper bound of the capillary force.

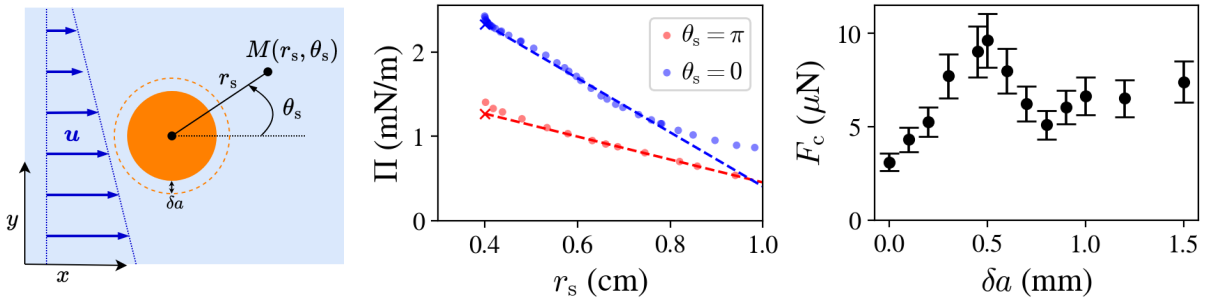

Figure 6.7: **Extrapolation of the capillary force.** Different method to extrapolate the capillary force at $\chi = 0.9$. (Left) Schematic of the notation used. (Center) Linear fit of the surface pressure Π with respect to the radial distance to the swimmer center for two angles, $\theta_s = 0$ corresponds to downstream and $\theta_s = \pi$ to the upstream position. The cross indicates the fitted value at the swimmer edge. (Right) Total capillary force on a circle with radius $a + \delta a$.

Value of the capillary force All methods to obtain the capillary force give a positive force along the parallel direction, confirming that the surfactant distribution propels the swimmer against the flow (Fig. 6.8). However, the extrapolated value of the capillary force is significantly different depending on the technique used. The capillary force from the surface pressure directly at the edge (dashed red line) is two times smaller than the one obtained with linear interpolation (full red line), and three times smaller than the one computed on a larger circle (dotted red line). Overall the average value remains relatively constant around 5 µN (red solid circle). The error bars are obtained propagating the $0.3\,\mathrm{mN\,m^{-1}}$ error on the surface pressure field close to the swimmer edge. Along the perpendicular direction, all methods give relatively similar results, so we report only the average values (blue dots) which remain almost 0 showing a symmetric distribution even if there is a small difference in advection speed.

Comparison to other results. Previous predictions for a camphor boat swimming at $6\,\mathrm{cm\,s^{-1}}$ estimated a capillary force of 4.2 µN using an effective diffusion coefficient [52]. However, their experimental measurements recorded a much higher value of 24 µN [52]. The discrepancy may be due to their measurements being taken with the boat fixed in still water, which likely caused surfactant to accumulate at the rear and resulted in a larger force.

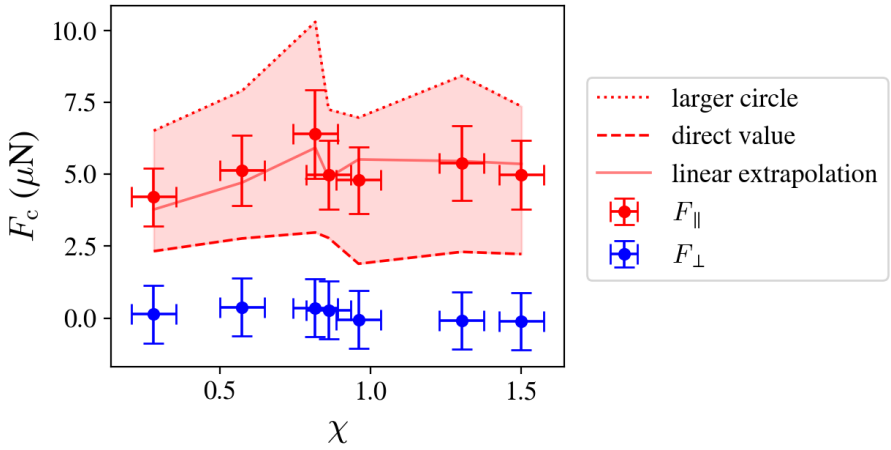

Figure 6.8: **Capillary force.** Value of the capillary force with respect to advection for different computation methods along the parallel direction: (dashed red line) direct integration of the surface pressure at the perimeter, (full red line) linear extrapolation of the surface pressure at the perimeter, (dotted red line) integration over larger contour $\delta a = 0.5\,\mathrm{mm}$. The results of each method are averaged, in the parallel (red solid circle) and perpendicular (blue solid circle) directions to the flow.

Given the comparable swimming velocities, it is reasonable to expect similar capillary forces between the camphor boat and our camphor swimmer. We obtain $F_c = 5 \pm 2\,\mu\mathrm{N}$. From our previous experimental measurements of the total force, subtracting the drag force on a passive disc gives a maximum capillary force of around $15\,\mu\mathrm{N}$ for $\chi = 0.7$. Such estimation is made assuming the capillary force and the drag are completely additive, which, as discussed in Chapter 3, is not accurate but serves as a reasonable first approximation. Overall, the magnitude of the capillary force we obtained is in good agreement with previous results.

6.3.3 Total force

Total force We can evaluate the total force $\mathbf{F}_{\mathrm{tot}}$ acting on the swimmer:

$$\mathbf{F}_{\mathrm{tot}} = \mathbf{F}_{\mathrm{c}} + \mathbf{F}_{\mathrm{d}}. \tag{6.5}$$

As the capillary and the drag forces are mainly along the flow direction we only report the parallel component of the total force (Fig. 6.9). The computed force and the one measured experimentally match qualitatively. First, the order of magnitude is similar. Second, the total force vanishes around $\chi = 1$ when the advection velocity matches the spontaneous swimming speed. However, the magnitude of the computed values is always lower. These discrepancies could be attributed to inaccuracies in estimating the capillary force which is highly sensitive to the conditions near the swimmer edge, where the vector field measurements are prone to significant noise leading to bad evaluation of the capillary force.

Conclusion. Although the current analysis provides a good first approximation, there is still work to be done to achieve truly quantitative results. Future efforts should focus

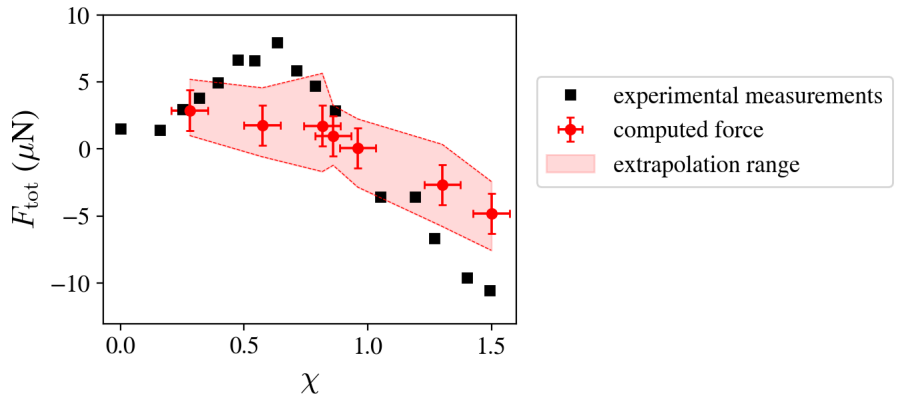

Figure 6.9: **Total force as a function of the flow velocity.** The points correspond to the force computed numerically from the experimental flow field. The total force $\mathbf{F}_{\text{tot}}$ is the sum of the drag force $\mathbf{F}_{\text{d}}$ (Eq. (6.3)) and the capillary force $\mathbf{F}_{\text{c}}$ (Eq. (6.4)) $\mathbf{F}_{\text{tot}} = \mathbf{F}_{\text{c}} + \mathbf{F}_{\text{d}}$.

on improving the quality of the flow field measurements, especially in the regions close to the swimmer.

6.4 Conclusion

In this chapter, we applied the new method developed to obtain the surface pressure field around a Marangoni swimmer. Our findings reveal that advection significantly impacts the surface pressure field, which transitions from symmetric to parabolic-like downstream as advection increases. Using an isotherm and assuming a linear relationship between surfactant concentration and surface pressure, we derived the surfactant distribution around the swimmer. Interestingly, our observations suggest that the release rate of camphor might increase with flow velocity, which contrasts with the constant flux hypothesis commonly used in existing models.

The total force computed qualitatively matches the experimental measurements, changing sign when the advection speed is close to the spontaneous swimming speed. However, the computed values are two to three times lower than expected. This discrepancy is likely due to the large noise in the interfacial flow data and the inability to probe the flow field up to the swimmer edge, leading to less quantitative results.

Future work should focus on improving the accuracy of flow field measurements close to the swimmer to achieve truly quantitative results. Another potential direction is to measure the 3D flow field directly, which could eliminate the need for finite element methods to compute it. However, obtaining the interfacial stress requires knowledge of the flow field in the boundary layer, which is experimentally challenging. Current 3D flow field measurements have a vertical resolution of 1 mm [83], limited by the thickness of the laser sheet used, which is insufficient to probe the boundary layer accurately.

6.5 Appendix: drag force on a passive disc

We consider a passive disc (not releasing surfactant) in a channel with the same geometry as for the camphor swimmer (Fig. 6.1). The drag force is computed from the stress field below the disc surface and the results are compared with the theoretical prediction from the Blasius equation for an interfacial disc :

$$F_{\text{drag}} = -\alpha\rho\sqrt{\nu}(aU)^{\frac{3}{2}} \tag{6.6}$$

where $\alpha = 1.64$ and ν is the kinematic viscosity of the fluid, a the radius of the disc and U the flow velocity. The theoretical prediction already matched our experimental measurement (Chap. 2) and also corresponds to the drag force evaluated with finite element method which suggest that the mesh is adequate to evaluate the force applied on an interfacial object.

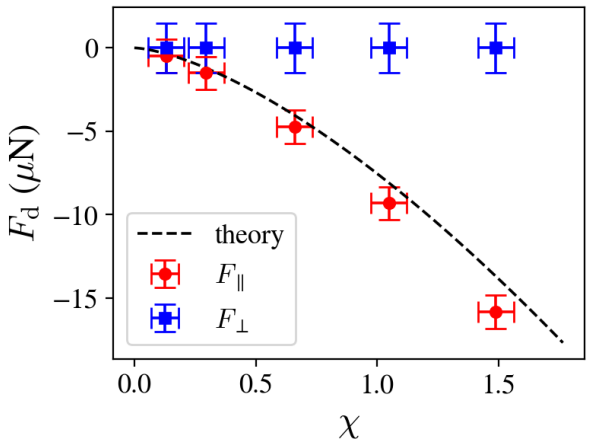

Appendix 6.1: **Drag force on a passive disc.** Drag force applied on an interfacial disc not releasing surfactant with respect to the advection speed. Points correspond to finite element computation, in the direction of the flow (red points) and parallel to the flow (blue points) and the dashed curve to the theoretical prediction from the Blasius equation.

Chapter 7

Trajectories of a Marangoni swimmer in imposed flows.

Table of Contents

The results presented in this chapter were obtained by Marianne Poussereau and Maxime Moskalenko during their M1 and L3 internships. I thank both of them again for the quality of their work, their curiosity, and the fresh perspective they brought during the end of my second and third year. It was a pleasure to supervise their internships.

7.1 Introduction

Many biological microswimmers, such as spermatozoa, bacteria, and phytoplankton, navigate through complex flow environments [140]. This also applies to synthetic microswimmers designed to transport cargo, *i.e.*, to serve as drug carriers in human blood vessels. Therefore, a detailed understanding of their behavior in varying flow conditions is essential for both biological and synthetic microswimmers. In the previous chapters, we adopted a fixed frame of reference to study a Marangoni swimmer attached to a spring in a stationary flow. This approach allowed us to comprehensively characterize the flow field, force, and surfactant distribution at various advection speeds. However, it did not enable us to investigate how the swimmer moves in response to the flow. This is the question that we address here. By releasing the constraints of the spring, we can now explore how Marangoni swimmers behave and navigate autonomously within diverse flow conditions.

Self-propelled objects can display several behaviors in a flow field, for example *E. coli* moves upstream against the flow, a phenomenon known as upstream rheotaxis an with implication, for instance, in invasion of medical devices. It was also observed in artificial self-propelled objects [141, 142]. Asymmetric active Janus particles demonstrate rheotactic behavior due to the interplay between their polarity and the external shear torque [143, 144]. Recently this behavior has been observed for symmetric self-propelled droplets where they exhibit a nonlinear behavior characterized by oscillations around the center of the channel [145, 146]. Theoretical work on pusher and puller swimmers in 2D Poiseuille flow also evidences oscillation [147]. As the flow velocity increases, the shear on the particles also increases, inducing a curvature of the trajectory. Limit cycles may be observed, and above a critical velocity, the particles reorient and swim with the flow. If bacteria, phoretic swimmers, or Marangoni droplets have been studied, to the best of our knowledge, there are no studies on the behavior of interfacial Marangoni swimmers in imposed flows.

For a Marangoni swimmer, the water flow will break the symmetry of the camphor cloud, leading to more surfactant downstream. Therefore, we expect the swimmer to move upstream for flow velocities lower than its spontaneous swimming velocity, similar to Marangoni droplets [145, 146]. However, anticipating the shape of the trajectories is more challenging. Even in the absence of advection, the swimming behavior of Marangoni swimmers depends on several factors. For instance, their shape can change the trajectory from circular to linear [22]. Additionally, variations in water depth within the pool can give rise to reverse Marangoni propulsion, where the swimmer moves towards regions of higher surfactant concentration [82, 83]. The geometry of the pool itself can modify the swimmer trajectory. In small circular containers with fluid at rest, the swimmer tends to follow the edge [84, 148], while in rectangular or square containers, it travels in a straight line and reorients when bumping against the edges [24]. Thus, if Marangoni swimmers are expected to move upstream, their trajectory in response to velocity gradients is less

clear. In a circular pool with a shear flow, will they follow the outside edge as without advection or exhibit more intricate swimming patterns as the Marangoni droplets?

7.2 Swimmer in a shear flow

In this section, we aim to understand the behavior of a Marangoni swimmer in a shear flow. First, we characterize experimentally the swimming trajectories for different advection speeds. We observed two swimming modes: one where the swimmer follows the outside edge of the tank and another where it travels throughout the tank and bounces. As flow velocity increases, the distance between bounces decreases, and the curvature radius of the trajectory increases. We explore two possible origins of these observations: the swimmer being deviated by the inside edge of the channel, or the curvature of the trajectory being due to the velocity gradient. We find that the inside edge has minimal effects on the trajectory. Using a toy model based on the 2D approach of Zöttl *et al.* [147], we conclude that, as with Marangoni droplets, the gradient of velocity is primarily responsible for the curvature of the trajectories.

7.2.1 Experimental caracterisation

Experimental setup and protocol. To study the motion of a Marangoni swimmer in a shear flow, the swimmer is not attached to the capillary anymore and is free to move in the channel. The tank rotates at an angular velocity ω generating a flow field $\mathbf{u}(r) = \mathbf{r} \times \boldsymbol{\omega}$. To image the whole tank, the camera is placed above the pool (Fig. 7.1). A black fabric is placed under the tank to have a good contrast between the white swimmer and the background. In the following, a given rotation speed will be referred by the ratio χ between $U_{\text{out}} = \omega R_{\text{out}}$ the maximal flow velocity inside the channel (*i.e.* at the outside edge R_{out}) and V the spontaneous swimming velocity in still water:

$$\chi = \frac{U_{\text{out}}}{V}. \tag{7.1}$$

Not that this definition differs from the earlier chapter where we used the middle channel velocity U instead of the outer velocity. The experimental protocol is the same as earlier, with 900 s of pre-swimming in a first tank to ensure a constant swimming velocity. The swimmer is then placed in the circular tank and its motion is recorded for 3 min.

a- Behavior without flow

We first study the swimming behavior of a Marangoni swimmer in the absence of water flow in a circular channel of 20 cm outer radius and 10 cm width. Two modes are observed: (*i*) **Transient bouncing mode:** the swimmer initially travels in straight lines within the tank, repeatedly bouncing off the outside edges and changing direction (Fig. 7.2 right). (*ii*) **Trapped mode:** after bouncing a few times, the swimmer reaches the outside edge and gets trapped. During the typical experimental time, once the swimmer is trapped it never seems to escape (Fig. 7.2 left). However, a swimmer could first travel in straight lines, bouncing against the edges, and then get trapped, demonstrating that the

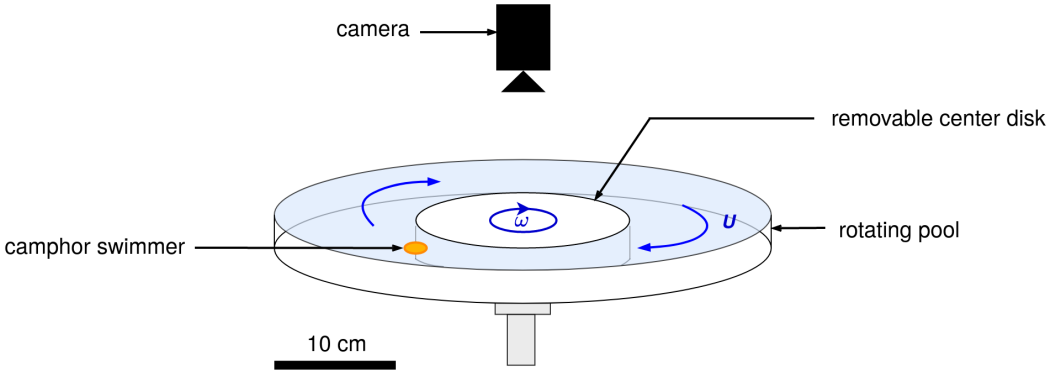

Figure 7.1: **Experimental setup.** The swimmer (orange circle) is placed in a circular channel of 10 cm width, and the inside disc of 10 cm can be removed. The tank can rotate at angular velocity ω generating a shear flow. To image the whole pool the camera is placed 1.5 m above the tank.

bouncing behavior is metastable. The primary variable observed among different swimmers is the time required to transition from the bouncing mode to the trapped mode. These two trajectory modes were already observed in different types of pools but without switching. In a small circular container with radius 9 cm, the swimmer is trapped at the outside edge [84, 148], wheras for a larger rectangular tank it travels in straight lines and bounces against the edge [24]. Here, the large size of the pool, 20 cm in radius, and the low curvature radius of the outside edge may explain the emergence of the two behaviors. In the next part, we explore how initial conditions and flow velocity influence the coexistence and transition between these modes.

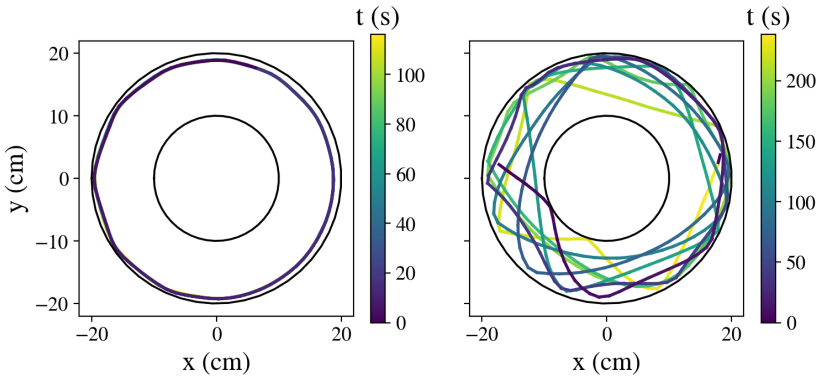

Figure 7.2: **Trajectories without water flow** Swimmer trajectory in the cylindrical pool without water flow, two behaviors are observed: following the edge (left), and straight lines (right). Each experiment lasts 300 s and was cropped for better visualization of the trajectories. The color indicates the time.

b- Behavior with flow

Swimming velocities. Before studying the swimming trajectory, we first characterize the swimming velocity within a water flow. Here as the swimmer moves through the flow, we can define two velocities: the global velocity $\mathbf{V}_\mathrm{m}$ measured in the laboratory frame of

reference and the relative velocity $\mathbf{V}$, which is the velocity of the swimmer with respect to the surrounding fluid. Assuming that the flow field is unperturbed by the presence of the swimmer, the relative velocity is given by the difference between the global velocity and the flow field:

$$\mathbf{V}(r,t) = \mathbf{V}_{\mathrm{m}}(r,t) - \mathbf{u}(r). \tag{7.2}$$

Using equation (7.2), we compute the relative swimming velocity with respect to the distance r to the tank center. If the shear flow has no impact, the relative velocity should correspond to the spontaneous swimming velocity without water flow. Here, the norm of relative swimming velocity is $6.5\mathrm{cm\,s^{-1}}$ which is consistent with the $7 \pm 1\,\mathrm{cm/s}$ spontaneous swimming velocity measured in a quiescent fluid after 9 min [24]. The relative velocity decreases when the distance to the wall becomes less than 2 cm (Fig. 7.3). This is consistent with previous experimental results for a similar swimmer in a square tank without water flow, where its swimming velocity decreased when the swimmer was closer than a distance equivalent to six swimmer radii from the wall, approximately 2.4 cm [24, 31].

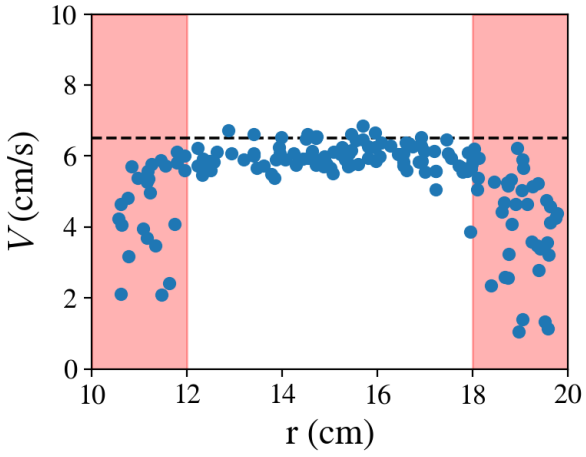

Figure 7.3: **Relative swimming velocity.** Difference between the swimmer velocity measured in the laboratory frame and the flow velocity. Dots correspond to the relative velocity between two consecutive positions of the swimmer for 5 frames per second. The red area indicates the zone where the velocity starts to decrease close to the channel edges and the black line indicates the average swimming velocity, here $6.5\,\mathrm{cm\,s^{-1}}$.

Trajectories and impact of the initial condition. Introducing a homogeneous flow breaks the symmetry of the camphor clouds, with more surfactant downstream, leading to propulsion against the flow. As a result, for sufficiently low flow velocity, when the tank rotates clockwise, the swimmer tends to move counterclockwise. With advection, both trapped or bouncing modes are observed and the swimmer can switch between the two whereas, without flow, the trapped mode seemed irreversible. To assess the impact of initial conditions on mode selection, the swimmer is released at different positions in the channel: on the inner side at $r = 10\,\mathrm{cm}$, at the center at $r = 15\,\mathrm{cm}$, and on the outer side at $r = 20\,\mathrm{cm}$. When the swimmer starts from outside, it is immediately trapped and follows the outside edge sometimes escaping. In contrast, the swimmer is almost always

in the bouncing mode when starting from the two other initial conditions. It seems that the trapped mode is more frequent when the swimmer arrives with a large angle, nearly parallel to the edge. On the contrary, bouncing is favored by a smaller impact angle, perpendicular to the edge.

Selecting the trajectories of interest. We narrow our focus to the second type of trajectory where the swimmer travels throughout the tank. We manually select the trajectories where the swimmer is not trapped and bounces against the edges. Given that the swimmer can transition between these trajectory types, we only keep the ones where the bouncing behavior was observed for at least 30 s and remove the part of the trajectory where the swimmer was transiently trapped. Typically, the swimmer spends about 70% of the experimental time in the bouncing mode. In the following, we study the impact of the flow velocity on these trajectories.

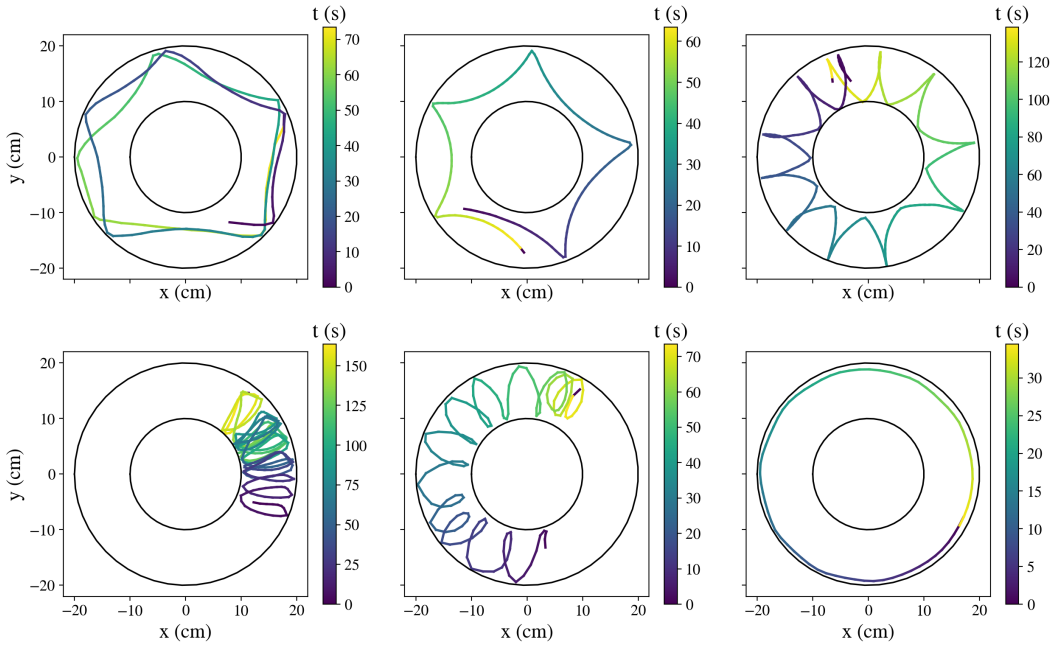

Figure 7.4: **Evolution of the trajectories in a shear flow.** Swimmer trajectories in a a circular channel of 20 cm outer radius and 10 cm width. The pool is rotating clockwise. The color of the lines indicates the time. The flow velocity is defined by the ratio between the maximal flow speed and the swimmer spontaneous velocity $\chi = U_{\text{out}}/V = 0.3$, 0.6, 0.9, 1, 1.05, or 1.2, left to right top to botom

Influence of the flow. With advection the bounces seem quite regular and the trajectory seems to have some periodicity. When the flow velocity increases the distance between successive bounces seems to decrease, and the radius of curvature of the trajectory increases (Fig. 7.4). For $\chi = 1$ when the outer flow speed is equal to the spontaneous swimming velocity, the trajectory becomes almost stationary with a left and right displacement between the two tank edges (Fig. 7.4 bottom left). This behavior will be referred to as the ping-pong regime. When the flow velocity at the outside exceeds the swimming velocity, $\chi > 1$, the same pattern is observed but in the flow direction (Fig. 7.4

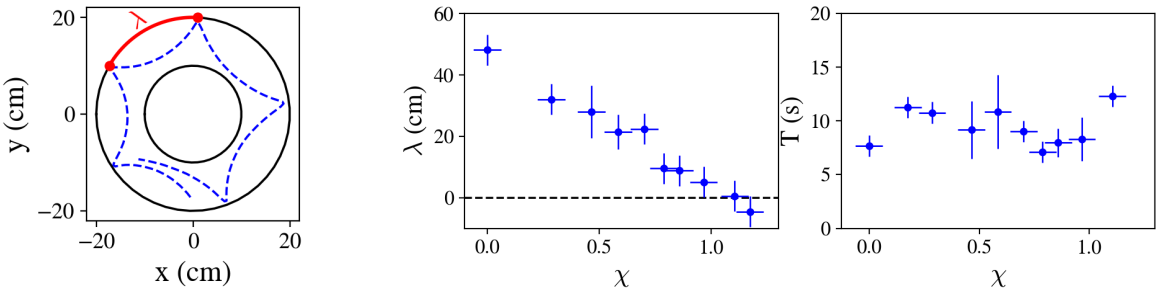

Figure 7.5: **Spatial and temporal period of the bounces with respect to the rotation speed.** χ is the ratio between the maximal flow velocity at the outside edge of the channel, at $r = 20\,\text{cm}$, and the spontaneous swimming velocity. (Left) Definition of the spatial period λ, spatial period (center), and temporal period (right) with respect to the maximal flow velocity.

bottom center). Finally, when $\chi > 1.2$ the swimmer is completely dragged away and swims clockwise with the flow along the outside edge (Fig. 7.4 bottom right). The transition from the swimmer bouncing to being trapped and moving with the flow seems quite sharp, which suggests a discontinuous transition.

As the bounces against the outside edge seem to be regular, we define λ as the spatial period and T as the temporal period between two consecutive contacts with the outside edge. The spatial period is defined as the distance along the outside edge between two consecutive bounces (Fig. 7.5 left). It decreases linearly with the flow speed up to $\chi = 1.0 \pm 0.1$, where the distance between bounces is almost zero (Fig. 7.5 center). For larger rotation speeds the spatial period becomes negative as the swimmer is dragged by the flow and swims downstream (Fig. 7.4 bottom center). Above $\chi = 1.3$, the period can no longer be defined as the swimmer is trapped at the outside edge and swimming with the flow. In contrast to the spatial period, the temporal period seems rather constant with $T = 10 \pm 2\,\text{s}$. (Fig. 7.5 left).

Conclusion. For a Marangoni swimmer in a shear flow inside a circular pool two swimming modes are observed: being trapped at the outside edge or bouncing across the tank. As the water flow increases, the distances between successive bounces decreases and the trajectory curvature increases. Similar behaviors have been noted in other experimental and theoretical studies respectively on Marangoni droplets and pusher/puller in a Poiseuille flow [145–147]. For low flow velocities, the swimmers oscillate around the channel center with spatial frequencies that increase with the flow speed up to the swimmer velocity where a closed limit cycle is observed. For higher flow velocities, the swimmers tumble and swim with the flow, staying at the center of the channel. For Marangoni droplets the oscillation of the trajectories are associated with the flow velocity gradients across the channel making the swimmer rotate [145, 146]. The swimmers in these works remain far from the edges, whereas, in our experiments, the swimmer regularly bumps against both the outside and inside edges, which may significantly influence its behavior. In the following sections, we will explore the origins of the regular bouncing observed and assess if this behavior is driven by the velocity gradient or the presence of the inside edge.

7.2.2 Origin of the periodic bouncing

This section discusses the origin of the increased curvature and decreased bounce distance observed as the flow velocity increases. We explore two possible hypotheses:

- the presence of the inner edge may deviate the swimmer trajectory. As noted earlier, the swimming velocity decreases within 2 cm from the edge (Fig. 7.3), and it may also modify the trajectory by interacting with the camphor cloud. At low velocities, this interaction may be negligible as the swimmer remains far from the inner edge. However, at higher flow velocities, especially during the ping-pong regime, the swimmer frequently touches the inner edge, and its presence is far from negligible possibly explaining the back and forth behavior we observe.

- the interaction between the swimmer and the shear flow. When the flow speed increases the shear also increases making the swimmer rotate. This could be the origin of the increase in curvature radius.

a- Interaction with the inside edge

To test the impact of the inside edge on the swimming trajectories, the central part of the tank is removed, giving a full cylindrical tank of 20 cm radius. As expected, for low rotation speeds below an outside velocity of $\chi = 0.6$, the swimmer remains far from the edge and there is no modification of the trajectories (Fig. 7.6 plots 1 and 2). Increasing the rotation speed still decreases the distance between the bounces and the radius of curvature increases. For an outside velocity between $\chi = 0.6$ and 0.8, in the presence of the inside edge, the swimmer was bouncing against the edge breaking the arc formed between bounces. Without the edge, these broken arcs are no longer observed, but the swimmer still displays small curved bounces (Fig. 7.6 plot 3). Finally for an outside velocity above $\chi = 0.9$, a loopy pattern emerges (Fig. 7.6 plots 4 and 5). Here we observe that the swimmer occasionally crosses the central region during the bounce, and the ping-pong behavior is less defined compared to when the inside edge was present. Overall the swimming trajectories are quite similar. We can conclude that even if the presence of the inside edge favors the ping-pong behavior and breaks the bounces it is not sufficient to explain the increase of the curvature radius and decrease in bouncing distance.

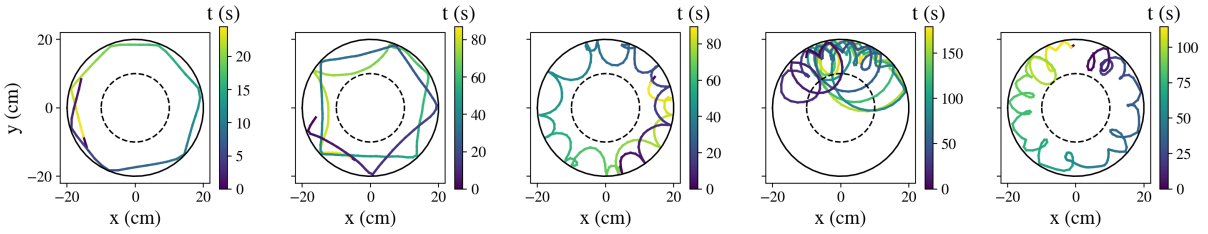

Figure 7.6: **Evolution of the trajectories without an inside edge.** Trajectory of the swimmer in the tank without inner disc, resulting in circular pool of 20 cm radius. The flow velocity $\chi = U_{\text{out}}/V$ are from left to right $\chi = 0.0, 0.3, 0.9, 1, 1.1$. The color indicates the time. Experiments were cropped for better visualization. The dashed black lines corresponds to the former position of the inside disc.

b- Toy model: self-propelled object in a shear flow

Physical situation. As the presence of the inside edge does not influence significantly the trajectory, we focus on the impact of the shear flow. To do so, we introduce a simple model inspired by the work of Zöttl *et al.* [147] with a purely hydrodynamical approach. We consider a pointlike microswimmer that moves along a swimming direction with a constant intrinsic swimming velocity. The particle is placed in a circular container and experiences a shear flow (Fig. 7.7). Here, we completely neglect the field of surfactant, and the direction of swimming can be modified by rotating the swimmer. This is the most basic and simplest model one could think of.

Notation and equation of motion. A natural way to adimensionalize is to use the container radius R as a length scale, and the particle spontaneous swimming velocity V:

$$r = R\tilde{r}, \qquad \mathbf{u} = V\tilde{\mathbf{u}}, \qquad \omega = \frac{V}{R}\tilde{\omega} \tag{7.3}$$

where dimensionless quantities are denoted with a tilde $\tilde{(\,)}$ and $\mathbf{u}$ is the imposed flow field. In the following, we will work only with dimensionless quantities, therefore, for simplification, they will be denoted without using the tilde $\tilde{(\,)}$. In this framework, the dimensionless swimming velocity is $V = 1$, and the swimming direction is defined by the unit vector $\mathbf{e}_\mathrm{s}$. As the shear flow is generated by the solid rotation of the pool (Fig. 7.7), the motion equations can be written as:

$$\frac{\mathrm{d}\mathbf{e}_\mathrm{s}}{\mathrm{d}t} = \frac{1}{2}\Big(\mathbf{rot}\ \mathbf{u}(r)\Big) \times \mathbf{e}_\mathrm{s}(t), \qquad \mathbf{V}_\mathrm{m}(r,t) = \mathbf{u}(r) + \mathbf{V}(t), \tag{7.4}$$

where $\mathbf{V}_\mathrm{m}$ is the swimming velocity of the particles in the laboratory frame of reference and the spontaneous swimming velocity is $\mathbf{V}(t) = \mathbf{e}_\mathrm{s}(t)$ (Fig.7.7). In polar coordinate $(\mathbf{e}_\mathrm{r}, \mathbf{e}_\phi)$, the motion equations become:

$$\dot{r} = (\mathbf{u} + \mathbf{e}_\mathrm{s}) \cdot \mathbf{e}_\mathrm{r} = \cos(\theta - \phi), \quad r\dot{\phi} = -\omega r + \mathbf{e}_\phi \cdot \mathbf{e}_\mathrm{s} = -\omega r + \sin(\theta - \phi), \tag{7.5}$$

where θ defines the orientation of the swimmer velocity direction. These equations can be simplified by introducing $\psi = \phi - \theta$, the relative angle between the orientation of the swimmer velocity direction and the angular position. Thus $\dot{\psi} = \dot{\phi} + \omega$, which simplifies the motion equations as:

$$\dot{r} = \cos\psi, \qquad r\dot{\psi} = -\sin\psi. \tag{7.6}$$

Combining both equations and solving the resulting differential equation, we get:

$$\psi(t) = \operatorname{arcotan}\Big(\operatorname{cotan}\psi(0) - \frac{\dot{\psi}(0)}{\sin^2\psi(0)}t\Big), \tag{7.7}$$

where $\psi(0)$ and $\dot{\psi}(0)$ are the initial conditions at $t = 0$.

Choice of initial conditions. From the experimental trajectories, one can notice that the trajectories between two bounces are roughly symmetric (Fig. 7.4 page 132). Moreover, the symmetry point corresponds to the apex of the bounce where the trajectory, and thus the swimming velocity, is parallel to the flow. Therefore, it is natural to take this point

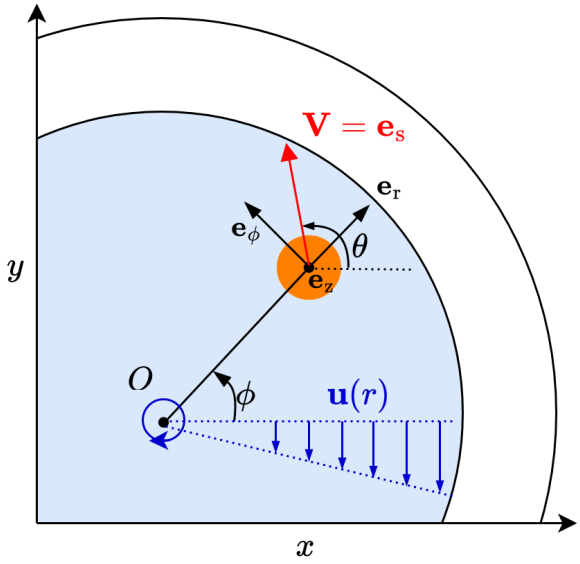

Figure 7.7: **Toy model: swimmer in a shear flow.** Self-propelled particle in a cylindrical pool with a shear flow. The particle spontaneous dimensionless velocity without flow is $\mathbf{V} = \mathbf{e}_s$

as the origin, meaning $\theta(t = 0) = \pi/2$ and $\phi(t = 0) = 0$ and so $\psi = -\pi/2$ and $\dot{\psi} = 1/r_0$. Thus the trajectories obtained will correspond to only half a bounce. The spatial period λ can easily be obtained by multiplying the distance along the outside edge by two. The initial radius r_0 is more difficult to choose, as it can vary during a given trajectory. The main explored region for the apex of the trajectory is between $r = 10\,\text{cm}$ and $15\,\text{cm}$ (Fig. 7.4 page 132). In the presence of the inside edge, the swimmer can bump against it, breaking the trajectory. To be able to compare the model results with experience with and without inside edge we consider $r_0 = 12\,\text{cm}$

Results of the model. In the absence of flow, the trajectory is straight. When the flow speed increases the curvature radius increases (Fig. 7.8 left). For maximal flow velocity slightly larger than the swimming velocity $\chi = 1$, the swimmer seems confined in a small part of the tank as for the ping-pong regime even without the presence of an inside edge. The spatial period between two consecutive bounces decreases linearly with the flow velocity (Fig. 7.8 right). The slope seems to depend on the starting radius but it reaches zero around $\chi = 1.1 \pm 0.1$ which is a bit larger than in the experiments. For larger flow, the spatial period becomes negative but is more difficult to interpret as it depends largely on the interaction with the outside edge. Either the swimmer bounces back and we are in the dragged ping-pong regime or it is trapped at the edge and is carried away by the flow. For $\chi > 0.7$ the model seems to overestimate the spatial period. Overall, this purely hydrodynamical model captures well qualitatively and quantitatively the impact of the shear flow on the shape of the trajectories for advection below the swimming velocity.

Relevance of the model. In this model the shear flow induced a rotation of the swimmer, which modified the swimming direction. However, in our experimental system, the swimming direction is defined by the orientation of the camphor cloud and the impact

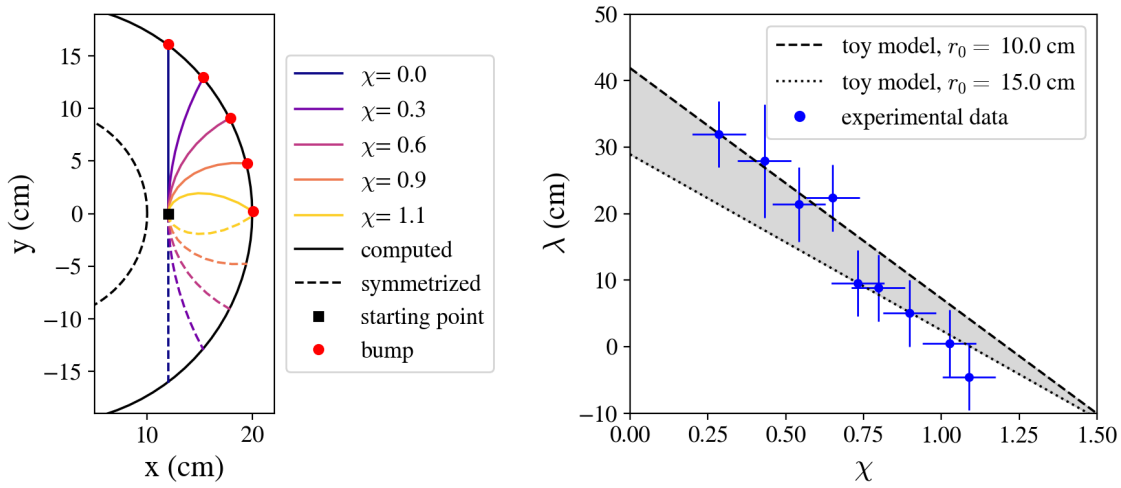

Figure 7.8: **Trajectories predicted by the toy model.** Theoretical trajectories for increasing rotation speed, for initial conditions $\theta(t=0) = \pi/2$ and $\phi(t=0) = 0$ and $r_0 = 12\,\text{cm}$ (left). Spatial period λ with respect to the ratio between the maximal flow velocity and the swimming velocity $\chi = U_{\text{out}}/V$ for a starting radius $r_0 = 12\,\text{cm}$ and $r_0 = 10\,\text{cm}$. (right)

of the torque induced by the shear flow could be more complex. To understand the effect of the shear flow on the camphor cloud, we consider the extreme limit of no diffusion $D = 0$. Without advection, the camphor emitted by a point source P forms a line behind the swimmer (Fig. 7.9). When it reaches the edge of the swimmer at point S it generates a capillary force in the direction of $\vec{SP}$ and defines the swimming direction $\mathbf{V}$. In the presence of a shear flow, the line of surfactant is advected and the contact point with the edge shifts to a point S' in the direction of the low advection velocity. Therefore, the capillary force and the swimming direction shift toward the larger velocity and the outside of the tank leading to a curvature of the trajectory. The simplified picture proposed by the string model allows us to understand qualitatively the effect of a shear flow on the camphor cloud, even if the situation is much more complex with a nonzero diffusive coefficient.

Comparison with related work. Other related experiments were performed with Marangoni droplets with a Poiseuille flow in a channel [145]. The main difference with our work is the strong vertical confinement close to the droplet height. The trajectories observed for increasing velocity are similar to ours:

1. without advection, $\chi = 0$, the trajectory is straight;

2. low advection, $\chi < 0.5$, the droplet moves upstream and oscillates around the center of the channel where the velocity is maximal. The spatial period decreases with the flow velocity.

3. large advection, $\chi = 0.5$, the droplet cannot move upstream and keeps oscillating with a ping-pong behavior;

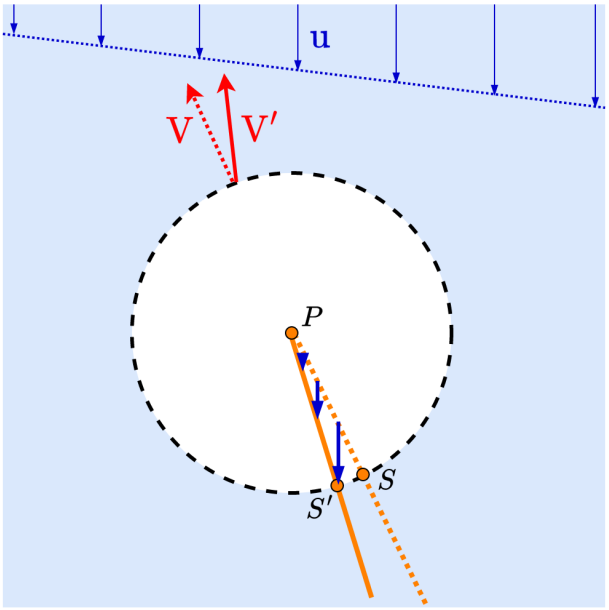

Figure 7.9: **Impact of the shear flow on the surfactant.** Illustration of the effect of the shear flow on the surfactant cloud in the limit of no diffusion $D = 0$. The case, $u = 0$ is illustrated with a dotted line. and the case, $u > 0$ corresponds to full line and ($'$) letters. The surfactant is emitted from a point source P and generates a capillary force at the swimmer edge at point S (or S'), $\vec{SP}$ (or $\vec{S'P}$) defines the swimming direction V (or V').

4. very large advection, $\chi > 0.5$ the droplet drifts downstream with a spatial period increasing with the flow speed.

Compared to our experiments, the flow velocity for which the swimmers are dragged by the flow is much lower, only half the swimming velocity. The trajectory is modeled using also a purely hydrodynamical model, considering a finite-size swimmer and its interaction with the confining walls and imposed flow. The model reproduces the trajectories observed experimentally with an overestimation of the spatial period.

7.2.3 Conclusion.

If not trapped, a Marangoni swimmer in a shear flow exhibits curved trajectories with periodical bounces against the outside edge. As the flow speed increases, both the curvature of the trajectories and the frequency of bounces increase, reducing the distance between consecutive bounces. At a critical flow velocity close to the swimming one, the trajectories remain localized in a small part of the pool alternating between each tank edge in a ping-pong behavior. Beyond this critical velocity, the swimmer is swept along by the flow. Interestingly, removing the inner edge did not alter the observed bouncing patterns, indicating that the edge does not primarily drive the periodic bouncing behavior. Instead, these dynamics appear to be governed more by the flow hydrodynamic effects rather than the swimmer interaction with physical boundaries. A simple hydrodynamic toy model, which neglects the surfactant distribution, was able to qualitatively and quantitatively replicate the observed experimental trajectories. Further investigation is needed to ex-

plore the time intervals between consecutive bounces, which remained nearly constant for all advection velocities.

7.3 Swimmer in a vortex

After the simple shear flow, we move toward a more complex situation: a swimmer in a vortex. Biological and artificial microswimmers often self-propel in external flows of a vortical nature; relevant examples include algae in small-scale ocean eddies, spermatozoa in uterine peristaltic flows, and bacteria in microfluidic devices. Experiments have shown that swimming bacteria in a vortex are expelled from the high-shear region near the center of the vortex [149], leading to a significant reduction in bacterial concentration in this area. If most of the bacteria are expelled a few get trapped at the center of the vortex. These experimental observations were confirmed by a model [150] that uses a similar approach to the one developed earlier in our study (Subsec. 7.2.2). The particle propels at constant velocity V and the flow field can modify its orientation. For elongated objects, the model first reveals the existence of bounded orbits near the center of the vortex and unbounded orbits elsewhere. When translational and rotational noise are added, the model predicts a comparable area devoid of swimmers at the vortex center. The study concludes that the dynamics of self-propelled particles in a vortex are strongly influenced by their motility and the alignment imposed by the vortical flow [150].

Trapping of self-propelled objects in vortical flows has attracted significant attention for modeling and identifying the right conditions [150, 151]. The trapping of microswimmers within a vortex is determined by a combination of their initial position, orientation, shape, swimming velocity, and noise. Microswimmers starting close to the vortex center are more likely to be trapped [150]. Elongated swimmers, due to their higher aspect ratio, align more effectively with the flow, increasing their likelihood of being trapped [150, 152]. The relative swimming velocity is critical; if higher than a specific threshold— surprisingly less than the maximal azimuthal velocity of the vortex—the swimmer never gets trapped [150–152]. Additionally, introducing translational and rotational noise increases the likelihood of swimmers escaping, even if they were initially trapped [150, 151].

From a broader perspective, multiple vortices can be combined to generate a cellular flow and study the diffusion of active particles. Most works [153–155] observe a diffusive regime at long time scales and investigate the impact of various properties of active particles, such as persistence time, rotational noise, and other factors, on the diffusion coefficient. A similar approach was initiated during the PhD of Clément Gouiller [86], although it could not conclusively determine the long-term properties of the dynamics due to the limited size of the vortex network (4×4). His work provided an initial characterization of the behavior of camphor swimmers in cellular flows, demonstrating trapping when the vortical flow speed is three times higher than the spontaneous swimming speed.

Here, we focus on the coupling between the flow field of one vortex and the swimmer trajectory. After presenting the experimental setup developed for this study, we describe the trajectories observed at different rotation speeds. Finally, we model the system using the same simple approach described earlier (Subsec. 7.2.2), finding a good qualitative agreement with the experimental observations.

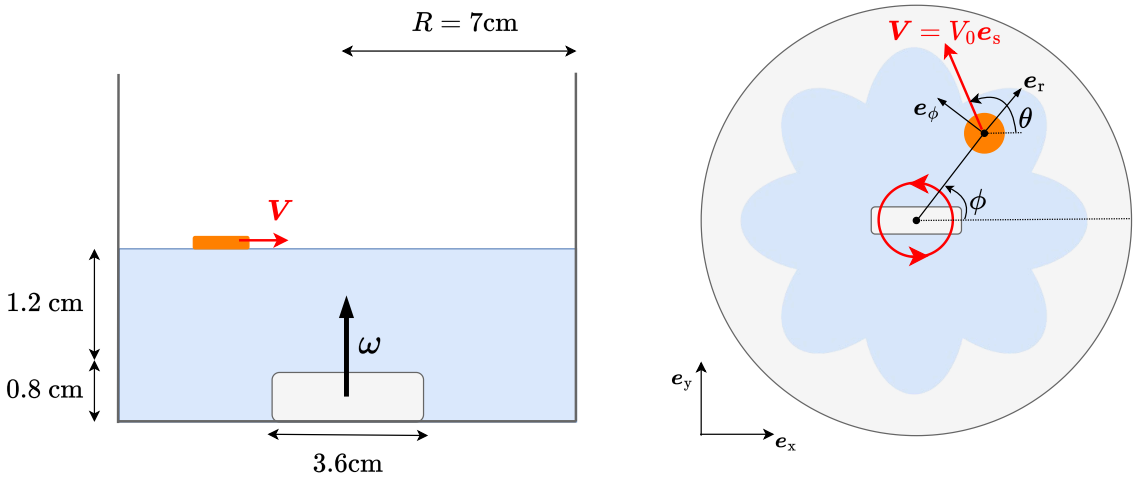

Figure 7.10: **Swimmer in a vortex, experimental setup.** Side view and top views of the experimental setup are shown (left and right respectively), drawings are not to scale. The swimmer is in orange and the magnetic stirrer in light gray. The rotation speed of the stirrer is controlled by a step motor placed below the tank. A plastic flower-shaped floating edge is placed at the surface to prevent trapping at the edge.

7.3.1 Experimental setup and characterization.

Generating the vortex flow. To generate the vortex, we use a step-by-step motor[1] coupled with a magnetic stirrer placed at the bottom of the pool (Fig. 7.10). The rotation of the stirrer generates a vortex in the fluid. In practice, the rotation speed is controlled through an Arduino card by choosing the time Δt between two consecutive motor steps. The motor induces the rotation of a magnet placed just below the tank, which in turn drives the magnetic stirrer above. The stirrer is 1.8 cm radius and placed into a circular pool of 7 cm radius (Fig. 7.10). The pool is filled with 2 cm of water, ensuring that the water height is everywhere at least 1 cm, a value for which the velocity of the swimmer reaches a plateau and does not depend anymore on the water height [24]. The setup is an adaptation of the one developed during Clément Gouiller's PhD [86].

Floating edges. Swimmers tend to follow the edges of the circular pool [84, 148], even in the presence of a vortex, resulting in circular trajectories along the wall and no interaction with the central vortex. To avoid such edge trapping, we use floating edges, designed to reintroduce the swimmers toward the center. Inspired by the work in [156], we used a flower-shaped floating edge (Fig. 7.10 right). The design is simple: as the swimmer follows the petal contour, the sharp ends of the petals direct it back toward the pool center. The floating edge is made from a thin plastic sheet and surrounds the free surface of the water.

[1] BL-TB6560 v2, 24 V

Characterization of the flow. The flow field $\mathbf{u}$ at the interface is characterized using PIV with glass bubbles as tracers (see Subsec. 2.3.2, page 37). The resulting flow field is a stationary vortex, with streamlines forming concentric circles (Fig. 7.11 left). In polar coordinate ($\mathbf{e}_r, \mathbf{e}_\phi$) (see notations Fig. 7.10 right) the velocity is orthoradial (Fig. 7.11 center), with the radial component u_r along $\mathbf{e}_r$ being approximately zero. The vortex generated by the magnetic stirrer can be approximated by a Rankine vortex [157]. In this model, the tangential velocity u_ϕ increases linearly from the center of the vortex up to a critical distance r_c where the flow velocity reaches its maximum value (Fig. 7.11 middle). Beyond r_c, the velocity decreases inversely with the radial distance:

$$u_\phi(r) = a \times r, \quad \text{for } r < r_\mathrm{c} \qquad u_\phi(r) = \frac{b}{r}, \quad \text{for } r > r_\mathrm{c}, \tag{7.8}$$

where a and b are positive constants related by $b = a \times r_\mathrm{c}^2$ [157]. Fitting the $u_\phi(r)$ curve with these expressions provides a good approximation (Fig. 7.11 middle, black lines). We find $r_\mathrm{c} = 1.2\,\mathrm{cm}$ which is smaller than the radius of the stirrer and remains the same for all rotation speeds used. In the following, the flow velocity will be indicated by $\chi = u(r = r_\mathrm{c})/V$, the ratio between the maximum velocity[2] generated by the vortex $u(r = r_\mathrm{c})$ and the swimmer spontaneous velocity V in quiescent water.

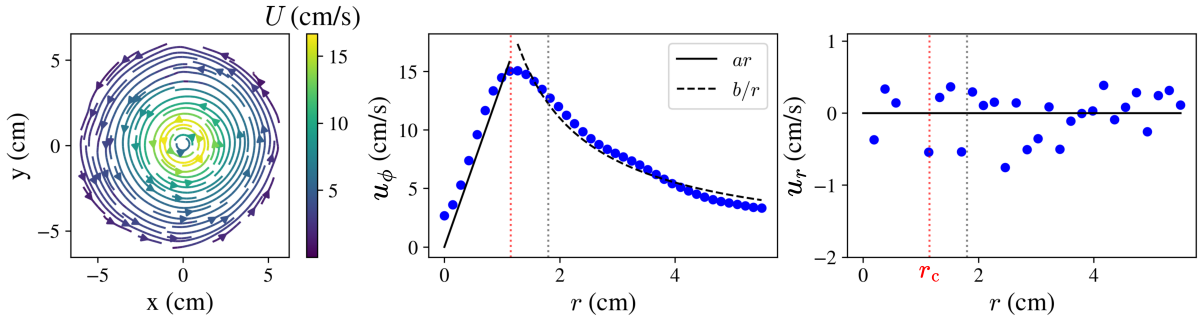

Figure 7.11: **Vortical flow.** Characterization of the flow field generated by the magnetic stirrer rotation. (Left) Time-averaged streamlines, the color indicates the norm of the flow velocity. (Center) Averaged orthoradial velocity u_ϕ at a distance r from the center of the vortex. The full black line corresponds to a linear fit $u_\phi = a \times r$, and the dashed line to the decay $u_\phi = b/r$. (Right) Averaged radial velocity u_r at a distance r from the center. The dashed gray dotted line corresponds to the limit of the stirrer and the red dotted line to the position r_c of velocity maximum.

The flow curves the trajectories. We study the impact of the vortex flow on the swimmer trajectory. In the presence of a vortical flow, the swimmer trajectory, which is normally straight (Fig. 7.12 left), becomes significantly curved (Fig. 7.12 right). In more detail, without flow, thanks to the floating edges the swimmer is reinjected toward the center of the tank and its trajectory is almost straight (Fig. 7.12 left). The swimming velocity is maximal at the center of the tank and gradually decreases as the swimmer moves closer to the floating edge. When a vortical flow is introduced (Fig. 7.12 right), the

[2]The maximum velocity observed at the interface depend on the rotation speed of the magnetic stirrer.

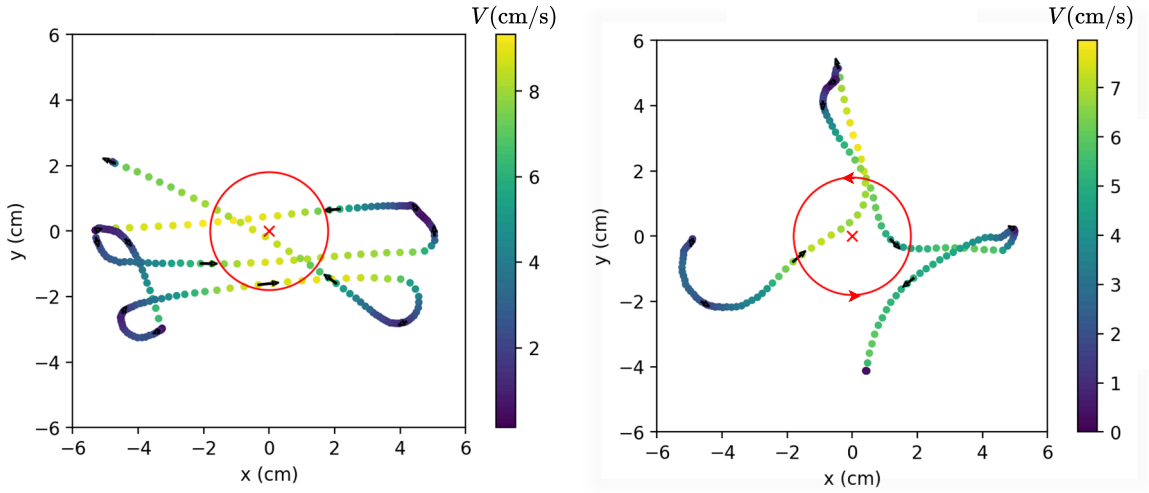

Figure 7.12: **Trajectories in a vortical flow**. One representative trajectory of a camphor swimmer of radius $a = 4\,\text{mm}$ in a circular tank of radius $R = 7\,\text{cm}$, without flow (left), and with a vortical flow (right). The colormap indicates the swimming velocity. The red circle corresponds to the position $r_c = 1.2\,\text{cm}$ of velocity maximum.

shape of the trajectories change significantly. The swimmer initially leaves the floating edge with a relatively straight trajectory, but as it approaches the center of the vortex, the advection induces a sharp curve of the trajectory. If the trajectory is initially not directed toward the center, the induced curvature is smoother (Fig. 7.12 bottom right trajectory).

7.3.2 Modeling.

7.3.2.1 Minimal toy model

As for the shear flow studied in Sec. ,we develop a minimal model that accounts only for the hydrodynamic interactions while neglecting the influence of surfactant distribution around the swimmer. In this simplified toy model, we consider a pointlike microswimmer that propels itself in a fixed swimming direction with a constant intrinsic velocity. The surfactant field is entirely disregarded, and the swimmer direction varies only under the influence of the surrounding flow. The toy model is the most basic and straightforward model possible. Despite its simplicity, the toy model has already demonstrated good predictive capability for the behavior of camphor swimmers in shear flow, as we have shown. Additionally, it has been successfully applied to the study of elongated particles in vortices, providing accurate predictions of ejection and trapping behavior [150].

The equation of motion is written as:

$$\mathbf{V}(\mathbf{r}_s, t) = \mathbf{u}(\mathbf{r}_s) + V_0 \mathbf{e}_s(t) \qquad \dot{\theta} = \Omega(\mathbf{r}_s), \tag{7.9}$$

where $\mathbf{V}$ is the absolute swimming velocity, $\mathbf{r}_s$ the position of the swimmer, V_0 the spontaneous swimming velocity in quiescent water, the swimming direction $\mathbf{e}_s$ is defined in Cartesian coordinate as $\mathbf{e}_s = \cos\theta \mathbf{e}_x + \sin\theta \mathbf{e}_y$ and Ω the rotational of the flow field. In a

Rankine vortex, the rotational is simply:

$$\Omega = \text{constant}, \quad \text{for } r < r_c \qquad \Omega = 0, \quad \text{for } r > r_c. \tag{7.10}$$

Numerical implementation. As the flow field is more complex, the problem can not be solved analytically and the swimmer motion is simulated numerically. The value of r_c is extracted from the experiment, and the velocity profile is given by Eq. (7.8). To implement the simulation, we use the Euler method, a straightforward numerical technique for solving ordinary differential equations. In the Euler method, the position and direction of the swimmer are updated step by step based on the current values. This iterative process allows us to reconstruct the swimmer trajectory over time. The simplicity of the Euler method makes it easy to implement, though it requires small time steps to ensure accuracy, especially in capturing the dynamics of the swimmer motion within the varying flow field. To simulate the trajectories we consider a circular domain of 4 cm radius (Fig. 7.13) which is equivalent to 1.5 cm away from the floating edges in the experiments, where the swimmer has a constant velocity. The swimmer enters the vortex at point M (Fig. 7.13) with an initial swimming direction θ_i. We study the impact of the vortex velocity and the initial swimmer direction on the trajectories.

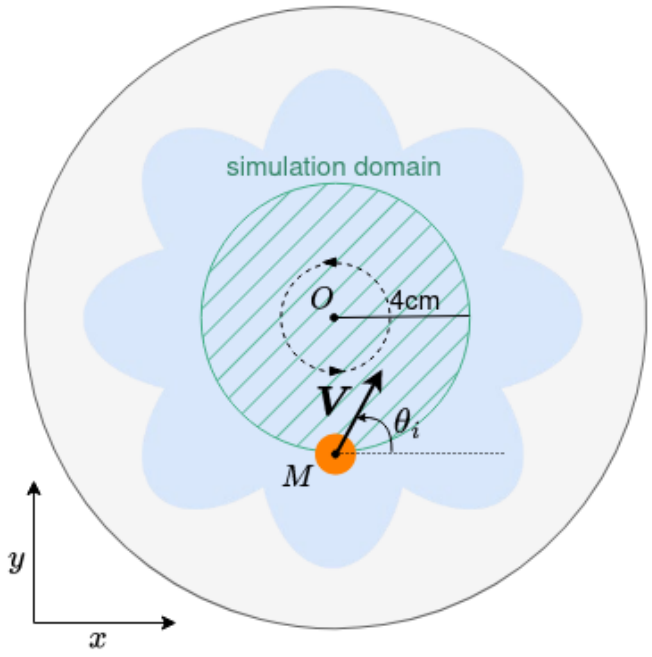

Figure 7.13: **Simulation domain.** To simulate the trajectory of a swimmer in a vortex, we consider a circle of 4 cm radius (green dashed area) whose distance to the floating edges is at least 1.5 cm. In this area the swimmer velocity is constant. The vortex is rotating counterclockwise with the maximum velocity position indicated by the black dashed circle. The swimmer enters the vortex at point M, with an initial swimming direction θ_i.

7.3.2.2 Results and comparison with experiments

Results of the simulation. In the absence of vortex ($\chi = 0$, Fig. 7.14 top left), all trajectories remain straight, with the swimmer maintaining a constant direction and velocity throughout the trajectory. As the vortical flow increases (Fig. 7.14 top center), the trajectories deviate from a straight line. Specifically, for initial swimming directions $\theta_i < \pi/3$ or $\theta_i > 2\pi/3$ the swimmer passes far from the vortex core ($r > r_c$) resulting in minimal deviation from the straight path observed without flow. However, for $\pi/3 < \theta_i < 2\pi/3$ the trajectories bend significally inside the vortex core ($r < r_c$). As a result, the swimmer exits the vortex farther to the left, with the exit position shifting counterclockwise (Fig. 7.14 top center). Notably, increasing θ_i does not lead to a monotonic increase in the exit position; instead, the interaction with the vortex flow causes varying levels of deviation depending on the specific entry angle, causing some trajectories to overlap. Further increasing the vortex flow to $\chi = 1$ (Fig. 7.14 top left) results in more curved trajectories, with the effect extending to paths passing farther from the vortex core.

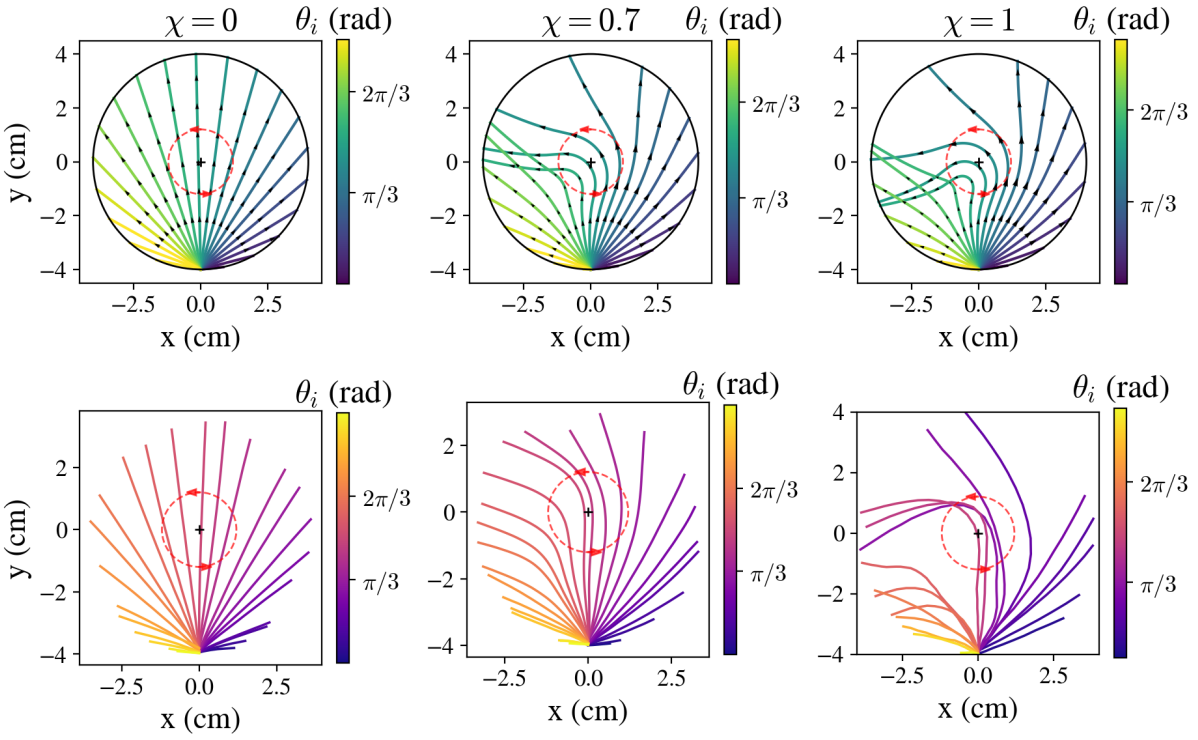

Figure 7.14: **Simulated and experimental trajectories in a vortex.** Here the area is restricted to a circle of 4 cm radius which corresponds to the area where the swimming velocity is almost constant. The vortex flow increases from left to right with $\chi = 0$, 0.7 and 1. (Top) Simulated trajectories, (bottom) averaged experimental trajectories rotated and aligned for comparison. The colormap corresponds to the initial swimming direction θ_i when the swimmer enters the vortex.

Experimental data processing and alignment for comparison. To facilitate a direct comparison between experimental data and simulation results, the experimental trajectories are first cropped and rotated. The motion data was segmented to include

only the portions where the swimmer remained within a 4 cm radius from the vortex center, aligning with the simulation domain. Next, these paths were rotated so that the swimmer consistently entered from the point $M\ (0, -4)$, while preserving the original swimming direction. For each swimmer, around 20 crossings inside the domain were recorded and processed within 2 min of the experiment. Finally, trajectories having similar initial swimming directions $\theta_i \pm \pi/40$ are averaged together. The results presented on Fig. 7.14 bottom, correspond to the trajectories of five different swimmers for three values of flow velocity.

Comparison with the simulation. The experimental results (Fig. 7.14 bottom), generally show qualitative agreement with the simulations. Specifically, for $\chi = 0$ (Fig. 7.14 bottom left) all trajectories remain straight. Increasing the vortical flow (Fig. 7.14 bottom center & right) results in more pronounced bending of the trajectories. As in the simulations, the change in swimming direction occurs when $r < r_c$. However, compared to the simulations, the swimmer paths in the experiments appear to be less altered for a similar ratio of vortex flow to swimming velocity. Only slight bending and no overlap of the trajectories are observed for $\chi = 0.7$ (Fig. 7.14 bottom center), and the experimental trajectories for $\chi = 1$ (Fig. 7.14 bottom right) seem closer to the numerical simulation results for $\chi = 0.7$ (Fig. 7.14 top center).

Regarding the swimming direction, when the swimmer arrives with $\theta_i < \pi/2$, its trajectory is already aligned with the direction of the vortex flow and it swims along with the vortex. If the swimmer arrives with $\theta_i > \pi/2$, its trajectory is opposite to the vortex flow, leading the swimmer to move against the flow. Finally, when $\theta_i = \pi/2$, the swimmer approaches the vortex perpendicularly to the flow direction. In this case, the trajectory bends in the flow direction and no spontaneous upstream rheotaxis is observed. This behavior could be due to the comparable size between the vortex core and the swimmer ($2 * a \simeq r_c$) which suggests that the interaction between the swimmer size and the flow structure plays a significant role in determining the swimmer trajectory. In a much larger vortex, one might expect to observe upstream swimming inside the vortex core, similar to the behavior observed in a large pool under shear flow (Subsec. 7.3.2.1).

Conclusion. Similar to the simple shear flow case, a minimal toy model effectively captures the qualitative impact of the vortex on the swimmer trajectories. However, further work is needed to extract quantitative data for a more precise comparison. One potential area for exploration is the impact of inertia, considering the swimmer as having finite mass. Incorporating inertia into the toy model could lead to more persistent swimming directions and a reduced influence of the vortex.

Conclusion and perspectives

This PhD work lies at the intersection of hydrodynamics and active matter, and aimed to address key questions in each field with a dual focus on studying single-body dynamics and exploring Marangoni flows generated by a mobile source. While propulsion using surface tension had reached a qualitative understanding of the mechanisms involved, a comprehensive quantitative description remained elusive.

Although theoretical and numerical approaches had been developed, current numerical methods are limited in their ability to accurately represent experimental systems, as key dimensionless numbers may differ by orders of magnitude. As a result, these methods do not yet provide a thorough understanding or a complete picture of the phenomena. On the experimental side, the characterization remained sparse, focusing primarily on the spontaneous swimming velocity—a global measure concealing numerous underlying mechanisms that are intricately interconnected. Therefore, a more detailed experimental characterization was needed to evaluate existing models, test their underlying assumptions, and gain deeper insights into the physical mechanisms driving the complex problem of Marangoni swimmer. Moreover, their interaction with external potential remain unexplored. Additionally, the motion of these swimmers is tied to Marangoni flows, which, despite having been studied for a long time and being present in a wide range of systems, continued to pose significant challenges in both theoretical understanding and modeling.

Accordingly, the goals of this thesis was twofold. First, to provide the first comprehensive characterization of a Marangoni swimmer in a stationary state, assessing the forces acting on the swimmer, the Marangoni flows generated, and the surfactant distribution. Second, to study the interaction of Marangoni swimmers with external couplings, such as a flow field or a harmonic potential. With these objectives in mind, we now summarize our achievements.

Complete experimental characterization

The first significant achievement of this PhD thesis is the experimental measurement of the force exerted by the fluid on the swimmer, the generated flows and the surface pressure field. To do so, we introduced a new experimental set up and novel, hybrid methodology that gives access to surface pressure, and ultimately, surfactant concentration.

Our experimental setup allows for simultaneous force and flow measurements in a stationary state, providing a new perspective by considering a fixed swimmer in a controlled flow. This approach enabled us to explore the effects of an imposed fluid flow at a pre-

scribed velocity. In contrast to many studies, our findings are not limited to the swimming velocity. In brief, we observed that the force exerted by the fluid on the swimmer changes sign, decreasing from 10 µN at $U = 4\,\mathrm{cm\,s^{-1}}$ to -30 µN at $U = 12\,\mathrm{cm\,s^{-1}}$. The numerical approach shows that the total force acting on the swimmer cannot simply be decomposed into a capillary force and the drag force experienced by a passive disc. Marangoni flows significantly influence the drag force, indicating their crucial role in modifying the overall force dynamics.

We then obtained the complete interfacial flow field in a stationary state under different advection velocities. Accessing the distribution of the surfactant proved to be the most challenging aspect. In the overwhelming majority of work, surfactant concentration remains a "hidden variable" [87]. In fact, only one previous study has measured surface tension behind a Marangoni swimmer [48]. To address this challenge, we introduced a hybrid approach that combines experimental data with numerical modeling to reconstruct the surface pressure field from the knowledge of the surface flow. Our method enables the deduction of a 3D flow field from a 2D flow, thereby accessing the Marangoni stress at the interface. By validating the method both numerically and experimentally on a well-known system, the Marangoni boat, we demonstrated that our approach remains reliable even under noisy and complex conditions that closely resemble real experimental scenarios.

Finally, we applied the developed method to the Marangoni swimmer, obtaining the first experimental characterization of the surface pressure field around a Marangoni swimmer and its chemical wake. Allowing us to assess the components of the force acting on the swimmer, such as drag and capillary forces, and opening new question into the transport dynamics of the surfactant.

Interaction with the flow

The earlier part of this thesis, which focused on the experimental characterization of swimming dynamics, proved to be both fruitful and complex. Building on this, the second goal was to explore the dynamics of Marangoni swimmers within an imposed flow. This exploration took two forms: first, a swimmer attached to a spring in an advective flow, and second, a free swimmer in both a simple shear flow and a vortex.

A swimmer attached to a spring exhibits unexpected behavior, displaying an ellipsoidal trajectory at low advection speeds, with amplitude decreasing as advection increases. Surprisingly motion stops before the advection speed matches the swimmer swimming velocity. While Marangoni flows are known for inducing instabilities, they are not the primary mechanism in this case. The observed behavior is well reproduced by a simple model that does not account for Marangoni flows, suggesting that the primary factors are the self-propulsion of the swimmer and the changes in surfactant distribution caused by advection.

For the second approach, we investigated Marangoni swimmers propelling in flow fields: a simple shear flow and a more complex one, a vortex. The trajectories of the swimmers were significantly impacted by advection. Despite the system complexity, a very simple toy model that forgets all the details of the surfactant distribution and propulsion mechanism—retaining only a spontaneous velocity and rotation by the flow—was able to capture the qualitative behavior of the swimmers. Preliminary work suggests that the observed differences between the model and the experimental results could be attributed to

inertia, indicating that this factor may play a more significant role than initially expected.

Perspectives

The experimental proposed methodology, that gives access to the surface pressure and concentration fields, provides a generic approach that could prove useful in lots of problems and a wide range of potential explorations that we have yet to embark on. One immediate area for investigation is the dynamics of surfactant transport, including flux, evaporation/dissolution, and absorption at the interface. This could involve comparisons with scaling laws from other studies [25, 31, 69]. Regarding Marangoni flows, the data obtained could be useful to discuss whether the treatment of Marangoni effects as an effective diffusion is appropriate or not. Another interesting perspective of study is whether there exists a simple relationship between the surfactant concentration field and the interfacial stress, analogous to the relationships observed in shallow water conditions under the lubrication approximation or in the Stokes flow where there is a closure relation [74].

More generally, the approach we developed could be extended to other problems that have been studied but remained incompletely characterized. For instance, it could be applied to a fixed source to explore the effects of different types of surfactants (soluble or insoluble, critical micelle concentration, etc.). Additionally, it could be used in very simple systems, such as a mobile punctual heat source, to provide direct comparisons with theoretical models. The decisive progress would be to have access to surfactant concentration, and thus avoid the curse of "hidden variables".

Coming back to Marangoni swimmers, another perspective opened by the present work is to investigate the interactions between swimmers. The developed experimental setup could be adapted to study two swimmers and measure the forces and flow fields they generate. Similarly, it could be used to investigate the interaction between a swimmer and a wall. In our current work, we have shown that the interaction with a simple flow is surprisingly well described by a basic model. It would be interesting to extend this research to more complex flow conditions, particularly network of vortices, which have been the focus of theoretical studies [153, 155]. Exploring such interactions could provide valuable insights and contribute to the development of more comprehensive models.

The findings and methods developed in this work open up numerous perspectives for addressing a wide range of Marangoni-related problems, offering a new path toward achieving a more complete understanding. As such, this work serves as a starting point rather than the final word on the subject. There is still much more to discover and understand about Marangoni flows and swimmers, indicating that this field remains ripe for further exploration.

Bibliography

[1] Étienne Fodor et al. "How Far from Equilibrium Is Active Matter?" In: *Physical Review Letters* 117.3 (July 13, 2016), p. 038103.

[2] Daniel Needleman et al. "Active Matter at the Interface between Materials Science and Cell Biology". In: *Nature Reviews Materials* 2.9 (July 20, 2017), pp. 1–14.

[3] Andrey Sokolov et al. "Physical Properties of Collective Motion in Suspensions of Bacteria". In: *Physical Review Letters* 109.24 (Dec. 14, 2012), p. 248109.

[4] Thierry Mora et al. "Local Equilibrium in Bird Flocks". In: *Nature Physics* 12.12 (Dec. 2016), pp. 1153–1157.

[5] Rémi Dreyfus et al. "Microscopic Artificial Swimmers". In: *Nature* 437.7060 (Oct. 2005), pp. 862–865.

[6] Jamel Ali et al. "Bacteria-Inspired Nanorobots with Flagellar Polymorphic Transformations and Bundling". In: *Scientific Reports* 7.1 (Oct. 26, 2017), p. 14098.

[7] Jeffrey Moran et al. "Microswimmers with No Moving Parts". In: *Physics Today* 72.5 (May 1, 2019), pp. 44–50.

[8] Hong-Ren Jiang et al. "Active Motion of a Janus Particle by Self-Thermophoresis in a Defocused Laser Beam". In: *Physical Review Letters* 105.26 (Dec. 20, 2010), p. 268302.

[9] Walter F. Paxton et al. "Catalytic Nanomotors: Autonomous Movement of Striped Nanorods". In: *Journal of the American Chemical Society* 126.41 (Oct. 1, 2004), pp. 13424–13431.

[10] Jonathan R. Howse et al. "Self-Motile Colloidal Particles: From Directed Propulsion to Random Walk". In: *Physical Review Letters* 99.4 (July 27, 2007), p. 048102.

[11] Ryan A. Pavlick et al. "A Polymerization-Powered Motor". In: *Angewandte Chemie International Edition* 50.40 (2011), pp. 9374–9377.

[12] Jeffrey L. Moran et al. "Phoretic Self-Propulsion". In: *Annual Review of Fluid Mechanics* 49 (Volume 49, 2017 Jan. 3, 2017), pp. 511–540.

[13] Nobuhiko J. Suematsu et al. "Evolution of Self-Propelled Objects: From the Viewpoint of Nonlinear Science". In: *Chemistry – A European Journal* 24.24 (2018), pp. 6308–6324.

[14] John W. M. Bush et al. "The Integument of Water-walking Arthropods: Form and Function". In: *Advances in Insect Physiology*. Ed. by J. Casas et al. Vol. 34. Insect Mechanics and Control. Academic Press, Jan. 1, 2007, pp. 117–192.

[15] Richard J. G. Löffler et al. “New Types of Complex Motion of a Simple Camphor Boat”. In: *Physical Chemistry Chemical Physics* 25.11 (Mar. 15, 2023), pp. 7794–7804.

[16] Yuichiro Karasawa et al. “Motion Modes of Two Self-Propelled Camphor Boats on the Surface of a Surfactant-Containing Solution”. In: *Journal of Colloid and Interface Science* 511 (Feb. 1, 2018), pp. 184–192.

[17] V. S. Akella et al. “Dynamics of a Camphoric Acid Boat at the Air–Water Interface”. In: *Physics Letters A* 382.17 (May 3, 2018), pp. 1176–1180.

[18] Ziane Izri et al. “Self-Propulsion of Pure Water Droplets by Spontaneous Marangoni Stress Driven Motion”. In: (2014).

[19] C. C. Maass et al. “Swimming Droplets”. In: *Annual Review of Condensed Matter Physics* 7 (2016), pp. 171–193.

[20] Sébastien Michelin. “Self-Propulsion of Chemically Active Droplets”. In: *Annual Review of Fluid Mechanics* 55 (Volume 55, 2023 Jan. 19, 2023), pp. 77–101.

[21] Matvey Morozov et al. “Self-Propulsion near the Onset of Marangoni Instability of Deformable Active Droplets”. In: *Journal of Fluid Mechanics* 860 (Feb. 2019), pp. 711–738.

[22] Nakata Satoshi et al. *Self-Rotation of a Camphor Scraping on Water: New Insight into the Old Problem*. ACS Publications. Aug. 6, 1997.

[23] Tamás Jr. Bánsági et al. “Motion and Interaction of Aspirin Crystals at Aqueous–Air Interfaces”. In: *The Journal of Physical Chemistry B* 117.43 (Oct. 31, 2013), pp. 13572–13577.

[24] Dolachai Boniface et al. “Self-Propulsion of Symmetric Chemically Active Particles: Point-source Model and Experiments on Camphor Disks”. In: *Physical Review E* 99.6 (June 17, 2019), p. 062605.

[25] Hendrik Ender et al. “Surfactant-Loaded Capsules as Marangoni Microswimmers at the Air–Water Interface: Symmetry Breaking and Spontaneous Propulsion by Surfactant Diffusion and Advection”. In: *The European Physical Journal E* 44.2 (Mar. 8, 2021), p. 21.

[26] Tetsu Mitsumata et al. “Shape Memory Functions and Motility of Amphiphilic Polymer Gels”. In: *Polymers for Advanced Technologies* 12.1-2 (2001), pp. 136–150.

[27] Noy Bassik et al. “Solvent Driven Motion of Lithographically Fabricated Gels”. In: *Langmuir* 24.21 (Nov. 4, 2008), pp. 12158–12163.

[28] Satoshi Nakata et al. “Mode Selection of a Camphor Boat in a Dual-Circle Canal”. In: *Chemical Physics Letters* 322.5 (May 26, 2000), pp. 419–423.

[29] Albina Musin et al. “Self-Propulsion of a Metallic Superoleophobic Micro-Boat”. In: *Journal of Colloid and Interface Science* 479 (Oct. 1, 2016), pp. 182–188.

[30] Charles Tomlinson. “On the Motions of Camphor on the Surface of Water. [Abstract]”. In: *Proceedings of the Royal Society of London* 11 (1860), pp. 575–577.

[31] Dolachai Boniface. “Dynamics of Interfacial Swimmers”. In: (2021).

[32] Yumihiko S. Ikura et al. “Collective Motion of Symmetric Camphor Papers in an Annular Water Channel”. In: *Physical Review E* 88.1 (July 30, 2013), p. 012911.

[33] Siowling Soh et al. “Dynamic Self-Assembly in Ensembles of Camphor Boats”. In: *The Journal of Physical Chemistry B* 112.35 (Sept. 4, 2008), pp. 10848–10853.

[34] Nobuhiko J. Suematsu et al. “Synchronized Intermittent Motion Induced by the Interaction between Camphor Disks”. In: *Journal of the Physical Society of Japan* 84.3 (Mar. 15, 2015), p. 034802.

[35] Jahir Orozco et al. “Efficient Biocatalytic Degradation of Pollutants by Enzyme-Releasing Self-Propelled Motors”. In: *Chemistry – A European Journal* 20.10 (2014), pp. 2866–2871.

[36] Abdon Pena-Francesch et al. “Multifunctional and Biodegradable Self-Propelled Protein Motors”. In: *Nature Communications* 10.1 (July 18, 2019), p. 3188.

[37] Yasuhiro Ikezoe et al. “Peptide Assembly-Driven Metal–Organic Framework (MOF) Motors for Micro Electric Generators”. In: *Advanced Materials* 27.2 (2015), pp. 288–291.

[38] Pierre-Gilles de Gennes et al. *Capillarity and Wetting Phenomena: Drops, Bubbles, Pearls, Waves*. Springer Science & Business Media, Sept. 12, 2003. 320 pp.

[39] M. V. Berry. “The Molecular Mechanism of Surface Tension”. In: *Physics Education* 6.2 (Mar. 1971), p. 79.

[40] Habil. Reinhard Miller. “Surfactants and Interfacial Phenomena”. In: *Tenside Surfactants Detergents* 49.5 (2012/09//Sep/Oct2012), pp. 361–361.

[41] Bidisha Das et al. “Comprehensive Review on Applications of Surfactants in Vaccine Formulation, Therapeutic and Cosmetic Pharmacy and Prevention of Pulmonary Failure Due to COVID-19”. In: *Chemistry Africa* 5.3 (2022), pp. 459–480.

[42] Maura C. Puerto. “Surfactants: Fundamentals and Applications in the Petroleum Industry: Cambridge University Press, 2000, Pp. 621, £85.00 (US$ 140.00) (Hardback), ISBN 0-521-64067-9”. In: *Chemical Engineering Journal* 83.1 (Apr. 15, 2001), p. 63.

[43] He Yunfei et al. “Surfactant Adsorption onto Interfaces: Measuring the Surface Excess in Time”. In: *Langmuir* 28.6 (Feb. 14, 2012), pp. 3146–3151.

[44] L. E. Scriven et al. “The Marangoni Effects”. In: *Nature* 187.4733 (July 1960), pp. 186–188.

[45] J. B. Fournier et al. “Tears of Wine”. In: *Europhysics Letters* 20.6 (Nov. 1992), p. 517.

[46] Isabelle Cantat et al. *Foams: Structure and Dynamics*. OUP Oxford, July 11, 2013. 278 pp.

[47] Wim Fyen et al. “Chapter 19 - A Detailed Study of Semiconductor Wafer Drying”. In: *Developments in Surface Contamination and Cleaning (Second Edition)*. Ed. by Rajiv Kohli et al. Oxford: William Andrew Publishing, Jan. 1, 2008, pp. 795–854.

[48] Tomonori Nomoto et al. “Time-Resolved Measurements of Interfacial Tension and Flow Speed of the Inclined Water Surface around a Self-propelled Camphor Boat by the Quasi-elastic Laser Scattering Method”. In: *The Journal of Physical Chemistry B* 127.12 (Mar. 30, 2023), pp. 2863–2871.

[49] Masahiro I. Kohira et al. “Synchronized Self-Motion of Two Camphor Boats”. In: *Langmuir* 17.22 (Oct. 1, 2001), pp. 7124–7129.

[50] Darren Crowdy. “Viscous Propulsion of a Two-Dimensional Marangoni Boat Driven by Reaction and Diffusion of Insoluble Surfactant”. In: *Physical Review Fluids* 6.6 (June 17, 2021), p. 064003.

[51] Tomasz Roliński et al. “Quantitative Analysis of the Complex Time Evolution of a Camphor Boat”. In: *Applied Sciences* 14.3 (3 Jan. 2024), p. 959.

[52] Nobuhiko J. Suematsu et al. “Quantitative Estimation of the Parameters for Self-Motion Driven by Difference in Surface Tension”. In: *Langmuir* 30.27 (July 15, 2014), pp. 8101–8108.

[53] Lisa J. Burton et al. “The Cocktail Boat”. In: *Integrative and Comparative Biology* 54.6 (2014), pp. 969–973.

[54] Eric Lauga et al. “Viscous Marangoni Propulsion”. In: *Journal of Fluid Mechanics* 705 (Aug. 2012), pp. 120–133.

[55] Hassan Masoud et al. “A Reciprocal Theorem for Marangoni Propulsion”. In: *Journal of Fluid Mechanics* 741 (Feb. 2014), R4.

[56] Alois Würger. “Thermally Driven Marangoni Surfers”. In: *Journal of Fluid Mechanics* 752 (Aug. 2014), pp. 589–601.

[57] J. P. Gong et al. “Motion of Polymer Gels by Spreading Organic Fluid on Water”. In: *The Journal of Physical Chemistry* 100.26 (Jan. 1, 1996), pp. 11092–11097.

[58] Yuko Hayashima et al. “A Camphor Grain Oscillates While Breaking Symmetry”. In: *The Journal of Physical Chemistry B* 105.22 (June 1, 2001), pp. 5353–5357.

[59] Clément Gouiller et al. “Mixing and Unmixing Induced by Active Camphor Particles”. In: *Physical Review Fluids* 6.1 (Jan. 27, 2021), p. 014501.

[60] Sébastien Michelin et al. “Spontaneous Autophoretic Motion of Isotropic Particles”. In: *Physics of Fluids* 25.6 (June 11, 2013), p. 061701.

[61] Xinfu Chen et al. “Self-Motion of Camphor Discs. Model and Analysis”. In: *Networks and Heterogeneous Media* 4.1 (Sun Feb 01 00:00:00 UTC 2009), pp. 1–18.

[62] Dolachai Boniface et al. “Role of Marangoni Forces in the Velocity of Symmetric Interfacial Swimmers”. In: *Physical Review Fluids* 6.10 (Oct. 21, 2021), p. 104006.

[63] Carlo Marangoni. *Sull’espansione delle goccie d’un liquido galleggianti sulla superfice di altro liquido*. Fratelli Fusi, 1865. 66 pp.

[64] Cesar L. Usma et al. “Fluorescent Marangoni Flows under Quasi-Steady Conditions”. In: *Langmuir* 38.30 (Aug. 2, 2022), pp. 9129–9135.

[65] Matthieu Roché et al. “Marangoni Flow of Soluble Amphiphiles”. In: *Physical Review Letters* 112 (May 1, 2014), p. 208302.

[66] Sébastien Le Roux et al. “Soluble Surfactant Spreading: How the Amphiphilicity Sets the Marangoni Hydrodynamics”. In: *Physical Review E* 93.1 (Jan. 6, 2016), p. 013107.

[67] Corentin Tregouet et al. “Stability of a Directional Marangoni Flow”. In: *Soft Matter* 16.38 (Oct. 7, 2020), pp. 8933–8939.

[68] M. M. Bandi et al. “Hydrodynamic Signatures of Stationary Marangoni-Driven Surfactant Transport”. In: *Physical Review Letters* 119.26 (Dec. 29, 2017), p. 264501.

[69] Shreyas Mandre. “Axisymmetric spreading of surfactant from a point source”. In: *Journal of Fluid Mechanics* 832 (Dec. 2017), pp. 777–792.

[70] Jobe Alan H. “Pulmonary Surfactant Therapy”. In: *New England Journal of Medicine* 328.12 (1993), pp. 861–868.

[71] Ivan B. Ivanov et al. “Stability of Emulsions under Equilibrium and Dynamic Conditions”. In: *Colloids and Surfaces A: Physicochemical and Engineering Aspects*.

A Collection of Papers Presented at the 11th International Symposium on Surfactants in Solution 128.1 (Aug. 1, 1997), pp. 155–175.

[72] Donald P. Gaver et al. "The Dynamics of a Localized Surfactant on a Thin Film". In: *Journal of Fluid Mechanics* 213 (Apr. 1990), pp. 127–148.

[73] Iu.K. Bratukhin et al. "Thermocapillary Convection in a Fluid Filling a Half-Space. PMM Vol. 31, No. 3, 1967, Pp. 577-580". In: *Journal of Applied Mathematics and Mechanics* 31.3 (Jan. 1, 1967), pp. 605–608.

[74] A. Thess et al. "Viscous Flow at Infinite Marangoni Number". In: *Physical Review Letters* 75.25 (Dec. 18, 1995), pp. 4614–4617.

[75] A. Thess. "Stokes Flow at Infinite Marangoni Number: Exact Solutions for the Spreading and Collapse of a Surfactant". In: *Physica Scripta* 1996.T67 (Jan. 1996), p. 96.

[76] Darren G. Crowdy. "Viscous Marangoni Flow Driven by Insoluble Surfactant and the Complex Burgers Equation". In: *SIAM Journal on Applied Mathematics* 81.6 (2021), pp. 2526–2546.

[77] Thomas Bickel et al. "Exact Solutions for Viscous Marangoni Spreading". In: *Physical Review E* 106.4 (2022), p. 045107.

[78] Thomas Bickel. "Spreading Dynamics of Reactive Surfactants Driven by Marangoni Convection". In: *Soft Matter* 15.18 (2019), pp. 3644–3648.

[79] Hiroyuki Kitahata et al. "Effective Diffusion Coefficient Including the Marangoni Effect". In: *The Journal of Chemical Physics* 148.13 (Apr. 7, 2018), p. 134906.

[80] Yui Matsuda et al. "Acceleration or Deceleration of Self-Motion by the Marangoni Effect". In: *Chemical Physics Letters* 654 (June 16, 2016), pp. 92–96.

[81] H. A. R. Williams. "Two-Dimensional Nonlinear Advection-Diffusion in a Model of Surfactant Spreading on a Thin Liquid Film". In: *IMA Journal of Applied Mathematics* 66.1 (Jan. 1, 2001), pp. 55–82.

[82] Vahid Vandadi et al. "Reverse Marangoni Surfing". In: *Journal of Fluid Mechanics* 811 (Jan. 2017), pp. 612–621.

[83] Saeed Jafari Kang et al. "Forward, Reverse, and No Motion of Marangoni Surfers under Confinement". In: *Physical Review Fluids* 5.8 (Aug. 12, 2020), p. 084004.

[84] Samrat Sur et al. "Translational and Rotational Motion of Disk-Shaped Marangoni Surfers". In: *Physics of Fluids* 31.10 (Oct. 2019), p. 102101.

[85] Hiroyuki Kitahata et al. "Self-Motion of a Camphor Disk Coupled with Convection". In: *Physical Chemistry Chemical Physics* 6.9 (2004), p. 2409.

[86] Clément Gouiller. "Nageurs Interfaciaux : Dynamique, Transport et Dispersion". These de doctorat. Lyon, July 13, 2021.

[87] Harishankar Manikantan et al. "Surfactant dynamics: hidden variables controlling fluid flows". In: *Journal of Fluid Mechanics* 892 (June 2020).

[88] Babak Vajdi Hokmabad et al. "Chemotactic Self-Caging in Active Emulsions". In: *Proceedings of the National Academy of Sciences* 119.24 (June 14, 2022), e2122269119.

[89] F. K Hansen et al. "Surface Tension by Pendant Drop: I. A Fast Standard Instrument Using Computer Image Analysis". In: *Journal of Colloid and Interface Science* 141.1 (Jan. 1, 1991), pp. 1–9.

[90] D. N Staicopolus. “The Computation of Surface Tension and of Contact Angle by the Sessile-Drop Method”. In: *Journal of Colloid Science* 17.5 (June 1, 1962), pp. 439–447.

[91] Nikhil Bagalkot et al. “Dynamic Interfacial Tension Measurement Method Using Axisymmetric Drop Shape Analysis”. In: *MethodsX* 5 (Jan. 1, 2018), pp. 676–683.

[92] K. Lunkenheimer et al. “Determination of the Surface Tension of Surfactant Solutions Applying the Method of Lecomte Du Noüy (Ring Tensiometer)”. In: *Colloid and Polymer Science* 259.3 (Mar. 1, 1981), pp. 354–366.

[93] Ning Wu et al. “Dynamic Surface Tension Measurement with a Dynamic Wilhelmy Plate Technique”. In: *Journal of Colloid and Interface Science* 215.2 (July 15, 1999), pp. 258–269.

[94] Jaroslaw Drelich et al. “Measurement of Interfacial Tension in Fluid-Fluid Systems”. In: *Encyclopedia of Surface and Colloid Science* (2002).

[95] Yuichiro Karasawa et al. “Simultaneous Measurement of Surface Tension and Its Gradient around Moving Camphor Boat on Water Surface”. In: *Chemistry Letters* 43.7 (July 5, 2014), pp. 1002–1004.

[96] Shogo Oshima et al. “Surface Tension Gradient around an Alcohol Droplet Moving Spontaneously on a Water Surface”. In: *Analytical Sciences: The International Journal of the Japan Society for Analytical Chemistry* 30.4 (2014), pp. 441–444.

[97] Siowling Soh et al. “Swarming in Shallow Waters”. In: *The Journal of Physical Chemistry Letters* 2.7 (Apr. 7, 2011), pp. 770–774.

[98] Giuseppe Pucci et al. “Friction on Water Sliders”. In: *Scientific Reports* 9.1 (1 Mar. 11, 2019), p. 4095.

[99] HK Yuen et al. “Comparative Study of Hough Transform Methods for Circle Finding”. In: *Image and Vision Computing* 8.1 (Feb. 1, 1990), pp. 71–77.

[100] M. D. Atkins. “Chapter 5 - Velocity Field Measurement Using Particle Image Velocimetry (PIV)”. In: *Application of Thermo-Fluidic Measurement Techniques*. Ed. by Tongbeum Kim et al. Butterworth-Heinemann, Jan. 1, 2016, pp. 125–166.

[101] C Brossard et al. “Principles and Applications of Particle Image Velocimetry”. In: 1 (2009).

[102] M. Raffel et al. *Particle Image Velocimetry: A Practical Guide*. Jan. 1, 2007.

[103] Sven Scharnowski et al. “Particle Image Velocimetry - Classical Operating Rules from Today’s Perspective”. In: *Optics and Lasers in Engineering* 135 (Dec. 1, 2020), p. 106185.

[104] Bruce D. Lucas et al. “An Iterative Image Registration Technique with an Application to Stereo Vision”. In: *Proceedings of Imaging Understanding Workshop, pp. 121-130* (1981).

[105] Jean-Yves Bouguet. “Pyramidal Implementation of the Lucas Kanade Feature Tracker Description of the Algorithm”. In: ().

[106] Jianbo Shi et al. “Good Features to Track”. In: *1994 Proceedings of IEEE Conference on Computer Vision and Pattern Recognition* (1994), pp. 593–600.

[107] R. Courant. “Variational Methods for the Solution of Problems of Equilibrium and Vibrations”. In: *Bulletin of the American Mathematical Society* 49.1 (Jan. 1943), pp. 1–23.

[108] L. Wang et al. “Modeling of Thermal Properties and Failure of Thermal Barrier Coatings with the Use of Finite Element Methods: A Review”. In: *Journal of the European Ceramic Society* 36.6 (2016/05/01/May 2016///), pp. 1313–1331.

[109] Andrea Bonito et al. “Adaptive Finite Element Methods”. In: (2024).

[110] Albert G. Prinn. “A Review of Finite Element Methods for Room Acoustics”. In: *Acoustics (2624-599X)* 5.2 (June 2023), pp. 367–395.

[111] Teemu Salminen et al. “Application of the Finite Element Method to the Multicomponent General Dynamic Equation of Aerosols”. In: *Journal of Aerosol Science* 174 (Nov. 1, 2023), p. 106260.

[112] Edward L. Wilson et al. “Application of the Finite Element Method to Heat Conduction Analysis”. In: *Nuclear Engineering and Design* 4.3 (Oct. 1, 1966), pp. 276–286.

[113] Marina A. Tsili et al. “Power Transformer Thermal Analysis by Using an Advanced Coupled 3D Heat Transfer and Fluid Flow FEM Model”. In: *International Journal of Thermal Sciences* 53 (Mar. 1, 2012), pp. 188–201.

[114] Jian-Ming Jin. *The Finite Element Method in Electromagnetics*. John Wiley & Sons, Feb. 18, 2015. 728 pp.

[115] John Happel et al. *Low Reynolds Number Hydrodynamics: With Special Applications to Particulate Media*. Red. by R. J. Moreau. Vol. 1. Mechanics of Fluids and Transport Processes. Dordrecht: Springer Netherlands, 1983.

[116] Randall J. LeVeque. “1. Finite Difference Approximations”. In: *Finite Difference Methods for Ordinary and Partial Differential Equations*. Other Titles in Applied Mathematics. Society for Industrial and Applied Mathematics, Jan. 2007, pp. 3–11.

[117] Masaharu Nagayama et al. “A Theoretical and Experimental Study on the Unidirectional Motion of a Camphor Disk”. In: *Physica D: Nonlinear Phenomena* 194.3-4 (July 2004), pp. 151–165.

[118] Keita Iida et al. “Theoretical Study on the Translation and Rotation of an Elliptic Camphor Particle”. In: *Physica D: Nonlinear Phenomena* 272 (Apr. 1, 2014), pp. 39–50.

[119] Hiroyuki Kitahata et al. “Spontaneous Motion of an Elliptic Camphor Particle”. In: *Physical Review E* 87.1 (Jan. 7, 2013), p. 010901.

[120] Alexander Mikhailov et al. “Self-Motion in Physico-Chemical Systems Far from Thermal Equilibrium”. In: *Stochastic Dynamics*. Ed. by Lutz Schimansky-Geier et al. Berlin, Heidelberg: Springer, 1997, pp. 334–345.

[121] Satoshi Nakata et al. “Physicochemical Design and Analysis of Self-Propelled Objects That Are Characteristically Sensitive to Environments”. In: *Physical Chemistry Chemical Physics* 17.16 (Apr. 8, 2015), pp. 10326–10338.

[122] Gerrit E. Elsinga et al. “Tomographic 3D-PIV and Applications”. In: *Particle Image Velocimetry: New Developments and Recent Applications*. Berlin, Heidelberg: Springer, 2008, pp. 103–125.

[123] I. Benouaguef et al. “"Solutocapillary Marangoni Flow Induced in Waterbody by Solute Source"”. In: *Journal of Fluid Mechanics* 922 (Sept. 10, 2021), A23.

[124] J. Drelich et al. *Interfacial Tension Measurement in Fluid–Fluid Systems*. 2015.

[125] Satoshi Nakata et al. “Characteristic Self-Motion of a Camphor Boat Sensitive to Ester Vapor”. In: *Langmuir* 21.3 (Feb. 1, 2005), pp. 982–984.

[126] Babak Vajdi Hokmabad et al. “Emergence of Bimodal Motility in Active Droplets”. In: *Physical Review X* 11.1 (Mar. 3, 2021), p. 011043.

[127] Tomonori Nomoto et al. “Flow-Driven Self-Propulsion of Oil Droplet on a Surfactant Solution Surface, as Observed by Time-Resolved Interfacial Tension and Surface Flow Speed Measurements”. In: *Langmuir: the ACS journal of surfaces and colloids* 40.8 (Feb. 27, 2024), pp. 4468–4474.

[128] Shoko Uemoto et al. “Assemblies of Molecular Aggregates in the Blebbing Motion of an Oil Droplet on an Aqueous Solution Containing Surfactant”. In: *Colloids and Surfaces A: Physicochemical and Engineering Aspects* 529 (Sept. 20, 2017), pp. 373–379.

[129] Ronald J. Adrian. “Particle-Imaging Techniques for Experimental Fluid Mechanics”. In: *Annual Review of Fluid Mechanics* 23 (Volume 23, 1991 Jan. 1, 1991), pp. 261–304.

[130] Pierre Bon et al. “Quadriwave Lateral Shearing Interferometry for Quantitative Phase Microscopy of Living Cells”. In: *Optic Express* 17.15 (July 20, 2009), pp. 13080–13094.

[131] Ben C Platt et al. “History and Principles of Shack-Hartmann Wavefront Sensing”. In: *Journal of Refractive Surgery* 17.5 (Sept. 2001).

[132] Mourad Idir et al. “X-Ray Active Mirror Coupled with a Hartmann Wavefront Sensor”. In: *Nuclear Instruments and Methods in Physics Research Section A: Accelerators, Spectrometers, Detectors and Associated Equipment* 616.2 (2010), pp. 162–171.

[133] Lei Huang et al. “Dynamic Three-Dimensional Sensing for Specular Surface with Monoscopic Fringe Reflectometry”. In: *Optics Express* 19.13 (June 20, 2011), pp. 12809–12814.

[134] Lei Huang et al. “Comparison of Two-Dimensional Integration Methods for Shape Reconstruction from Gradient Data”. In: *Optics and Lasers in Engineering* 64 (Jan. 2015), pp. 1–11.

[135] Claudio Mancinelli et al. “A Comparison of Methods for Gradient Field Estimation on Simplicial Meshes”. In: *Computers & Graphics* 80 (May 2019), pp. 37–50.

[136] O. K. Matar et al. “Dynamics of Surfactant-Assisted Spreading”. In: *Soft Matter* 5.20 (2009), p. 3801.

[137] Abdallah Daddi-Moussa-Ider et al. “Hydrodynamic Efficiency Limit on a Marangoni Surfer”. In: *Journal of Fluid Mechanics* 986 (May 10, 2024), A32.

[138] M R Abdulwahab et al. “A Review in Particle Image Velocimetry Techniques (Developments and Applications)”. In: (Jan. 1, 2020).

[139] H. a. R. Williams et al. “Two-Dimensional Nonlinear Advection–Diffusion in a Model of Surfactant Spreading on a Thin Liquid Film”. In: *IMA Journal of Applied Mathematics* 66.1 (Jan. 2001), pp. 55–82.

[140] D.R. Brumley et al. “Flagella, Flexibility and Flow: Physical Processes in Microbial Ecology”. In: *The European Physical Journal Special Topics* 224.17 (Dec. 1, 2015), pp. 3119–3140.

[141] Jérémie Palacci et al. “Artificial Rheotaxis”. In: *Science Advances* 1.4 (May 2015), e1400214.

[142] Abdallah Daddi-Moussa-Ider et al. “Tuning the Upstream Swimming of Microrobots by Shape and Cargo Size”. In: *Physical Review Applied* 14.2 (Aug. 25, 2020), p. 024071.

[143] Priyanka Sharan et al. “Upstream Rheotaxis of Catalytic Janus Spheres”. In: (Dec. 8, 2021).

[144] Bishwa Ranjan Si et al. “Self-Propelled Janus Colloids in Shear Flow”. In: *Langmuir* 36.40 (Oct. 13, 2020), pp. 11888–11898.

[145] Ranabir Dey et al. “Oscillatory Rheotaxis of Artificial Swimmers in Microchannels”. In: *Nature Communications* 13.1 (1 May 26, 2022), p. 2952.

[146] Prateek Dwivedi et al. “Rheotaxis of Active Droplets”. In: *Physics of Fluids* 33.8 (Aug. 18, 2021), p. 082108.

[147] Andreas Zöttl et al. “Nonlinear Dynamics of a Microswimmer in Poiseuille Flow”. In: *Physical Review Letters* 108.21 (May 22, 2012), p. 218104.

[148] Yuki Koyano et al. “Rotational Motion of a Camphor Disk in a Circular Region”. In: *Physical Review E* 99.2 (Feb. 19, 2019), p. 022211.

[149] Andrey Sokolov et al. “Rapid Expulsion of Microswimmers by a Vortical Flow”. In: *Nature Communications* 7.1 (Mar. 23, 2016), p. 11114.

[150] Ivan Tanasijević et al. “Microswimmers in Vortices: Dynamics and Trapping”. In: *Soft Matter* 18.47 (Dec. 7, 2022), pp. 8931–8944.

[151] José-Agustín Arguedas-Leiva et al. “Microswimmers in an Axisymmetric Vortex Flow”. In: *New Journal of Physics* 22.5 (May 2020), p. 053051.

[152] Simon A. Berman et al. “Trapping of Swimmers in a Vortex Lattice”. In: *Chaos: An Interdisciplinary Journal of Nonlinear Science* 30.6 (June 1, 2020), p. 063121.

[153] Lorenzo Caprini et al. “Diffusion Properties of Self-Propelled Particles in Cellular Flows”. In: *Soft Matter* 16.23 (June 17, 2020), pp. 5431–5438.

[154] Yunyun Li et al. “Diffusion of Chiral Janus Particles in Convection Rolls”. In: *Physical Review Research* 2.1 (Mar. 3, 2020), p. 013250.

[155] Pulak K. Ghosh et al. “Diffusion of Active Particles in Convective Flows”. In: *Soft Matter* 17.8 (Mar. 4, 2021), pp. 2256–2264.

[156] Julien Deseigne et al. “Collective Motion of Vibrated Polar Disks”. In: *Physical Review Letters* 105.9 (Aug. 23, 2010), p. 098001.

[157] Gábor Halász et al. “Vortex Flow Generated by a Magnetic Stirrer”. In: *American Journal of Physics* 75.12 (Dec. 1, 2007), pp. 1092–1098.